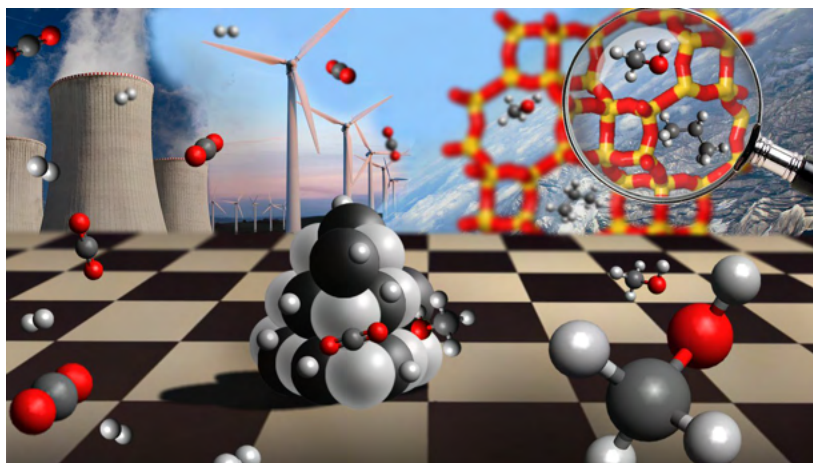




Università degli Studi di Torino
Doctoral School of the University of Torino
PhD Programme in Chemical and Materials Sciences XXXV Cycle

Spectroscopic characterization of bifunctional catalysts for CO₂ hydrogenation to methanol and conversion to hydrocarbons



Pierfrancesco Ticali

Supervisor:
Prof. Silvia Bordiga

Co-supervisor:
Dr. Sara Morandi



Università degli Studi di Torino

Doctoral School of the University of Torino

PhD Programme in Chemical and Materials Sciences XXXV cycle

Spectroscopic characterization of bifunctional catalysts for CO₂ hydrogenation to methanol and conversion to hydrocarbons

Candidate: **Pierfrancesco Ticali**

Supervisor: Prof. **Silvia Bordiga**

Jury Members: Prof. **Elena Groppo**
Università degli studi di Torino
Dipartimento di Chimica

Prof. **Enrica Gianotti**
Università del Piemonte Orientale
Dipartimento per lo Sviluppo Sostenibile e la Transizione Ecologica

Prof. **Davide Ferri**
Paul Scherrer Institute
Applied Catalysis and Spectroscopy group

Head of the Doctoral School: Prof.ssa Eleonora Bonifacio

PhD Programme Coordinator: Prof. Bartolomeo Civalieri

Torino, 2022

CONTENTS

INTRODUCTION.....	1
CHAPTER I	
CO₂ hydrogenation.....	3
1.1 State of the art: from waste to value-added products.....	3
<i>1.1.1 Variety of target products: DME, methanol, CO, etc.</i>	<i>6</i>
<i>1.1.2 Variety of process approaches: thermocatalysis, electrocatalysis, photocatalysis, etc.....</i>	<i>10</i>
1.2 Methanol as energetic vector for a new platform for the synthesis of simple hydrocarbon. COZMOS Concept.....	13
1.3 Bifunctional catalysts.....	15
<i>1.3.1 The role of the metallic/oxidic phase.....</i>	<i>15</i>
<i>1.3.2 Mixed oxides.....</i>	<i>16</i>
<i>1.3.3 The role of the zeolite.....</i>	<i>18</i>
REFERENCES.....	24

CHAPTER II

Samples and characterization techniques	36
2.1 PdZn/ZrO₂ + SAPO-34 catalyst	36
2.1.1 <i>Synthesis and basic characterization</i> <i>of PdZn/ZrO₂ catalyst catalyst</i>	37
2.1.2 <i>SAPO-34: structure and textural properties</i>	38
2.1.3 <i>Synthesis and basic characterization</i> <i>of the scaled up catalysts</i>	39
2.2 ZnZrO_x + ZSM-5 catalyst	43
2.2.1 <i>Synthesis of ZnZrO_x catalysts</i>	43
2.2.2 <i>ZSM-5: structure and textural properties</i>	45
2.3 ZnCeZrO_x + RUB-13 catalyst	46
2.3.1 <i>Synthesis of ZnCeZrO_x catalyst</i>	46
2.3.2 <i>Synthesis and basic characterization</i> <i>of RUB-13</i>	47
2.4 GaZrO_x + SSZ-13 catalyst	49
2.4.1 <i>Synthesis of GaZrO_x catalyst</i>	49
2.4.2 <i>Synthesis and basic characterization</i> <i>of RUB-13</i>	50
2.4.3 <i>Synthesis of the scaled-up catalysts</i>	52

2.5 Characterization techniques	52
2.5.1 <i>Textural characterization</i>	52
2.5.2 <i>Spectroscopic characterization</i>	53
 REFERENCES	 59
 CHAPTER III	
PdZn/ZrO₂	61
3.1 Lab scale:	
structural characterization	61
3.2 Lab scale:	
spectroscopic characterization	63
3.2.1 <i>FT-IR: H₂ interaction with the stand-alone PdZn/ZrO₂</i>	63
3.2.2 <i>FT-IR: CO₂ adsorption on the stand-alone PdZn/ZrO₂</i>	67
3.2.3 <i>FT-IR: CO adsorption on the stand-alone PdZn/ZrO₂</i>	69
3.2.4 <i>NAP-XPS on stand-alone PdZn/ZrO₂</i>	80
3.2.5 <i>XAS: Pd and Zn K-edge</i>	
<i>on PdZn/ZrO₂ + ZSM-5</i>	83
3.2.6 <i>FT-IR: CO adsorption at LNT</i>	
<i>on combined PdZn/ZrO₂ + SAPO-34</i>	86
3.3 Lab scale: catalytic tests	89

3.4 Scale up: structural characterization	92
3.5 Scale up: spectroscopic characterization	93
3.5.1 XAS measurements	95
3.5.2 FT-IR: CO adsorption at room temperature	97
3.6 Scale up: catalytic tests	101
REFERENCES	104

CHAPTER IV

ZnZrO_x mixed oxides	113
4.1 Textural and structural characterization	113
4.1.1 Textural characterization	113
4.1.2 Structural characterization	115
4.2 Spectroscopic characterization	119
4.2.1 FT-IR: H ₂ interaction with stand-alone ZnZr-X	119
4.2.2 FT-IR: CO adsorption at LNT on stand-alone ZnZr-X	123
4.2.3 XAS measurements performed on combined ZnZr-X/ZSM-5	127
4.3 Catalytic tests	131

REFERENCES	136
 CHAPTER V	
ZnCeZrO_x	139
5.1 Structural characterization	139
5.2 Spectroscopic characterization	140
5.2.1 <i>FT-IR: H₂ interaction with stand-alone ZnCeZrO_x</i>	141
5.2.2 <i>FT-IR: CO adsorption on stand-alone ZnCeZrO_x</i>	144
5.2.3 <i>FT-IR: CO₂ adsorption on stand-alone ZnCeZrO_x</i>	156
5.2.4 <i>FT-IR: CO adsorption at LNT on RUB-13</i>	157
5.2.5 <i>XAS: Ce K-edge on stand-alone ZnCeZrO_x</i>	158
5.3 Catalytic tests	161
 REFERENCES	 162
 CHAPTER VI	
GaZrO_x	169
6.1 Lab scale: structural characterization	169

6.2 Lab scale: spectroscopic characterization	
of stand-alone GaZrO_x	170
6.2.1 FT-IR: CO adsorption.....	170
6.2.2 FT-IR: H ₂ adsorption	177
6.2.3 FT-IR: CO ₂ adsorption.....	179
6.2.4 XAS: Ga K-edge.....	181
6.3 Lab scale: catalytic tests	183
6.4 Scale up: spectroscopic characterization	
of stand-alone GaZrO_x	185
REFERENCES	188
Conclusions and perspectives:	
towards COZMOS-2	194
APPENDIX	197

INTRODUCTION

The present thesis is related to a European project, named COZMOS (CO₂ conversion over multisite Zeolite-Metal nanocatalysts to fuels and OlefinS), which aims at creating a bifunctional catalyst to produce methanol from CO₂ and convert it into C₃ hydrocarbons. The bifunctional catalysts studied are made up of a supported-metal or oxidic phase, involved in CO₂ conversion to methanol, and a zeolite/zeotype phase for the conversion of methanol to hydrocarbons, via methanol-to-hydrocarbons or methanol-to-olefines processes.

COZMOS is a joint project between several partners belonging to academia and industrial field.

The project focused the attention on several bifunctional catalysts proposed during the course of the last three years. However, only four of them had been chosen to be investigated, focusing the attention firstly on their catalytic activity, and then on their structure and semiconductive properties, in order to understand their activity mechanism and to enhance their functioning. The present Ph.D. work is focused on four main systems: (i) PdZn/ZrO₂ + SAPO-34, (ii) ZnZrO_x + ZSM-5, (iii) ZnCeZrO_x + RUB-13 and (iv) GaZrO_x + SSZ-13.

Not only lab-scale catalyst were analyzed, but also the scaled-up version of PdZn/ZrO₂ + SAPO-34, and GaZrO_x oxidic phase in combination with a different zeolite, MgAPO-18. For sake of brevity, the last one has not been reported in this thesis.

Introduction

The entire research work was mainly focused on FT-IR spectroscopic characterization of the above-mentioned catalysts, employing probe molecules, such as CO, H₂ and CO₂, to study their surface properties. Since the bifunctional catalysts were mainly obtained by a physical mixture, both stand-alone phases and the combined systems were analyzed, with a major attention on the oxidic phase. Infrared results were supported by several other techniques, such as X-Ray Absorption Spectroscopy (XAS), Transmission Electron Microscopy (TEM) and gas volumetric measurement for the most part. In some cases, X-Ray Photoelectron Spectroscopy (XPS) and Solid State Nuclear Magnetic Resonance (SS-NMR) demonstrated to be valuable allies to highlight specific features of some samples.

The present thesis is divided as follows: Chapter I describes the state-of-art of CO₂ hydrogenation process; Chapter II summarizes both the synthesis and the basic characterization of the analyzed materials; all the following chapters, from Chapter III to Chapter VI, deal with the single oxidic phase and their combination with the zeolites; finally, the last pages report conclusion and perspectives.

CHAPTER I

CO₂ hydrogenation

1.1 State of the art: from waste to value-added products

The rapid change in global temperature has been demonstrate to correlate to the human activity. According to the Sixth Assessment Report released by IPCC [1,2], the human activity has been responsible for the increase of greenhouse gases (GHG) in the atmosphere and, thus, global warming. Human activity means every action carried out by mankind to produce electricity, food, fuel for transport, and so on. As for the electricity production is well known that oil, natural gas and coal are still the main energy sources, and they represent the most dangerous sources of environmental impact. Thus, it is clear that their consumption should be drastically reduced.

However, reducing fossil fuel consumptions means that humanity could still use them, but should involve some technologies in order to reduce greenhouse gases emissions. For example, carbon capture, utilization and storage systems (CCUS) include technologies in order to reduce CO₂ emissions by storing and convert the gas into other products.

According to the World Energy Outlook published by the International Energy Agency (IEA) [3], oil demand is declining, even though it is dropping very widely. According to the Net Zero Emission by 2050 scenario (NZE) [4] oil

demand should drop from around 90 million barrel per day (mb/d) in 2020 to 24 mb/d in 2050. This scenario limits oil consumption at 55% just for petrochemical uses.

As for natural gas, the demand will increase in the next five years [3], but the NZE scenario limits natural gas consumption to 1750 billion of cubic meters. According to the same report, by 2050, more than 50% of natural gas will be used to produce low-carbon hydrogen and 70% of gas use in facilities will be equipped with CCUS. In July 2022, with a delegated act, the European Commission approved the inclusion of natural gas, together with nuclear power, into the taxonomy for sustainable activities [5]. The EU Taxonomy is a tool to increase transparency in financial markets for sustainable investments in the private sector. Unlike nuclear power, natural gas undoubtedly releases CO₂, so by including it in the EU taxonomy some limits to gas-related activities have been imposed: i) lifecycle emissions are below 100gCO_{2eq}/kWh or ii) until 2030, and where renewables are not available at a sufficient scale, direct emissions are below 270gCO_{2eq}/kWh or their direct emissions of the facility must not exceed an average of 550kgCO_{2eq}/kW over 20 years. In this case, the activities must meet some conditions, such as replacing a facility using solid fossil fuels and the activity ensures a full switch to renewable sources or low-carbon gases by 2035 [5].

As for coal, it is well known to be responsible of several contaminations and its consumption should be reduce the most. According to the NZE scenario [3], coal

demand should drop by 55% to 2030 and by 90% to 2050. Around 80% of the remaining amount of coal will be used in plants equipped with CCUS.

As mentioned in IEA's report, CCUS will play an important role. There is a growing role for alternatives, such as bioenergy and hydrogen-based fuels. In particular, hydrogen-based liquids, including ammonia, methanol and other synthetic liquid hydrocarbons with a very low emissions intensity. According to the Global Hydrogen Report 2021 [6], 17 governments have published hydrogen strategies and more than 20 countries are developing them.

In order to achieve all the goals for a Net Zero scenario, it is important to produce hydrogen from sustainable sources like renewable energy, nuclear power and natural gas (H₂ production by methane steam reforming) equipped with CCUS.

Speaking of CCUS, it is the combination of CCS (Carbon Capture and Storage) and CCU (Carbon Capture and Utilization). CCS plays a key role in the reduction of GHG, accompanying the mitigation of the climate change. CCU is, to date, a very attractive approach, but the amount of CO₂ recovered is about 11-17% [7].

Nonetheless, CCU gives value-added chemicals in addition to CO₂ emissions reduction [8]. In this view, among the most CO₂-intensive fields, ammonia plants, cement and steel industry could integrate their production with the synthesis of CO₂-offspring compounds.

1.1.1 Variety of target products: DME, methanol, CO, etc.

CO₂ hydrogenation could lead to several compounds obtained by reaction of CO₂ with H₂ at different H₂/CO₂ ratios.

Olah et al. [9] and Centi et al. [10,11] proposed different routes for CO₂ hydrogenation to produce some products, such as methanol, dimethyl ether (DME), methane and hydrocarbons. Saiedi et al. [12] schematized some potential routes to produce different compounds via CO₂ hydrogenation (Figure 1).

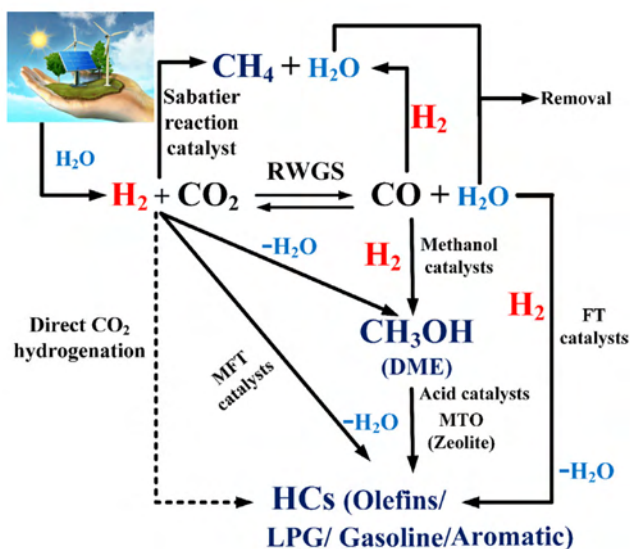


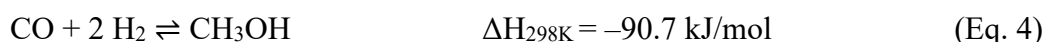
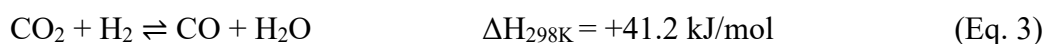
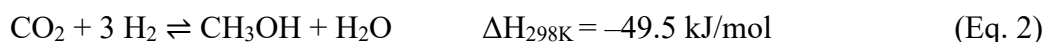
Figure 1 – Scheme taken from Saiedi et al. [12] representing potential paths to synthesize different products via CO₂ hydrogenation.

Methane can be produced via the Sabatier reaction (Eq. 1), but the reaction is limited by several *technical* issues related to H₂ consumption, difficulties in

methane storage – with respect to some other products – and low energy per unit volume.



Methanol is a very versatile compound and could have several industrial applications in chemical/petrochemical industry because it could be used as solvent, energy source (e.g. fuel) or chemical raw material (e.g. production of dimethyl carbonate, formaldehyde, acetic acid, etc.). Moreover, it can be implemented in the so-called methanol-to-olefins (MTO) and methanol-to-hydrocarbon (MTH) process (see section 1.3.1). To date methanol is one of the compounds which can easily be included in the “Power-to-Fuel” concept. The reactions reported below (in Eq. 2-4 [12,13]) could be appropriately achieved in the view of incrementing the hydrogen production with low-carbon technology, with energy “excess” produced by sustainable energy sources, such as renewables and nuclear energy.



Methanol is far easier to store than H₂ and all the efforts in the new reactor designs for CO₂ hydrogenation could make this technology competitive with industrial methanol synthesis from syngas.

Methanol can also be involved to produce DME, which is not corrosive or toxic, can be used to produce light olefins [14] and can replace chlorofluorocarbon in aerosols [15]. DME is produced by methanol dehydration (Eq. 5) and both DME and water act as inhibitors during the reaction [16].



Eq. 3 is known as reverse-water gas shift (RWGS) reaction, an endothermic reaction that leads to the formation of CO.

Carbon monoxide can be involved in several reactions to produce hydrocarbons. The most known reaction is the Fischer-Tropsch (FT) reaction, which mainly leads to alkanes (Eq. 6), while competing reactions lead to alkenes or other products.



To date, a direct hydrocarbon production from RWGS and FT reaction are the most significant processes involved in CCU, as clearly comprehensible from Figure 1 [18].

Indeed, a direct CO₂ hydrogenation to hydrocarbon is not easy to achieve. Eq. 7 requires more energy, more H₂ consumption and more reaction steps, so that it is not implemented in fuel production [19].



As for hydrocarbons, CO₂ transformation to light alkanes and alkenes could follow two main routes: i) modified Fischer-Tropsch (MFT) process and ii) methanol-mediated pathway. In the MFT processes, CO production from RWGS reaction is followed by a further hydrogenation of CO as in a typical Fischer-Tropsch process. In this case, there is a high competition between CO₂ and CO to react with H₂ and cannot be ruled out [20].

At present, research laboratories, companies and start-ups head towards these processes and many of them aim at the conversion of CO₂ in organic molecules, like C₃-hydrocarbons, i.e. propane and propene. Propane can be produced using methanol-to-hydrocarbon catalysis, while propene can be obtained from propane dehydrogenation (PDH), olefins metathesis and methanol-to-olefins (MTO) processes [21]. In particular, propane is a key feedstock molecule and strictly linked to the propylene market. Propylene was historically produced from naphtha steam cracking, but the shift towards the shale gas cracking seemed to have impacted on the propylene market [5]. Despite propane is a by-product of natural gas processing and petroleum refining, perhaps affected by a plausible contraction of natural gas and oil production by 2050 [6], several research groups headed to

synthesis propane from CO₂ and tried to produce propylene via propane dehydrogenation (PDH) processes during the last decade. Because of its high selectivity towards propylene, at present several plants have already been commercialized and already available on the market [5,7,8].

PDH is energy demanding [22] and since this implies the usage of fossil fuels it is important to find another route to produce that energy. Many industrial processes use MTO process because it has an autocatalytic mechanism, though the first reaction is the rate-determining step, so it can be speeded up co-feeding initiators, such as ethylene and other alkenes. The aim is using hydrogen obtained from sustainable sources to produce methanol (hydrogenation of CO₂) which can be used to produce hydrocarbons.

1.1.2 Variety of process approaches: thermocatalysis, electrocatalysis, photocatalysis, etc.

Dealing with CO₂ is not straightforward. It is the most oxidized form of carbon and it is located in such a thermodynamic well that makes its chemical reduction hard to achieve [23]. The single C atom CO₂ possesses can be recovered and added to other organic chemicals to obtain useful products for further fields.

Currently, there are different ways involving CO₂ conversion, such as photochemical (i.e. photocatalysis), electrochemical (i.e. electrocatalysis) and thermocatalytic processes.

Both photo- and electrochemical processes are strictly linked together, since solar energy can be “*directly*” used as in a sort of artificial photosynthesis and/or it can be converted into electricity to be used in electrochemical processes.

As a matter of fact, solar energy can be used in different ways: i) artificial photosynthesis via photoinduced electrons; ii) bulk electrolysis of a CO₂-full solution using photovoltaic electricity; iii) solar-produced H₂ (i.e. green H₂) for CO₂ hydrogenation; iv) thermochemical process at extremely high temperature in solar collectors.

Several research groups are investigating both photo- and electrochemical reduction of CO₂ to CO, formate and methanol, using transition metal electrodes, semiconductors, metal complexes, etc. [24–30]. Since CO₂ is a very stable molecule, sometimes these systems could decompose their carbon-based impurities (e.g. on semiconductor surface) giving an overestimation of the catalytic activity, thus when product formation is very low all the reaction must be carefully investigated.

The homogeneous photochemical CO₂ reduction is very hard to achieve, due to some factors such as: single-electron-transfer and a single-photon processes, which limit the multielectron requirement for reduction; the employment of a catalyst; a sacrificial reductant with low oxidation potential; and a photosensitizer. Usually, the reductive quenching of the photosensitizer excited state by the electron donor drives the reaction, so that when one-electron-transfer from the reduced photosensitizer to the catalyst precursor occurs, the catalysis begins.

Furthermore, despite the difficulty in monitoring the electron transfer steps, an attentive check is necessary to control the decomposition of the photosensitizer [24].

To date, the photochemical approach has several limitations that need to be overcome, as for: i) low turnover numbers and frequencies; ii) product selectivity towards CO, formate, methanol, etc.; iii) implementation of precious metals; iv) pH control; v) use of organic solvents and sacrificial reactants; vi) the demand of an oxidative-reductive coupled half-reactions. Moreover, according to some authors [31] the catalytic results are difficult to compare between laboratories activities, because of different parameters involved (i.e. light wavelength, electron donors, light intensity, etc.).

On the other hand, electrocatalysis and thermocatalysis are the most widely used processes with several pros and cons on both sides. To give an idea about them, Guzmán et al. [32] published a very good work to compare both electrocatalysis (EC) and thermocatalysis (TC).

Thermocatalysis is the eldest processes applied for CO₂ hydrogenation, but has some limitations, such as poor stability of the support in presence of steam, it requires high energy demand, it is not as thermodynamically favorable as the actual syngas route for methanol production and requires hydrogen, which is mainly produced by steam methane reforming [33]. Indeed, methanol production via TC is significantly more carbon-intensive when compared to EC [32].

However, according to a report published by the Joint Research Centre (JRC) in 2016 [34] methanol synthesis reached TRL 6-7 at prototypal scale, thus thermocatalytic approach could be already industrialized in the near future.

As for EC, has some advantages compared to TC, such as: i) direct use of sustainable energy sources; ii) use of water for the in-situ generation of H⁺ and iii) mild conditions for conversion of CO₂ into fuels and chemicals (produced today from petroleum). Nonetheless, large potentials (> 3.0 V) are required for the electrochemical reduction of CO₂ to produce significant amount of fuel. In addition, methanol productivity and low selectivity are still not overcome. At the moment, TRL for methanol synthesis is lower than that of TC (TRL 3-6) and it is mainly due to the low level of commercialization [32], despite the high level of investments in this technology [35].

Nonetheless, according to Guzmán et al. [32], EC is economically more advantageous than TC on the low scale production of methanol, but when scaled-up both the processes start to be economically competitive. Hence, more efforts should be applied in this direction, especially on thermocatalysis side because, to date, it represents the most technologically advanced approach to be involved in CO₂ hydrogenation to methanol.

1.2 Methanol as energetic vector for a new platform for the synthesis of simple hydrocarbon. COZMOS Concept.

As already mentioned in the previous sections, methanol is convenient compound that can be involved as a liquid fuel or raw material for hydrocarbon production, offering an alternative source to substitute oil-derived substances. It can be obtained from H₂ and CO₂, reducing the burden concerning to global warming. Focusing the attention on methanol conversion towards hydrocarbon, here comes the role of COZMOS project. COZMOS stands for **CO₂ conversion over multisite Zeolite-Metal nanocatalysts to fuels and OlefinS**. It is an EU-funded project that aims to provide an innovative technology to convert CO₂ to C₃ fuel and chemical building blocks. The focus is the development of original catalyst and process technology to cross the thermodynamic limitations related to the conversion of CO₂ to produce value-added products.

COZMOS is a joint project between several partners belonging to academia and industrial field. Even though it is financed by the European Union, the project includes some non-EU partners. The partners are: University of Oslo (Norway), University of Turin (Italy), Centre National de la Recherche Scientifique (CNRS, France), Haldor Topsoe AS (Denmark), Linde AG (Germany), STIFTELSEN SINTEF (Norway), Tata Steel (United Kingdom), University of Sheffield (United Kingdom), Tüpraş (Turkey), King Abdullah University of Science and Technology (KAUST, Saudi Arabia) and Institute of Coal Chemistry Chinese Academy of Sciences (ICC, China).

One of the main goals of COZMOS is to develop and demonstrate the possibility to produce a technology at TRL 5, meeting the LCA targets related to CO₂ emissions and the social acceptance of carbon dioxide-derived fuels and chemicals. Needless to say, COZMOS also aims to meet EU goals regarding independence on fossil resources by replacing fossil fuels and contributing to a circular economy.

To achieve this goal, the project aims to the development, optimization and upscaling of bifunctional catalysts made up of an oxidic or supported-metal phase, involved in CO₂ hydrogenation to methanol, and a zeolitic phase, to convert methanol to C₃ hydrocarbon (e.g. via methanol-to-olefins or methanol-to-hydrocarbon process).

1.3 Bifunctional Catalyst

1.3.1 The role of the metallic/oxidic phase

The main challenge in catalysis consists in compromising the catalyst performances, such as activity, selectivity, and conversion, with the energy cost of the total reaction, i.e. low pressure and temperature (e.g. 1 bar, < 400 °C). As for CO₂ hydrogenation and conversion to hydrocarbons, the main reactions involved are:





Recently, several groups [36–41] investigated bifunctional catalysts obtained combining a metallic phase (metal or metal oxide) involved in methanol production with a selective zeolitic material to convert methanol into hydrocarbons (methanol-to-hydrocarbons process, MTH). Nonetheless, the coexistence of two catalysts under the same reaction conditions is still challenging. Indubitably, each catalyst must be the most appropriate for each reaction step and the two active phases must not contaminate each other, e.g. water production in Eq. 3 may lead to sintering of the catalyst dedicated to methanol synthesis [42]. Furthermore, the possibility the two materials undergo mutual interactions (e.g. inter-phase ion-exchange phenomena) altering their physico-chemical properties at high temperature must be considered [37].

Starting from the first step consisting in CO_2 hydrogenation to methanol, it is important to find a trade-off with the thermodynamics of the reaction [43], in particular methanol synthesis at low temperature and high pressures. For sake of clarity, low temperature favors methanol production on the first catalyst, while high temperature enhances methanol dehydration and C-C coupling in the zeolite. Hence, high temperature moves the equilibrium of the first catalyst towards the endothermic reverse water gas shift (RWGS) reaction (Eq. (3)).

1.3.2 Mixed oxides

In recent years, different research studies [44–51] are still focused on using the same types of catalysts involved in RWGS reaction.

Some metal-based oxidic supports can be involved in CO₂ hydrogenation to lower olefins (CTLO) without the need of a zeolitic phase. In particular, those catalysts have been reported to catalyze the CTLO process by a modified Fischer-Tropsch (MFT) pathway [52]. The most studied materials are Fe-based catalysts (Fe₃O₄, Fe₂O₃, etc.) due to its known performances in water gas shift (WGS) and Fischer-Tropsch (FT) process. In particular, it has been revealed that different facets of the catalyst can be subjected to electronic modification to generate new phases capable of catalyzing both CO formation and its hydrogenation to hydrocarbons [52]. Some authors [53,54] stated that Fe₃O₄ behaves as an active phase for the RWGS process, while Fe₅C₂ is active for the FT step. Unfortunately, this catalyst yields large hydrocarbons, with low selectivity to lower olefins and wide product distribution. This leads to a lower selectivity, but also to a high cost of product separation. This is a reason why researchers found the possibility of using the tandem catalyst strategy [49,55,56].

An ideal CO₂ hydrogenation catalyst should promote: i) stabilization of intermediates for hydrogenation to methanol or other hydrocarbons instead of RWGS ones; ii) H₂ dissociation by heterolytic splitting and iii) inhibition of water poisoning effect, which hampers the catalytic hydrogenation activity [49]. For this purpose multicomponent catalytic systems have been proposed to balance the

above-mentioned capabilities. In particular, oxide-supported metals, working at the oxide-metal interface [44,50,57–62] or via the formation of alloys [48,63–69], have shown to be very promising.

As for the support, research is even wider due to the possibility of using several oxides (e.g., ZnO, ZrO₂, Al₂O₃, SiO₂, TiO₂, CeO₂, Ga₂O₃, Nb₂O₅) that have been described in several scientific works [49,60,70–74].

Among the above-mentioned oxides, ZrO₂ has been investigated as support material in many binary and ternary systems for CO/CO₂ hydrogenation to methanol [75–81]. According to some studies over pristine zirconia [82], CO and CO₂ are mainly adsorbed, as HCO⁻, CO₃²⁻ and HCO₃⁻, respectively. Especially, as the strength of Zr⁴⁺ Lewis acid sites, O²⁻ Lewis basic sites and higher concentration and basicity of hydroxyl groups increase, so does CO₂ adsorption capacity. However, according to other works, the main CO₂/ZrO₂ interaction occurs through the oxide basic sites [80,83]; principally, with the formation of bicarbonate b-HCO₃-Zr [78], which following hydrogenation is promoted from the weak hydrophilic character of the support [84].

Moreover, some catalysts exploit the activity of some other metals (such as Pd) or alloys (such as PdZn) which are able to bind hydrogen in order to enhance CO₂ hydrogenation [46,48,69,85,86]. As a matter of fact, some metals are able to split the molecule to facilitate the reduction.

Using ZrO₂ as a model system Li et al. [49] aimed at offer further insights about structural and surface properties of catalysts. Specifically, they aimed at

understanding the reaction mechanism and the synergy between the ZrO₂ support and the supported metal to design a high-performance catalyst.

In addition, some mixed oxides could exhibit semiconductive properties, which can lead to the formation of oxygen vacancies that have been demonstrated playing a key role in CO₂ hydrogenation [45,46,49,87–89].

1.3.3 The role of the zeolite

As for the zeolitic part of the bifunctional catalyst, it is a complete distinctive story. As already mentioned, zeolites play a key role in both MTO and MTH processes. According to several works [90–92], several zeolites can be involved to aim hydrocarbons production. Nonetheless, defining a specific mechanism is not straightforward. Indeed, since the first application of zeolites in the petrochemical field, several mechanisms have been proposed.

In the recent years, a massive consensus has been reached regarding the existence of a direct mechanism highlighted by the formation of a surface methoxy species (SMS) (Figure 2) upon methanol adsorption on Brønsted acid sites [90,93,94]. From SMS several mechanisms can occur leading to the formation of a C-C through several routes. A review work of Yarulina et al. [90] elegantly summarizes the most studied mechanisms that still have a huge influence in several recent papers.

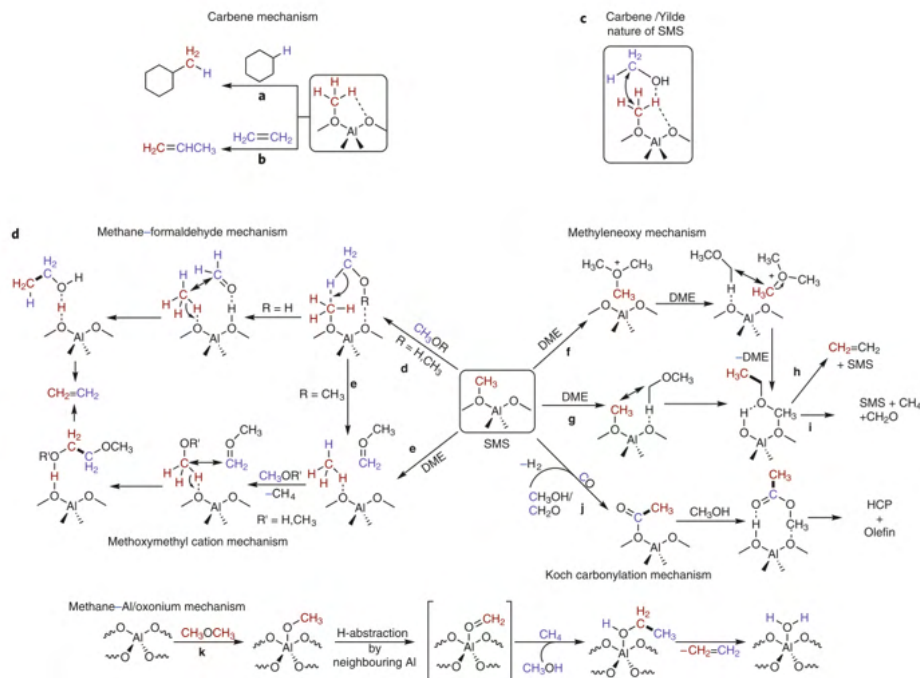


Figure 2 – Several proposed mechanisms for hydrocarbon production starting from a SMS precursor. Courtesy of Yarulina et al. [90].

Among the SMS there would be oxonium ylides [95,96], carbocations [97,98], carbenes [99,100] and free radicals [101].

After the formation of C-C bond, it is important to define a possible route to drive through in order to generate hydrocarbons. Literature focused the attention on three main pathways highlighting two main systems: ZSM-5 and SAPO-34. Chronologically, the first mechanism was theorized by Dessau and LaPierre [102] based on consecutive methylation and cracking, producing ethene and higher alkenes over ZSM-5 (Figure 2a). The second mechanism was illustrated by Dahl and Kolboe [103] enlightened by the low reactivity of propene and ethene when

co-reacted with methanol over SAPO-34. Their mechanism is based on a hydrocarbon-pool concept [104], represented as $(CH_2)_n$ in Figure 2b. Last but not the least, a more recent mechanism representation is the dual-cycle concept which highlights the strict interconnection between two cycles: an olefinic and an aromatic cycle (Figure 2c). According to this concept, it is possible to generate ethylene from the aromatic cycle. Indeed, according to Sun et al. [105], both the cycles are active for ethylene and propylene, but the olefinic cycle is more selective than the aromatic cycle toward propene production. Hence, these cycles compete for the production of ethene and propene, so that a product can be obtained by stimulating or suppressing one cycle over the other.

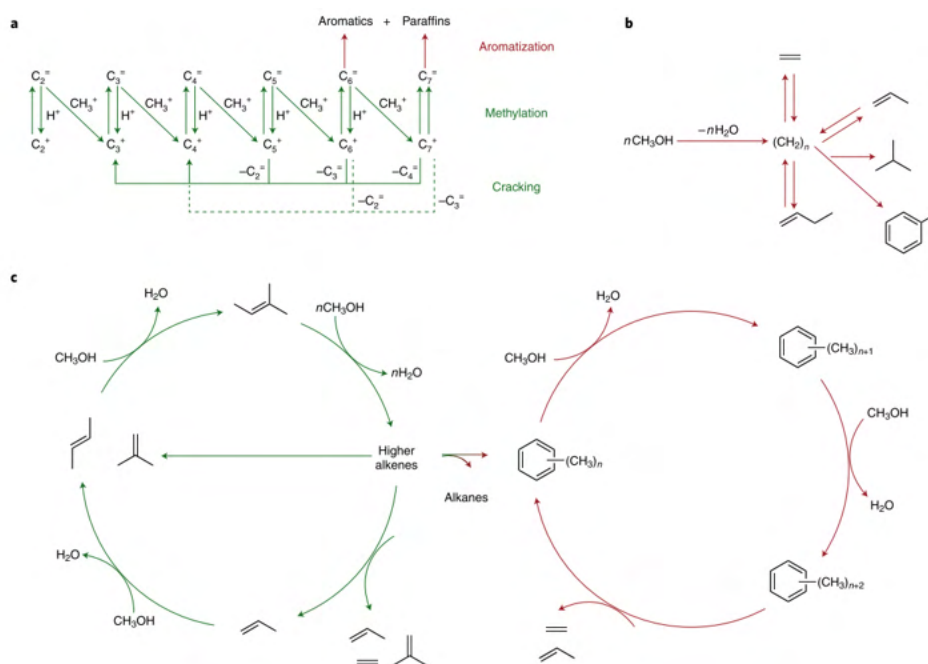


Figure 3 - Possible mechanism development of MTH process. a) mechanism illustrated by Dessau and LaPierre in 1982 [102]; b) hydrocarbons-pool mechanism theorized by

Dahl and Kolboe in 1993 [103]; c) dual-cycle concept schematized by Olsbye and co-workers in 2012 [91]. All the schemes were adapted by Yarulina et al. [90]

In order to complete a very light and introductive *excursus* in the world of methanol conversion to hydrocarbons, it is important to highlight the role of the acid sites in a zeolitic system which are strictly connected to the coke generation as a by-product of process which often leads to the deactivation of a catalysts.

In 2009, Guisnet and co-workers [106] elegantly described the role of acidity characteristics: (i) the stronger the acidic sites, the faster the chemical steps and the more conspicuous the retention of coke precursors, hence the higher the coking rate; (ii) the higher the acid sites density, the closer the sites, the faster the chemical steps and, hence, the coke formation.

Despite of the difficulties in understanding the mechanism of polycyclic arene formation, some authors [107] suggest 4 main sequences such as (1) a dehydration of two methanol molecules to dimethyl-ether (DME), followed by (2) loss of another water molecule to produce an olefin and (3) other olefins, and finally (4) conversion of some olefins into aromatics featured by a possible hydrogen transfer from some olefins to produce saturated alkanes. Focusing on Si-substituted AlPO_4 (SAPOs) the above-mentioned work highlights that a hydrogen transfer seems to play a key step in the process.

SAPO-34 has been widely studied in the last decades [108–110] due to its application in methanol-to-hydrocarbons (MTH) processes and it was observed

that varying its composition both the deactivation rate and the synthesized molecule could widely change [107,111,112]. Indeed, according to Wilson and Barger [111] a reduction in Si content decreases propane yield and increases catalyst life-time. These results were confirmed [107,112] with different chabazite zeolites and by varying the acid sites density. Dahl et al. [113] further investigate how the acid strength could influence the catalyst deactivation behavior.

A very interesting study was performed by Bleken et al. [110] where the authors compared chabazite zeolites, H-SSZ-13 and H-SAPO-34, with similar acid site density, but different acid strength. According to their work, H-SSZ-13 showed higher activity and more rapid deactivation than H-SAPO-34. This behavior is in line with its higher acid sites strength, despite of the same type of hydrocarbon retained in the pores of both the zeolites.

REFERENCES

- [1] V. Masson-Delmotte, P. Zhai, A. Pirani, S.L. Connors, C. Péan, S. Berger, N. Caud, Y. Chen, L. Goldfarb, M.I. Gomis, M. Huang, K. Leitzell, E. Lonnoy, J.B.R. Matthews, T.K. Maycock, T. Waterfield, O. Yelekçi, R. Yu, B. Zhou, *Climate Change 2021: The Physical Science Basis. Contribution of Working Group I to the Sixth Assessment Report of the Intergovernmental Panel on Climate Change*, Cambridge Univ. Press. (2021) 3949. <https://www.ipcc.ch/report/ar6/wg1/>.
- [2] V. Masson-Delmotte, P. Zhai, A. Pirani, S.L. Connors, C. Péan, S. Berger, N. Caud, Y. Chen, L. Goldfarb, M.I. Gomis, M. Huang, K. Leitzell, E. Lonnoy, J.B.R. Matthews, T.K. Maycock, T. Waterfield, O. Yelekçi, R. Yu, B. Zhou, Summary for Policymakers. In: *Climate Change 2021: The Physical Science Basis. Contribution of Working Group I to the Sixth Assessment Report of the Intergovernmental Panel on Climate Change*, Cambridge Univ. Press. Press. (2021) 42. <https://www.ipcc.ch/report/ar6/wg1/>.
- [3] IEA, *World Energy Outlook 2021*, Paris, 2021. <https://www.iea.org/reports/world-energy-outlook-2021>.
- [4] IEA, *Net Zero by 2050*, Paris, 2021. <https://doi.org/10.1787/c8328405-en>.
- [5] European Commission, *EU taxonomy for sustainable activities*, (n.d.). https://ec.europa.eu/info/business-economy-euro/banking-and-finance/sustainable-finance/eu-taxonomy-sustainable-activities_en.
- [6] IEA, *Global Hydrogen Review 2021 – Analysis*, (n.d.). <https://www.iea.org/reports/global-hydrogen-review-2021> (accessed November 11, 2022).
- [7] M. Aresta, *Carbon dioxide as chemical feedstock*, John Wiley & Sons, 2010.
- [8] M. Aresta, F. Nocito, A. Dibenedetto, *What Catalysis Can Do for Boosting CO₂ Utilization*, 1st ed., Elsevier Inc., 2018. <https://doi.org/10.1016/bs.acat.2018.08.002>.
- [9] G.A. Olah, A. Goeppert, G.K.S. Prakash, *Chemical recycling of carbon dioxide to methanol and dimethyl ether: From greenhouse gas to renewable, environmentally carbon neutral fuels and synthetic hydrocarbons*, *J. Org. Chem.* 74 (2009) 487–498. https://doi.org/10.1021/JO801260F/ASSET/IMAGES/MEDIUM/JO-2008-01260F_0003.GIF.
- [10] G. Centi, S. Perathoner, *Opportunities and prospects in the chemical recycling of carbon dioxide to fuels*, *Catal. Today.* 148 (2009) 191–205. <https://doi.org/10.1016/J.CATTOD.2009.07.075>.

- [11] G. Centi, E.A. Quadrelli, S. Perathoner, Catalysis for CO₂ conversion: a key technology for rapid introduction of renewable energy in the value chain of chemical industries, *Energy Environ. Sci.* 6 (2013) 1711. <https://doi.org/10.1039/c3ee00056g>.
- [12] S. Saeidi, S. Najari, V. Hessel, K. Wilson, F.J. Keil, P. Concepción, S.L. Suib, A.E. Rodrigues, Recent advances in CO₂ hydrogenation to value-added products — Current challenges and future directions, *Prog. Energy Combust. Sci.* 85 (2021) 100905. <https://doi.org/10.1016/J.PECS.2021.100905>.
- [13] M. Pérez-Fortes, J.C. Schöneberger, A. Boulamanti, E. Tzimas, Methanol synthesis using captured CO₂ as raw material: Techno-economic and environmental assessment, *Appl. Energy.* 161 (2016) 718–732. <https://doi.org/10.1016/J.APENERGY.2015.07.067>.
- [14] S. Bhattacharya, K.B. Kabir, K. Hein, Dimethyl ether synthesis from Victorian brown coal through gasification – Current status, and research and development needs, *Prog. Energy Combust. Sci.* 39 (2013) 577–605. <https://doi.org/10.1016/J.PECS.2013.06.003>.
- [15] T.A. Semelsberger, R.L. Borup, H.L. Greene, Dimethyl ether (DME) as an alternative fuel, *J. Power Sources.* 156 (2006) 497–511. <https://doi.org/10.1016/J.JPOWSOUR.2005.05.082>.
- [16] S. Hosseinejad, A. Afacan, R.E. Hayes, Catalytic and kinetic study of methanol dehydration to dimethyl ether, *Chem. Eng. Res. Des.* 90 (2012) 825–833. <https://doi.org/10.1016/J.CHERD.2011.10.007>.
- [17] L. Fratalocchi, C.G. Visconti, G. Groppi, L. Lietti, E. Tronconi, Intensifying heat transfer in Fischer-Tropsch tubular reactors through the adoption of conductive packed foams, *Chem. Eng. J.* 349 (2018) 829–837. <https://doi.org/10.1016/J.CEJ.2018.05.108>.
- [18] G. Centi, E.A. Quadrelli, S. Perathoner, Catalysis for CO₂ conversion: a key technology for rapid introduction of renewable energy in the value chain of chemical industries, *Energy Environ. Sci.* 6 (2013) 1711–1731. <https://doi.org/10.1039/C3EE00056G>.
- [19] J. Artz, T.E. Müller, K. Thenert, J. Kleinekorte, R. Meys, A. Sternberg, A. Bardow, W. Leitner, Sustainable Conversion of Carbon Dioxide: An Integrated Review of Catalysis and Life Cycle Assessment, *Chem. Rev.* 118 (2018) 434–504. https://doi.org/10.1021/ACS.CHEMREV.7B00435/ASSET/IMAGES/MEDIUM/CR-2017-004352_0051.GIF.
- [20] W. Zhou, K. Cheng, J. Kang, C. Zhou, V. Subramanian, Q. Zhang, Y. Wang, New horizon in C1 chemistry: breaking the selectivity limitation in

- transformation of syngas and hydrogenation of CO₂ into hydrocarbon chemicals and fuels, *Chem. Soc. Rev.* 48 (2019) 3193–3228. <https://doi.org/10.1039/C8CS00502H>.
- [21] P. Tian, Y. Wei, M. Ye, Z. Liu, Methanol to olefins (MTO): From fundamentals to commercialization, *ACS Catal.* 5 (2015) 1922–1938. <https://doi.org/10.1021/acscatal.5b00007>.
- [22] J.J.H.B. Sattler, J. Ruiz-Martinez, E. Santillan-Jimenez, B.M. Weckhuysen, Catalytic dehydrogenation of light alkanes on metals and metal oxides, *Chem. Rev.* 114 (2014) 10613–10653. <https://doi.org/10.1021/cr5002436>.
- [23] Z. Jiang, T. Xiao, V.L. Kuznetsov, P.P. Edwards, Turning carbon dioxide into fuel, *Philos. Trans. R. Soc. A Math. Phys. Eng. Sci.* 368 (2010) 3343–3364. <https://doi.org/10.1098/rsta.2010.0119>.
- [24] W.H. Wang, Y. Himeda, J.T. Muckerman, G.F. Manbeck, E. Fujita, CO₂ Hydrogenation to Formate and Methanol as an Alternative to Photo- and Electrochemical CO₂ Reduction, *Chem. Rev.* 115 (2015) 12936–12973. https://doi.org/10.1021/ACS.CHEMREV.5B00197/ASSET/IMAGES/ACS.CHEMREV.5B00197.SOCIAL.JPEG_V03.
- [25] D. Wei, R. Sang, A. Moazezbarabadi, H. Junge, M. Beller, Homogeneous Carbon Capture and Catalytic Hydrogenation: Toward a Chemical Hydrogen Battery System, *J. Am. Chem. Soc.* (2021). https://doi.org/10.1021/JACSAU.1C00489/ASSET/IMAGES/LARGE/AU1C00489_0003.JPEG.
- [26] M. Marx, H. Frauendorf, A. Spannenberg, H. Neumann, M. Beller, Revisiting Reduction of CO₂ to Oxalate with First-Row Transition Metals: Irreproducibility, Ambiguous Analysis, and Conflicting Reactivity, *JACS Au.* 2 (2022) 731–744. <https://doi.org/10.1021/JACSAU.2C00005>.
- [27] E. Fujita, D.C. Grills, G.F. Manbeck, D.E. Polyansky, Understanding the Role of Inter- and Intramolecular Promoters in Electro- and Photochemical CO₂ Reduction Using Mn, Re, and Ru Catalysts, *Acc. Chem. Res.* 55 (2022) 616–628. https://doi.org/10.1021/ACS.ACCOUNTS.1C00616/ASSET/IMAGES/MEDIUM/AR1C00616_0015.GIF.
- [28] R.N. Sampaio, B.N. Dimarco, J.J. Concepcion, Proton-Coupled Group Transfer Enables Concerted Protonation Pathways Relevant to Small-Molecule Activation, *Inorg. Chem.* 60 (2021) 16953–16965. https://doi.org/10.1021/ACS.INORGCHEM.1C01609/SUPPL_FILE/IC1C01609_SI_001.PDF.
- [29] J.A. Buss, N. Shida, T. He, T. Agapie, Carbon dioxide reduction with dihydrogen and silanes at low-valent molybdenum terphenyl diphosphine

- complexes: Reductant identity dictates mechanism, *ACS Catal.* 11 (2021) 13294–13302.
https://doi.org/10.1021/ACSCATAL.1C02922/SUPPL_FILE/CS1C02922_SI_002.PDF.
- [30] S. Wang, L. Zhang, W. Zhang, P. Wang, Z. Qin, W. Yan, Selective conversion of CO₂ into propene and butene, (n.d.) 1–38.
- [31] P. Chen, X. Dong, M. Huang, K. Li, L. Xiao, J. Sheng, S. Chen, Y. Zhou, F. Dong, Rapid Self-Decomposition of g-C₃N₄ During Gas-Solid Photocatalytic CO₂ Reduction and Its Effects on Performance Assessment, *ACS Catal.* 12 (2022) 4560–4570.
https://doi.org/10.1021/ACSCATAL.2C00815/SUPPL_FILE/CS2C00815_SI_001.PDF.
- [32] H. Guzmán, F. Salomone, E. Batuecas, T. Tommasi, N. Russo, S. Bensaid, S. Hernández, How to make sustainable CO₂ conversion to Methanol: Thermocatalytic versus electrocatalytic technology, *Chem. Eng. J.* 417 (2021) 127973. <https://doi.org/10.1016/J.CEJ.2020.127973>.
- [33] A. Zachopoulos, E. Heracleous, Overcoming the equilibrium barriers of CO₂ hydrogenation to methanol via water sorption: A thermodynamic analysis, *J. CO₂ Util.* 21 (2017) 360–367. <https://doi.org/10.1016/J.JCOU.2017.06.007>.
- [34] M. Pérez-Fortes, E. Tzimas, Techno-economic and environmental evaluation of CO₂ utilisation for fuel production. Synthesis of methanol and formic acid, 2016. <https://doi.org/10.2790/89238>.
- [35] S.M. Jarvis, S. Samsatli, Technologies and infrastructures underpinning future CO₂ value chains: A comprehensive review and comparative analysis, *Renew. Sustain. Energy Rev.* 85 (2018) 46–68.
<https://doi.org/10.1016/J.RSER.2018.01.007>.
- [36] J.R. Gallagher, D.J. Childers, H. Zhao, R.E. Winans, R.J. Meyer, J.T. Miller, Structural evolution of an intermetallic Pd-Zn catalyst selective for propane dehydrogenation, *Phys. Chem. Chem. Phys.* 17 (2015) 28144–28153.
<https://doi.org/10.1039/c5cp00222b>.
- [37] C. Ahoba-Sam, E. Borfecchia, A. Lazzarini, A. Bugaev, A.A. Isah, M. Taoufik, S. Bordiga, U. Olsbye, On the conversion of CO₂ to value added products over composite PdZn and H-ZSM-5 catalysts: excess Zn over Pd, a compromise or a penalty?, *Catal. Sci. Technol.* (2020) 4373–4385.
<https://doi.org/10.1039/D0CY00440E>.
- [38] M. Gentzen, D.E. Doronkin, T.L. Sheppard, A. Zimina, H. Li, J. Jelic, F. Studt, J.D. Grunwaldt, J. Sauer, S. Behrens, Supported Intermetallic PdZn Nanoparticles as Bifunctional Catalysts for the Direct Synthesis of Dimethyl Ether from CO-Rich Synthesis Gas, *Angew. Chemie - Int. Ed.* 58 (2019)

- 15655–15659. <https://doi.org/10.1002/anie.201906256>.
- [39] M.W. Tew, H. Emerich, J.A. Van Bokhoven, Formation and characterization of PdZn alloy: A very selective catalyst for alkyne semihydrogenation, *J. Phys. Chem. C*. 115 (2011) 8457–8465. <https://doi.org/10.1021/jp1103164>.
- [40] K. Cheng, B. Gu, X. Liu, J. Kang, Q. Zhang, Y. Wang, Direct and Highly Selective Conversion of Synthesis Gas into Lower Olefins: Design of a Bifunctional Catalyst Combining Methanol Synthesis and Carbon-Carbon Coupling, *Angew. Chemie - Int. Ed.* 55 (2016) 4725–4728. <https://doi.org/10.1002/anie.201601208>.
- [41] Z. Li, J. Wang, Y. Qu, H. Liu, C. Tang, S. Miao, Z. Feng, H. An, C. Li, Highly Selective Conversion of Carbon Dioxide to Lower Olefins, *ACS Catal.* 7 (2017) 8544–8548. <https://doi.org/10.1021/acscatal.7b03251>.
- [42] G. Bonura, M. Migliori, L. Frusteri, C. Cannilla, E. Catizzone, G. Giordano, F. Frusteri, Acidity control of zeolite functionality on activity and stability of hybrid catalysts during DME production via CO₂ hydrogenation, *J. CO₂ Util.* 24 (2018) 398–406. <https://doi.org/10.1016/j.jcou.2018.01.028>.
- [43] W.J. Thomas, S. Portalski, Thermodynamics in methanol synthesis, *Ind. Eng. Chem. Res.* 50 (1958) 967–970.
- [44] S. Kattel, P. Liu, J.G. Chen, Tuning Selectivity of CO₂ Hydrogenation Reactions at the Metal/Oxide Interface, *J. Am. Chem. Soc.* 139 (2017) 9739–9754. <https://doi.org/10.1021/jacs.7b05362>.
- [45] J. Ye, C. Liu, D. Mei, Q. Ge, Active oxygen vacancy site for methanol synthesis from CO₂ hydrogenation on In₂O₃(110): A DFT study, *ACS Catal.* 3 (2013) 1296–1306. <https://doi.org/10.1021/cs400132a>.
- [46] A.S. Malik, S.F. Zaman, A.A. Al-Zahrani, M.A. Daous, H. Driss, L.A. Petrov, Development of highly selective PdZn/CeO₂ and Ca-doped PdZn/CeO₂ catalysts for methanol synthesis from CO₂ hydrogenation, *Appl. Catal. A Gen.* 560 (2018) 42–53. <https://doi.org/10.1016/j.apcata.2018.04.036>.
- [47] A.S. Malik, S.F. Zaman, A.A. Al-Zahrani, M.A. Daous, H. Driss, L.A. Petrov, Selective hydrogenation of CO₂ to CH₃OH and in-depth DRIFT analysis for PdZn/ZrO₂ and CaPdZn/ZrO₂ catalysts, *Catal. Today*. 357 (2020) 573–582. <https://doi.org/10.1016/j.cattod.2019.05.040>.
- [48] H. Bahruji, M. Bowker, W. Jones, J. Hayward, J. Ruiz Esquiús, D.J. Morgan, G.J. Hutchings, PdZn catalysts for CO₂ hydrogenation to methanol using chemical vapour impregnation (CVI), *Faraday Discuss.* 197 (2017) 309–324. <https://doi.org/10.1039/c6fd00189k>.
- [49] K. Li, J.G. Chen, CO₂ Hydrogenation to Methanol over ZrO₂-Containing

- Catalysts: Insights into ZrO₂ Induced Synergy, *ACS Catal.* 9 (2019) 7840–7861. <https://doi.org/10.1021/acscatal.9b01943>.
- [50] S. Kattel, P.J. Ramírez, J.G. Chen, J.A. Rodriguez, P. Liu, Comment on “Active sites for CO₂ hydrogenation to methanol on Cu/ZnO catalysts,” *Science* (80-.). 357 (2017) 1296–1299. <https://doi.org/10.1126/science.aal3573>.
- [51] W. Wang, S. Wang, X. Ma, J. Gong, Recent advances in catalytic hydrogenation of carbon dioxide, *Chem. Soc. Rev.* 40 (2011) 3703–3727. <https://doi.org/10.1039/c1cs15008a>.
- [52] O.A. Ojelade, S.F. Zaman, A review on CO₂ hydrogenation to lower olefins: Understanding the structure-property relationships in heterogeneous catalytic systems, *J. CO₂ Util.* 47 (2021) 101506. <https://doi.org/10.1016/j.jcou.2021.101506>.
- [53] E. de Smit, B.M. Weckhuysen, The renaissance of iron-based Fischer–Tropsch synthesis: on the multifaceted catalyst deactivation behaviour, *Chem. Soc. Rev.* 37 (2008) 2758. <https://doi.org/10.1039/b805427d>.
- [54] M. Zhu, I.E. Wachs, Iron-Based Catalysts for the High-Temperature Water–Gas Shift (HT-WGS) Reaction: A Review, *ACS Catal.* 6 (2016) 722–732. <https://doi.org/10.1021/acscatal.5b02594>.
- [55] S. De, A. Dokania, A. Ramirez, J. Gascon, Advances in the Design of Heterogeneous Catalysts and Thermocatalytic Processes for CO₂ Utilization, *ACS Catal.* 10 (2020) 14147–14185. <https://doi.org/10.1021/acscatal.0c04273>.
- [56] R.-P. Ye, J. Ding, W. Gong, M.D. Argyle, Q. Zhong, Y. Wang, C.K. Russell, Z. Xu, A.G. Russell, Q. Li, M. Fan, Y.-G. Yao, CO₂ hydrogenation to high-value products via heterogeneous catalysis, *Nat. Commun.* 10 (2019) 5698. <https://doi.org/10.1038/s41467-019-13638-9>.
- [57] S. Kattel, W. Yu, X. Yang, B. Yan, Y. Huang, W. Wan, P. Liu, J.G. Chen, CO₂ Hydrogenation over Oxide-Supported PtCo Catalysts: The Role of the Oxide Support in Determining the Product Selectivity, *Angew. Chemie Int. Ed.* 55 (2016) 7968–7973. <https://doi.org/10.1002/anie.201601661>.
- [58] S. Kattel, B. Yan, Y. Yang, J.G. Chen, P. Liu, Optimizing Binding Energies of Key Intermediates for CO₂ Hydrogenation to Methanol over Oxide-Supported Copper, *J. Am. Chem. Soc.* 138 (2016) 12440–12450. <https://doi.org/10.1021/jacs.6b05791>.
- [59] F. Liao, Y. Huang, J. Ge, W. Zheng, K. Tedsree, P. Collier, X. Hong, S.C. Tsang, Morphology-Dependent Interactions of ZnO with Cu Nanoparticles at the Materials’ Interface in Selective Hydrogenation of CO₂ to CH₃OH, *Angew. Chemie Int. Ed.* 50 (2011) 2162–2165.

<https://doi.org/10.1002/anie.201007108>.

- [60] J.A. Rodriguez, D.C. Grinter, Z. Liu, R.M. Palomino, S.D. Senanayake, Ceria-based model catalysts: fundamental studies on the importance of the metal–ceria interface in CO oxidation, the water–gas shift, CO₂ hydrogenation, and methane and alcohol reforming, *Chem. Soc. Rev.* 46 (2017) 1824–1841. <https://doi.org/10.1039/C6CS00863A>.
- [61] K. Larmier, W.-C. Liao, S. Tada, E. Lam, R. Verel, A. Bansode, A. Urakawa, A. Comas-Vives, C. Copéret, CO₂-to-Methanol Hydrogenation on Zirconia-Supported Copper Nanoparticles: Reaction Intermediates and the Role of the Metal-Support Interface, *Angew. Chemie Int. Ed.* 56 (2017) 2318–2323. <https://doi.org/10.1002/anie.201610166>.
- [62] H. Bahruji, M. Bowker, G. Hutchings, N. Dimitratos, P. Wells, E. Gibson, W. Jones, C. Brookes, D. Morgan, G. Lalev, Pd/ZnO catalysts for direct CO₂ hydrogenation to methanol, *J. Catal.* 343 (2016) 133–146. <https://doi.org/10.1016/j.jcat.2016.03.017>.
- [63] D. Gasser, A. Baiker, Hydrogenation of carbon dioxide over copper—zirconia catalysts prepared by in-situ activation of amorphous copper—zirconium alloy, *Appl. Catal.* 48 (1989) 279–294. [https://doi.org/10.1016/S0166-9834\(00\)82799-2](https://doi.org/10.1016/S0166-9834(00)82799-2).
- [64] S. Kuld, C. Conradsen, P.G. Moses, I. Chorkendorff, J. Sehested, Quantification of Zinc Atoms in a Surface Alloy on Copper in an Industrial-Type Methanol Synthesis Catalyst, *Angew. Chemie Int. Ed.* 53 (2014) 5941–5945. <https://doi.org/10.1002/anie.201311073>.
- [65] X. Nie, X. Jiang, H. Wang, W. Luo, M.J. Janik, Y. Chen, X. Guo, C. Song, Mechanistic Understanding of Alloy Effect and Water Promotion for Pd-Cu Bimetallic Catalysts in CO₂ Hydrogenation to Methanol, *ACS Catal.* 8 (2018) 4873–4892. <https://doi.org/10.1021/acscatal.7b04150>.
- [66] E.M. Fiordaliso, I. Sharafutdinov, H.W.P. Carvalho, J.-D. Grunwaldt, T.W. Hansen, I. Chorkendorff, J.B. Wagner, C.D. Damsgaard, Intermetallic GaPd₂ Nanoparticles on SiO₂ for Low-Pressure CO₂ Hydrogenation to Methanol: Catalytic Performance and In Situ Characterization, *ACS Catal.* 5 (2015) 5827–5836. <https://doi.org/10.1021/acscatal.5b01271>.
- [67] V. Lebarbier, R. Dagle, T. Conant, J.M. Vohs, A.K. Datye, Y. Wang, CO/FTIR spectroscopic characterization of Pd/ZnO/Al₂O₃ catalysts for methanol steam reforming, *Catal. Letters.* 122 (2008) 223–227. <https://doi.org/10.1007/s10562-008-9407-7>.
- [68] J.R. Gallagher, D.J. Childers, H. Zhao, R.E. Winans, R.J. Meyer, J.T. Miller, Structural evolution of an intermetallic Pd-Zn catalyst selective for propane dehydrogenation, *Phys. Chem. Chem. Phys.* 17 (2015) 28144–28153.

- <https://doi.org/10.1039/c5cp00222b>.
- [69] O.A. Ojelade, S.F. Zaman, M.A. Daous, A.A. Al-Zahrani, A.S. Malik, H. Driss, G. Shterk, J. Gascon, Optimizing Pd:Zn molar ratio in PdZn/CeO₂ for CO₂ hydrogenation to methanol, *Appl. Catal. A Gen.* 584 (2019). <https://doi.org/10.1016/j.apcata.2019.117185>.
- [70] J. Wambach, A. Baiker, A. Wokaun, CO₂ hydrogenation over metal/zirconia catalysts, *Phys. Chem. Chem. Phys.* 1 (1999) 5071–5080. <https://doi.org/10.1039/a904923a>.
- [71] R.J. da Silva, A.F. Pimentel, R.S. Monteiro, C.J.A. Mota, Synthesis of methanol and dimethyl ether from the CO₂ hydrogenation over Cu·ZnO supported on Al₂O₃ and Nb₂O₅, *J. CO₂ Util.* 15 (2016) 83–88. <https://doi.org/10.1016/j.jcou.2016.01.006>.
- [72] V.I. Bogdan, A.E. Koklin, S.A. Nikolaev, L.M. Kustov, Carbon Dioxide Hydrogenation on Au Nanoparticles Supported on TiO₂, ZrO₂ and Sulfated ZrO₂ Under Supercritical Conditions, *Top. Catal.* 59 (2016) 1104–1109. <https://doi.org/10.1007/s11244-016-0629-4>.
- [73] J. Ruiz Esquisus, H. Bahruji, M. Bowker, G.J. Hutchings, Identification of C₂–C₅ products from CO₂ hydrogenation over PdZn/TiO₂–ZSM-5 hybrid catalysts, *Faraday Discuss.* 230 (2021) 52–67. <https://doi.org/10.1039/D0FD00135J>.
- [74] S. Kattel, P. Liu, J.G. Chen, Tuning Selectivity of CO₂ Hydrogenation Reactions at the Metal/Oxide Interface, *J. Am. Chem. Soc.* 139 (2017) 9739–9754. <https://doi.org/10.1021/jacs.7b05362>.
- [75] Y. Amenomiya, METHANOL SYNTHESIS FROM CO, + H₂, II. COPPER-BASED BINARY AND TERNARY CATALYSTS, *Appl. Catal. A Gen.* 30 (1987) 57–68.
- [76] X. Dong, F. Li, N. Zhao, F. Xiao, J. Wang, Y. Tan, CO₂ hydrogenation to methanol over Cu/ZnO/ZrO₂ catalysts prepared by precipitation-reduction method, *Appl. Catal. B Environ.* 191 (2016) 8–17. <https://doi.org/10.1016/j.apcatb.2016.03.014>.
- [77] H. Gu, J. Ding, Q. Zhong, Y. Zeng, F. Song, Promotion of surface oxygen vacancies on the light olefins synthesis from catalytic CO₂ hydrogenation over Fe[sbnd]K/ZrO₂ catalysts, *Int. J. Hydrogen Energy.* 44 (2019) 11808–11816. <https://doi.org/10.1016/j.ijhydene.2019.03.046>.
- [78] I.A. Fisher, A.T. Bell, In Situ Infrared Study of Methanol Synthesis from CO₂/H₂ on Titania and Zirconia Promoted Cu/SiO₂, *J. Catal.* 184 (1999) 144–156.
- [79] G. Wang, D. Mao, X. Guo, J. Yu, Methanol synthesis from CO₂

- hydrogenation over CuO-ZnO-ZrO₂-M_xO_y catalysts (M=Cr, Mo and W), *Int. J. Hydrogen Energy*. 44 (2019) 4197–4207.
<https://doi.org/10.1016/j.ijhydene.2018.12.131>.
- [80] F. Arena, G. Italiano, K. Barbera, S. Bordiga, G. Bonura, L. Spadaro, F. Frusteri, Solid-state interactions, adsorption sites and functionality of Cu-ZnO/ZrO₂ catalysts in the CO₂ hydrogenation to CH₃OH, *Appl. Catal. A Gen.* 350 (2008) 16–23. <https://doi.org/10.1016/j.apcata.2008.07.028>.
- [81] J. Huang, W. Li, K. Wang, J. Huang, X. Liu, D. Fu, Q. Li, G. Zhan, M_xO_y-ZrO₂ (M = Zn, Co, Cu) Solid Solutions Derived from Schiff Base-Bridged UiO-66 Composites as High-Performance Catalysts for CO₂ Hydrogenation, *ACS Appl. Mater. Interfaces*. 11 (2019) 33263–33272.
<https://doi.org/10.1021/acsami.9b11547>.
- [82] K. Pokrovski, K.T. Jung, A.T. Bell, Investigation of CO and CO₂ Adsorption on Tetragonal and Monoclinic Zirconia, (2001) 4297–4303.
- [83] J. Wang, G. Li, Z. Li, C. Tang, Z. Feng, H. An, H. Liu, T. Liu, C. Li, A highly selective and stable ZnO-ZrO₂ solid solution catalyst for CO₂ hydrogenation to methanol, *Sci. Adv.* 3 (2017) 1–11.
<https://doi.org/10.1126/sciadv.1701290>.
- [84] A. Wokaun, CO₂ hydrogenation over metal / zirconia catalysts, *Phys. Chem. Chem. Phys.* 1 (1999) 5071–5080.
- [85] A.S. Malik, S.F. Zaman, A.A. Al-Zahrani, M.A. Daous, H. Driss, L.A. Petrov, Selective hydrogenation of CO₂ to CH₃OH and in-depth DRIFT analysis for PdZn/ZrO₂ and CaPdZn/ZrO₂ catalysts, *Catal. Today*. (2019).
<https://doi.org/10.1016/j.cattod.2019.05.040>.
- [86] O.A. Ojelade, S.F. Zaman, A Review on Pd Based Catalysts for CO₂ Hydrogenation to Methanol: In-Depth Activity and DRIFTS Mechanistic Study, *Catal. Surv. from Asia*. 24 (2020) 11–37.
<https://doi.org/10.1007/s10563-019-09287-z>.
- [87] Y. Luo, S. Wang, S. Guo, K. Yuan, H. Wang, M. Dong, Z. Qin, W. Fan, J. Wang, Conversion of syngas into light olefins over bifunctional ZnCeZrO/SAPO-34 catalysts: Regulation of the surface oxygen vacancy concentration and its relation to the catalytic performance, *Catal. Sci. Technol.* 11 (2021) 338–348. <https://doi.org/10.1039/d0cy01759k>.
- [88] Q. Song, Y. Men, J. Wang, S. Liu, S. Chai, W. An, K. Wang, Y. Li, Y. Tang, Methanol steam reforming for hydrogen production over ternary composite Zn_yCe₁Zr₉O_x catalysts, *Int. J. Hydrogen Energy*. 45 (2020) 9592–9602.
<https://doi.org/10.1016/J.IJHYDENE.2020.01.175>.
- [89] K.M. Eblagon, P.H. Concepción, H. Silva, A. Mendes, Ultraselective low

- temperature steam reforming of methanol over PdZn/ZnO catalysts— Influence of induced support defects on catalytic performance, *Appl. Catal. B Environ.* 154–155 (2014) 316–328. <https://doi.org/10.1016/J.APCATB.2014.02.032>.
- [90] I. Yarulina, A.D. Chowdhury, F. Meirer, B.M. Weckhuysen, J. Gascon, Recent trends and fundamental insights in the methanol-to-hydrocarbons process, *Nat. Catal.* 1 (2018) 398–411. <https://doi.org/10.1038/s41929-018-0078-5>.
- [91] U. Olsbye, S. Svelle, M. Bjorgen, P. Beato, T.V.W. Janssens, F. Joensen, S. Bordiga, K.P. Lillerud, Conversion of Methanol to Hydrocarbons: How Zeolite Cavity and Pore Size Controls Product Selectivity, *Angew. Chemie-International Ed.* 51 (2012) 5810–5831. <https://doi.org/10.1002/anie.201103657>.
- [92] C. Wang, J. Xu, F. Deng, Mechanism of Methanol-to-hydrocarbon Reaction over Zeolites: A solid-state NMR Perspective, *ChemCatChem.* 12 (2020) 965–980. <https://doi.org/10.1002/cctc.201901937>.
- [93] A.D. Chowdhury, K. Houben, G.T. Whiting, M. Mokhtar, A.M. Asiri, S.A. Al-Thabaiti, S.N. Basahel, M. Baldus, B.M. Weckhuysen, Initial Carbon-Carbon Bond Formation during the Early Stages of the Methanol-to-Olefin Process Proven by Zeolite-Trapped Acetate and Methyl Acetate, *Angew. Chemie.* 128 (2016) 16072–16077. <https://doi.org/10.1002/ange.201608643>.
- [94] X. Wu, S. Xu, W. Zhang, J. Huang, J. Li, B. Yu, Y. Wei, Z. Liu, Direct Mechanism of the First Carbon-Carbon Bond Formation in the Methanol-to-Hydrocarbons Process, *Angew. Chemie.* 129 (2017) 9167–9171. <https://doi.org/10.1002/ange.201703902>.
- [95] G.A. Olah, Higher coordinate (hypercarbon containing) carbocations and their role in electrophilic reactions of hydrocarbons, *Pure Appl. Chem.* 53 (1981) 201–207. <https://doi.org/doi:10.1351/pac198153010201>.
- [96] G.J. Hutchings, F. Gottschalk, M.V.M. Hall, R. Hunter, Hydrocarbon formation from methylating agents over the zeolite catalyst ZSM-5. Comments on the mechanism of carbon-carbon bond and methane formation, *J. Chem. Soc. Faraday Trans. 1 Phys. Chem. Condens. Phases.* 83 (1987) 571–583. <https://doi.org/10.1039/F19878300571>.
- [97] Y. Ono, T. Mori, Mechanism of methanol conversion into hydrocarbons over ZSM-5 zeolite, *J. Chem. Soc. Faraday Trans. 1 Phys. Chem. Condens. Phases.* 77 (1981) 2209–2221. <https://doi.org/10.1039/F19817702209>.
- [98] D. Kagi, Mechanism of conversion of methanol over ZSM-5 catalyst, 69:1 (1981). [https://doi.org/10.1016/0021-9517\(81\)90154-8](https://doi.org/10.1016/0021-9517(81)90154-8).
- [99] C.D. Chang, Reply to Kagi: mechanism of conversion of methanol over

- ZSM-5 catalyst, 69:1 (1981). [https://doi.org/10.1016/0021-9517\(81\)90155-X](https://doi.org/10.1016/0021-9517(81)90155-X).
- [100] C.D. Chang, A.J. Silvestri, The conversion of methanol and other O-compounds to hydrocarbons over zeolite catalysts, *J. Catal.* 47 (1977) 249–259. [https://doi.org/https://doi.org/10.1016/0021-9517\(77\)90172-5](https://doi.org/https://doi.org/10.1016/0021-9517(77)90172-5).
- [101] J.K.A. Clarke, R. Darcy, B.F. Hegarty, E. O'Donoghue, V. Amir-Ebrahimi, J.J. Rooney, Free radicals in dimethyl ether on H-ZSM-5 zeolite. A novel dimension of heterogeneous catalysis, *J. Chem. Soc. Chem. Commun.* (1986) 425–426. <https://doi.org/10.1039/C39860000425>.
- [102] R.M. Dessau, R.B. LaPierre, On the mechanism of methanol conversion to hydrocarbons over HZSM-5, *J. Catal.* 78 (1982) 136–141. [https://doi.org/https://doi.org/10.1016/0021-9517\(82\)90292-5](https://doi.org/https://doi.org/10.1016/0021-9517(82)90292-5).
- [103] I.M. Dahl, S. Kolboe, On the reaction mechanism for propene formation in the MTO reaction over SAPO-34, *Catal. Letters.* 20 (1993) 329–336. <https://doi.org/10.1007/BF00769305>.
- [104] W. Wang, Y. Jiang, M. Hunger, Mechanistic investigations of the methanol-to-olefin (MTO) process on acidic zeolite catalysts by in situ solid-state NMR spectroscopy, *Catal. Today.* 113 (2006) 102–114. <https://doi.org/10.1016/J.CATTOD.2005.11.015>.
- [105] X. Sun, S. Mueller, Y. Liu, H. Shi, G.L. Haller, M. Sanchez-Sanchez, A.C. van Veen, J.A. Lercher, On reaction pathways in the conversion of methanol to hydrocarbons on HZSM-5, *J. Catal.* 317 (2014) 185–197. <https://doi.org/https://doi.org/10.1016/j.jcat.2014.06.017>.
- [106] M. Guisnet, L. Costa, F.R. Ribeiro, Prevention of zeolite deactivation by coking, *J. Mol. Catal. A Chem.* 305 (2009) 69–83. <https://doi.org/https://doi.org/10.1016/j.molcata.2008.11.012>.
- [107] L.-T. Yuen, S.I. Zones, T. V Harris, E.J. Gallegos, A. Auroux, Product selectivity in methanol to hydrocarbon conversion for isostructural compositions of AFI and CHA molecular sieves, *Microporous Mater.* 2 (1994) 105–117. [https://doi.org/https://doi.org/10.1016/0927-6513\(93\)E0039-J](https://doi.org/https://doi.org/10.1016/0927-6513(93)E0039-J).
- [108] M. Stöcker, Methanol-to-hydrocarbons: catalytic materials and their behavior, *Microporous Mesoporous Mater.* 29 (1999) 3–48. [https://doi.org/10.1016/S1387-1811\(98\)00319-9](https://doi.org/10.1016/S1387-1811(98)00319-9).
- [109] U. Olsbye, M. Bjørgen, S. Svelle, K.P. Lillerud, S. Kolboe, Mechanistic insight into the methanol-to-hydrocarbons reaction, *Catal. Today.* 106 (2005) 108–111. <https://doi.org/10.1016/J.CATTOD.2005.07.135>.
- [110] F. Bleken, M. Bjørgen, L. Palumbo, S. Bordiga, S. Svelle, K.P. Lillerud, U.

- Olsbye, The effect of acid strength on the conversion of methanol to olefins over acidic microporous catalysts with the CHA topology, *Top. Catal.* 52 (2009) 218–228. <https://doi.org/10.1007/s11244-008-9158-0>.
- [111] S. Wilson, P. Barger, The characteristics of SAPO-34 which influence the conversion of methanol to light olefins, *Microporous Mesoporous Mater.* 29 (1999) 117–126. [https://doi.org/10.1016/S1387-1811\(98\)00325-4](https://doi.org/10.1016/S1387-1811(98)00325-4).
- [112] Q. Zhu, J.N. Kondo, R. Ohnuma, Y. Kubota, M. Yamaguchi, T. Tatsumi, The study of methanol-to-olefin over proton type aluminosilicate CHA zeolites, *Microporous Mesoporous Mater.* 112 (2008) 153–161. <https://doi.org/10.1016/J.MICROMESO.2007.09.026>.
- [113] I.M. Dahl, H. Mostad, D. Akporiaye, R. Wendelbo, Structural and chemical influences on the MTO reaction: a comparison of chabazite and SAPO-34 as MTO catalysts, *Microporous Mesoporous Mater.* 29 (1999) 185–190. [https://doi.org/10.1016/S1387-1811\(98\)00330-8](https://doi.org/10.1016/S1387-1811(98)00330-8).

CHAPTER II

Samples and characterization techniques

The following chapter summarizes the information regarding all the samples and characterization techniques described in the next chapters of this thesis. In particular, as for the oxidic phase, the synthesis protocol and basic characterization results are herein reported. Advanced characterization results are reported in the next following chapters.

As for the zeolite/zeotype, this chapter also includes the specifications of commercial zeolites and the synthesis protocol, supported by basic characterization.

The last paragraph of the chapter describes the characterization techniques employed for studying the catalysts, whose results are reported in the next chapters.

2.1 PdZn/ZrO₂ + SAPO-34 catalyst

After a complete screening based on catalytic testing, this sample is the first catalyst chosen in the COZMOS project to be scaled-up and applied on larger scale. The following sections are related to the lab-scale catalyst (2.1.1) and to the scaled-up catalyst (2.1.2). The lab-scale catalyst was synthesized by the partner

team at University of Oslo, while the scaled-up catalyst was prepared at Haldor Topsoe.

2.1.1 Synthesis and basic characterization of PdZn/ZrO₂ catalyst

PdZn/ZrO₂ was obtained starting from the following precursors and chemicals: Pd(CH₃COO)₂ (>99.9%), Zn(CH₃COO)₂ (99.99%), Zr(OH)₄ PVP (Mwt 10000), DMF (99.8%), and ethylene glycol (99.8%). All of them were purchased from Sigma-Aldrich and used as received.

The catalyst was obtained by a colloidal impregnation method. 5 g L⁻¹ of Pd(CH₃COO)₂ in DMF solution and 20 g L⁻¹ Zn(CH₃COO)₂ ethylene glycol solution were prepared. 8 g of PVP were added to 80 mL of the zinc acetate solution and heated to 80 °C to obtain a clear yellow solution. 50 mL of palladium acetate solution were added to the clear yellow zinc acetate/PVP solution upon stirring and heated up to 100 °C under reflux for 2 h. The mixture was then cooled, centrifuged, washed with acetone and dispersed in ethanol. 6 g of Zr(OH)₄ powder were added to the dispersed colloidal mixture and stirred at room temperature for 20 h. The resulting mixture was dried in oven and calcined at 500 °C for 3 h.

The chemical characterization was performed by EDX measurements using a transmission electron microscope equipped with a Cs-probe corrected Titan microscope from Thermo Fisher Scientific, which operated at 300 kV accelerating voltage and a beam current of 0.5-0.8 nA.

Table 1 shows the estimated elemental composition of PdZn/ZrO₂ determined by EDS, by means of an X-ray energy-dispersive spectrometer FEI SuperX (~0.7 sr collection angle). This composition is not significantly different from the theoretical synthesis value. The textural characterization determined a BET specific surface area of 47 m²/g.

Table 1 – Estimated composition by EDS for PdZn/ZrO₂ (mol%)

Pd	Zn	Zr
2 ± 1	13 ± 3	85 ± 2

The bifunctional PdZn/ZrO₂+SAPO-34 catalyst was prepared by a physical mixture of both components with a 1:1 mass ratio.

2.1.2 SAPO-34: structural and textural properties

The SAPO-34 employed (SiO₂/Al₂O₃ = 0.5) was purchased from ACS materials. The zeolite were dried at 120 °C for 12 h and calcined at 550 °C for 2 h before testing. [1]

SAPO-34 is a CHA-type zeotype material composed of nanometer-sized cages interconnected by 8-membered rings.

SAPOs are obtained from aluminophosphates (AlPOs), which have alternating AlO₂⁻ and PO₂²⁺ units with a neutral framework [2]. When phosphorus is substituted with silicon into an aluminosilicate lattice, the structure gains cation-exchange abilities, inducing acidity at low Si content. Indeed, by introducing a 4+

cation for a 5+ cation, the structure acquires a net negative charge, balanced with a H⁺ ion. This is the reason why it is possible to substitute Al or P with other metals to obtain metal-aluminophosphates (MeAPOs or MAPOs), new phosphate-based frameworks with several and peculiar properties. As for SAPOs, at higher Si concentrations, silicious islands are formed, reducing the number of acid sites <1 site per Si atom [3].

On this sample, a textural characterization was carried out. Nitrogen adsorption and desorption were performed by using a Micromeritics ASAP 2040 at liquid-nitrogen temperature. All the samples were previously evacuated at 100 °C for 16 h and the Brunauer-Emmet-Teller (BET) method was applied to calculate the specific surface area (SSA) in the range of p/p_0 of 0.067-0.249. The analyses were performed at King Abdullah University of Science and Technology. Table 2 reports all the textural properties of SAPO-34 used and reported in this text.

Table 2 – Textural properties of SAPO-34

Zeolite	S_{BET} (m²/g)	S_{meso/ext} (m²/g)	S_{micro} (m²/g)	V_{total} (ml/g)	V_{micro} (ml/g)	NH₃ desorb/mass (mmol/g)
SAPO-34	770	8	762	0.28	0.27	0.66

2.1.3 Synthesis and basic characterization of the scaled-up catalysts

The scaled-up PdZn/ZrO₂ catalyst was formulated and designed to produce both tablets and extrudates. The preparation of this catalyst is different from that of the lab-scale catalyst, due to some limitations regarding the synthesis and cost concerns, which lead to adapt the procedure using different precursors. Inevitably, the synthesis induced a variation in the composition and the element distribution, affecting the catalytic activity of the scaled-up catalyst. However, the main scope related to scaling up this system was to highlight both advantages and drawbacks of the process and try to find the best protocol for the synthesis of the combined system.

The PdZn/ZrO₂ precursor was prepared by aqueous incipient wetness impregnation of Zn- and Pd-nitrate on ZrO₂ (Aldrich), dried and calcined for 5 hours at 500 °C. The calcined catalyst precursor was mixed with SAPO-34 (China Catalyst Holding CO) and alumina binder, and then pelletized. The SAPO-34 was calcined for 2 hours at 475 °C to decompose the template and to remove the organic residues in the as-received material. The final composition of the tablets as oxide:SAPO-34:binder was approximately 45:45:10 wt%.

Extrudates were prepared by mixing the calcined catalyst precursor, SAPO-34 and alumina binder with water, after acidification using nitric acid to obtain a paste. The paste was extruded through a piston extruder, dried and calcined at 500°C for 5 hours to obtain catalysts with approximately 30:30:40 wt% of PdZnZrO_x, SAPO-34 and Al₂O₃, respectively.

A dual strategy was pursued for both tablets and extrudates, using calcined and reduced precursors, respectively. The reduction process of the calcined PdZn/ZrO₂ precursor was carried out in a flow of hydrogen (2 vol%) in Ar for 20 hours at 400°C. Afterwards, the catalyst was calcined as above-mentioned, except for a small amount, which was pelletized and not calcined, for spectroscopic measurements.

All the physico-chemical properties of the scaled-up catalyst are summarized in Table 3. The chemical composition was determined by EDX.

Regarding the textural characterization, the extrudates featured a lower micropore volume and a reduced ammonia capacity than the pelletized (tablets) catalyst, suggesting that those losses occurred during mixing and extrusion.

Table 3 reports the names that will be used in this present work.

Table 3 – Summary of the prepared samples with their main physico-chemical properties

Sample Name	Sample description	Composition (wt%)*(rest to 100% is oxygen)	NH ₃ capacity (mmol/g)	Surface Areas (Hg) m ² /g	Pore volume < 6Å Ar BET cm ³ /kg
SAPO-34	-	-	0.70	-	224
PZZ-ox	Precursors calcination	Pd(1.8) Zn(8.7) Zr(62.8)	-	16	-
PZZ-red	PZZ-ox reduction	Pd(1.8) Zn(8.8) Zr(62.4)	-	15	-
PZZ-ox-tab	PZZ-ox mixed with SAPO-34+Al(O)OH, tableted and calcined	Pd(0.7) Zn(3.9) Zr(27.4) Al(13.1) Si(0.9) P(9.1)	0.36	34	104
PZZ-red-tab	PZZ-red mixed with SAPO-34+Al(O)OH, tableted and calcined	Pd(0.8) Zn(3.9) Zr(27.4) Al(12.6) Si(0.9) P(9.2)	0.35	31	106
PZZ-ox-ext	PZZ-ox mixed with SAPO-34+Al(O)OH, extruded and calcined	Pd(0.5) Zn(2.7) Zr(19.2) Al(26.0) Si(0.6) P(5.4)	0.12	123	58
PZZ-red-ext	PZZ-red mixed with SAPO-34+Al(O)OH, extruded and calcined	Pd(0.5) Zn(2.7) Zr(19.5) Al(26.5) Si(0.6) P(5.5)	0.12	125	57

2.2 ZnZrO_x + ZSM-5 catalyst

2.2.1 Synthesis of ZnZrO_x catalysts

ZnZrO_x samples were prepared by University of Oslo team by co-precipitation of zirconium and zinc inorganic salt precursors using the same receipt reported by Wang et al.[4]. The procedure was used to obtain three samples at different Zn loading and named in the form ZnZr-X, where X represents the Zn loading determined by ICP-AES analysis, in particular ZnZr-5, ZnZr-15 and ZnZr-30. The precursors used were Zn(NO₃)₂·6H₂O and ZrN₂O₇·xH₂O. Quantities were different according to the sample. For example, as for ZnZr-30, 0.6 g Zn(NO₃)₂·6H₂O and 2.15 g ZrN₂O₇·xH₂O were mixed in 100 ml of type 2 H₂O in a round bottom flask. For all the samples, the mixture was heated up to 70 °C under reflux and stirring. 3.06 g of (NH₄)CO₃ were dissolved in 100 ml of type 2 H₂O and added dropwise to the precursor solutions: a white precipitate was obtained. The precipitates were further stirred at 70 °C for 2 h, cooled at room temperature, centrifuged, and washed twice with type 2 H₂O. The wet powders were dried at 110 °C in oven and finally calcined at 500 °C for 3 h.

Zirconium and zinc content in the ZnZr-X samples were measured by a Perkin Elmer Optima 7000 DV (Perkin Elmer, Norwalk, Connecticut, USA) inductively coupled plasma-atomic emission spectrometer (ICP-AES) equipped with a PEEK Mira Mist nebulizer, a cyclonic spray chamber and an Echelle monochromator. The wavelengths used for Zr and Zn determination were 339.197 nm and 213.857

nm, respectively. Before the analyses, a pre-treatment of the samples was required. An acid digestion of the oxides was performed by a Milestone MLS-1200 MEGA microwave laboratory unit (Milestone, Sorisole, Italy). 200 mg of each sample were collected in tetrafluoromethoxyl (TFM) bombs and digested with 5 mL of aqua regia and 2 mL of hydrofluoric acid. Four 5-mins heating steps (250, 400, 600, 250 W power, respectively), followed by 25 mins of ventilation step, were applied. After an addition of 0.7 g of boric acid, the bombs were heated for 5 min at 250 W and cooled by a ventilation step of 15 min. At the end, the samples appeared completely dissolved. The digested solutions were then diluted to 20 mL with high purity water.

Each sample was analyzed twice, and each concentration value was averaged on the basis of three instrumental measurements. Blanks were run simultaneously. It is well known that every Zr-based compound contains Hf as common natural contaminant; Hf presence was determined to be less than 2 wt.% in each sample, using a wavelength at 277.336 nm.

A portion of all powders was mixed with H-ZSM-5 zeolite to obtain a 1:1 (mass ratio) physical mixture for catalytic tests.

2.2.2 ZSM-5: structural and textural properties

H-ZSM-5 ($\text{SiO}_2/\text{Al}_2\text{O}_3=23$, $S_{\text{BET}} = 417 \text{ m}^2/\text{g}$) was purchased from Zeolyst. The zeolite was dried at $120 \text{ }^\circ\text{C}$ for 12 h and calcined at $550 \text{ }^\circ\text{C}$ for 2 hours prior to testing [5].

ZSM-5 (MFI-type) is one of the most versatile zeolites. It consists of circular structures of 5-membered rings arranged in a column or connected together, with a very flexible structure, which symmetry depends on the chemical composition, temperature and presence of adsorbed molecules. The channels are arranged along two dimensions and defined as "sinusoidal" and "straight" channels that are arranged toward the (100) and (010) direction of the zeolite, respectively. Both channel systems are characterized by apertures with 10-membered rings (10-MR) with size $5.3 \times 5.6 \text{ \AA}$ for one-dimensional channels and $5.1 \times 5.5 \text{ \AA}$ for three-dimensional channels, interconnected with each other (Figure 1) [2,6].

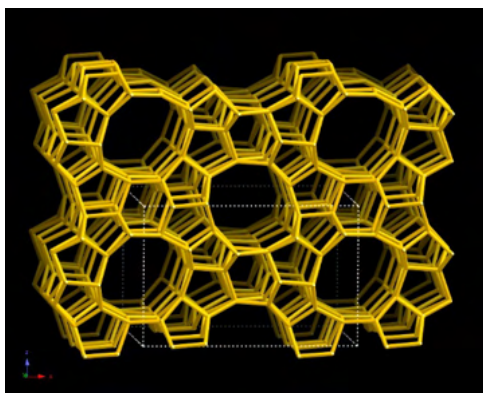


Figure 1 – ZSM-5 zeolite structure along [010] plane [6].

One of the most important advantages of this type of zeolite is the possibility of preparing it with variable composition, adding B, Ga, Fe, Ti, Co, but especially with Si/Al ratios greater than or equal to 8 (high silica), in order to obtain a material that respects certain properties for adequate catalytic activity.

ZSM-5 is well known since the very first experiment involving hydrocarbon synthesis starting from methanol or oil cracking [7] to produce ethene and higher alkenes.

2.3 ZnCeZrO_x + RUB-13 catalyst

2.3.1 Synthesis of ZnCeZrO_x catalyst

ZnCeZrO_x solid solution was prepared by the sol-gel synthesis method. A designed amounts of zinc nitrates (Zn(NO₃)₂•6H₂O), zirconium nitrates (Zr(NO₃)₄•5H₂O) and cerium nitrates (Ce(NO₃)₃•6H₂O) were dissolved in deionized water and stirred at room temperature for 2 hours. Afterwards, glucose was slowly added at 80 °C and vigorously stirred for at least 8 hours. The obtained colloid was dried for 12 hours at 100 °C, calcined at 300 °C and 500 °C for 1 hour and 3 hours in air, respectively.

The synthesis of ZnCeZrO_x was performed at SINTEF (Norway).

The bifunctional catalyst was obtained by a physical mixture in 1:1 mass ratio.

2.3.2 Synthesis and basic characterization of RUB-13

For the synthesis of RUB-13 zeolite, the procedure is reported in Wang et al. [8]. The RUB-13 was synthesized at the Institute of Coal Chemistry (ICC, China). Seed crystals were obtained by mixing 1,2,2,6,6-pentamethylpiperidine (PMP, 0.098 mol) and ethylenediamine (EDA, 0.39 mol) with distilled water (19.6 mol) under stirring. Boric acid (0.049 mol) and fumed silica (0.196 mol) were added to the mixture, to obtain a gel with a molar composition of 1.0 SiO₂:0.25 H₃BO₃:0.5 PMP:2.0 EDA:100 H₂O. The resultant gel was kept stirring at room temperature for 3 h and then crystallized in a Teflon-lined stainless-steel autoclave under rotation at 170 °C for 7 days. The solid products were centrifuged, washed, dried overnight at 100 °C, and then calcined at 560 °C in air for 12 h.

The Al-B-RUB-13 zeolite was synthesized adding boric acid and aluminum sulfate to an aqueous mixture of sodium hydroxide, PMP and EDA under agitation. Fumed silica was then added to the mixture, which was stirred for 1 hour at room temperature, forming a gel with a molar composition of 1.0 SiO₂:(0.5/a) Al₂(SO₄)₃:(1.0/b) H₃BO₃:0.2 NaOH:0.5 PMP:2.0 EDA:100 H₂O, where $a = 30-\infty$ and $b = 1-\infty$ are the Si/Al and Si/B molar ratios in the synthesis gel. Then, the calcined RUB-13 seed (10 wt% fumed silica) was added to the synthesis gel, under stirring for 3 hours at room temperature, which was then crystallized in the Teflon-lined stainless-steel autoclave under rotation at 170 °C for 7 days. Similarly, the solid products were centrifuged, washed, dried and calcined following the same above-mentioned procedure for preparing the RUB-

13 zeolite seed. The H-form of the Al-B-RUB-13 zeolite was obtained by ion exchanging the as-calcined samples twice with NH_4NO_3 aqueous solution (1 M) for 4 hours at 80 °C, which was then calcined at 550 °C in air for 9 hours.

RUB-13 zeolite (RTH-type) has two dimensional channels with aperture sizes of $4.1 \times 3.8 \text{ \AA}$ and $5.6 \times 2.5 \text{ \AA}$, in *a* and *c* direction respectively. RUB-13 has larger channels apertures and cages than SAPO-34 (CHA-type), but smaller volume. In MTO processes, RUB-13 showed to be highly selective towards olefins and a lower coke formation than SAPO-34 [8–10]. From the crystallography point of view, RUB-13 has four nonequivalent tetrahedral sites highlighted in Figure 2: T1 and T2 are located in the 8-membered ring (8-MR) channels, T4 is located in the distorted 8-MR channels and T3 does not appear at all in these rings. T1 and T2 are known to be the active centers in MTO and according to Zhang et al. [8] the activity increases as Al atoms in T1 and T2 increase.

However, the presence of boron is well known to negatively affect the acidity of the zeolites [11] by reducing the strength of the OH groups and, then, the affection of the hydrocarbon conversion yield cannot be ruled out.

The RUB-13 studied and involved in the project has $\text{SiO}_2/\text{Al}_2\text{O}_3 \approx 100$ (i.e. $\text{Si}/\text{Al} \approx 200$) and $\text{Si}/\text{B} \approx 9$, with a BET Specific Surface Area of 401 m^2/g , in line with literature related to RTH-type zeolite [12]

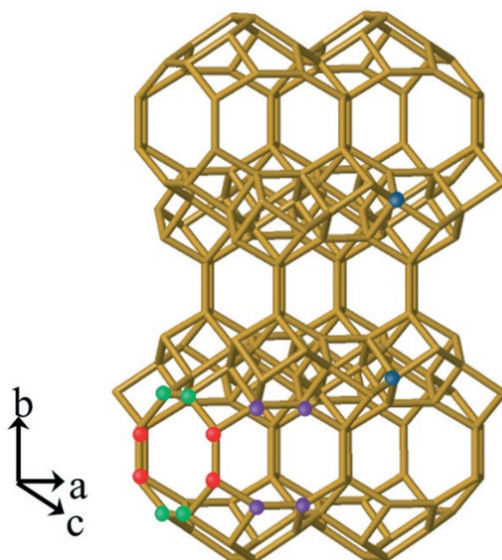


Figure 2 – Framework structure of RUB-13 (RTH-type) zeolite along [001] plane. The green, red, blue, and purple balls identify the T1, T2, T3 and T4 sites, respectively.[8]

2.4 GaZrO_x + SSZ-13 catalyst

2.4.1 Synthesis of GaZrO_x

Gallium-zirconium oxide, GaZrO_x, was prepared by the sol-gel method. A designed amounts of zirconium nitrate (Zr(NO₃)₄) and gallium nitrate (Ga(NO₃)₃) were dissolved in deionized water (150 mL) under agitation for 2 hours at room temperature. The glucose was slowly added at 80 °C and vigorously stirred for 8 hours. The molar ratio of glucose to the total metal ions in the solution is 3.0. The resultant colloidal mixture was dried at 100 °C for 12 hours, and subsequently calcined at 300 °C for 1 hour and 500 °C for 3 hours in air, respectively. The analyzed sample has Ga/Zr ratio equals to 0.5.

The GaZrO_x phase was then physically mixed to a synthesized SSZ-13 zeolite in a 1:1 mass ratio.

The synthesis of this sample was carried out by the Institute of Coal Chemistry (ICC, China).

2.4.2 Synthesis and basic characterization of SSZ-13

SSZ-13 zeolite was prepared with aluminum sulfate (Al₂(SO₄)₃), silica sol (JN-25), N,N,N-trimethyl-1-adamantammonium hydroxide (TMAdaOH), deionized water and potassium hydroxide (KOH) with the chemical compositions of 1.0SiO₂: xAl₂O₃: 0.4TMAdaOH: 0.6KOH: 88H₂O ($x = 0.151, 0.083, 0.052, 0.032$ and 0.023). The mixture was stirred at room temperature for 3 h. The gel was then transferred into a Teflon-lined stainless-steel autoclave and crystallized at 150 °C for 144 h for SSZ-13. H-type zeolite samples of H-SSZ-13 were then obtained by repeatedly ion-exchanging calcined Na-type samples with 1 M NH₄NO₃ aqueous solution at 80 °C for three times, drying at 100 °C for 12 h, and calcining at 560 °C for 5 h.

The H-SSZ-13 used for catalytic tests has a SiO₂/Al₂O₃ equals to 3.

Chabazite (CHA) is one of the most common and widely used zeolites. It is composed of a one-dimensional channel system with 8-membered apertures, with aperture sizes $3.8 \times 3.8 \text{ \AA}$.

Its fame is related, mainly, to the capability of being prepared in variable composition. Compared with natural chabazites, which can also reach Si/Al ratios

of 1, synthetic ones can only be prepared with a ratio higher than 5. According to some authors in the literature [2], chabazite is one of the few zeolites that can be prepared with Si/Al ratios belonging to a very wide range, which is uncommon since most zeolites can only be synthesized in narrower ranges.

Among the most widely used chabazites is SSZ-13: this zeolite is widely used as a solid acid catalyst and, by combining it with some metals, can be used for selective catalytic reduction processes.

SSZ-13 is a CHA-type zeolite ($[H^+_3[Al_3Si_{33}O_{72}]]$) which typically contains three aluminum atoms per unit cell. Aluminum is responsible for the negative charge induced by the substitution of Si atoms, generating Brønsted acid sites. This zeolite is well known to be an excellent acid catalyst for the synthesis of propene from methanol [13].

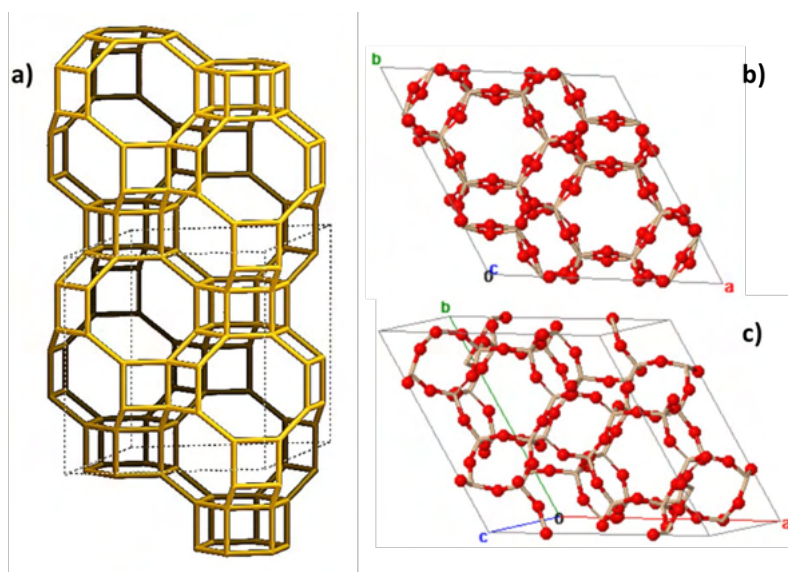


Figure 3 – a) Typical CHA framework [6]; b) and c) CHA framework obtained by computational approach [14]

2.4.3 Synthesis of the scaled-up catalysts.

GaZrO_x oxidic phase, together with Mg-APO-18, was chosen as the second oxidic phase to be scaled up. At the moment, the synthesis protocol of the catalyst is still confidential and not reported in any public document, neither reports nor scientific paper. However, only preliminary characterization results are present. Two batches of GaZrO_x were synthesized and calcined at two different temperatures: 350 °C and 500 °C, namely GaZrO_x-350 and GaZrO_x-500. Both the samples are featured by amorphous structure, with a Ga/Zr ratio of about 0.58. In addition, the first sample has a BET surface area of 188 m²/g, while the second one has a BET surface area of 151 m²/g.

2.5 Characterization techniques

2.5.1 Textural characterization

Specific surface areas of the oxide powders (ZnZrO_x and PdZn/ZrO₂) were carried out by N₂ adsorption at 77 K on a Micromeritics ASAP 2020 after 30 min of evacuation at 30 °C and 2 hours of heating at 120 °C.

As for RUB-13, the powders were outgassed at 120 °C for 720 min and heated at 400 °C over-night. The analysis conditions for both the phases were almost similar, but longer equilibration times were applied for RUB-13 (40 secs of equilibration time and a maximum of 2 hours for the equilibration delay upon

dosing, versus 10 secs of equilibration time and 1 hour for equilibration delay for the oxidic phases).

2.5.2 Spectroscopic characterization

Spectroscopic techniques can be used to study the bifunctional catalysts. For instance, some catalysts have a semiconductive properties, which can be used to determine the depth of electron energy levels in the band gap: indeed, some catalyst include ZnO, which is a well-known semiconductor [15–17]; in addition, gaseous molecule adsorption can be used to probe some specific surface sites, such as Lewis and Brønsted acid sites, or to determine the formation of specific products like carbonates or hydrides.

FT-IR spectroscopy is a valuable spectroscopic technique suitable to unveil various and specific features. Considering the semiconductive properties of some catalyst, a medium IR radiation ($400\text{--}4000\text{ cm}^{-1}$) can be absorbed evidencing an electronic transition from defect levels to the conduction band. The absorption leads to a broad band characterized by an asymmetric “hump” which maximum is centered at a frequency corresponding to the energy difference between the defect level and the bottom of the C.B., while the hump slope can be more or less steep according to the electronic level organization.

It is also very common to observe an absorption related to “free” electrons: in some cases, a thermal transition in the conduction band can occur at room temperature, leading to a monotonic absorption. An utterly “free” electron cannot

absorb as photon because of a mismatch between the required energy and the conservation momentum. However, in a solid state, the absorption can be due to different phenomena such as a band-to-band transition, phonon modes and other scattering centers.

As already mentioned, gaseous molecules can be used to probe the catalyst surface to reveal potential active sites, specific oxidation state of metals and other features regarding both Lewis and Brønsted acid sites. Almost the entirety of this work is based on the characterization of bifunctional catalysts by means of FT-IR. Infrared spectroscopy is a very powerful techniques that allows to derive several information from the analyzed samples by using probe molecules to study certain surface properties. As for the materials studied in this work, i.e. bifunctional catalysts, it was possible to carry out studies on:

- oxidic phase, zeolitic phase and the combined system, by adsorption of CO, eventually at room and liquid-nitrogen temperature;
- CO₂ adsorption properties of the oxidic phase;
- semiconductive properties of the oxidic phase, via H₂ interaction at different temperatures.

Carbon monoxide is one of the most commonly used probe molecules for analyzing properties of reduced or oxidized metal phases present either in the form of aggregates or as isolated ions. CO can behave either as an acid or as a

base, depending on the chemical and physical characteristics of the metal (M) present in the adsorbent phase.

The $5\sigma^*$ and $2\pi^*$ molecular orbitals of CO are those involved in adsorption. The weakly antibonding $5\sigma^*$ orbital is located on the carbon atom and is responsible for the basic character, due to the presence of an electron pair; the strongly antibonding $2\pi^*$ empty degenerate orbitals are located on the oxygen atom.

The bond order is three, with a partial positive charge on oxygen and a partial negative charge on carbon.

During the adsorption either σ donation from CO or π backdonation from a metal site can be observed. The reason is connected to the above-mentioned CO molecular orbitals:

- when CO behaves as a (weak) base, the donation of the electron doublet of the weakly antibonding $5\sigma^*$ orbital to empty d orbitals (σ donation from CO) of the adsorption site results in an increase in the order of the C-O bond, which causes the shift from the characteristic stretching frequency of the free molecule (2143 cm^{-1}) towards higher frequencies;
- when CO behaves as an acid, it receives electrons (π backdonation) from a d orbital of the adsorption site to the CO empty $2\pi^*$ orbitals. Since these orbitals have a strong antibonding character, the electronic transfer causes a decrease in the C-O bond order and, thus, a decrease in the bond stretching frequency.

The strength of CO σ donation or π backdonation will depend on the nature of adsorption sites: the higher the oxidation state, the lower the probability of π backdonation and the higher the σ donation.

As for zeolites, IR spectroscopy makes it possible to obtain information about the acid-base properties of the surface – in particular, Brønsted acid sites – determined by the stretching of O-H bond of the hydroxyl groups present on the structure or by probe molecule adsorption (e.g. CO).

Absorption IR spectra were collected using a Perkin-Elmer FTIR 2000 spectrophotometer equipped with a Hg-Cd-Te cryo-detector, at a resolution of 2 cm^{-1} in the range of 7200-580 cm^{-1} . All sample powders were compressed in self-supporting discs ($\sim 20 \text{ mg cm}^{-2}$) and placed in a quartz IR cell suitable for thermal treatments in controlled atmosphere and spectra recording at room and liquid-nitrogen temperature (RT and LNT, respectively).

Moreover, some experiments were performed using a commercial stainless-steel cell (Aabspec) allowing in situ thermal treatments under vacuum or controlled atmosphere and simultaneous registration of spectra at temperatures up to 600 °C. Infrared spectroscopy was used for the characterization of all studied catalysts.

X-ray Absorption Spectroscopy (XAS) is a spectroscopic technique capable of providing structural information on the local surroundings of a selected atomic species, in terms of coordination number, interatomic distances and oxidation state. XAS is a very powerful and sensitive technique to little concentration of specific absorber. The photoelectric effect is the phenomenon on which the

technique is based: the absorption of radiation causes the ejection of an electron from a core orbital by the atomic species of interest, which undergoes a series of interactions that allow local information of structural and electronic nature to be obtained. When examining an XAS spectrum, it is possible to identify two energy regions, from which several information could be obtained: the XANES (X-ray Absorption Near Edge Spectroscopy) region and the EXAFS (Extended X-ray Absorption Fine Structure) region. The former encompasses the entire region around the threshold energy, E_0 , namely the energy required to ionize the atom or ion of the element being studied and extends to a few tens of electron volts (eV) beyond the edge of the spectrum. The XANES region provides us with information regarding the geometry and oxidation number, as the position of the threshold changes depending on the formal or net charge of the atom.

The EXAFS region, on the other hand, comprises the entire region at higher energy than XANES, typically up to 1 keV above the threshold. This region is characterized by a fine structure whose oscillations are caused by constructive and destructive interference phenomena generated by the chemical surround on the photoelectron wavefunction. From the amplitude, frequency and damping of the function, it is possible to derive information on the coordination number, the interatomic distance, and the degree of disorder of the surround, respectively. In some cases, it is possible to qualitatively estimate the size of aggregates such as clusters or particles.

X-Ray Absorption Spectroscopy (XAS) measurements were performed by Dr. Davide Salusso at different facilities, such as ESRF (BM31 and BM23) and SOLEIL (Rock) beamlines, during the course of the project.

Finally, structural characterization by Powder X-Ray Diffraction (PXRD) was carried out in different conditions and geometry (e.g. Bragg-Brentano or capillary), with different instruments (Bruker D8 Discover, PanAlytical X'Pert Pro, etc.) and in different places (university laboratories or synchrotron facilities). Hence, the specifications and other information regarding the analyses are shortly summarized in each chapter.

PXRD was employed to determine if the oxidic phases analyzed were solid solutions, evaluating the inclusion of specific atoms in the support matrix, or mixed oxides. As for PdZn/ZrO₂, PXRD was implemented to determine the formation of a PdZn alloy. Dr. Davide Salusso was in charge for the data collection and elaboration regarding this characterization technique.

REFERENCES

- [1] A. Ramirez, P. Ticali, D. Salusso, T. Cordero-Lanzac, S. Ould-Chikh, C. Ahoba-Sam, A.L. Bugaev, E. Borfecchia, S. Morandi, M. Signorile, S. Bordiga, J. Gascon, U. Olsbye, Multifunctional Catalyst Combination for the Direct Conversion of CO₂ to Propane, *JACS Au*. 1 (2021) 1719–1732. <https://doi.org/10.1021/jacsau.1c00302>.
- [2] S.M. Auerbach, K.A. Carrado, P.K. Dutta, *HANDBOOK OF ZEOLITES SCIENCE AND TECHNOLOGY*, 2003. <https://doi.org/10.1201/9780203911167-7>.
- [3] J.F. Haw, D.M. Marcus, Examples of Organic Reactions on Zeolites: Methanol to Hydrocarbon Catalysis, in: *Handb. Zeolite Sci. Technol.*, Marcel Dekker, Inc., 2003.
- [4] J. Wang, G. Li, Z. Li, C. Tang, Z. Feng, H. An, H. Liu, T. Liu, C. Li, A highly selective and stable ZnO-ZrO₂ solid solution catalyst for CO₂ hydrogenation to methanol, *Sci. Adv.* 3 (2017) 1–11. <https://doi.org/10.1126/sciadv.1701290>.
- [5] P. Ticali, D. Salusso, R. Ahmad, C. Ahoba-Sam, A. Ramirez, G. Shterk, K.A. Lomachenko, E. Borfecchia, S. Morandi, L. Cavallo, J. Gascon, S. Bordiga, U. Olsbye, CO₂ hydrogenation to methanol and hydrocarbons over bifunctional Zn-doped ZrO₂/zeolite catalysts, *Catal. Sci. Technol.* 11 (2021) 1249–1268. <https://doi.org/10.1039/D0CY01550D>.
- [6] Database of Zeolite Structures, (n.d.). <https://europe.iza-structure.org/IZA-SC/framework.php?STC=CHA>.
- [7] R.M. Dessau, R.B. LaPierre, On the mechanism of methanol conversion to hydrocarbons over HZSM-5, *J. Catal.* 78 (1982) 136–141. [https://doi.org/https://doi.org/10.1016/0021-9517\(82\)90292-5](https://doi.org/https://doi.org/10.1016/0021-9517(82)90292-5).
- [8] L. Zhang, S. Wang, D. Shi, Z. Qin, P. Wang, G. Wang, J. Li, M. Dong, W. Fan, J. Wang, Methanol to olefins over H-RUB-13 zeolite: Regulation of framework aluminum siting and acid density and their relationship to the catalytic performance, *Catal. Sci. Technol.* 10 (2020) 1835–1847. <https://doi.org/10.1039/c9cy02419k>.
- [9] Structure Commission of the International Zeolite Association, (n.d.). http://asia.iza-structure.org/IZA-SC/material_tm.php?STC=RTH.
- [10] S. Vortmann, B. Marler, H. Gies, P. Daniels, Synthesis and crystal structure of the new borosilicate zeolite RUB-13, *Microporous Mater.* 4 (1995) 111–121. [https://doi.org/10.1016/0927-6513\(94\)00090-I](https://doi.org/10.1016/0927-6513(94)00090-I).
- [11] L. Regli, S. Bordiga, C. Lamberti, K.P. Lillerud, S.I. Zones, A. Zecchina,

- Effect of boron substitution in chabazite framework: IR studies on the acidity properties and reactivity towards methanol, *J. Phys. Chem. C.* 111 (2007) 2992–2999.
<https://doi.org/10.1021/JP064048W/ASSET/IMAGES/LARGE/JP064048WH00004.JPEG>.
- [12] Jong BinLim, D. Jo, S. BongHong, Palladium-exchanged small-pore zeolites with different cage systems as methane combustion catalysts, *Appl. Catal. B Environ.* 219 (2017) 155–162.
- [13] I.M. Dahl, H. Mostad, D. Akporiaye, R. Wendelbo, Structural and chemical influences on the MTO reaction: a comparison of chabazite and SAPO-34 as MTO catalysts, *Microporous Mesoporous Mater.* 29 (1999) 185–190. [https://doi.org/10.1016/S1387-1811\(98\)00330-8](https://doi.org/10.1016/S1387-1811(98)00330-8).
- [14] ZEOMICS, (n.d.). <http://ares.tamu.edu/zeomics/>.
- [15] Ü. Özgür, Y.I. Alivov, C. Liu, A. Teke, M.A. Reshchikov, S. Doğan, V. Avrutin, S.J. Cho, H. Morkoç, A comprehensive review of ZnO materials and devices, *J. Appl. Phys.* 98 (2005) 1–103.
<https://doi.org/10.1063/1.1992666>.
- [16] W. Göpel, U. Lampe, Influence of defects on the electronic structure of zinc oxide surfaces, *Phys. Rev. B.* 22 (1980) 6447–6462.
<https://doi.org/10.1103/PhysRevB.22.6447>.
- [17] S. Morandi, A. Fioravanti, G. Cerrato, S. Lettieri, M. Sacerdoti, M.C. Carotta, Facile synthesis of ZnO nano-structures: Morphology influence on electronic properties, *Sensors Actuators, B Chem.* 249 (2017) 581–589. <https://doi.org/10.1016/j.snb.2017.03.114>.

CHAPTER III

PdZn/ZrO₂: from lab to technical catalyst

In the following section, characterization results on stand-alone PdZn/ZrO₂ and lab-scale and technical bifunctional catalyst are reported.

Synthesis and basic characterization of these samples are described in Chapter II – section 2.1, while structural and advanced spectroscopic characterization, and catalytic test results are herein discussed.

The first sections deal with the lab scale catalyst, whereas the last sections are related to the technical (scaled-up) catalyst. Further details about the paper published and submitted on the lab scale are reported in Appendix A.1 and A.3 while further information about the technical catalyst are reported in Appendix A.4.

3.1 Lab scale: structural characterization

Powder X-ray diffraction (PXRD) measurements were carried out by means of a Bruker D8 Discover equipped with a Cu K α source and a Lynx Eye silicon detector. All the diffractograms were acquired with steps of 0.02° from 10 to 90°. The database used is the ICSD, Inorganic Crystal Structure Database. All the measurements and data elaboration were performed by Dr. Davide Salusso.

The diffractogram of the as prepared sample reported in Figure 1 shows the presence of PdO, zincite (hexagonal ZnO) and tetragonal/cubic ZrO₂. Tetragonal and cubic ZrO₂ reflection are not distinguishable, but the determination of the specific phase was out of the scope of the work and, thus, not furtherly investigated.

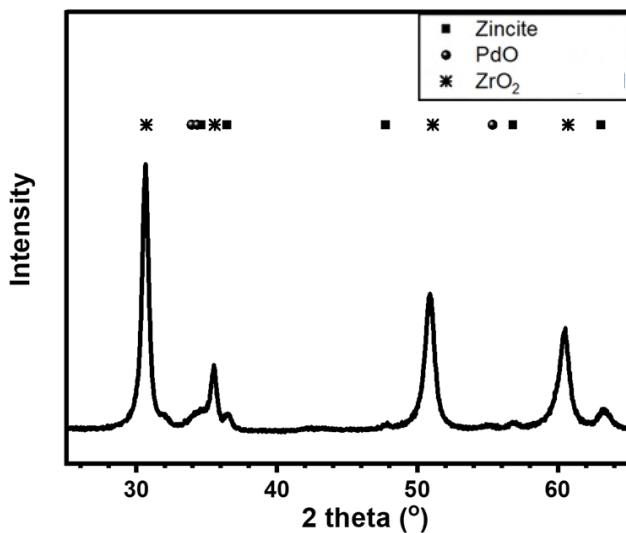


Figure 1 – Powder X-ray diffractograms of the as prepared PdZn/ZrO₂ sample.

3.2 Lab scale: spectroscopic characterization

Spectroscopic characterization measurements were performed on both the stand-alone and combined bifunctional catalysts. In the following sections, I will firstly focus on the characterization of the stand-alone catalyst to further compare the results with those related to the combined system. In particular, the first section will mainly deal with FT-IR of adsorbed probe molecules, supported by XAS, XPS and NMR measurements. By means of H₂ adsorption, it was possible to study the electronic properties of the stand-alone phase, associated to the presence of the semiconducting ZnO phase. In addition, CO₂ adsorption was carried out to study the formation of carbonate species on the stand-alone oxidic phase, to evaluate the relationship between properties and catalytic activity before and after activation. By means of CO at both room and liquid-nitrogen temperature, XAS and XPS, it was possible to study the bimetallic sites supported on the oxidic phase, i.e. Pd and Zn. Finally, a further investigation concerning the zeotype and the combined catalyst by means of CO adsorption followed by FT-IR and ssNMR measurements was carried out to focus on the deactivation and the nature of the main hydrocarbons produced by the CO₂ hydrogenation.

3.2.1 FT-IR: H₂ interaction with the stand-alone PdZn/ZrO₂

Zinc oxide plays a key role in H₂ heterolytic splitting and stabilization of intermediate species which is intimately correlated to the formation of stoichiometric defects, such as oxygen vacancies [1–5]. In this case study, ZnO was demonstrated to be present on the as-prepared catalyst as reported by PXRD and XAS measurements (*vide infra*), and oxygen vacancies could have been produced during the activation procedure. In the light of the composition of the sample, CO₂ hydrogenation can be linked to the formation of oxygen vacancies on defective ZnO phase [3]. To investigate the formation of oxygen vacancies (V_O), the catalyst was treated in H₂ atmosphere and increasing temperature. All IR spectra reported in Figure 2 are difference spectra, obtained by subtracting pre-acquired spectra in O₂ atmosphere from those acquired in H₂.

Figure 2 displays all spectra obtained in H₂ from 50 °C to 400 °C and an electronic absorption is highlighted by the absorption profile of all the bands. In particular, from 50 °C to 150 °C the band increased in intensity. From 150 °C to 400 °C an intensity loss was observed, maybe related to the formation of a PdZn alloy, which is also confirmed by XAS, XPS and further FT-IR findings (*vide infra*)

All the absorption spectra represent a typical pattern related to the photo-ionization of mono-ionized oxygen vacancies [4–6]. As already mentioned in Chapter II, the infrared absorption gives rise to a specific pattern characterized by an asymmetric “hump” whose maximum can be assumed as the band gap

energy, while the hump slope can be more or less steep according to the electronic level organization.

It is well known that ZnO is a semiconductor due to the presence of lattice defects, namely oxygen vacancies (V_O) [4,5]. In particular, two electronic bands below the conduction band (C.B.) at 0.05 and 0.18 eV are associated with V_O . For instance, neutral vacancies display two trapped electrons occupying the two levels, related to the first and the second ionization energy. The first ionization energy is so low that the majority of V_O can be easily mono-ionized (V_O^+) at room temperature and the excited electrons move in the C.B. The second ionization can occur by means of IR radiation, as a photo-ionization of V_O^+ . Pure ZnO should have an absorption band centered at 1450 cm^{-1} , ca. 0.18 eV, obtained for instance after a reduction treatment in H_2 which creates mono-ionized oxygen vacancies following two pathways:

- i) Filling of bi-ionized oxygen vacancies, V_O^{2+} , with an electron by consuming adsorbed oxygen species like O_2^{2-} , O^- and O_2^- ;
- ii) Generating a new V_O^+ by extraction of O atoms from the surface.

This route is typically followed at high temperature.

Unfortunately, IR technique is not able to distinguish the two pathways.

Much is known about the formation of PdZn alloys in PdZn-based catalysts on several supported oxides, such as CeO_2 , TiO_2 , ZrO_2 , etc. [7–11].

In this case scenario, the reduction of Zn^{2+} to Zn^0 could occur at the expense of those electrons trapped inside the V_O^+ , which would explain the intensity loss of the band related to the electronic transition from V_O^+ to the conduction band with increasing temperature.

As for the last two spectra at 350 and 400 °C, the band seems to have a different pattern, compared to all the other spectra acquired at lower temperature. This can be due to a contribution related to “free” electrons in the C.B. Hence at higher temperature both the transition of electrons belonging to defect levels and those in the C.B. are observed.

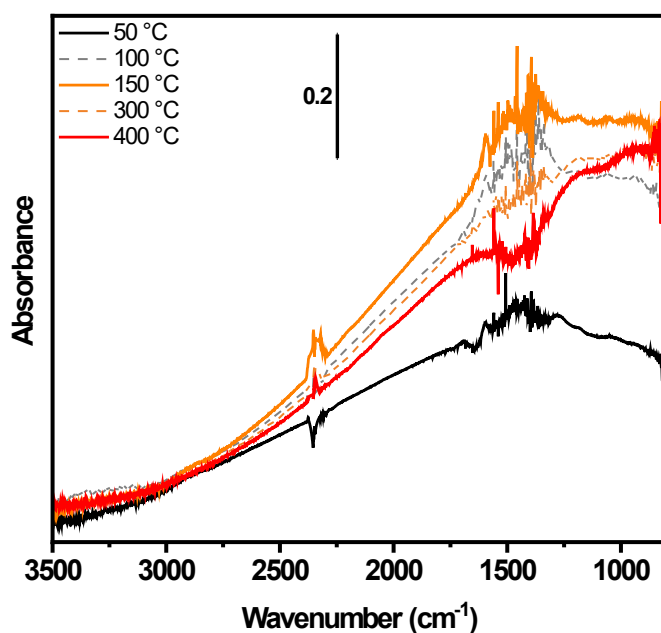


Figure 2 – FT-IR difference spectra of PdZn/ZrO₂ catalyst in H₂ at increasing temperature. All spectra are obtained by subtracting each spectrum acquired in O₂ to those in H₂ at the same temperature.

As for all the spectra the maximum absorption is centered at 1250 cm⁻¹, this is related to electronic levels at about 0.15 eV under the C.B., i.e. very close to the second ionization energy related for ZnO (0.18 eV).

All these findings suggested the presence of highly defective ZnO phase.

3.2.2 FT-IR: CO₂ adsorption on the stand-alone PdZn/ZrO₂

To explore and study the interaction between CO₂ and the catalyst surface, CO₂ adsorption was followed by FT-IR spectroscopy on both oxidized and activated PdZn/ZrO₂.

The adsorption of CO₂, reported in Figure 3, originated several bands related to different carbonate species, that could be mainly related to ZnO and ZrO₂ phases. However, on the basis of literature data, neither CO₂ adsorbed on ZnO [12,13] or tetragonal ZrO₂ (t-ZrO₂) [14] gives the same absorption bands reported in Figure 3. In particular, ZnO gives a high amount of bicarbonates [12,13], while t-ZrO₂ gives more polydentate bridging carbonate species than our sample [14]. In addition, the PdZn/ZrO₂ at hand gives bridged and monodentate species that are not observed in any of the previously mentioned phases. For the sake of clarity, the identified species for this sample are:

- i. bicarbonates – weak band at 1689 and 1221 cm⁻¹, related to $\nu(\text{C}=\text{O})$ and $\delta(\text{C}-\text{O}-\text{H})$ modes, respectively;

- ii. bridged carbonates – bands at 1647, 1322 and 1044 cm^{-1} , assigned to $\nu(\text{C}=\text{O})$, $\nu_{\text{asym}}(\text{O}-\text{C}-\text{O})$ and $\nu_{\text{sym}}(\text{O}-\text{C}-\text{O})$ modes, respectively;
- iii. bidentate carbonates – bands at 1582, 1363 and 1044 cm^{-1} , related to $\nu(\text{C}=\text{O})$, $\nu_{\text{asym}}(\text{O}-\text{C}-\text{O})$ and $\nu_{\text{sym}}(\text{O}-\text{C}-\text{O})$ modes, respectively;
- iv. monodentate carbonates – bands at 1489, 1408 and 1090 cm^{-1} , assigned to $\nu_{\text{asym}}(\text{O}-\text{C}-\text{O})$, $\nu_{\text{sym}}(\text{O}-\text{C}-\text{O})$ and $\nu(\text{C}-\text{O})$ modes, respectively.

The band at 847 cm^{-1} can be related to the $\delta(\text{O}-\text{C}-\text{O})$ mode of both monodentate and bidentate carbonates [15,16].

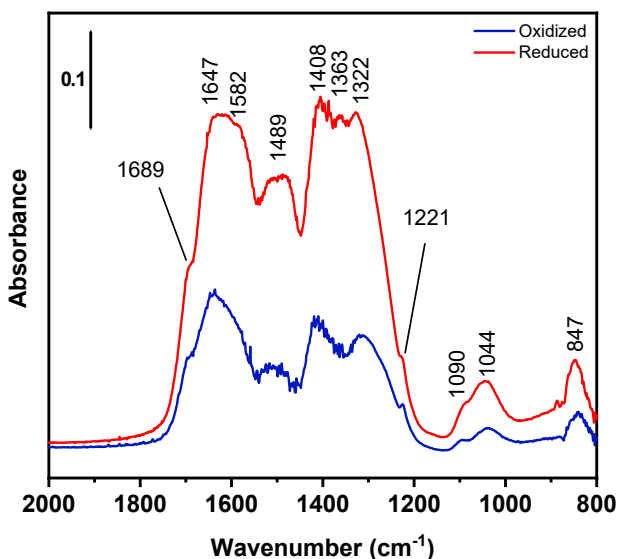


Figure 3 – FT-IR spectra of CO_2 adsorbed at RT on oxidized and activated PdZn/ ZrO_2 at equilibrium pressure of 20 mbar.

The spectral features observed for the oxidized sample are the same of the activated one, but the intensity of the bands reported in Figure 3 suggests that there are more carbonates formed on the activated PdZn/ ZrO_2 than on the

oxidized sample. The reason could be linked to the stoichiometric defect formation: a reduction process generates oxygen vacancies on the surface of the ZnO phase, generating a highly defective domain that could promote the formation of carbonate species. Hence, we reasonably assigned all the carbonates described above to this phase. However, an expert eye could recognize some differences between the carbonate species formed on bare ZnO, reported in literature [12,13], and those observed on this sample. As a matter of fact, it would suggest that the ZnO detected on the catalyst at hand is a supported phase and this would cause the presence of huge amount of surface defects, such as kinks, corners and edges, beside stoichiometric defectiveness which is characteristic of ZnO itself. Moreover, the interaction between the ZnO phase, ZrO₂ and Pd could contribute to increase the heterogeneity of the adsorbed surface species.

3.2.3 FT-IR: CO adsorption on the stand-alone PdZn/ZrO₂

As mentioned in section 3.2.1, PdZn-based catalyst are featured by the formation of PdZn alloys. CO adsorption followed by FT-IR at both room (RT) and liquid-nitrogen temperature (LNT) is a useful mean to investigate the chemical properties of metallic sites and Lewis acid sites.

CO adsorption at RT was carried out on catalyst after oxidation step in pure O₂ at 400 °C and activation in H₂ at 400 °C. Figure 4 displays all the spectra acquired after these two thermal treatment conditions: CO adsorption at RT on

materials like the examined PdZn/ZrO₂ would mainly give rise to Pd-carbonyls and, according to the thermal treatment, CO could be adsorbed on both ionic (Pdⁿ⁺) or metallic (Pd⁰) sites. In addition it is noteworthy to remember that CO can reduce Pdⁿ⁺ species to metallic Pd⁰.

Figure 4a displays all the spectra acquired after oxidation and CO probing, and three main bands can be identified. The highest, characterized by the peak at 2130 cm⁻¹ that can be assigned to Pdⁿ⁺-CO species, that could belong to PdO particles [17,18], as highlighted by PXRD results. At lower frequencies, two absorption features, centered at 2090 and 2063 cm⁻¹ could be assigned to metallic Pd carbonyls [17,19–25]. Indeed, the presence of metallic Pd is not surprising, because CO adsorption induces reduction of Pdⁿ⁺ (n > 0) to Pd⁰. However, these components are not referring to the same carbonyls. The peak at 2090 cm⁻¹ can be ascribed to Pd⁰-CO, while the band at 2063 cm⁻¹ should be ascribed to Pd sites with higher electronic density driving to a reduction of $\nu(\text{C}\equiv\text{O})$ frequency. According to literature [20,24,26], this band can be ascribed to (Zn)Pd-CO, thus CO adsorbed on a PdZn alloy. In this case, the Zn involved in the alloy formation seems to donate electrons to Pd atoms, which are then back-donated to the CO molecules, inducing a decrease in the stretching frequency of the probe molecule.

Looking at the band at 2063 cm⁻¹, a shift to higher frequency (blue-shift) is well evident. In particular, the band is featured by a first peak at 2036 cm⁻¹ at low CO coverages (θ_{CO}), which shifts towards 2063 cm⁻¹ at higher θ_{CO} .

The blue-shift can have several explanations:

- i) “through space” dipole-dipole interaction between parallel vibrating molecules [27];
- ii) “through solid” *via* vibrational coupling across binding electrons [28];
- iii) “chemical effect” deriving from adsorbed molecules [28,29];
- iv) “electrostatic” or “solvent” effect caused by perturbation between adsorbed molecules [30].

Among these effects, the first two effects are dynamic, whereas the last two are static. As for the dynamic effects, the second (ii) effect is negligible when the adsorption is featured by a small adsorption enthalpy, or generally when adsorbed CO stretching frequency, $\nu(\text{C}\equiv\text{O})$, is near that of free CO (2143 cm^{-1}).

Among the static effects, the second (iv) is typically small and negligible [31]. Hence, only the dipolar coupling and the “chemical effect” could explain the blue shift upon increasing θ_{CO} . Typically, the dipolar coupling is predominant on regular facets, like terrace sites, induced by the proximity of atoms belonging to the same element. It always causes a blue-shift, but since the component was ascribed to (Zn)Pd-CO, Pd atoms are separated by the presence of Zn atoms; thus, the dipolar coupling must be neglected.

On the other hand, the *chemical effect* is due to the decrease of π -backdonation character – which typically reduces the stretching frequency $\nu(\text{C}\equiv\text{O})$ – upon

increasing ν_{CO} , caused by the decrease of donated electron density to each adsorbed CO molecule. As a consequence, as ν_{CO} increases, π -backdonation decreases and $\nu(\text{C}\equiv\text{O})$ increases. To explain why this phenomenon is very well visible only for the PdZn alloy components and not for the Pd⁰-CO band at 2090 cm⁻¹ is not straightforward. First of all, the PdZn alloy seems to have a negative charge on Pd atoms as highlighted by Kast and co-workers [17]. In this case, the electron density could move from Zn to Pd. Further details will be reported in section 3.2.4, where XPS measurements are reported, confirming the electron transfer and suggesting a strong *chemical effect* (solid-line arrow in Figure 4a). As for the Pd⁰-CO at 2090 cm⁻¹, the shift is less pronounced. It is possible to suggest the presence of small Pd⁰ clusters, thus the dipolar coupling would be absent and the *chemical effect* would have less strength, so that the shift is barely detectable (dotted arrow in Figure 4a). The presence of small Pd⁰ clusters could be confirmed by the presence of the band at 1930 cm⁻¹, which could be related to bridged carbonyls, Pd₂(CO) [32]. As a matter of fact, these species are only formed when “pure” Pd domains are present.

After outgassing (Figure 4a, dashed black line), the band at 2090 cm⁻¹ is reduced to a small shoulder of the band at 2063 cm⁻¹ that, on the contrary, is stable enough to resist at the dynamic vacuum. This confirms the strong interaction between CO and Pd sites of the PdZn alloy, induced by the stronger electron backdonation due to the alloy itself. As for the other components, all of them are completely removed by the outgassing.

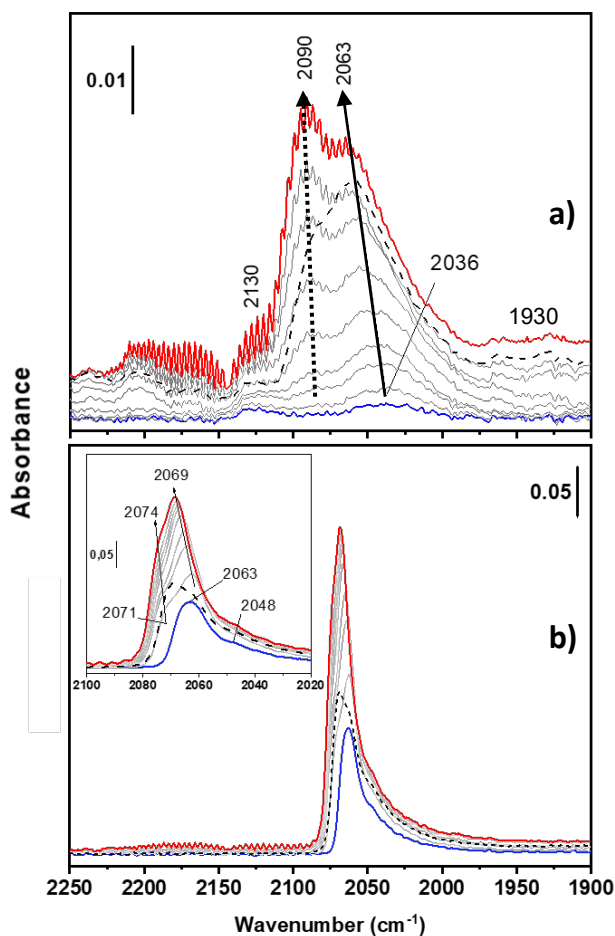


Figure 4 – FT-IR spectra of CO adsorbed at RT on a) oxidized and b) activated PdZn/ZrO₂. Spectra were acquired at increasing dosage of CO up to 20 mbar (from blue to red line) and after outgassing (black dashed line).

After activation in pure H₂ at 400 °C, followed by CO adsorption at RT, the scenario is the one reported in Figure 4b. Differently from the spectra acquired on the oxidized PdZn/ZrO₂, on the activated catalyst only one major component is observed. At very low CO dosing (Figure 4b, blue line), a first component at 2063 cm⁻¹ is already very intense. Upon increasing ρ_{CO} , the peak exhibited a blue-shift up to 2069 cm⁻¹. In addition, new components become more visible: a

shoulder at 2071 cm^{-1} , which upward shifted to 2074 cm^{-1} , and one at 2049 cm^{-1} .

All the above-mentioned components can be attributed to different families of metallic Pd sites with different coordination. The $\text{Pd}^0\text{-CO}$ bond shows a very strong π -backdonation character. As a matter of fact, if Pd^0 atoms are coordinatively unsaturated, a major electronic density to the adsorbate is observed [33]. This phenomenon is translated in a reduction of the $\nu(\text{C}\equiv\text{O})$ of adsorbed CO molecules compared to the that of free CO molecule. Hence, the lower the frequency the lower the coordination of the metallic site.

Moreover, all these components are very low in frequency to be “pure $\text{Pd}^0\text{-CO}$ ”. As already mentioned for the peaks discussed for Figure 4a, these peaks can only be related to $(\text{Zn})\text{Pd-CO}$ [17,19–21,23,24]. The blue-shift has the same origin of that already discussed for panel **a**). However, this spectroscopic feature could not explain the formation of the PdZn alloy by itself. Looking at the Figure 4b, below 2000 cm^{-1} no peaks are present and Pd is well known to give bridged Pd carbonyls [17,21,34]. Hence, in the case at hand the absence of these species could be translated in the absence of neighboring Pd atoms and further confirmed the PdZn alloy formation.

The different intensity of the peaks in Figure 4b with respect to Figure 4a is strictly connected to the performed thermal treatment. Differently from the oxidized sample, where the reduction – and following formation of the alloy – was induced by CO adsorption, the reduced sample underwent a reduction in

pure H₂, so that the amount of alloy produced is significantly higher. It cannot be excluded that all Pd atoms alloyed with Zn. Indeed, the sharpness of the band in the range 2080-2020 cm⁻¹ confirmed that no other species, but the PdZn alloy could be formed after the activation.

A further investigation concerning the oxidic phase was performed at liquid-nitrogen temperature (LNT), after the oxidation and the reduction/activation treatment, by CO adsorption monitored by FT-IR.

Starting with the oxidized catalyst, Figure 5a shows all the spectra acquired at increasing ϑ_{CO} . Differently from the spectra acquired at RT, only a single band is observable, which lies in the region of both Zr⁴⁺-CO and Pdⁿ⁺-CO, but unfortunately the components are not distinguishable. Moreover, RT spectra were featured by the reduction of Pd induced by CO adsorption, which is not visible in this case. The phenomenon is completely hindered by the low temperature, which slows down every possible reaction, and explains why we chose to investigate this catalyst at both the temperatures.

A completely different scenario is observed for the activated sample (Figure 5b). CO adsorption gives rise to spectral features lying in two main regions: the lowest in frequency in the range 2090-2020 cm⁻¹, attributed to the Pd⁰ sites related to PdZn alloy, and the highest in the range 2190-2120 cm⁻¹, ascribed to Zr⁴⁺ and Zn²⁺ sites.

Starting from very low CO coverages (blue line), CO is firstly adsorbed on (Zn)Pd⁰ sites, with an asymmetric band centered at 2062 cm⁻¹.

Upon increasing ϑ_{CO} , a peculiar behavior is observed. Moving from the blue line, through the green line, to the red line, the spectra exhibit increasing and then decreasing intensity related to Pd carbonyls, combined with a shift towards higher frequencies (blue-shift). From now on, this behavior will be named as *bell-shaped shift*. The intensity modulation reaches a maximum (green line) that will be indicated as “*breakdown pressure*”. At the *breakdown pressure*, the broad band related to Zr⁴⁺- and Zn²⁺-carbonyls starts to increase.

In particular, the highest frequency region is centered at 2180 cm⁻¹ (Figure 5b, green line) and could be ascribed to Zn²⁺-CO [18,35], which seems to be completely covered by Zr⁴⁺-CO band as ϑ_{CO} keep increasing. In this case, we could reasonably ascribe the entire band to Zr⁴⁺, since Pd is reasonably entirely reduced to form the alloy. This band exhibits a red-shift that is evident in both oxidized and reduced samples. However, ascribing this band to zirconium(IV) components, the shift is simple to explain. The red-shift can be easily related to the so-called *chemical effect*. Differently from Pd⁰, Zr⁴⁺ is a σ -acceptor center: as ϑ_{CO} increases the electronic density moving from CO molecules decreases and $\nu(\text{C}\equiv\text{O})$ decreases [18,36,37].

An expert eye may ask why Zn²⁺-CO is only visible on the activated sample and not for the oxidized one. A possible explanation could be related to the adsorption of CO molecules on highly defective Zn²⁺ sites, whose formation is

induced by the reducing treatment and, then, the formation of oxygen vacancies, as already mentioned.

Metallic Zn (Zn⁰) was excluded as, to the best of our knowledge, no literature data reported Zn⁰-CO species. Rationally, Zn⁰ orbitals (i.e. d-orbitals) that would have been involved in the interaction with CO molecular orbitals, are not suitable in the bond formation. It clearly explains why some works determined, by subtraction, the amount of metallic Zn produced during reducing processes by using Zn²⁺ carbonyls of oxidized and reduced materials [38].

After outgassing (black dashed line) the intensity of all bands reduces: the band at 2155 cm⁻¹ disappeared, highlighting the weak interaction between CO and Zr⁴⁺/Zn²⁺ sites, while a single band centered at 2064 cm⁻¹, related to (Zn)Pd⁰-CO carbonyls remained, but with a comparable intensity to the spectrum acquired at the maximum θ_{CO} .

The comprehension of the *bell-shaped shift* is not straightforward. Before going into the details, we can separate the *bell-shaped shift* into its components: the blue-shift and the intensity modulation.

The blue-shift of Pd⁰-CO band observed at increasing θ_{CO} is based on the same *chemical effect* mentioned for the spectra acquired at RT. As for the intensity modulation, the band related to Pd starts decreasing when CO is adsorbed on Zr⁴⁺ and Zn²⁺ sites. At first glance, the intensity loss could be associated to CO desorbed from Pd sites, but it would have also caused a red-shift of the band. A more detailed hypothesis could be linked to a reduction of (Zn)Pd⁰-CO

absorption coefficient induced by CO adsorption onto ZnO and ZrO₂-support, nearby Pd sites without hindering the *chemical effect*.

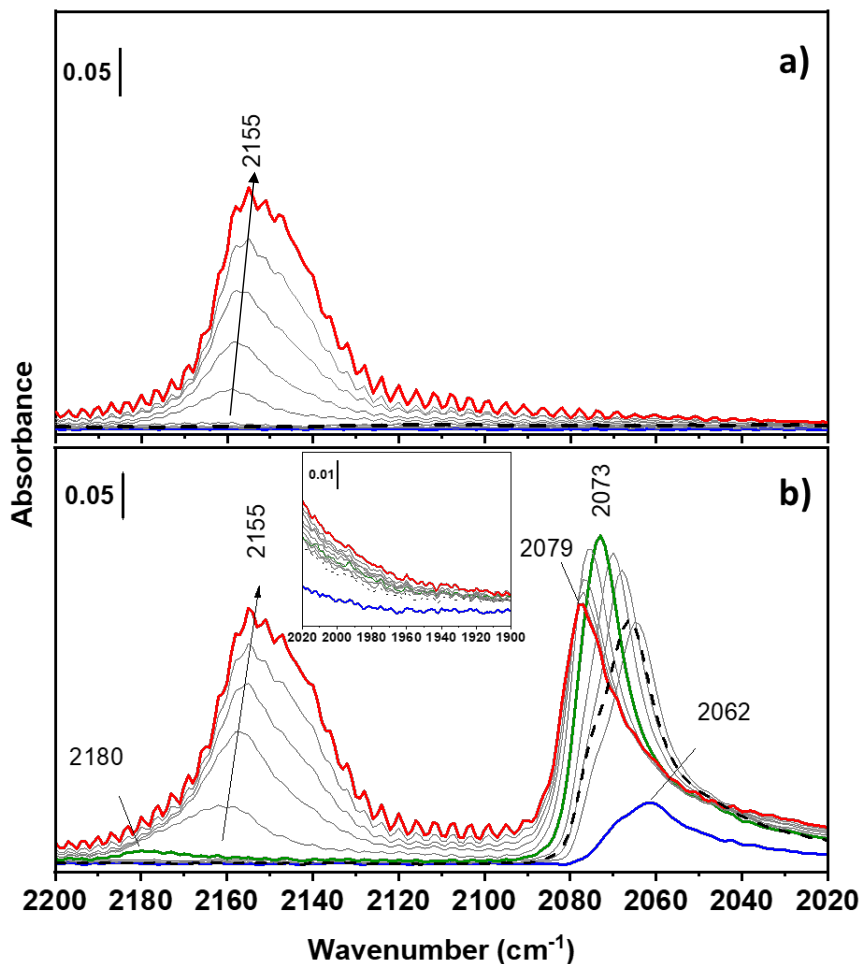


Figure 5 – FT-IR spectra of CO adsorbed at LNT on a) oxidized and b) activated PdZn/ZrO₂. Spectra were acquired at increasing dosage of CO up to 20 mbar (from blue to red line) and after outgassing (black dashed line). Green line represents the CO pressure (“breakdown” pressure) beyond which Zn²⁺-CO and Zr⁴⁺-CO bands pop up and Pd⁰-CO band starts decreasing.

In the light of this hypothesis, during the outgassing, by removing CO molecules firstly from Zn²⁺ and Zr⁴⁺ sites the absorption coefficient of CO adsorbed on Pd⁰ rises again, and then the successive CO desorption from Pd sites causes the red-shift.

The hypothesis could be further explained and confirmed by the model described by Hammaker, Francis and Eischens (HFE) in 1965 [39], and subsequently modified [37,44], dealing with the dipolar coupling.

The modified model predicts that the dipolar coupling induces two observable effects as the interaction with adsorbed molecules increases: a shift of the bands to higher frequencies and an absorption coefficient diminution. The dipolar coupling occurs when the adsorbate belongs to the same surface species, i.e. adsorbed molecules with equal singleton frequency. Hence, CO molecules adsorbed on the ZnO and ZrO₂ phase cannot contribute to the observed *bell-shaped shift*. In addition, as already mentioned, the dipolar coupling related to CO adsorbed on Pd atoms in the alloy has been formerly excluded. However, the adsorption at very low temperature, like liquid-nitrogen temperature (LNT), reasonably lead to the adsorption of much more molecules than at RT, which could be disguised by the intensity loss induced by the strong reduction of the absorption coefficient. Hence, the band reduces in intensity despite the eventual adsorption of CO molecule that would have increased the intensity. If the amount of adsorbed CO is too high, the dipolar coupling can even occur on Pd sites of the PdZn alloy. Indeed, the maximum CO coverage at LNT is centered at 2079

cm^{-1} , 10 cm^{-1} higher than the peak observed at RT (2069 cm^{-1}), suggesting a stronger contribution of the *chemical effect*. Furthermore, this hypothesis is supported by the HAADF-STEM images reported by Ramirez et al. [40] (Appendix A.1), highlighting a strong interaction between PdZn alloy particles and both ZnO and ZrO_2 phases. Further information about this sample can be found in that work.

3.2.4 NAP-XPS on stand-alone PdZn/ ZrO_2

To determine the different Pd and Zn species on the activated catalyst, NAP-XPS measurements were performed. The analyses were carried out using an EnviroESCA spectrometer (SPECS GmbH) equipped with a monochromatic Al $K\alpha$ X-ray source ($h\nu = 1486.71 \text{ eV}$) which operates at 42 W and X-ray emission of 3.00 mA. The catalyst powder was mixed with carbon black powder in 10:1 ratio to avoid an excessive charging of the surface, and then pressed into a pellet ($d=2 \text{ mm}$, $h=0.5 \text{ mm}$) in a steel plate cavity. All the spectra were obtained at energy interval of 10 eV, 0.5 second dwell time and step of 0.1 eV for all regions (i.e. Zr(3d), C(1s), Pd(3d), O(1s) and Zr(2p)).

PdZn/ ZrO_2 sample was measured with HR-XPS before NAP experiments. The sample was outgassed in the loading chamber for 1h at $400 \text{ }^\circ\text{C}$ under ultrahigh vacuum conditions. Then, the powder was treated with a flow of 40 ml/min of H_2 at 20 mbar for 2h.

The set of experiments were carried out by Dr. Genrikh Shterk and will be herein briefly summarized. Further details are reported in Appendix A.3.

PdZn alloy formation was studied using model systems [23,41–43], which demonstrated that for PdZn alloys, the Pd⁰(3d_{5/2}) peak is shifted towards higher binding energies, from 335 to 336.1 eV. This shift in PdZn alloys was studied by Rodriguez [44] using MO-SCF calculation and XPS to explain the effect of the alloying upon CO adsorption. In particular, it was demonstrated that Pd(4d)→Zn(4p) charge transfer and Pd(4d)→Pd(5s,5p) rehybridization during alloy formation induce a shift of the binding energy and a weakening of Pd(4d)→CO(2π) bonding interactions. Recently, further studies about the interaction between Pd and Zn reported a negative charge over Pd and a positive charge over Zn, an opposite transfer compared to that observed by Rodriguez [42,45,46]. Hence, the shift of the bands to higher and lower energies related to Pd(3d) and Zn(2p), respectively, are accepted to be a *fingerprint* of PdZn alloys [23,42,47,48].

The as-prepared PdZn/ZrO₂ is characterized by the presence of PdO and ZnO (Figure 6 panels a and c), with a Pd(3d_{5/2}) and Zn(2p_{3/2}) centered at 337.4 eV and 1022.5 eV, respectively. The Pd(3d_{5/2}) binding energy is slightly higher than the one reported in literature (0.4 – 0.2 eV) for Pd²⁺ [49–51], maybe due to surface charging or fitting uncertainty related to the overlapping with Zr(3p) band. The Zn(2p_{3/2}) component at ca. 1024 eV could be related to ZnO anchored on ZrO₂ hydroxyls species or an asymmetric ZnO peak.

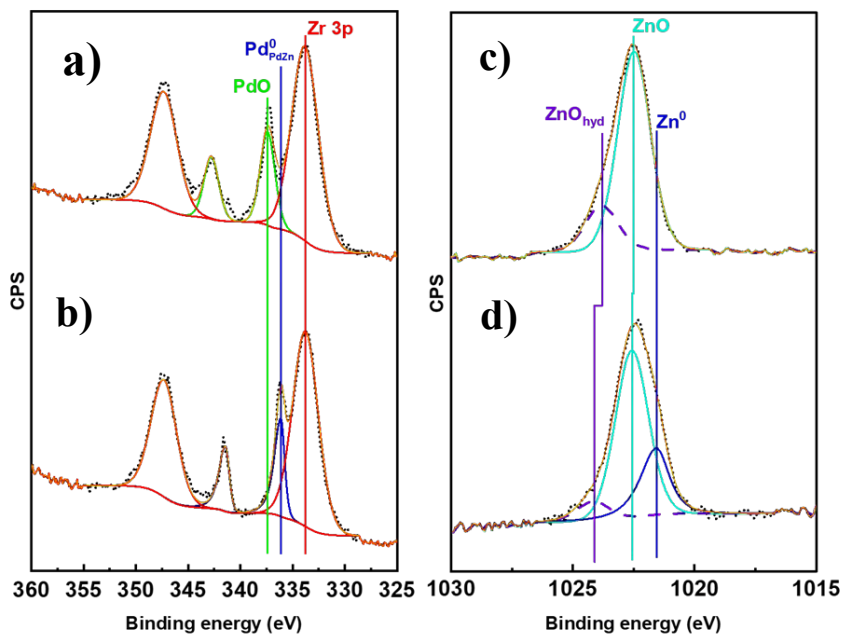


Figure 6 – NAP-XPS spectra of Pd(3d) and Zn(2p) regions of PdZn/ZrO₂ as-prepared catalyst (a, c) and after activation in H₂ (b, d).

After activation at 400 °C with 20 mbar of H₂ (Figure 6 panels b and d) a full reduction of Pd and partial reduction of Zn were observed. As for Pd(3d_{5/2}), the binding energy is 336.1 eV, 1 eV higher than the typical Pd⁰ binding energy [52] which confirms the formation of the alloy in line with literature results [41–43,53–55]. On the other hand, Zn reduction is in good agreement with both FT-IR and the following XAS results, that evidenced the presence of a defective ZnO phase.

3.2.5 XAS: Pd and Zn K-edge on PdZn/ZrO₂ + ZSM-5

XAS measurements were carried out at the Quick-XAS ROCK beamline of the SOLEIL French synchrotron [56]. Specific details about the equipment are reported in Ramirez et al. [40] (Appendix A.1). All the following results were elaborated by Dr. Davide Salusso and were performed on the combined catalyst PdZn/ZrO₂ + ZSM-5 aiming at characterizing both Pd and Zn species before, during and after the activation in pure H₂ at 400 °C.

The following XAS spectra reported in Figure 7 show both XANES and EXAFS (insets) spectra and both are related to the combined system PdZn/ZrO₂ + ZSM-5. Panels **a)**, **b)** and **c)** display the Pd K-edge, while panels **d)**, **e)** and **f)** show the Zn K-edge. All the spectra were compared with a PdO and a metallic Pd references.

Starting with Pd K-edge, Figure 7a shows the spectra acquired on the as-prepared catalyst. All the features are similar to those of PdO and these findings are in line with the PXRD results shown in section 6.1. During the activation (Figure 7b), XANES spectra exhibited a down shift of the absorption edge passing from RT (black line) to 400 °C (red line), specific for a reduction of Pd, and a remarkable change in the oscillation. Indeed, as also highlighted in the EXAFS region, a change from Pd-O to metallic Pd was observed. In addition, as the temperature increased and XANES spectra flattened, a shift to lower *R values* of Pd-Pd coordination shell, up to 2.15 Å, was observed. The spectrum acquired at 400

°C, in H₂, did not change after the activation (Figure 7c) and it was ascribed to the formation of a PdZn alloy [9,17,57–63].

From the Zn point of view, both XANES and EXAFS spectra of the as-prepared catalyst (Figure 7d) resembled the ZnO reference, in line once again with the PXRD results. The lower intensity displayed by the sample could be ascribed to the higher defectiveness compared to the ZnO reference. During the activation (Figure 7e), a remarkable reduced intensity of both the XANES oscillation and the bands in the EXAFS region and subtle red-shift of the edge energy position were observed. The inset in the top right in Figure 7e reports the XANES first derivative to highlight a component below 9660 eV, ascribed to the formation of metallic Zn, matching the Zn(0) reference reported in light grey.

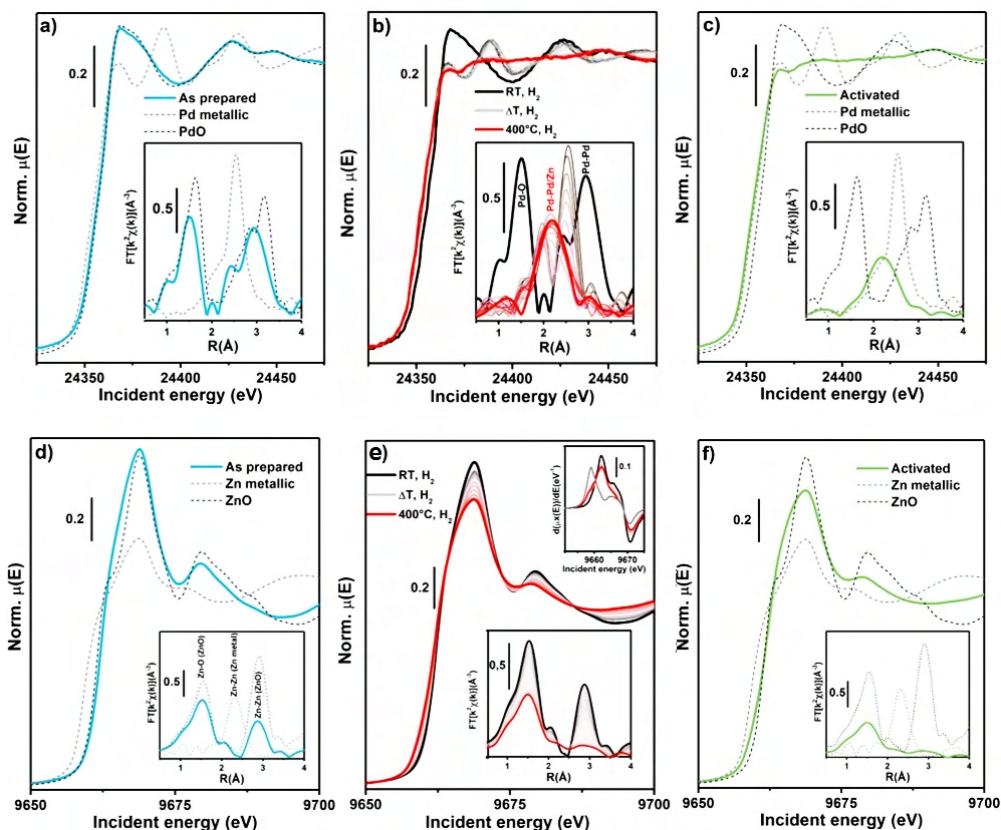


Figure 7 – Pd K-edge and Zn K-edge XANES in main panels and EXAFS spectra in insets. Dashed lines report reference compounds. **a)** Pd K-edge of as-prepared catalyst. **b)** Pd K-edge acquired during activation (RT-400 °C) under H₂ gas flow. **c)** Pd K-edge after activation at 400°C in H₂ atmosphere. **d)** Zn K-edge of as-prepared catalyst. **e)** Zn K-edge during activation (RT-400°C) under H₂ gas flow. Inset: first derivative of the XANES spectra of as-prepared catalyst (black), activated catalyst (red) and metallic Zn (light grey) as reference. **f)** Zn K-edge after activation at 400°C under H₂ gas flow. Note: the EXAFS signal of Pd metallic foil was rescaled by a factor 1/2. All the EXAFS spectra reported in the bottom insets were obtained by transforming the corresponding $k^2\chi(k)$ EXAFS function in the 2.5-11.0 Å⁻¹ range.

It is worth to point out that only a small fraction of Zn underwent a reduction to the Zn(0). The huge intensity decrease in the EXAFS region is related to both a thermal Debye-Waller effect and the presence of a highly defective ZnO phase. Indeed, after the activation (Figure 7f), the EXAFS spectrum of the sample does

not show a significant variation of the intensity, that could be explained by the high defectiveness.

Since no specific fingerprints in Zn local environment were not observed, Zn migration into the zeolite was excluded [58,64], suggesting that impregnating both Zn and Pd on a ZrO₂ stabilizes the elements and avoids diffusion into the zeolite.

3.2.6 FT-IR: CO adsorption at LNT on combined PdZn/ZrO₂ + SAPO-34

In the attempt to characterize the combined catalysts, CO adsorption at liquid-nitrogen temperature followed by FT-IR was performed to study the catalyst surface before and after the catalytic tests, and after regeneration (Figure 8b, c and d). For sake of comparison, CO adsorption was also carried out on SAPO-34 (Figure 8a).

All the spectra show two main absorption features at 2170 and 2140 cm⁻¹, respectively. The former is related to CO adsorption on Brønsted acid sites (BAS) of SAPO-34, while the latter is ascribed to CO molecules entrapped inside the pores of the zeotype [65]. This last band starts to increase at high ϑ_{CO} when a high amount of CO is already engaged in binding Brønsted acid sites (BAS).

CO adsorption gives rise to a third band at 2090 cm⁻¹, which was observed in some works related to Ca-Y and Na-ZSM-5 [66,67]. The frequency of this band changes according to the cation on which CO is adsorbed. When CO is bound through the C-end it could also interact with the lattice via the O-end with a guest

cation or other Lewis acid sites. A second hypothesis is that CO could bind framework O atoms [68].

CO absorption bands on SAPO-34 clearly prevail in the combined system. As for the activated bifunctional catalyst (Figure 8b and inset) the *bell-shaped shift* is visible in Pd⁰ region, as already seen for the stand alone PdZn/ZrO₂. However, after the catalysis the pattern is no longer present (Figure 8c and inset), maybe due to the presence of coke or any other reaction products.

The presence of polycyclic aromatic species and alkenes was determined by means of UV-Raman and ssNMR spectroscopy. For the sake of brevity, I will only refer to two papers we published about this sample [40] (Appendix A.1 and A.3) and I will summarize the main results obtained.

UV-Raman findings showed the presence of both aromatic compounds and olefins, which are typical compounds observed during an intimal deactivation of this kind of catalysts. The higher the amount of hydrocarbon on the surface (hence, the deactivation degree) the lower the number of BAS available to bind CO. In addition, ssNMR results determined a high amount of olefinic and aromatic species, suggesting SAPO-34 underwent a dual-cycle mechanism, involving both olefinic and aromatic cycles, which push the hydrocarbon pool towards C3 hydrocarbon species [69,70]. This hypothesis was supported by the presence of methylated olefinic species, presumably adsorbed in the zeolite framework (Appendix A.3).

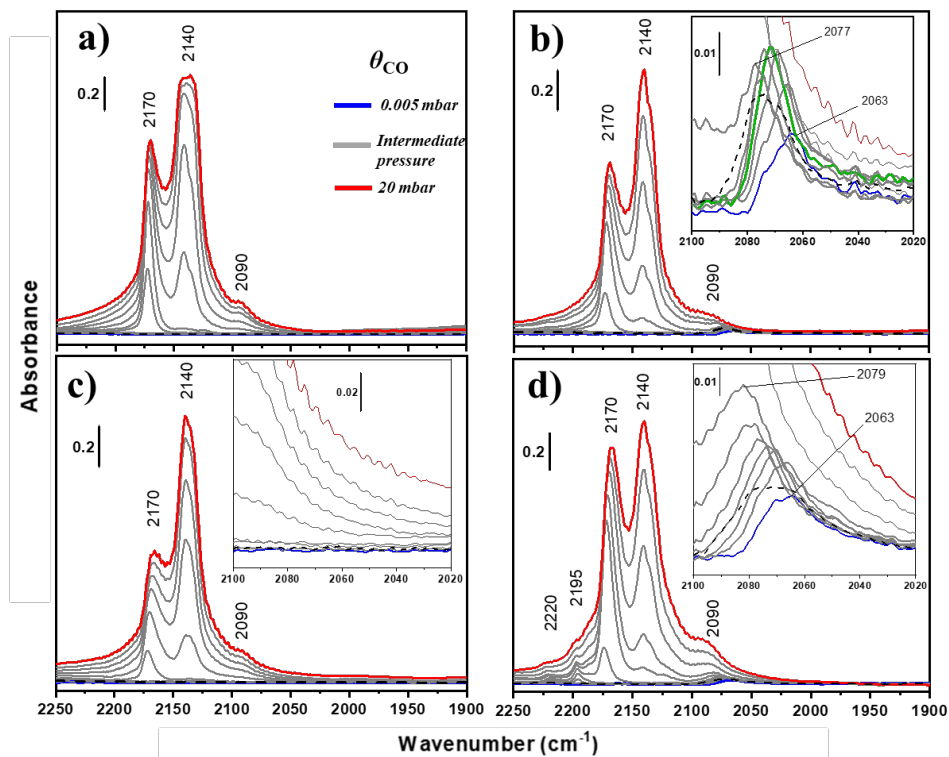


Figure 8 – FT-IR spectra of CO adsorbed at LNT on the following activated systems: SAPO-34 (a), fresh PdZn/ZrO₂ + SAPO-34 (b), used PdZn/ZrO₂ + SAPO-34 (c) and used PdZn/ZrO₂ + SAPO-34 after regeneration in O₂ at 600 °C and activation step (d). Spectra were acquired at increasing CO pressure up to 20 mbar (from blue to red line) and after outgassing (black dashed line). Green line in section b): CO “breakdown” pressure for Pd carbonyls.

All the mentioned findings explain why the peak at 2170 cm⁻¹ is less intense on the used catalyst (Figure 8c) than the fresh one (Figure 8b). Hence, we performed a regeneration at 600 °C in pure O₂ in order to remove all the above-mentioned adsorbed hydrocarbon species and then the sample was activated again at 400 °C in H₂. The spectra reported in Figure 8d show some similarities with those reported in Figure 8b. For instance, the inset in Figure 8d shows a *bell-shaped*

shift-like pattern in Pd⁰ range, suggesting a restoration of those components. However, the pattern looks different because of the SAPO-34 components, which tail ends in Pd⁰ region and “pushes” the (Zn)Pd-CO bands upwards. On the other hand, BAS seemed to be restored as highlighted by the intensity of the band at 2170 cm⁻¹. All these findings indicate the regeneration is mandatory to restore the catalytic activity.

Nonetheless, it is noteworthy to highlight the presence of two more peaks which are only present on the regenerated bifunctional catalyst (Figure 8d). The two peaks are centered at 2220 and 2195 cm⁻¹ and were ascribed to Pd²⁺ dicarbonyls [18,34,71]. The assignment is line with a possible Pd²⁺ ionic exchange with a small fraction of SAPO-34 Brønsted acid sites. According to these results, the exchange should necessarily be driven by the thermal oxidative/regenerating treatment. The exchange stabilizes the Pd²⁺ ions, which seems to be unperturbed by the reduction treatment.

3.3 Lab scale: catalytic tests

In the following section, a summary about the catalytic tests is reported. Any further detail can be found in Ramirez et al. [40] (Appendix A.1). The following data were elaborated by Dr. Adrian Ramirez.

The catalytic tests were run to evaluate the effect of pressure (20, 30 and 40 bar) and temperature (250, 300 and 350 °C). Figure 9a summarizes all the results

obtained comparing PdZn/ZrO₂ stand-alone phase with two bifunctional catalysts where PdZn/ZrO₂ had been mixed with ZSM-5 and SAPO-34.

All the samples showed almost the same CO₂ conversion, which increases with temperature and pressure, following the process thermodynamics, as reported by De et al. [72].

As for the MeOH selectivity, PdZn/ZrO₂ follows the thermodynamics increasing with pressure and decreasing with temperature. As for propane selectivity, in both cases no propane is observable before 350 °C, but SAPO-34 gives a higher selectivity (16%) than ZSM-5 (3%). Further investigations related the methanol selectivity and reported in Ramirez et al. [40] (Appendix A.1), lead us to focus on the PdZn/ZrO₂ + SAPO-34 catalyst which confirmed to be the most promising catalyst. Indeed, a further investigation dealt with the evaluation of the effect of different space velocity (GHSV: 1500, 3000, 6000, 12000 mL/g/h) and pressure values (30, 40 and 50 bar) at a constant temperature of 350 °C, proved that at 50 bar and 1500 mL/g/h, the total propane selectivity is more than 50%. To the best of our knowledge, this is the highest total selectivity reported for a CO₂ hydrogenation process towards C₂₊ hydrocarbons.

Finally, the hydrocarbon distribution reported in Figure 9b shows that the majority of all products are paraffins, which could be related to the hydrogenating effect of Pd and could facilitate the product separation in a potential industrial process.

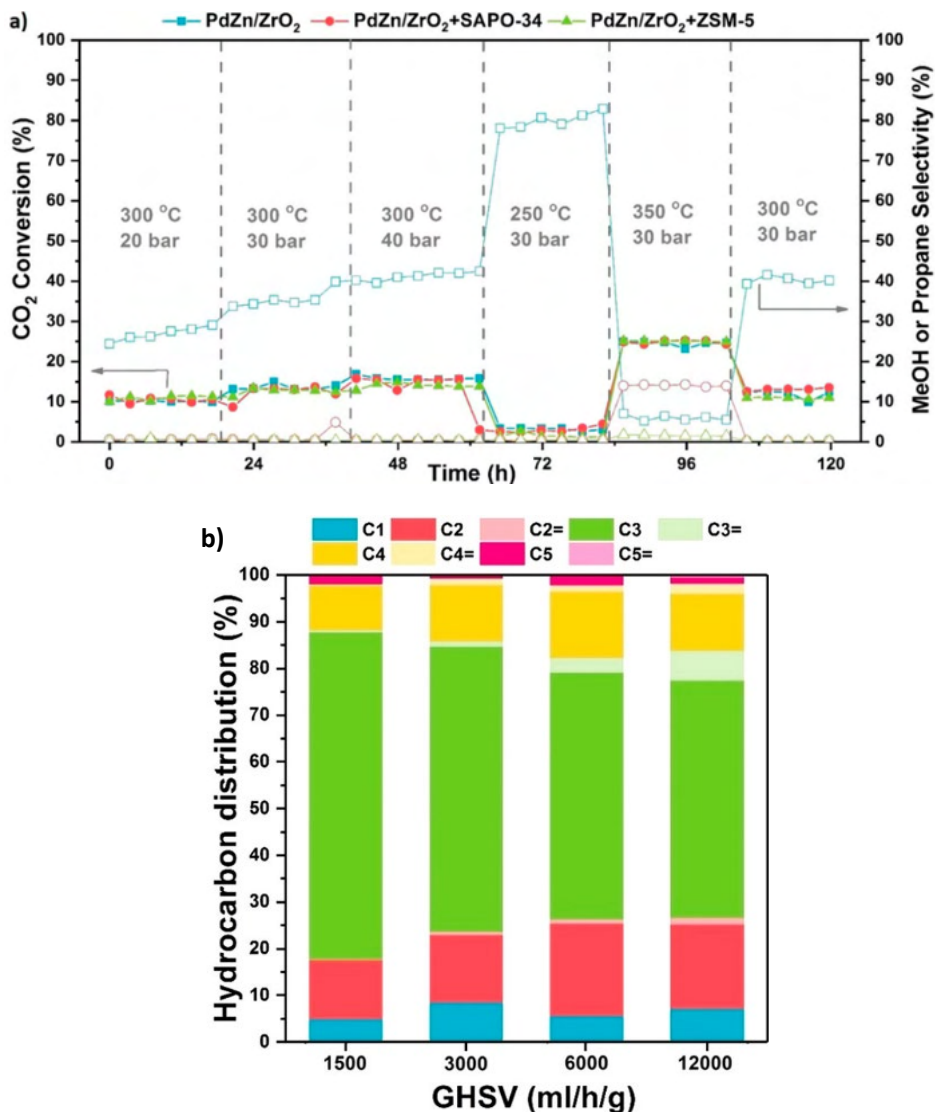


Figure 9 – (a) CO₂ conversion (filled symbols) and MeOH (for PdZn/ZrO₂) or propane (for PdZn/ZrO₂+SAPO-34 and PdZn/ZrO₂+ZSM-5) selectivity (empty symbols) at several screening conditions. H₂/CO₂ = 3, 12 000 mL g⁻¹ h⁻¹. (b) Detailed hydrocarbon distribution (CO free) of the PdZn/ZrO₂+SAPO-34 combined system for the CO₂ conversion to hydrocarbons at different space velocities. CO₂:H₂ 1:3, 350 °C, 50 bar.

3.4 Scale up: structural characterization

After a massive and multi-technique investigation, PdZn/ZrO₂ + SAPO-34 was the first combined catalyst to be scaled up. The catalyst was shaped in two forms: tablet and extrudates. The following section will deal with all the analyses carried out to understand how the catalyst shaping influenced the catalytic activity. All the results related to this catalyst are reported in Ticali et al. (Appendix A.4). The name of all the samples has been reported in Chapter II, section 2.1.3 – Table 3.

Before describing the results, I would like to spend few lines to explain some drawbacks related to this first scale up. As reported in Chapter II, the lab scale and scaled-up bifunctional catalysts are not prepared in the same way. If the preparation of the lab scale catalyst would have been scaled up, then several costs concerns would have affected the testing in the pilot plant. This “recipe variation” interested both the stand-alone PdZn/ZrO₂ (that was tested and characterized again only for comparison purposes) and the bifunctional catalyst. In order to avoid any project blockages, the synthesis was changed, but this change had a cost in terms of catalytic activity. As reported in detail in next sections, a loss in the activity was mainly observed on tablets and extrudates, maybe due to the addition of a binder suitable to produce the two shapes. The samples were investigated by PXRD (PanAlytical X’Pert Pro) in Bragg-Brentano Geometry in reflectance mode using Cu K α radiation source ($\lambda = 1.541$

Å) at ambient conditions. The scan range was 5–70° with a step size of 0.017°. Rietveld refinement was performed using Topas software provided by Bruker. Wavelength-dispersive X-ray spectrometry was performed on a FEG-EPMA JEOL JXA-8530F electron microprobe (d=1 μm) operated at 20 kV, from 20 nA to 55 nA on cross sections of shaped samples, embedded in epoxy and ground with silicon carbide. I would like to acknowledge that Powder X-Ray Diffraction and morphological analyses were performed by Dr. Davide Salusso and TOPSOE team, respectively.

PXRD measurements evidenced the presence of PdO, ZnO and monoclinic ZrO₂ reflections on the stand-alone catalyst. After activation/reduction, the intensity of PdO and ZnO reflections decreased, reasonably due the formation of a PdZn alloy and evidenced by the (101) reflection on the activated PdZnZrO₂ (PZZ-red) pattern reported in Figure 10. After shaping in tablets and extrudates the PdZn alloy reflection is not observable anymore and could be related to the loss of ZnO content which is highlighted by the reduced reflection intensity. These results could suggest a possible ion-exchange of SAPO-34 acid sites during the shaping.

These results have been further supported by morphological characterization, that I will not show for the sake of brevity, but they can be found in Ticali et al. (Appendix A.4). In particular, the microscopic measurements determined that Zn in both tablets and extrudates was not evenly distributed and created ZnO islands. In opposition, Pd is uniformly distributed all over the ZrO₂ support.

Thus, some zones were only covered by Pd. Furthermore, after the activation treatments, Zn was observed to migrate onto both the alumina binder (in particular, in extrudates) and SAPO-34 phases, while Pd appeared to be strongly adsorbed on the ZrO_2 support, in line with the loss of ZnO.

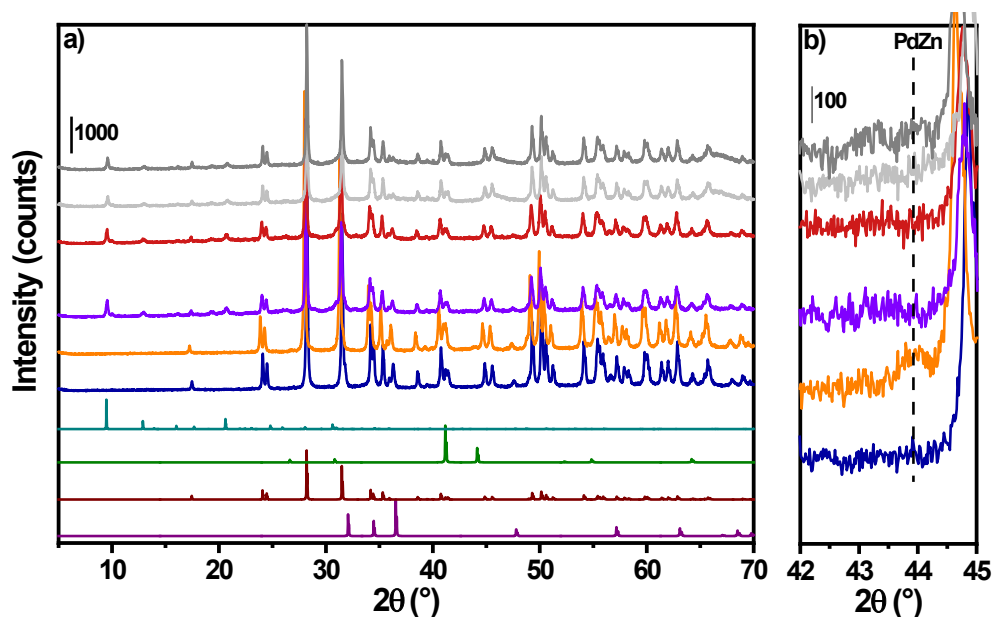


Figure 10 – a) XRD patterns (bottom to top) of: simulated h-ZnO (purple), m-ZrO₂ (wine), t-PdZn (green), SAPO-34 (light blue) and experimental PZZ-ox (dark blue), PZZ-red (orange), PZZ-ox-tab (violet), PZZ-red-tab (dark red), PZZ-ox-ext (light grey) and PZZ-red-ext (dark grey). b) Magnification of the range 42-45° to highlight the PdZn alloy reflection.

3.5 Scale-up: spectroscopic characterization

In order to get the clearest outlook about the synthesized technical catalysts, the spectroscopic characterization was performed by comparing both tablets and extrudates with the physical mixture, obtained by mixing PZZ-ox/red with the

binder and SAPO-34. For sake of clarity I will firstly focus on XAS measurements, followed by FT-IR using CO as probe molecule and performed only at room temperature.

3.5.1 XAS measurements

The XAS measurements were performed by Dr. Davide Salusso, at ESRF synchrotron (BM31 beamline). In this section I will briefly summarize what has been already published in Ticali et al. (Appendix A.4).

Several studies and results regarding the formation of PdZn alloy have been already discussed in the previous paragraphs. Indeed, CO adsorption followed by FT-IR illustrated a complete overview about Pd, while Zn seems to be “spectroscopically silent” in vibrational spectroscopy when reduced to metallic Zn [9,40,58,59,73]. Hence, XAS measurements were focused on Zn K-edge in order to complete the spectroscopic characterization combined with FT-IR and, in addition, to investigate the ZnO migration, mentioned in the previous section. Figure 11a shows that PZZ-ox (prepared by calcination of the precursors) fully matches the ZnO reference spectrum, suggesting that Zn has a ZnO local geometry. After activation in H₂ a slight energy shift is observable and remarked by the inset reported in Figure 11b (purple line). The shift is associated to the formation of the PdZn alloy [40,73] and confirmed by both PXRD and FT-IR (*vide infra*). Thus, the shift can be used to track the presence (or absence) of the alloy.

In the case of the pelletized catalysts, no remarkable variations are observed for PZZ-ox-tab samples. Instead, the reduced sample, PZZ-red-tab, shows some differences compared to PZZ-red. Firstly, looking at the inset in Figure 11b (pink line), no PdZn alloy shift is observed. In addition, a shoulder at a few eV to the left of the absorption edge could be ascribed to a minor fraction of Zn migrated into the Al₂O₃ binder. Indeed, as reported in Ticali et al. (Appendix A.4), no shoulder was observed on the uncalcined pelletized catalyst, suggesting that Zn reoxidation, and its subsequent migration, is induced by calcination.

A completely different scenario concerns the XANES spectra of the extrudates. PZZ-ox-ext and PZZ-red-ext show Zn K-edge spectra matching those studied by Pinilla-Herrero and co-workers [74]. In both oxidized and reduced extrudate catalysts XANES spectra match the spectrum of Zn(10%)-Al₂O₃ reported in both panels a and b of Figure 11 with a dark grey line. Moreover, both panels display two histograms reporting the amount of Zn-aluminates determined by linear combination fit (LCF) (Appendix A.4). It is worth to highlight that both tablets and extrudates exhibited a Zn migration after the reduction treatment. Furthermore, these findings could explain the activity loss that was highlighted by reduced and nil propane selectivity for the tablets and extrudate, respectively (*vide infra*). In particular, all these results linked to the disruption of the PdZn alloy and SAPO-34 poisoning.

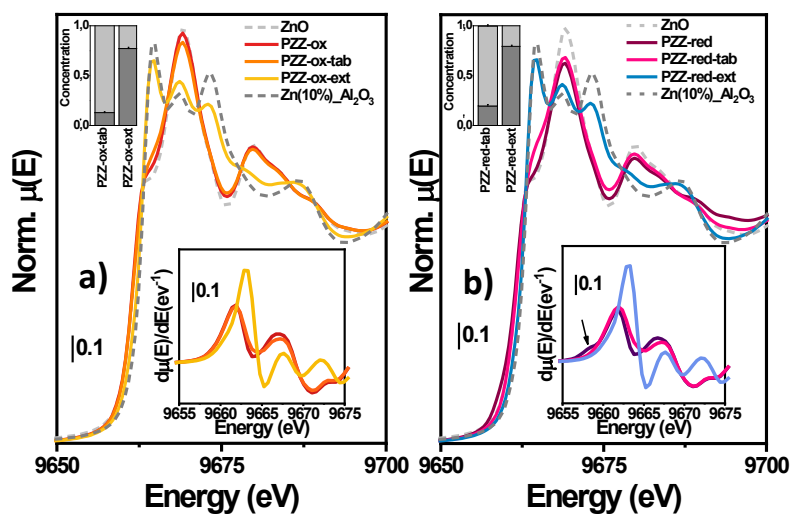


Figure 11 – Zn K-edge EXAFS spectra for the analyzed samples, ZnO and Zn(10%)Al₂O₃. Spectra first derivative and LCF results are reported in the bottom and top insets, respectively. Zn(PdZn) contribution is indicated with the arrow.

3.5.2 FT-IR: CO adsorption at room temperature

Focusing the attention on the surface-active sites, CO adsorption followed by FT-IR was performed at room temperature, in order to probe only Pd sites and exclude the zeotype components.

Figure 12 shows a comparison between the reduced PdZn/ZrO₂ (PZZ-red) with reduced pelletized (PZZ-red-tab) and extruded (PZZ-red-ext) catalyst. CO adsorption on PZZ-red occurs on Pd sites only: the peak at 2070 cm⁻¹ (light violet line) is related to (Zn)Pd⁰-CO [9,20,40,57,60]. Despite the different preparation, the absorption bands are very similar to those reported in Figure 3 in section 3.2.3. The blue-shift from 2070 cm⁻¹ towards 2080 cm⁻¹ has been already widely

discussed in the previous paragraphs and it is related to the *chemical effect* induced by the π -backdonation of metallic Pd. The effect disappears upon outgassing, leading the band back to its former position (yellow line). The lack of bridged Pd-carbonyls confirmed, once again, the formation of the alloy.

As for the combined bifunctional catalyst PZZ-red-tab, no absorption features are observed in the Pd region below 2100 cm^{-1} , but the roto-vibrational pattern of gaseous (non-adsorbed) CO. The absence of any Pd-CO suggests that Pd sites are not available to bind CO. However, catalytic tests (*vide infra*) showed a higher amount of methane produced by tablets, compared to PZZ-red, indicating the potential presence of metallic Pd, which is well known in literature to act as methanation catalyst [75,76]. Hence, we proposed two hypothesis that did not find any evidence in any analysis and would need a further investigation: i) metallic Pd sites anchored on ZrO_2 or ZnO phase are covered by a ZnO extra-phase, as already reported by Kast et al. [17] in a study regarding a Pd/ ZnO catalyst; ii) a possible influence of ZrO_2 support; iii) the available Pd sites are below the detection limit of the technique (e.g. SAPO-34 limits CO adsorption on Pd sites).

On the other hand, compared to PZZ-red, some signals are observable in the OH region and ascribable to isolated Si-OH (3745 cm^{-1}) and P-OH (3670 cm^{-1}), and bridged Si-(OH)-P related to two crystallographic positions at 3620 and 3596 cm^{-1} .

As for the extruded catalyst, PZZ-red-ext, CO adsorption gives rise to a broad band at 2090 cm^{-1} , that could be easily ascribed to $\text{Pd}^0\text{-CO}$, where Pd^0 is not involved in alloying with Zn [32]. The presence of metallic Pd, thus, suggests that Zn is no more available to alloy with Pd and further confirms the Zn migration. At higher frequency, in the OH region, CO adsorption gives rise almost to the same species observed for tablets, with even a higher intensity, except a band at 3767 cm^{-1} related to Al-OH species. Aluminum hydroxyls can be ascribed to defective SAPO-34 sites or, reasonably, to the alumina binder used during the catalyst preparation.

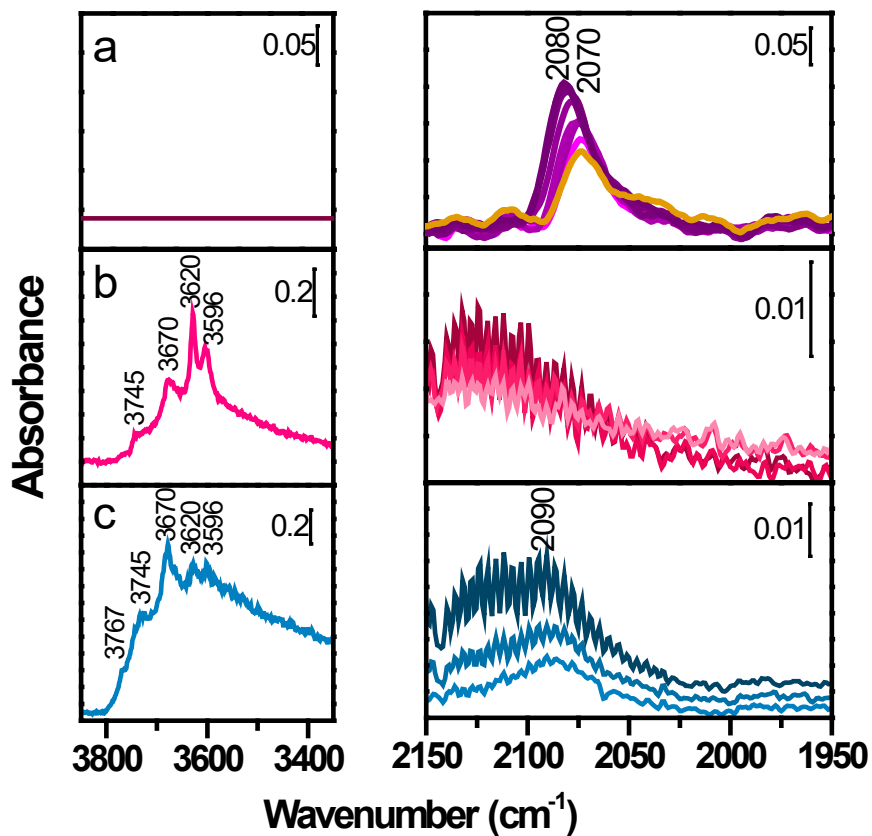


Figure 12 – CO adsorption at increasing dosages at RT followed by *in situ* IR spectra of a) PdZn@ZrO₂-red (PZZ-red), b) PZZ-red-tab and c) PZZ-red-ext. Darker colors indicate higher CO pressure. The yellow line in panel a) refers to the outgas at RT.

3.6 Scale-up: catalytic tests

All the scaled-up samples reported in Table 3 of section 2.13 were tested for CO₂ hydrogenation using typical conditions implemented for lab scale catalyst [40] (Appendix A.1). The tests were performed by Dr. Adrian Ramirez and elaborated by Dr. Tomas Corder-Lanzac.

Figure 13a illustrates the hydrocarbon distribution and CO₂ conversion. Starting with the stand-alone PdZn/ZrO₂ catalyst, both PZZ-ox and PZZ-red produce methanol. In particular, PZZ-red produces more methanol, despite the *ex-situ* reduction, with similar CO₂ conversion and higher methanol selectivity (decreased CO selectivity). In order to compare the performance of the two types of technical catalysts, PZZ-red was mixed with SAPO-34 (namely, PZZ-red + SAPO-34). CO₂ conversion is boosted by the physical mixture, passing from 12% to 25%, due to the *in situ* conversion of methanol to hydrocarbons. CO selectivity reduced from around 85% observed on PZZ-ox to 65% observed for the physical mixture, and the hydrocarbon distribution is comparable with those reported for the lab scale catalyst, mentioned in the previous section and reported in Ramirez et al. [40] (Appendix A.1), despite the different preparation. However, this behavior was not preserved for the technical catalysts.

Pelletized PZZ-ox-tab and PZZ-red-tab catalysts are capable of producing propane and the reduced catalyst outperformed the oxidized one, in line with the results obtained on stand-alone catalysts. Furthermore, Figure 13b shows a huge

stability of the tablets after 72 hours of testing. Nevertheless, this technical catalyst is worse than the physical mixture, achieving 14% of CO₂ conversion and more methane selectivity.

The scenario worsens for the extrudates (PZZ-ox-ext and PZZ-red-ext). The activity of these samples was lost and no propane was yielded. CO₂ conversion is slightly higher than tablets with a lot of unconverted methanol and methane as main product. These findings suggest SAPO-34 poisoning and the remaining methane-yielding activity could be linked either to the presence of metallic palladium or zinc aluminates [75–78].

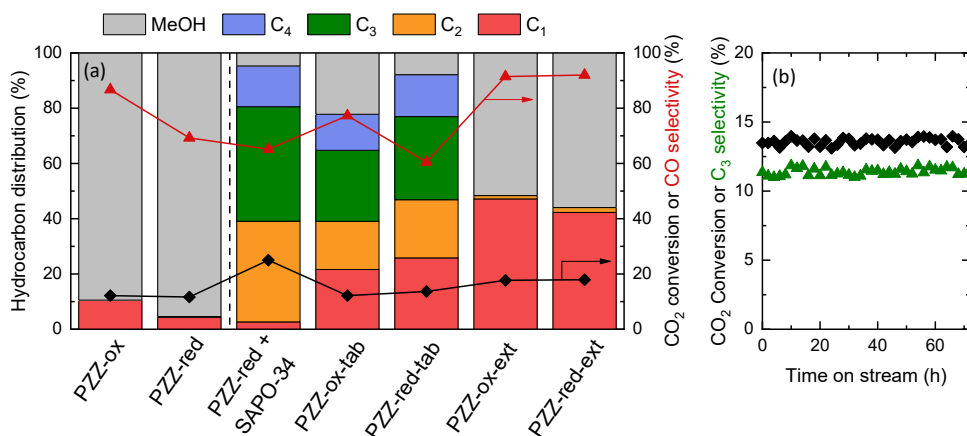


Figure 13 – (a) CO₂ conversion and hydrocarbon distribution for the different technical catalysts and (b) evolution with time on stream of CO₂ conversion and C₃ selectivity for the PZZ-red-tab catalyst. Reaction conditions: 350 C, 30 bar, 6000 cm³/g/h, 1:3 CO₂:H₂.

In conclusion, from the catalytic point of view, the different preparation of the catalyst did not drastically change the catalytic activity of the PdZn/ZrO₂ +

SAPO-34 physical mixture, which show comparable results on both lab scale and scale-up catalysts. However, the synthesis procedure seems to be unsuitable for the scale up. The presence of a binder induces Zn migration from the oxidic phase to the alumina binder in both tablets and extrudates. In the first case more catalytic cycles need to be performed to determine a loss of activity, but as reported by XAS and FT-IR the PdZn alloy is disrupted and Zn migration is enhanced by the activation procedure.

From this failure, COZMOS project gained important information: despite the very promising results obtained on the PdZn/ZrO₂ + SAPO-34 bifunctional catalyst, the catalyst needs to be scaled-up in a different way and more efforts should be implemented to enhance the synthesis of this catalyst on large scale.

REFERENCES

- [1] V. V. Rozanov, O. V. Krylov, Hydrogen spillover in heterogeneous catalysis, *Usp. Khim.* 66 (1997) 127–130. <https://doi.org/10.1070/rc1997v066n02abeh000308>.
- [2] W.C. Conner, J.L. Falconer, Spillover in heterogeneous catalysis, *Chem. Rev.* 95 (1995).
- [3] J. Ye, C. Liu, D. Mei, Q. Ge, Active oxygen vacancy site for methanol synthesis from CO₂ hydrogenation on In₂O₃(110): A DFT study, *ACS Catal.* 3 (2013) 1296–1306. <https://doi.org/10.1021/cs400132a>.
- [4] Ü. Özgür, Y.I. Alivov, C. Liu, A. Teke, M.A. Reshchikov, S. Doğan, V. Avrutin, S.J. Cho, H. Morkoç, A comprehensive review of ZnO materials and devices, *J. Appl. Phys.* 98 (2005) 1–103. <https://doi.org/10.1063/1.1992666>.
- [5] W. Göpel, U. Lampe, Influence of defects on the electronic structure of zinc oxide surfaces, *Phys. Rev. B.* 22 (1980) 6447–6462. <https://doi.org/10.1103/PhysRevB.22.6447>.
- [6] S. Morandi, A. Fioravanti, G. Cerrato, S. Lettieri, M. Sacerdoti, M.C. Carotta, Facile synthesis of ZnO nano-structures: Morphology influence on electronic properties, *Sensors Actuators, B Chem.* 249 (2017) 581–589. <https://doi.org/10.1016/j.snb.2017.03.114>.
- [7] O.A. Ojelade, S.F. Zaman, CO₂ hydrogenation to methanol over PdZn/CeO₂ catalyst, *Comptes Rendus l'Académie Bulg. Des Sci.* 72 (2019).
- [8] J. Ruiz Esquiús, H. Bahruji, M. Bowker, G.J. Hutchings, Identification of C₂–C₅ products from CO₂ hydrogenation over PdZn/TiO₂–ZSM-5 hybrid catalysts, *Faraday Discuss.* 230 (2021) 52–67. <https://doi.org/10.1039/D0FD00135J>.
- [9] M.W. Tew, H. Emerich, J.A. Van Bokhoven, Formation and characterization of PdZn alloy: A very selective catalyst for alkyne semihydrogenation, *J. Phys. Chem. C.* 115 (2011) 8457–8465. <https://doi.org/10.1021/jp1103164>.
- [10] J.R. Gallagher, D.J. Childers, H. Zhao, R.E. Winans, R.J. Meyer, J.T. Miller, Structural evolution of an intermetallic Pd-Zn catalyst selective for propane dehydrogenation, *Phys. Chem. Chem. Phys.* 17 (2015) 28144–28153. <https://doi.org/10.1039/c5cp00222b>.
- [11] O.A. Ojelade, S.F. Zaman, M.A. Daous, A.A. Al-Zahrani, A.S. Malik,

- H. Driss, G. Shterk, J. Gascon, Optimizing Pd:Zn molar ratio in PdZn/CeO₂ for CO₂ hydrogenation to methanol, *Appl. Catal. A Gen.* 584 (2019). <https://doi.org/10.1016/j.apcata.2019.117185>.
- [12] D. Esken, H. Noei, Y. Wang, C. Wiktor, S. Turner, G. Van Tendeloo, R.A. Fischer, ZnO@ZIF-8: Stabilization of quantum confined ZnO nanoparticles by a zinc methylimidazolate framework and their surface structural characterization probed by CO₂ adsorption, *J. Mater. Chem.* 21 (2011) 5907–5915. <https://doi.org/10.1039/c1jm10091b>.
- [13] G. Busca, V. Lorenzelli, *Materials Chemistry* 7 (1982) 89–126
INFRARED SPECTROSCOPIC IDENTIFICATION OF SPECIES ARISING FROM REACTIVE ADSORPTION OF CARBON OXIDES ON METAL OXIDE SURFACES G BUSCA, V LORENZELLI, *Mater. Chem.* 7 (1982) 89–126.
- [14] B. Bachiller-Baeza, I. Rodriguez-Ramos, A. Guerrero-Ruiz, Interaction of carbon dioxide with the surface of zirconia polymorphs, *Langmuir.* 14 (1998) 3556–3564. <https://doi.org/10.1021/la970856q>.
- [15] H.J. Freund, M.W. Robert, Surface chemistry of carbon dioxide, *Surf. Sci. Rep.* 25 (1996) 225–273.
- [16] G. Ramis, G. Busca, V. Lorenzelli, Low-temperature CO₂ adsorption on metal oxides: spectroscopic characterization of some weakly adsorbed species, *Mater. Chem. Phys.* 29 (1991) 425–435. [https://doi.org/10.1016/0254-0584\(91\)90037-U](https://doi.org/10.1016/0254-0584(91)90037-U).
- [17] P. Kast, M. Friedrich, F. Girgsdies, J. Kröhnert, D. Teschner, T. Lunkenbein, M. Behrens, R. Schlögl, Strong metal-support interaction and alloying in Pd/ZnO catalysts for CO oxidation, *Catal. Today.* 260 (2016). <https://doi.org/10.1016/j.cattod.2015.05.021>.
- [18] K.I. Hadjiivanov, G.N. Vayssilov, Characterization of oxide surfaces and zeolites by carbon monoxide as an IR probe molecule, *Adv. Catal.* 47 (2002) 307–511. [https://doi.org/10.1016/S0360-0564\(02\)47008-3](https://doi.org/10.1016/S0360-0564(02)47008-3).
- [19] K. Föttinger, J.A. Van Bokhoven, M. Nachttegaal, G. Rupprechter, Dynamic structure of a working methanol steam reforming catalyst: In situ quick-EXAFS on Pd/ZnO nanoparticles, *J. Phys. Chem. Lett.* 2 (2011) 428–433. <https://doi.org/10.1021/jz101751s>.
- [20] K. Föttinger, The effect of CO on intermetallic PdZn/ZnO and Pd₂Ga/Ga₂O₃ methanol steam reforming catalysts: A comparative study, *Catal. Today.* 208 (2013) 106–112. <https://doi.org/10.1016/J.CATTOD.2012.12.004>.

- [21] K. Föttinger, W. Emhofer, D. Lennon, G. Rupprechter, Adsorption and Reaction of CO on (Pd-)Al₂O₃ and (Pd-)ZrO₂: Vibrational Spectroscopy of Carbonate Formation, *Top. Catal.* 60 (2017) 1722–1734. <https://doi.org/10.1007/s11244-017-0852-7>.
- [22] M. Friedrich, D. Teschner, A. Knop-Gericke, M. Armbrüster, Influence of bulk composition of the intermetallic compound ZnPd on surface composition and methanol steam reforming properties, *J. Catal.* 285 (2012) 41–47. <https://doi.org/10.1016/J.JCAT.2011.09.013>.
- [23] C. Rameshan, C. Weilach, W. Stadlmayr, S. Penner, H. Lorenz, M. Hävecker, R. Blume, T. Rocha, D. Teschner, A. Knop-Gericke, Steam reforming of methanol on PdZn near-surface alloys on Pd(111) and Pd foil studied by in-situ XPS, LEIS and PM-IRAS, *J. Catal.* 276 (2010) 101–113. <https://doi.org/10.1016/j.jcat.2010.09.006>.
- [24] T. Conant, A.M. Karim, V. Lebarbier, Y. Wang, F. Girgsdies, R. Schlögl, A. Datye, Stability of bimetallic Pd-Zn catalysts for the steam reforming of methanol, *J. Catal.* 257 (2008) 64–70. <https://doi.org/10.1016/j.jcat.2008.04.018>.
- [25] K.M. Eblagon, P.H. Concepción, H. Silva, A. Mendes, Ultraselective low temperature steam reforming of methanol over PdZn/ZnO catalysts—Influence of induced support defects on catalytic performance, *Appl. Catal. B Environ.* 154–155 (2014) 316–328. <https://doi.org/10.1016/J.APCATB.2014.02.032>.
- [26] C. Rameshan, W. Stadlmayr, C. Weilach, S. Penner, H. Lorenz, M. Hävecker, R. Blume, T. Rocha, D. Teschner, A. Knop-Gericke, R. Schlögl, N. Memmel, D. Zemlyanov, G. Rupprechter, B. Klötzer, Subsurface-Controlled CO₂ Selectivity of PdZn Near-Surface Alloys in H₂ Generation by Methanol Steam Reforming, *Angew. Chemie Int. Ed.* 49 (2010) 3224–3227. <https://doi.org/10.1002/ANIE.200905815>.
- [27] B.N.J. Persson, R. Ryberg, Vibrational interaction between molecules adsorbed on a metal surface: The dipole-dipole interaction, *Phys. Rev. B.* 24 (1981) 6954–6970. <https://doi.org/10.1103/PhysRevB.24.6954>.
- [28] M. Moskovits, J.E. Hülse, Frequency shifts in the spectra of molecules adsorbed on metals, with emphasis on the infrared spectrum of adsorbed CO, *Surf. Sci.* 78 (1978) 397–418. [https://doi.org/10.1016/0039-6028\(78\)90088-2](https://doi.org/10.1016/0039-6028(78)90088-2).
- [29] G.D. Mahan, A.A. Lucas, Collective vibrational modes of adsorbed CO, *J. Chem. Phys.* 68 (1978) 1344–1348. <https://doi.org/10.1063/1.435952>.

- [30] G.L. Griffin, J.T. Yates, Adsorption studies of H₂ isotopes on ZnO: Coverage-induced IR frequency shifts and adsorbate geometry, *J. Chem. Phys.* 77 (1982) 3744–3750. <https://doi.org/10.1063/1.444249>.
- [31] D. Scarano, A. Zecchina, CO adsorption at 77 K on KCl films. An infrared investigation, *J. Chem. Soc. Faraday Trans. 1 Phys. Chem. Condens. Phases.* 82 (1986) 3611–3624. <https://doi.org/10.1039/F19868203611>.
- [32] E. Groppo, S. Bertarione, F. Rotunno, G. Agostini, D. Scarano, R. Pellegrini, G. Leofanti, A. Zecchina, C. Lamberti, Role of the support in determining the vibrational properties of carbonyls formed on Pd supported on SiO₂-Al₂O₃, Al₂O₃, and MgO, *J. Phys. Chem. C.* 111 (2007) 7021–7028. <https://doi.org/10.1021/jp0666434>.
- [33] P. Hollins, The influence of surface defects on the infrared spectra of adsorbed species, *Surf. Sci. Rep.* 16 (1992) 51–94. [https://doi.org/10.1016/0167-5729\(92\)90008-Y](https://doi.org/10.1016/0167-5729(92)90008-Y).
- [34] K. Khivantsev, N.R. Jaegers, L. Kovarik, J.C. Hanson, F. (Feng) Tao, Y. Tang, X. Zhang, I.Z. Koleva, H.A. Aleksandrov, G.N. Vayssilov, Y. Wang, F. Gao, J. Szanyi, Achieving Atomic Dispersion of Highly Loaded Transition Metals in Small-Pore Zeolite SSZ-13: High-Capacity and High-Efficiency Low-Temperature CO and Passive NO_x Adsorbers, *Angew. Chemie - Int. Ed.* 57 (2018) 16672–16677. <https://doi.org/10.1002/anie.201809343>.
- [35] D. Scarano, S. Bertarione, G. Spoto, A. Zecchina, C. Otero Areán, FTIR spectroscopy of hydrogen, carbon monoxide, and methane adsorbed and co-adsorbed on zinc oxide, *Thin Solid Films.* 400 (2001) 50–55. [https://doi.org/10.1016/S0040-6090\(01\)01472-9](https://doi.org/10.1016/S0040-6090(01)01472-9).
- [36] C. Morterra, V. Bolis, B. Fubini, L. Orto, T.B. Williams, A FTIR and HREM study of some morphological and adsorptive properties of monoclinic ZrO₂ microcrystals, *Surf. Sci.* 251–252 (1991) 540–545. [https://doi.org/10.1016/0039-6028\(91\)91051-X](https://doi.org/10.1016/0039-6028(91)91051-X).
- [37] P. Ticali, D. Salusso, R. Ahmad, C. Ahoba-Sam, A. Ramirez, G. Shterk, K.A. Lomachenko, E. Borfecchia, S. Morandi, L. Cavallo, J. Gascon, S. Bordiga, U. Olsbye, CO₂ hydrogenation to methanol and hydrocarbons over bifunctional Zn-doped ZrO₂/zeolite catalysts, *Catal. Sci. Technol.* 11 (2021) 1249–1268. <https://doi.org/10.1039/D0CY01550D>.
- [38] A.I. Serykh, Y.A. Agafonov, On the nature of active sites in alumina-supported zinc propane dehydrogenation catalysts, *Mol. Catal.* 493 (2020) 111055.

<https://doi.org/https://doi.org/10.1016/j.mcat.2020.111055>.

- [39] R.M. Hammaker, S.A. Francis, E. R.P., Infrared study of intermolecular interactions for carbon monoxide chemisorbed on platinum, *Spectrochim. Acta.* 21 (1965) 1295–1309.
- [40] A. Ramirez, P. Ticali, D. Salusso, T. Cordero-Lanzac, S. Ould-Chikh, C. Ahoba-Sam, A.L. Bugaev, E. Borfecchia, S. Morandi, M. Signorile, S. Bordiga, J. Gascon, U. Olsbye, Multifunctional Catalyst Combination for the Direct Conversion of CO₂ to Propane, *JACS Au.* 1 (2021) 1719–1732. <https://doi.org/10.1021/jacsau.1c00302>.
- [41] A. Bayer, K. Flechtner, R. Denecke, H.-P. Steinrück, K.M. Neyman, N. Rösch, Electronic properties of thin Zn layers on Pd(111) during growth and alloying, *Surf. Sci.* 600 (2006) 78–94. <https://doi.org/10.1016/j.susc.2005.09.049>.
- [42] H.H. Holzapfel, A. Wolfbeisser, C. Rameshan, C. Weilach, G. Rupprechter, PdZn Surface Alloys as Models of Methanol Steam Reforming Catalysts: Molecular Studies by LEED, XPS, TPD and PM-IRAS, *Top. Catal.* 57 (2014) 1218–1228. <https://doi.org/10.1007/s11244-014-0295-3>.
- [43] C. Rameshan, W. Stadlmayr, C. Weilach, S. Penner, H. Lorenz, M. Hävecker, R. Blume, T. Rocha, D. Teschner, A. Knop-Gericke, R. Schlögl, N. Memmel, D. Zemlyanov, G. Rupprechter, B. Klötzer, Subsurface-Controlled CO₂ Selectivity of PdZn Near-Surface Alloys in H₂ Generation by Methanol Steam Reforming, *Angew. Chemie Int. Ed.* 49 (2010) 3224–3227. <https://doi.org/10.1002/anie.200905815>.
- [44] J.A. Rodriguez, Interactions in Bimetallic Bonding: Electronic and Chemical Properties of PdZn Surfaces, *J. Phys. Chem.* 98 (1994) 5758–5764. <https://doi.org/10.1021/j100073a031>.
- [45] K.M. Neyman, R. Sahnoun, C. Inntam, S. Hengrasmee, N. Rösch, Computational Study of Model Pd–Zn Nanoclusters and Their Adsorption Complexes with CO Molecules, *J. Phys. Chem. B.* 108 (2004) 5424–5430. <https://doi.org/10.1021/jp049830f>.
- [46] Z.-X. Chen, K.M. Neyman, A.B. Gordienko, N. Rösch, Surface structure and stability of PdZn and PtZn alloys: Density-functional slab model studies, *Phys. Rev. B.* 68 (2003) 075417. <https://doi.org/10.1103/PhysRevB.68.075417>.
- [47] K.M. Neyman, K.H. Lim, Z.-X. Chen, L. V. Moskaleva, A. Bayer, A. Reindl, D. Borgmann, R. Denecke, H.-P. Steinrück, N. Rösch,

- Microscopic models of PdZn alloy catalysts: structure and reactivity in methanol decomposition, *Phys. Chem. Chem. Phys.* 9 (2007) 3470–3482. <https://doi.org/10.1039/B700548B>.
- [48] M. Friedrich, A. Ormeci, Y. Grin, M. Armbrüster, PdZn or ZnPd: Charge Transfer and Pd-Pd Bonding as the Driving Force for the Tetragonal Distortion of the Cubic Crystal Structure, *Zeitschrift Für Anorg. Und Allg. Chemie.* 636 (2010) 1735–1739. <https://doi.org/10.1002/zaac.201000097>.
- [49] A. V. Naumkin, A. Kraut-Vass, S.W. Gaarenstroom, C.J. Powell, NIST Standard Reference Database 20, version 4.1 (web version)., 2012.
- [50] M.C. Militello, S.J. Simko, Palladium Oxide (PdO) by XPS, *Surf. Sci. Spectra.* 3 (1994) 395–401. <https://doi.org/10.1116/1.1247784>.
- [51] M. Brun, A. Berthet, J. Bertolini, XPS, AES and Auger parameter of Pd and PdO, *J. Electron Spectros. Relat. Phenomena.* 104 (1999) 55–60. [https://doi.org/10.1016/S0368-2048\(98\)00312-0](https://doi.org/10.1016/S0368-2048(98)00312-0).
- [52] L.S. Kibis, A.I. Titkov, A.I. Stadnichenko, S. V. Koscheev, A.I. Boronin, X-ray photoelectron spectroscopy study of Pd oxidation by RF discharge in oxygen, *Appl. Surf. Sci.* 255 (2009) 9248–9254. <https://doi.org/10.1016/J.APSUSC.2009.07.011>.
- [53] C. Rameshan, W. Stadlmayr, C. Weilach, S. Penner, H. Lorenz, M. Hävecker, R. Blume, T. Rocha, D. Teschner, A. Knop-Gericke, R. Schlögl, N. Memmel, D. Zemlyanov, G. Rupprechter, B. Klötzer, Subsurface-controlled CO₂ selectivity of PdZn near-surface alloys in H₂ generation by methanol steam reforming, *Angew. Chemie - Int. Ed.* 49 (2010) 3224–3227. <https://doi.org/10.1002/anie.200905815>.
- [54] N. Iwasa, S. Masuda, N. Ogawa, N. Takezawa, Steam reforming of methanol over Pd/ZnO: Effect of the formation of PdZn alloys upon the reaction, *Appl. Catal. A Gen.* 125 (1995) 145–157. [https://doi.org/10.1016/0926-860X\(95\)00004-6](https://doi.org/10.1016/0926-860X(95)00004-6).
- [55] C. Huang, Z. Wu, H. Luo, S. Zhang, Z. Shao, H. Wang, Y. Sun, CO₂ Hydrogenation to Methanol over PdZnZr Solid Solution: Effects of the PdZn Alloy and Oxygen Vacancy, *ACS Appl. Energy Mater.* 4 (2021) 9258–9266. <https://doi.org/10.1021/acsaem.1c01502>.
- [56] C. La Fontaine, S. Belin, L. Barthe, O. Roudenko, V. Briois, ROCK: A Beamline Tailored for Catalysis and Energy-Related Materials from ms Time Resolution to μm Spatial Resolution, *Synchrotron Radiat. News.* 33 (2020) 20–25. <https://doi.org/10.1080/08940886.2020.1701372>.

- [57] J.R. Gallagher, D.J. Childers, H. Zhao, R.E. Winans, R.J. Meyer, J.T. Miller, Structural evolution of an intermetallic Pd-Zn catalyst selective for propane dehydrogenation, *Phys. Chem. Chem. Phys.* 17 (2015) 28144–28153. <https://doi.org/10.1039/c5cp00222b>.
- [58] C. Ahoba-Sam, E. Borfecchia, A. Lazzarini, A. Bugaev, A.A. Isah, M. Taoufik, S. Bordiga, U. Olsbye, On the conversion of CO₂ to value added products over composite PdZn and H-ZSM-5 catalysts: excess Zn over Pd, a compromise or a penalty?, *Catal. Sci. Technol.* (2020) 4373–4385. <https://doi.org/10.1039/D0CY00440E>.
- [59] M. Gentzen, D.E. Doronkin, T.L. Sheppard, A. Zimina, H. Li, J. Jelic, F. Studt, J.D. Grunwaldt, J. Sauer, S. Behrens, Supported Intermetallic PdZn Nanoparticles as Bifunctional Catalysts for the Direct Synthesis of Dimethyl Ether from CO-Rich Synthesis Gas, *Angew. Chemie - Int. Ed.* 58 (2019) 15655–15659. <https://doi.org/10.1002/anie.201906256>.
- [60] E. Jeroro, V. Lebarbier, A. Datye, Y. Wang, J.M. Vohs, Interaction of CO with surface PdZn alloys, *Surf. Sci.* 601 (2007) 5546–5554. <https://doi.org/10.1016/j.susc.2007.09.031>.
- [61] R.S. Johnson, A. DeLaRiva, V. Ashbacher, B. Halevi, C.J. Villanueva, G.K. Smith, S. Lin, A.K. Datye, H. Guo, The CO oxidation mechanism and reactivity on PdZn alloys, *Phys. Chem. Chem. Phys.* 15 (2013) 7768–7776. <https://doi.org/10.1039/c3cp00126a>.
- [62] L. Bollmann, J.L. Ratts, A.M. Joshi, W.D. Williams, J. Pazmino, Y. V. Joshi, J.T. Miller, A.J. Kropf, W.N. Delgass, F.H. Ribeiro, Effect of Zn addition on the water-gas shift reaction over supported palladium catalysts, *J. Catal.* 257 (2008) 43–54. <https://doi.org/10.1016/j.jcat.2008.04.005>.
- [63] S. Kattel, P.J. Ramirez, J.G. Chen, J.A. Rodriguez, P. Liu, Comment on “Active sites for CO₂ hydrogenation to methanol on Cu/ZnO catalysts,” *Science* (80-.). 357 (2017) 1296–1299. <https://doi.org/10.1126/science.aal3573>.
- [64] I. Pinilla-herrero, E. Borfecchia, J. Holzinger, U. V Mentzel, F. Joensen, K.A. Lomachenko, S. Bordiga, C. Lamberti, G. Berlier, U. Olsbye, S. Svelle, J. Skibsted, P. Beato, High Zn / Al ratios enhance dehydrogenation vs hydrogen transfer reactions of Zn-ZSM-5 catalytic systems in methanol conversion to aromatics, *J. Catal.* 362 (2018) 146–163. <https://doi.org/10.1016/j.jcat.2018.03.032>.
- [65] F. Bleken, M. Bjørgen, L. Palumbo, S. Bordiga, S. Svelle, K.P. Lillerud, U. Olsbye, The effect of acid strength on the conversion of methanol to

- olefins over acidic microporous catalysts with the CHA topology, *Top. Catal.* 52 (2009) 218–228. <https://doi.org/10.1007/s11244-008-9158-0>.
- [66] V. Bolis, B. Fubini, E. Garrone, E. Giamello, C. Morterra, A Comparison Between the Lewis Acidity of Non-D Metal Cations in Y-Zeolites and on Ionic Surfaces, *Stud. Surf. Sci. Catal.* 48 (1989) 159–166. [https://doi.org/10.1016/S0167-2991\(08\)60679-5](https://doi.org/10.1016/S0167-2991(08)60679-5).
- [67] S. Bordiga, E. Escalona Platero, C. Otero Areán, C. Lamberti, A. Zecchina, Low temperature CO adsorption on Na-ZSM-5 zeolites: An FTIR investigation, *J. Catal.* 137 (1992) 179–185. [https://doi.org/10.1016/0021-9517\(92\)90147-A](https://doi.org/10.1016/0021-9517(92)90147-A).
- [68] S. Bordiga, D. Scarano, G. Spoto, A. Zecchina, C. Lamberti, C. Otero Areán, Infrared study of carbon monoxide adsorption at 77 K on faujasites and ZSM-5 zeolites, *Vib. Spectrosc.* 5 (1993) 69–74. [https://doi.org/10.1016/0924-2031\(93\)87056-Y](https://doi.org/10.1016/0924-2031(93)87056-Y).
- [69] W. Wang, Y. Jiang, M. Hunger, Mechanistic investigations of the methanol-to-olefin (MTO) process on acidic zeolite catalysts by in situ solid-state NMR spectroscopy, *Catal. Today.* 113 (2006) 102–114. <https://doi.org/10.1016/J.CATTOD.2005.11.015>.
- [70] I. Yarulina, A.D. Chowdhury, F. Meirer, B.M. Weckhuysen, J. Gascon, Recent trends and fundamental insights in the methanol-to-hydrocarbons process, *Nat. Catal.* 1 (2018) 398–411. <https://doi.org/10.1038/s41929-018-0078-5>.
- [71] L. Castoldi, R. Matarrese, S. Morandi, P. Ticali, L. Lietti, Low-temperature Pd/FER NO_x adsorbers: Operando FT-IR spectroscopy and performance analysis, *Catal. Today.* 360 (2021) 317–325. <https://doi.org/10.1016/j.cattod.2020.02.019>.
- [72] S. De, A. Dokania, A. Ramirez, J. Gascon, Advances in the Design of Heterogeneous Catalysts and Thermocatalytic Processes for CO₂ Utilization, *ACS Catal.* 10 (2020) 14147–14185. <https://doi.org/10.1021/acscatal.0c04273>.
- [73] P. Ruzzi, D. Salusso, M. Baravaglio, K.C. Szeto, A. De Mallmann, L.G. Jiménez, C. Godard, A. Benayad, S. Morandi, S. Bordiga, M. Taoufik, Supported PdZn nanoparticles for selective CO₂ conversion, through the grafting of a heterobimetallic complex on CeZrO_x, *Appl. Catal. A Gen.* 635 (2022) 118568. <https://doi.org/10.1016/J.APCATA.2022.118568>.
- [74] I. Pinilla-herrero, E. Borfecchia, T. Cordero-lanzac, U. V Mentzel, F. Joensen, K.A. Lomachenko, S. Bordiga, U. Olsbye, P. Beato, S. Svelle, Finding the active species : The conversion of methanol to aromatics

- over Zn-ZSM-5 / alumina shaped catalysts, *J. Catal.* 394 (2021) 416–428. <https://doi.org/10.1016/j.jcat.2020.10.024>.
- [75] K. Stangeland, D. Kalai, H. Li, Z. Yu, CO₂ Methanation: The Effect of Catalysts and Reaction Conditions, *Energy Procedia.* 105 (2017) 2022–2027. <https://doi.org/10.1016/j.egypro.2017.03.577>.
- [76] J. Wambach, A. Baiker, A. Wokaun, CO₂ hydrogenation over metal/zirconia catalysts, *Phys. Chem. Chem. Phys.* 1 (1999) 5071–5080. <https://doi.org/10.1039/a904923a>.
- [77] M.A. Kipnis, P. V. Samokhin, E.A. Volnina, M. V. Magomedova, T. V. Turkova, Features of Carbon Dioxide and Monoxide Hydrogenation in the Presence of ZnO/Al₂O₃ and ZnO, *Kinet. Catal.* 63 (2022) 292–303. <https://doi.org/10.1134/S0023158422030041/FIGURES/7>.
- [78] X. Liu, M. Wang, H. Yin, J. Hu, K. Cheng, J. Kang, Q. Zhang, Y. Wang, Tandem Catalysis for Hydrogenation of CO and CO₂ to Lower Olefins with Bifunctional Catalysts Composed of Spinel Oxide and SAPO-34, *ACS Catal.* 10 (2020) 8303–8314. https://doi.org/10.1021/ACSCATAL.0C01579/SUPPL_FILE/CS0C01579_SI_001.PDF.

CHAPTER IV

ZnZrO_x mixed oxides

4.1 Textural and structural characterization

4.1.1 Textural characterization of stand-alone ZnZr-X

Specific surface areas (SSAs) and pore size distribution (PSD) of the ZnZr-X samples were obtained by Brunauer–Emmett–Teller (BET) method and DFT method, respectively, from the adsorption and/or desorption isotherms of N₂ at 77 K using a Micromeritics ASAP 2010 physisorption analyzer. The isotherms were obtained over a range of relative pressures from 10⁻⁶ to 1. Before the analyses, all the samples underwent an evacuation step under dynamic vacuum at 120 °C (5 °C/min) for 5 h (up to residual pressure of 10⁻⁴ mbar) to remove physisorbed species from the surface. DFT method on cylindrical pores, using the Tarazona NLDFT approach was used to determine the PSD.

N₂ adsorption/desorption isotherms and the pore size distribution (PSD) of all as prepared ZnZr-X catalysts are reported in Figure 1 and Figure 2, respectively.

For all samples the isotherms showed a hysteresis loop due to the capillary condensation [1]. In particular, ZnZr-5 showed a different adsorption hysteresis than those of ZnZr-15 and ZnZr-30. ZnZr-5 is featured by a H2-like loop, peculiar for mesoporous oxides with tubular/ink-bottle pores with inhomogeneous dimension [2]. On the other hand, both ZnZr-15 and ZnZr-30 presented a H1-like

loop, distinctive for mesoporous materials with narrow pore distribution and homogenous sized particles agglomerates.

However, there are no evidence regarding the origin of the porosity, thus it could be related to inter-grains pores, intra-grains pores, or both.

Figure 2 displays the pore size distribution obtained using a DFT method for all the analyzed samples. The PSD is almost the same for all the cases, but ZnZr-30 shows a higher amount of pores in the range of 3-10 nm. As evidenced in the next sections, these results could be linked to the presence of a ZnO phase, which is responsible for the formation of defects that could cause the different distribution herein reported.

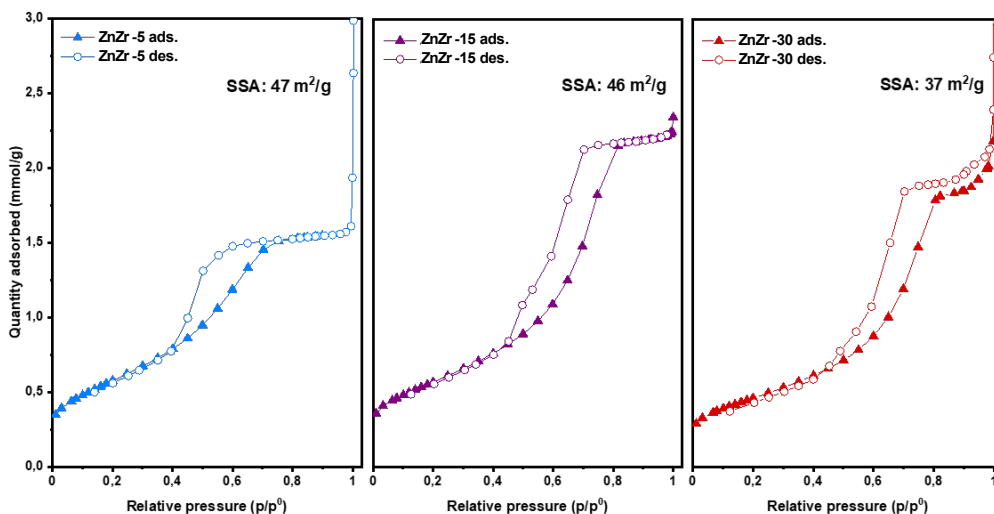


Figure 1 – Adsorption/desorption isotherms of N₂ at 77 K for ZnZr-5, ZnZr-15 and ZnZr-30 catalysts.

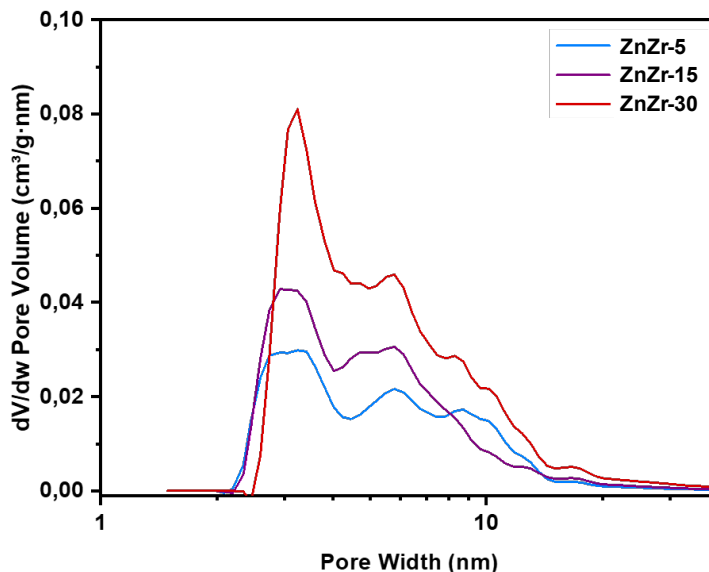


Figure 2 – Pore size distribution of ZnZr-X catalysts, obtained by DFT method.

4.1.2 Structural characterization of stand-alone ZnZr-X

Powder X-Ray Diffraction (PXRD) measurements were carried out at room temperature in a glass capillary ($\varnothing = 0.3$ mm) on the as prepared ZnZr-X using a PW3050/60 X'Pert PRO MPD diffractometer from PANalytical in the Bragg-Brentano geometry equipped with a Cu K $_{\alpha 1,2}$ X-Ray source. The analyses were performed from 10° to 90° , 0.0156° step size and 150s as integration time. FullProf software package [3] was used to extract lattice parameters and average crystallite size from all the samples to perform a Rietveld refinement.

All the measurements were performed by Dr. Davide Salusso. A detailed information about the Rietveld refinement is reported in the Supporting Materials of Ticali et al. [4] (Appendix A.2).

Figure 3 reports PXRD patterns of all the studied samples. The spectra are only offset-shifted. All the diffractograms show reflections of crystalline zirconia reflection: no monoclinic ZrO_2 was observed, while cubic and tetragonal structure were not distinguishable. The inset reports the (101) reflection of all the samples with respect to the one of pure ZrO_2 . The shift is related to the lattice shrinking of ZrO_2 lattice due to the smaller-Zn (0.74 Å) inclusion in substitution for the larger- Zr^{4+} (0.82 Å) [5]. Indeed, the shift is coherent with the elemental analysis, so that the higher the Zn loading the more pronounced the shift. Same behavior was observed for the peak broadening. Further investigation reported in Ticali et al. [4] (Appendix A.2) demonstrated that the amorphous fraction is the same for all three samples. Thus, the crystallite size determined by the Rietveld refinement decreases as the Zn concentration increases, passing from 55 ± 1 nm for ZnZr-5, to 20 ± 1 nm for ZnZr-15 and 12 ± 1 for ZnZr-30.

Chemical, textural and structural features of ZnZr-X catalysts are all reported in Table 1.

Furthermore, diamonds symbol in Figure 3 represent reflections of a wurtzite (ZnO) secondary phase, which was distinguishable only for ZnZr-30. With a detailed Rietveld refinement [4], it was possible to determine that ZnZr-30 had around 15 wt.% of ZnO , suggesting a fraction of Zn is not incorporated in the ZrO_2 lattice, justifying the observed reflections. It was then hypothesized that the co-precipitation technique could not allow more than 15 wt.% of Zn to enter in the ZrO_2 lattice.

A further investigation carried out by Salusso et al. [6], and more recently by other research groups [7], unveiled the presence of ZnO nanoclusters (hexagonal or cubic) embedded and chemically bonded to the ZrO₂ matrix, highlighting that the presence of a chemical interaction at ZnO/ZrO₂ interface could promote CO₂ hydrogenation.

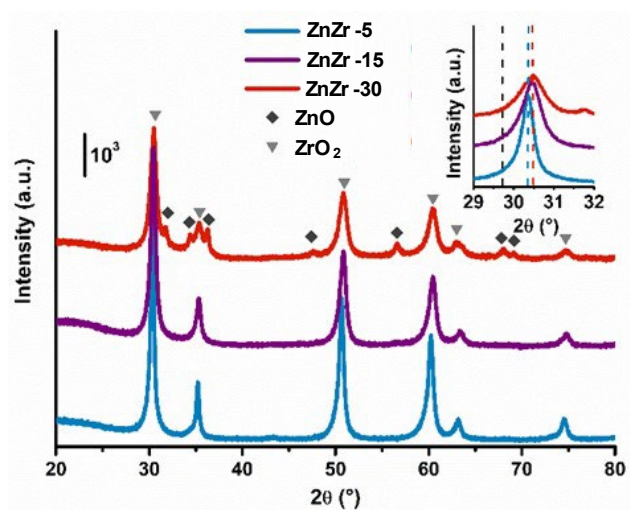


Figure 3 – PXRD patterns of the as prepared ZnZr-*X* samples. Diamonds and triangles are related to the peak positions of cubic/tetragonal ZrO₂ and hexagonal ZnO, respectively. Inset: magnification of the ZrO₂ (101) reflection with the peak position for a pure ZrO₂ reference [8] (dashed black line) and peak position of ZnZr-*X* samples (dashed coloured lines). [4]

Table 1 – Chemical, textural and structural features of ZnZr-X catalysts. In order: Zn loading, specific surface area (SSA), pore volume, lattice parameter ($a = b$), and average crystallite size (d)

	ZnZr-5	ZnZr-15	ZnZr-30
Zn loading (wt.%)	5	15	30
SSA (m²/g)	47	46	37
DFT Cumulative Pore Volume (cm³/g)	0.24	0.21	0.49
Space group	P 4 ₂ /n m c	P 4 ₂ /n m c	P 4 ₂ /n m c
a (=b) (Å)	3.6049 ± 0.0008	3.58900 ± 0.00018	3.59440 ± 0.0008
c (Å)	5.0980 ± 0.0015	5.1020 ± 0.0005	5.082 ± 0.002
Crystallite size (nm)	55±1	20±1	12±1

From the results reported in Table 1, the specific surface area value does not reflect the decreasing trend observed for the crystallite size. To explain these results, SEM images of the catalysts reported in Ticali et al. [4] (Appendix A.2) demonstrated that they consist of particles with small aggregated crystallites. Therefore, the area exposed is correlated to the dimensions of these aggregates rather than to the crystallite size.

4.2 Spectroscopic characterization

4.2.1 FT-IR: H₂ interaction with stand-alone ZnZr-X

The presence of a ZnO extra phase could play a key role in CO₂ hydrogenation. Indeed, ZnO is well known for its semiconductive properties related to the formation of oxygen vacancies under reducing conditions [9]. To study the semiconductive properties, IR spectroscopy is suitable to monitor the generation of oxygen vacancies.

Before focusing on the interaction with hydrogen, it is worth to highlight the IR absorption spectra of the materials. Figure 4 reports all the spectra acquired after oxidation and reduction treatments in pure O₂ and H₂, respectively. Three main regions could be identified (from higher to lower frequencies): the first region between 4000 and 3000 cm⁻¹, ascribable to surface hydroxyls; the second region in the range 2500-2000 cm⁻¹ related to encapsulated CO₂ in the pores of the material (evidenced by the bands related to ¹²CO₂ and ¹³CO₂ at 2340 and 2210 cm⁻¹, respectively); the third region between 1700 and 1000 cm⁻¹ ascribed to carbonates/nitrates species. The species belonging to the last two ranges derived from the precursors used for the synthesis. Despite the calcination at 500 °C and the following thermal treatment at 400 °C in O₂ and H₂, these species are still present. Moreover, it is noteworthy that the amount of OH species (4000-3000 cm⁻¹) decreases as Zn loading increases, suggesting the OH groups are related to ZrO₂.

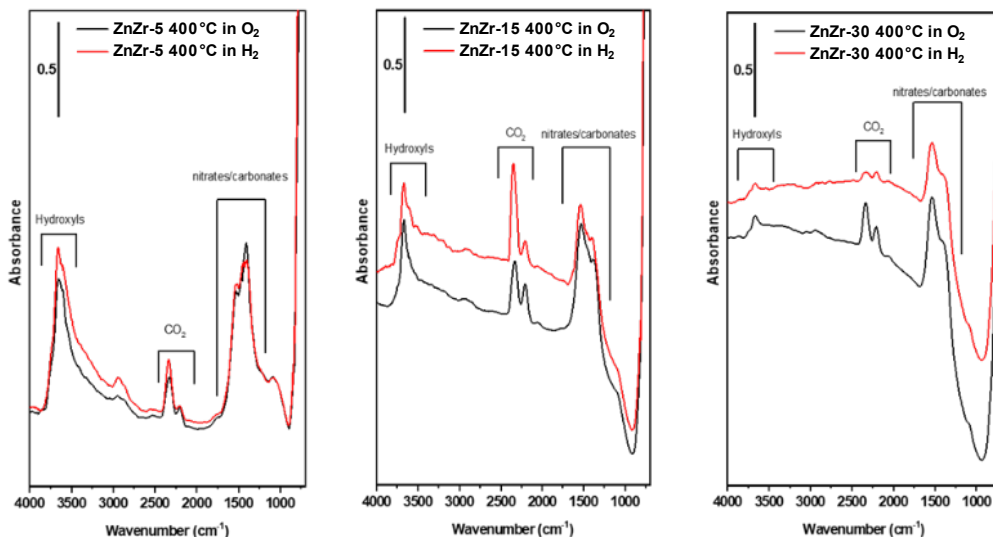


Figure 4 – FT-IR spectra of ZnZr-X catalysts recorded at 400 °C in 40 mbar of oxygen (black curves) and 40 mbar of hydrogen (red curves).

A variation in the overall absorption of the spectra passing from the oxidized to reduced samples is well visible, especially for ZnZr-15 and ZnZr-30. This phenomenon is even better distinguished when the spectrum in O₂ is subtracted from the spectrum in H₂ as reported in Figure 5. This absorbance variation is linked to the presence of oxygen vacancies.

As mentioned in Chapter III, neutral V_O in ZnO contains two electrons located in levels at 0.05 and 0.18 eV below the conduction band (C.B.). The first ionization occurs at room temperature to generate mono-ionized oxygen vacancies (V_O⁺). The second ionization is promoted by the absorption of IR radiation, which is centred at around 1450 cm⁻¹ (0.18 eV) for ZnO [9]. The generation of V_O⁺ mainly

occurs via two main pathways: (i) filling pre-existing bi-ionized oxygen vacancies ($V_{O^{2+}}$) with one electron obtained from adsorbed oxygen species, like O_2^{2-} , O_2^- and O^- ; (ii) the formation of a new V_{O^+} by extraction of lattice O ions, but this pathway mainly occurs at high temperature. Distinguishing each pathway from the other is not straightforward and not easy by means of IR spectroscopy.

Concerning the studied samples, the maxima of the absorption related to V_{O^+} (dashed grey lines) are centered at around 1100 cm^{-1} for ZnZr-30 and 2200 cm^{-1} for ZnZr-5, which can be associated to electronic levels at about 0.14 and 0.27 eV below the C.B., respectively. Moreover, it is worth to highlight that the V_{O^+} ionization energy at 0.14 eV, related to ZnZr-30, is very close to the one of pure ZnO (0.18 eV). As reported by the PXRD (section 4.2.1) and EXAFS (section 4.2.3) data [4] (Appendix A.2), ZnZr-30 was the one with a secondary ZnO phase, hence the influence of this phase on the position of the oxygen vacancy band cannot be ruled out.

On the other hand, as for the sample with lower Zn loading, namely ZnZr-5, the ionization energy of V_{O^+} is centered at around 0.27 eV, much higher than the one of pure ZnO, meaning a deeper energy level in the band gap.

As for ZnZr-15 the identification of the maximum absorption is not easily detectable, due to the presence of negative peaks observed also for ZnZr-5 and ZnZr-30. These peaks, which arose from the mathematical subtraction of the spectra, are related to the vibrational modes of encapsulated CO_2 and carbonate/nitrate species, as above-mentioned. However, these species are not

removed from the samples after the reduction treatment, but their intensity loss could have another origin. Indeed, a coupling between the electronic absorption of the mono-ionized oxygen vacancies and the surface species variation could occur. It is already known in literature [10] that, using a continuum model consisting of a phonon term and a free electron term, a similar phenomenon could happen when plasmon absorption occurs on small particles of conducting and semiconducting materials. When plasmon frequency overcomes a phonon frequency, a plasmon-phonon coupling could take place leading to the decrease of any band with a pure vibrational nature. This phenomenon was already discussed in some papers related to semiconducting oxides, such as ZnO, SnO₂, MoO₃ and WO₃ [11,12].

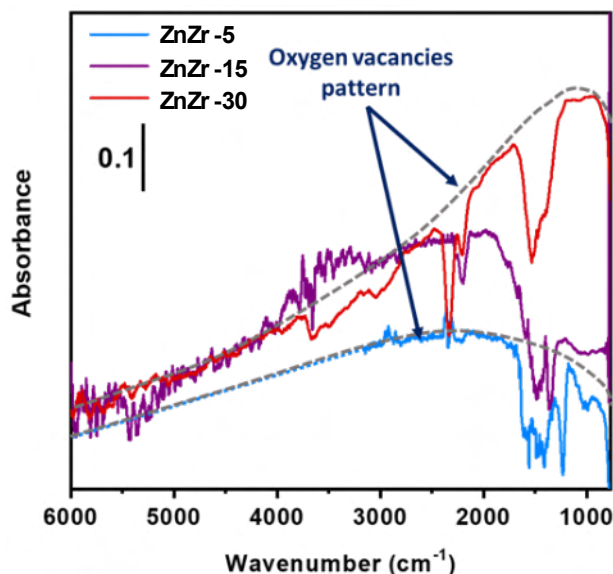


Figure 5 – FT-IR difference spectra of ZnZr-X catalysts recorded at 400 °C in H₂ (after subtrahend spectrum is that recorded in O₂ at 400 °C). ZnZr-5 spectrum is cut from 3155

cm⁻¹ onwards, because data are affected by low signal-to-noise ratio; the cut part has been substituted with a dotted blue line, aiming at reproducing the trend.

The intensity of the electronic absorption related to the oxygen vacancies and reported in Figure 5 decreases from ZnZr-30 and ZnZr-15 towards ZnZr-5 and it is in line with the chemical composition determined by ICP-OES, PXRD and EXAFS results, stating that Zn loading decreases in the order: ZnZr-30 > ZnZr-15 > ZnZr-5. The higher the Zn content the higher the amount of oxygen vacancies generated.

In conclusion, IR findings determined the importance of a pre-reducing treatment to induce the generation of reactive oxygen vacancies which could be strictly related to the catalytic performances; indeed, ZnZr-30 performs better than the other two samples, reasonably due to the presence of secondary ZnO phase.

4.2.2 FT-IR: CO adsorption at LNT on stand-alone ZnZr-X

CO adsorption was carried out at liquid-nitrogen temperature (LNT) in order to study specific surface sites that weakly bind CO, such as Zn²⁺ and Zr⁴⁺ cations. Figure 6 displays several spectra acquired after CO dosing at increasing coverages (θ_{CO}) on both oxidized and reduced ZnZr-X.

As for the oxidized samples (Figure 6a, c, and e) two main peaks were observed. The first at 2166 cm⁻¹ was attributed to coordinatively unsaturated (*cus*) Zr⁴⁺-CO, which refers to Zr⁴⁺ cation located on edges and steps. According to literature, the

second peak was centered at 2146 cm^{-1} and was associated to $\text{Zr}^{4+}\text{-CO}$, with Zr^{4+} cations located on facets [13].

The peak ascribed to *cus*- $\text{Zr}^{4+}\text{-CO}$ showed a red-shift from $2179/2192\text{ cm}^{-1}$ (according to the sample) towards 2166 cm^{-1} . As highlighted in the previous chapter, the shift can have several explanations, but only the dipolar coupling and the “chemical effect” can be considered. In this case study, a dipole-dipole coupling would cause a blue-shift upon θ_{CO} increasing, due to dipolar coupling occurring between “equal” oscillator on extended regular facets. Typically, the phenomenon is interrupted by surface defects. Hence, only the “chemical effect” could be the responsible for the observed red-shift. The red-shift upon θ_{CO} is typically observed for σ -donating cations (like Zr^{4+}), when the σ -donation contribution of all adsorbed CO molecules becomes smaller and smaller and, thus, $\nu(\text{C}\equiv\text{O})$ decreases.

As for the peak at 2146 cm^{-1} the assignment was based on literature [13,14] data. This band did not feature neither blue- nor red-shift, which could be explained by a balance between dipole-dipole coupling and chemical effect. Consequently, the peak is stationary, and it is in line with the assignment to CO on Zr^{4+} cation of regular facets.

Besides Zr^{4+} sites, Zn^{2+} are not observable. Since its concentration is lower than zirconium, it is not surprising that some Zn components could be under the detection limit or hidden by $\text{Zr}^{4+}\text{-CO}$. Indeed, according to some authors [14,15] zinc carbonyls should lie in the region between 2190 and 2160 cm^{-1} . For the sake

of clarity, the peak at 2192 and 2179 cm⁻¹ could have been associated to Zn²⁺-CO species, but there were neither references nor evidence regarding the studied ZnZr-X systems to correctly assign some absorption to zinc carbonyls.

As for the reduced samples reported in (Figure 6b, d, and f), all the peaks were attributed to the same species mentioned for the oxidized sample.

Nonetheless, there are some differences between oxidized and reduced samples and between all the three materials, as reported in Figure 7 (all the spectra are normalized). First of all, the intensity ratio between the peaks at 2166 and 2146 cm⁻¹ is higher for the oxidized catalysts. It is well evident considering the case of ZnZr-30: the peak related to *cus*-Zr⁴⁺-CO is almost absent for the oxidized catalyst. After the reduction in pure H₂ the peak is well distinguished, while the intensity of the peak at 2146 cm⁻¹ decreased.

This result can be explained considering the effect of the reduction treatment in generating defect sites and oxygen vacancies. However, among all the samples, ZnZr-30 showed the lowest intensity for *cus*-Zr⁴⁺-CO, and this result can be in line with BET findings reported in Table 1, showing a lower SSA for ZnZr-30 compared with ZnZr-5 and ZnZr-15.

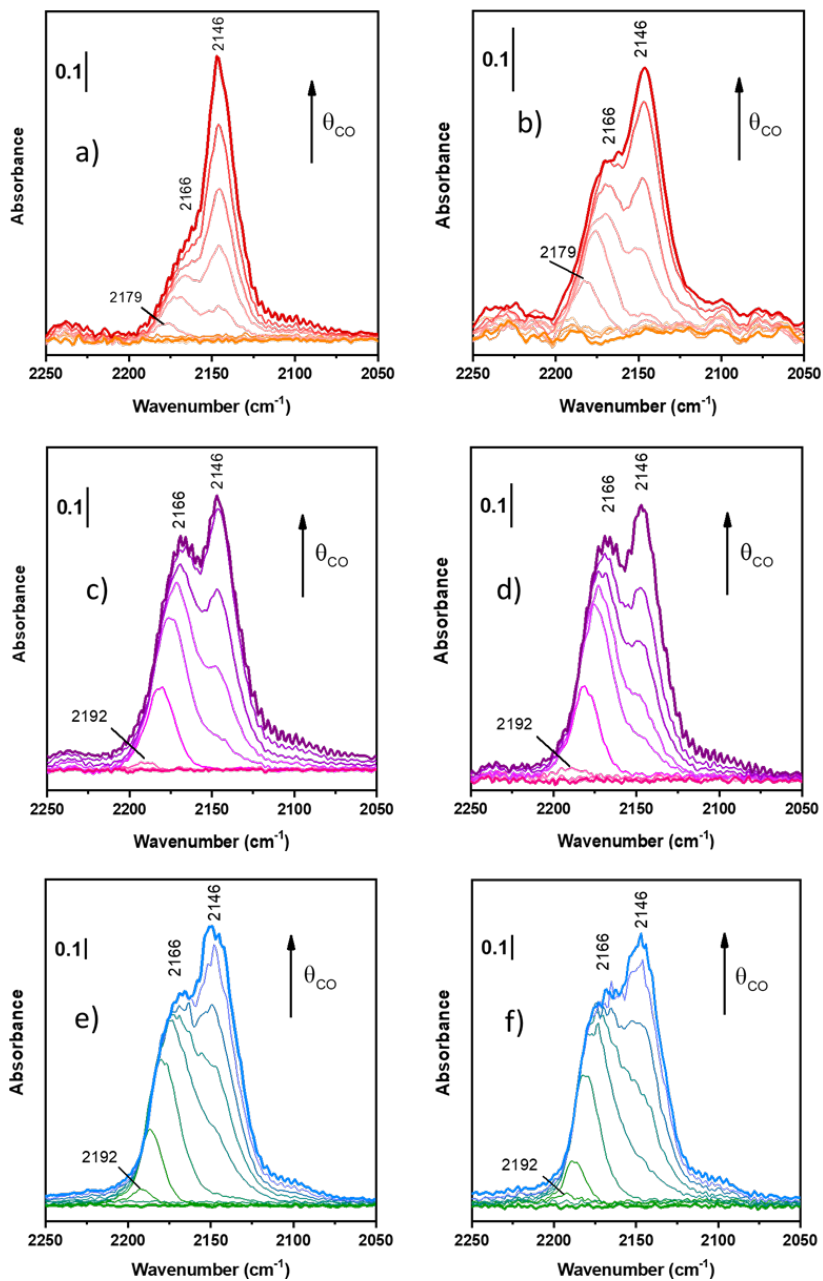


Figure 6 – FT-IR spectra of CO adsorption at LNT on oxidized ZnZr-30 (a), ZnZr-15 (c), ZnZr-5 (e) and reduced ZnZr-30 (b), ZnZr-15 (d), ZnZr-5 (f) at increasing doses up to 20 mbar.

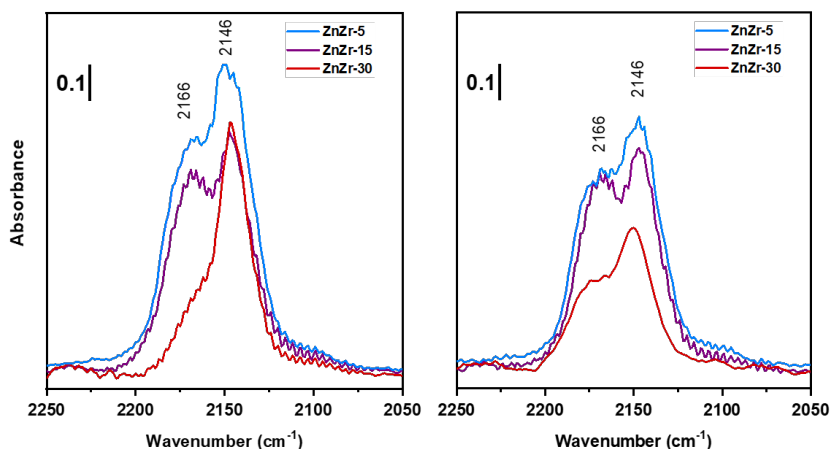


Figure 7 – Comparison between FT-IR spectra collected at the highest CO coverage for oxidized (left) and reduced (right) ZnZr-X catalysts.

Moreover, comparing the integrated intensity of the bands in the region between 2200 and 2100 cm^{-1} (Figure 7), it decreases as the Zn loading increases, in the order: ZnZr-5 > ZnZr-15 > ZnZr-30. This is in good agreement with the EXAFS data reported in details in Ticali et al. [4] describing the Zn content in the ZrO₂ lattice: as Zn content increases the amount of Zr⁴⁺ decreases.

4.2.3 XAS measurements performed on combined ZnZr-X + ZSM-5

For sake of clarity, I decided to briefly summarize some key results obtained by X-ray absorption spectroscopy in order to give a complete overview regarding the characterization of this sample. The following results were collected and explained by Dr. Davide Salusso and reported in detail in our joint work [4] (Appendix A.2).

XAS measurements were collected *in situ* and *operando* conditions on the combined catalysts in order to investigate the electronic properties, the local

structure of Zn and Zr sites and the preservation of the zeolite functionalities. This last point was already studied by Ahoba-Sam et al. [16] highlighting the ion exchange phenomenon in combined systems obtained by a physical mixture of acid zeolites and Zn-containing catalysts.

XAS measurements were carried out at the ROCK beamline [17] of SOLEIL synchrotron by our team. More details are reported in Ticali et al. [4] (Appendix A.2).

Figure 8 displays the Zn K-edge XAS spectra obtained at RT (Figure 8a) and during activation at 400 °C (Figure 8b). In Figure 8a, it was determined that all the as-prepared samples contain Zn^{2+} species, as evidenced by the edge energy position which matches that of ZnO model reference. Among them, ZnZr-30/ZSM-5 shows XANES line-shape comparable to ZnO spectroscopic features, reasonably linked to the secondary phase observed in this sample.

FT-EXAFS spectra reported in the inset are related only to ZnZr-30/ZSM-5 and ZnZr-15/ZSM-5, because the S/N ratio of ZnZr-5/ZSM-5 was too low to be reliable. The first shell peaks (Figure 8a) are similar to those of ZnO reference in R-space positions, but with lower intensity, reasonably due to the distortion of the local coordination. The variation in the second shell is even more conspicuous and it is related to Zn next nearest neighbour (NNN) atoms. As for ZnZr-30/ZSM-5 the position of this shell clearly matches the position of the ZnO reference. The reduced intensity can be explained by i) partial substitution of Zr^{4+} ions with Zn^{2+} in the zirconia lattice and ii) defectiveness of the segregated ZnO extra-phase.

Differently, ZnZr-15/ZSM-5 showed a reduced intensity of the second shell band, presumably due to the structural disorder of NNN atoms related to Zn ions inside the ZrO₂ lattice.

During activation (Figure 8b) the Zn K-edge remained unchanged: no change in Zn edge position, hence no oxidation state variation and no Zn²⁺ diffusion in the zeolite. Both the first and second shell were affected by Debye-Waller factor due to thermal effect, leading to a major dampening for ZnZr-30/ZSM-5. These findings are in line with IR results, because after thermal treatment a major disorder due to oxygen vacancies generation occurred.

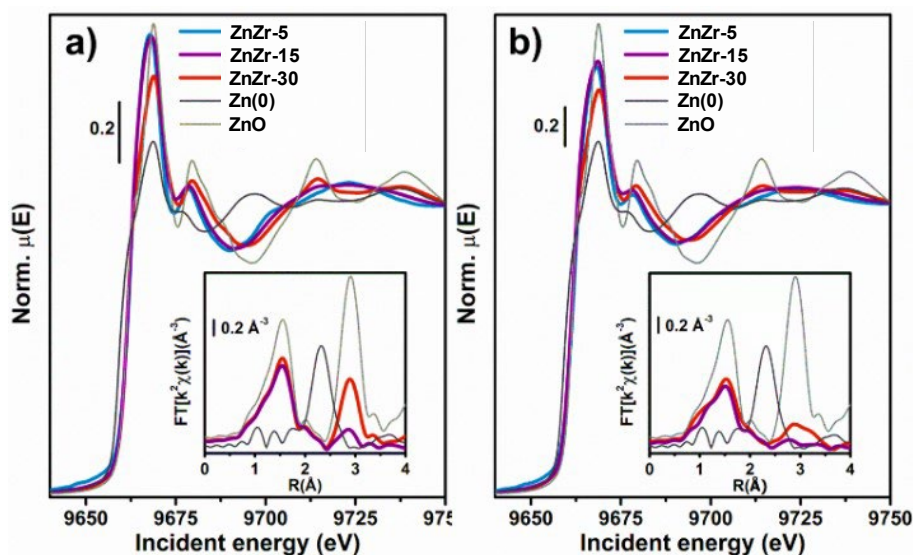


Figure 8 – K-edge XANES (main panel) and phase-uncorrected FT-EXAFS (bottom inset) spectra of the three samples and of Zn metal and ZnO model compounds, collected at (a) RT under He flux and (b) during the activation process (400 °C, H₂). The EXAFS spectra reported in the bottom insets have been obtained transforming the corresponding $k^2\chi(k)$ EXAFS function in the 2.5-13.0 Å⁻¹ range.

From the Zr point of view, Figure 9 shows Zr K-edge spectra at RT (Figure 9a) and during activation (Figure 9b). Via XAS measurements it was possible to distinguish ZrO₂ tetragonal structure from cubic and monoclinic structures. Indeed as reported by Li et al. [18], the tetragonal structure is distinguished by the presence of three features i) pre-edge electronic 1s → 4s transition, ii) white line splitting (not observable for monoclinic structure) and iii) broad post-edge resonance up to 35 eV after the edge.

For all the samples the pre-edge transition was observed confirming the presence of a tetragonal structure, highlighted by the first derivative reported in Figure 9c. A further explanation was reported in Ticali et al. [4] (Appendix A.2).

Another evidence to confirm the tetragonal structure comes from literature and the chemical composition of these samples. Indeed, all these samples included Hf: both Hf and Zn are well known to stabilize the tetragonal structure [5,19].

In conclusion, the ZrO₂ lattice maintained the tetragonal structure, Zn²⁺ did not exchange in the zeolite and both Zn and Zr oxidation state was not altered by the thermal reducing treatment. In addition, a further detailed analysis of this data conducted by Salusso et al. [6], demonstrated the presence of embedded ZnO nanoclusters in ZrO₂ matrix.

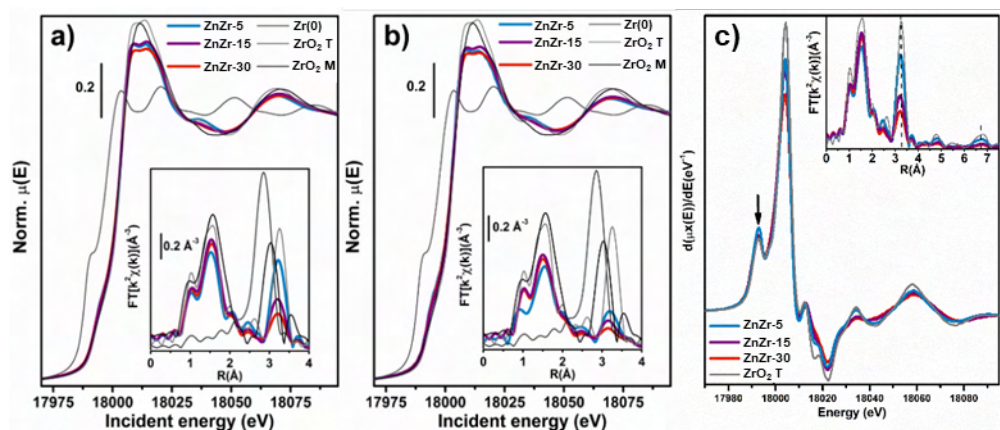


Figure 9 – K-edge XANES (main panel) and phase-uncorrected FT-EXAFS (bottom inset) spectra of the three samples and of Zr metal and ZrO₂ model compounds, collected at (a) RT under He flux and (b) during the activation process (400 °C, H₂). The EXAFS spectra reported in the bottom insets have been obtained transforming the corresponding $k^2\chi(k)$ EXAFS function in the 2.5-13.0 Å⁻¹ range.

3.3 Catalytic tests

For sake of completeness, I would like to briefly summarize the catalytic results obtained by combining ZnZr-X catalyst with ZSM-5. Herein, I am reporting both the measurements obtained on ZnZr-X alone and then on the combined system. All the measurements were performed by Dr. Adrian Ramirez.

The screening was performed varying the pressure (20, 30 and 40 bar), the temperature (250, 300 and 350 °C) and adding CO (10% in the feed) obtained from recycling it with CO₂ and H₂.

Figure 10 summarizes the results obtained on ZnZr-X catalysts alone. In line with other research works [20,21], the methanol selectivity and conversion increase with pressure for all three samples. CO is the main by-product, together with small

amount of CH₄ (selectivity <1%) [4]. The same occurs by decreasing the temperature. The MeOH selectivity is almost 100% at 250 °C and 30 bar. However, a drastic decrease at ca. 50% of MeOH selectivity was observed at 350 °C and 30 bar. Despite these bad conditions, no deactivation was observed after 150 hours of tests.

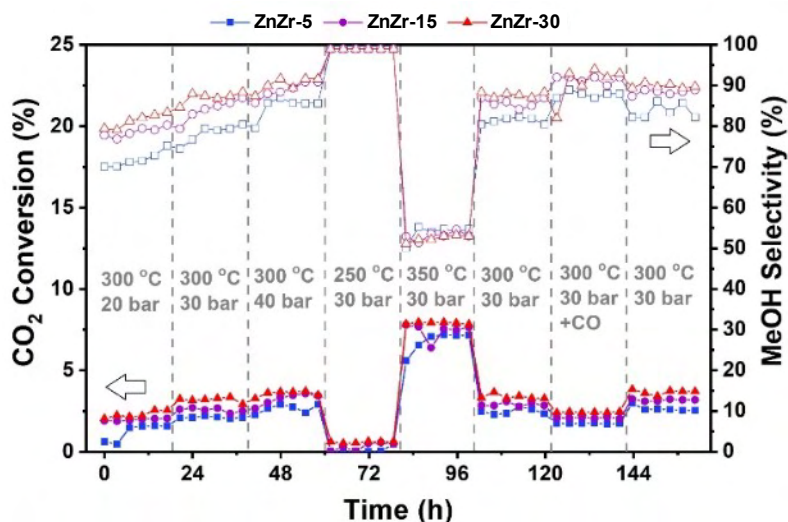


Figure 10 – Catalytic performance of all ZnZr-X stand-alone samples for the CO₂ conversion to MeOH. CO₂:H₂ 1:3, 12000 mL/h/g.

The combined bifunctional catalysts displayed very stable performances and, as reported in Figure 11, the best conditions are 350 °C and 30 bar displaying the highest conversion with a C₃ selectivity of about 40%. In particular, the best system is the one combining ZSM-5 with ZnZr-30, which showed the highest CO₂ conversion in the up-mentioned conditions, in line with the characterization

findings. Further details regarding the catalytic tests could be found in Ticali et al. [4] (Appendix A.2).

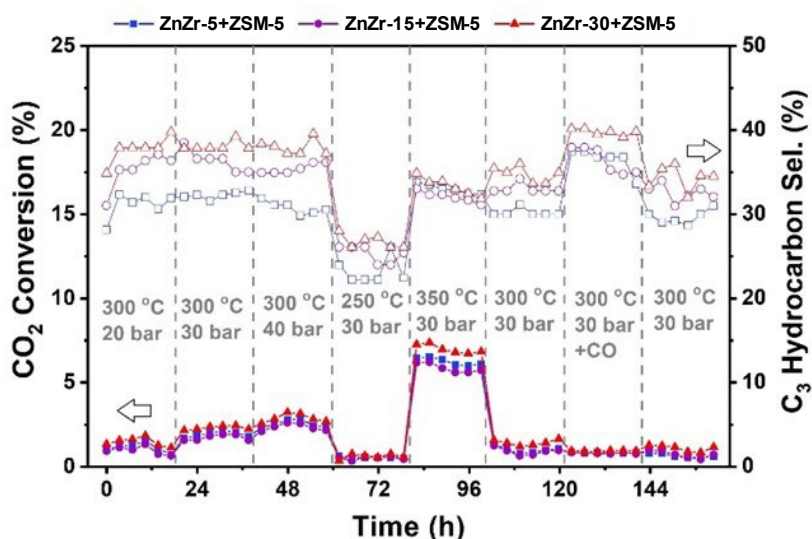


Figure 11 – Catalytic performance of the combined ZnZr-X+ZSM-5 systems for the CO₂ conversion to hydrocarbons. CO₂:H₂ 1:3, 12000 mL/h/g. Please note that the secondary Y axis refers to the C₃ selectivity among hydrocarbons (CO free).

Furthermore, we investigated the same system (which included a ZSM-5 with Si/Al = 8) using two more ZSM-5 zeolites with higher Si/Al ratio (SAR) equal to 25 and 360. In both cases, we observed lower MeOH yield and CO selectivity with the increasing SAR. This suggests that CO is involved in the hydrocarbon generation [22,23]. Moreover, we compared the influence of the space velocity on the production of aromatic species and of the acidity on the hydrocarbon distribution.

Surprisingly, the aromatics selectivity was typically lower than 10%, except for the measurements at 6000 mL/h/g (Figure 12). We attributed these findings to the high space time employed in the catalytic runs. As a matter of fact, it is already known that the selectivity to aromatic species increases with decreasing space time [24]. We also determined that the higher the acid sites density the higher the amount of aliphatic products and less the aromatic distribution. However, we chose the ZSM-5 with SAR = 8 because of the decrease of MeOH yield with the increase of the zeolite acidity, and this zeolite composition was the best compromise.

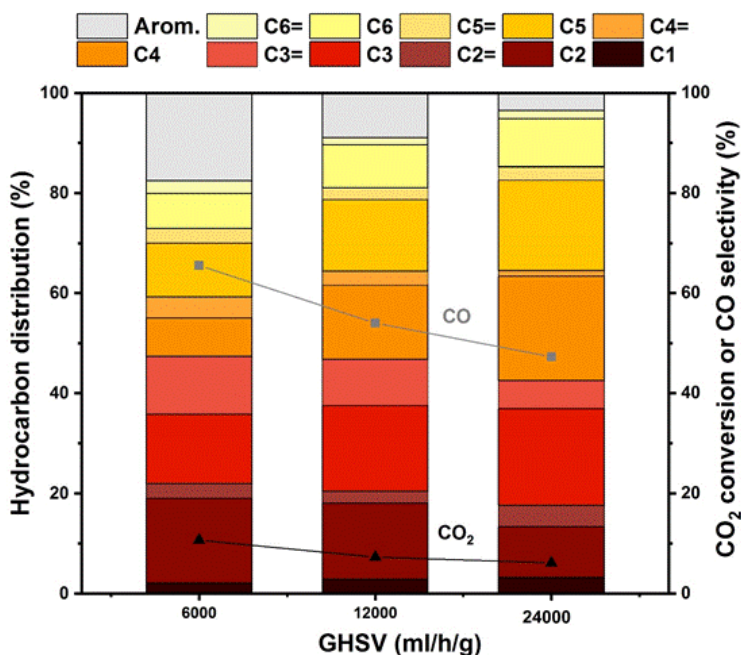


Figure 12 – Hydrocarbon distribution of the ZnZr-30/ZSM-5 combined system for the CO₂ conversion to hydrocarbons at different space times. CO₂:H₂ 1:3, 350 °C, 30 bars.

Finally, at higher space times paraffins predominate over the olefins, maybe due to the reaction kinetics over ZSM-5, which was demonstrated to be favorable to towards paraffins production [25,26].

In conclusion, it is worth to say that, despite the low conversion, the productivity of this catalyst is the highest reported for this kind of catalyst when compared to the state-of-the-art catalysts [27], and it could be probably due to the absence of aromatics and the high space velocity employed.

REFERENCES

- [1] K.S.W. Sing, D.H. Everett, R.A.W. Haul, L. Moscou, R.A. Pierotti, J. Rouquerol, T. Siemieniewska, Reporting Physisorption Data for Gas/Solid Systems with Special Reference to the Determination of Surface Area and Porosity, *Pure Appl. Chem.* 57 (1985) 603–619. <https://doi.org/10.1351/pac198557040603>.
- [2] K. Stafford, W. Sing, Physisorption Hysteresis Loops and the Characterization of Nanoporous Physisorption Hysteresis Loops and the Characterization of Nanoporous Materials, (2014). <https://doi.org/10.1260/0263617053499032>.
- [3] J. Rodríguez-Carvajal, Recent developments of the program FULLPROF, *Comm. Powder Diffr. (IUCr). Newsl.* 26 (2001) 12–19.
- [4] P. Ticali, D. Salusso, R. Ahmad, C. Ahoba-Sam, A. Ramirez, G. Shterk, K.A. Lomachenko, E. Borfecchia, S. Morandi, L. Cavallo, J. Gascon, S. Bordiga, U. Olsbye, CO₂ hydrogenation to methanol and hydrocarbons over bifunctional Zn-doped ZrO₂/zeolite catalysts, *Catal. Sci. Technol.* 11 (2021) 1249–1268. <https://doi.org/10.1039/D0CY01550D>.
- [5] J. Wang, G. Li, Z. Li, C. Tang, Z. Feng, H. An, H. Liu, T. Liu, C. Li, A highly selective and stable ZnO-ZrO₂ solid solution catalyst for CO₂ hydrogenation to methanol, *Sci. Adv.* 3 (2017) 1–11. <https://doi.org/10.1126/sciadv.1701290>.
- [6] D. Salusso, E. Borfecchia, S. Bordiga, Combining X-ray Diffraction and X-ray Absorption Spectroscopy to Unveil Zn Local Environment in Zn-Doped ZrO₂ Catalysts, *J. Phys. Chem. C.* 125 (2021) 22249–22261. <https://doi.org/10.1021/acs.jpcc.1c06202>.
- [7] S. Tada, N. Ochiai, H. Kinoshita, M. Yoshida, N. Shimada, T. Joutsuka, M. Nishijima, T. Honma, N. Yamauchi, Y. Kobayashi, K. Iyoki, Active Sites on Zn_xZr_{1-x}O₂ Solid Solution Catalysts for CO₂-to-Methanol Hydrogenation, *ACS Catal.* 12 (2022) 7748–7759. https://doi.org/10.1021/ACSCATAL.2C01996/ASSET/IMAGES/LARGE/CS2C01996_0017.JPEG.
- [8] G. Teufer, The crystal structure of tetragonal ZrO₂, *Acta Crystallogr.* 15 (1962) 1187. <https://doi.org/10.1107/S0365110X62003114>.
- [9] J. Ye, C. Liu, D. Mei, Q. Ge, Active oxygen vacancy site for methanol synthesis from CO₂ hydrogenation on In₂O₃(110): A DFT study, *ACS Catal.* 3 (2013) 1296–1306. <https://doi.org/10.1021/cs400132a>.
- [10] L. Genzel, T.P. Martin, Infrared absorption by surface phonons and

- surface plasmons in small crystals, *Surf. Sci.* 34 (1973) 33–49.
[https://doi.org/10.1016/0039-6028\(73\)90185-4](https://doi.org/10.1016/0039-6028(73)90185-4).
- [11] G. Ghiotti, A. Chiorino, F. Prinetto, Chemical and electronic characterization of pure SnO₂ and Cr-doped SnO₂ pellets through their different response to NO, *Sensors Actuators B. Chem.* 25 (1995) 564–567. [https://doi.org/10.1016/0925-4005\(95\)85123-2](https://doi.org/10.1016/0925-4005(95)85123-2).
- [12] S. Morandi, M.C. Paganini, E. Giamello, M. Bini, D. Capsoni, V. Massarotti, G. Ghiotti, Structural and spectroscopic characterization of Mo_{1-x}W_xO_{3-δ} mixed oxides, *J. Solid State Chem.* 182 (2009) 3342–3352. <https://doi.org/10.1016/j.jssc.2009.09.025>.
- [13] C. Morterra, E. Giamello, L. Orio, M. Volante, Formation and reactivity of Zr³⁺ centers at the surface of vacuum-activated monoclinic zirconia, *J. Phys. Chem.* 94 (1990) 3111–3116. <https://doi.org/10.1021/j100370a067>.
- [14] K.I. Hadjiivanov, G.N. Vayssilov, Characterization of oxide surfaces and zeolites by carbon monoxide as an IR probe molecule, *Adv. Catal.* 47 (2002) 307–511. [https://doi.org/10.1016/S0360-0564\(02\)47008-3](https://doi.org/10.1016/S0360-0564(02)47008-3).
- [15] D. Scarano, S. Bertarione, G. Spoto, A. Zecchina, C. Otero Areán, FTIR spectroscopy of hydrogen, carbon monoxide, and methane adsorbed and co-adsorbed on zinc oxide, *Thin Solid Films.* 400 (2001) 50–55.
[https://doi.org/10.1016/S0040-6090\(01\)01472-9](https://doi.org/10.1016/S0040-6090(01)01472-9).
- [16] C. Ahoba-Sam, E. Borfecchia, A. Lazzarini, A. Bugaev, A.A. Isah, M. Taoufik, S. Bordiga, U. Olsbye, On the conversion of CO₂ to value added products over composite PdZn and H-ZSM-5 catalysts: excess Zn over Pd, a compromise or a penalty?, *Catal. Sci. Tech.* (2020).
<https://doi.org/10.1039/x0xx00000x>.
- [17] C. La Fontaine, S. Belin, L. Barthe, O. Roudenko, C. La, S. Belin, L. Barthe, O. Roudenko, ROCK : A Beamline Tailored for Catalysis and Energy-Related Materials from ms Time Resolution to μm Spatial Resolution ROCK : A Beamline Tailored for Catalysis and Energy-Related Materials from ms Time Resolution to μm Spatial Resolution, 0886 (2020). <https://doi.org/10.1080/08940886.2020.1701372>.
- [18] P. Li, I.W. Chen, J.E. Penner-Hahn, X-ray-absorption studies of zirconia polymorphs. I. Characteristic local structures, *Phys. Rev. B.* 48 (1993) 10063–10073. <https://doi.org/10.1103/PhysRevB.48.10063>.
- [19] D.Y. Cho, H.S. Jung, C.S. Hwang, Structural properties and electronic structure of HfO₂-ZrO₂ composite films, *Phys. Rev. B - Condens. Matter Mater. Phys.* 82 (2010) 1–7.
<https://doi.org/10.1103/PhysRevB.82.094104>.

- [20] A. Bavykina, I. Yarulina, A.J. Al Abdulghani, L. Gevers, M.N. Hedhili, X.H. Miao, A.R. Galilea, A. Pustovarenko, A. Dikhtiarenko, A. Cadiou, A. Aguilar-Tapia, J.L. Hazemann, S.M. Kozlov, S. Oud-Chikh, L. Cavallo, J. Gascon, Turning a Methanation Co Catalyst into an In-Co Methanol Producer, *Acs Catal.* 9 (2019) 6910–6918. <https://doi.org/10.1021/acscatal.9b01638>.
- [21] Y. Slotboom, M.J. Bos, J. Pieper, V. Vrieswijk, B. Likozar, S.R.A. Kersten, D.W.F. Brilman, Critical assessment of steady-state kinetic models for the synthesis of methanol over an industrial Cu/ZnO/Al₂O₃ catalyst, *Chem. Eng. J.* 389 (2020). <https://doi.org/Artn12418110.1016/J.Cej.2020.124181>.
- [22] K. Cheng, W. Zhou, J. Kang, S. He, S. Shi, Q. Zhang, Y. Pan, W. Wen, Y. Wang, Bifunctional Catalysts for One-Step Conversion of Syngas into Aromatics with Excellent Selectivity and Stability, *Chem.* 3 (2017) 334–347. <https://doi.org/10.1016/J.CHEMPR.2017.05.007>.
- [23] Q. Song, Y. Men, J. Wang, S. Liu, S. Chai, W. An, K. Wang, Y. Li, Y. Tang, Methanol steam reforming for hydrogen production over ternary composite Zn_yCe₁Zr₉O_x catalysts, *Int. J. Hydrogen Energy.* 45 (2020) 9592–9602. <https://doi.org/10.1016/J.IJHYDENE.2020.01.175>.
- [24] X. Cui, P. Gao, S.G. Li, C.G. Yang, Z.Y. Liu, H. Wang, L.S. Zhong, Y.H. Sun, Selective Production of Aromatics Directly from Carbon Dioxide Hydrogenation, *Acs Catal.* 9 (2019) 3866–3876. <https://doi.org/10.1021/acscatal.9b00640>.
- [25] J.S. Martinez-Espin, M. Mortén, T.V.W. Janssens, S. Svelle, P. Beato, U. Olsbye, New insights into catalyst deactivation and product distribution of zeolites in the methanol-to-hydrocarbons (MTH) reaction with methanol and dimethyl ether feeds, *Catal. Sci. Technol.* 7 (2017) 2700–2716. <https://doi.org/10.1039/c7cy00129k>.
- [26] T. Cordero-Lanzac, A. Ateka, P. Pérez-Uriarte, P. Castaño, A.T. Aguayo, J. Bilbao, Insight into the Deactivation and Regeneration of HZSM-5 Zeolite Catalysts in the Conversion of Dimethyl Ether to Olefins, *Ind. Eng. Chem. Res.* 57 (2018) 13689–13702. <https://doi.org/10.1021/acs.iecr.8b03308>.
- [27] A. Dokania, A. Ramirez, A. Bavykina, J. Gascon, Heterogeneous Catalysis for the Valorization of CO₂: Role of Bifunctional Processes in the Production of Chemicals, *Acs Energy Lett.* 4 (2019) 167–176. <https://doi.org/10.1021/acsenerylett.8b01910>.

CHAPTER V

ZnCeZrO_x

5.1 Structural characterization

PXRD measurements were performed almost simultaneously with XAS analysis at BM31 beamline at ESRF synchrotron. All the data were collected from powder in a capillary with a diameter of 0.7 mm and during activation of ZnCeZrO_x with a temperature ramp of 5°C/min from room temperature (RT) to 400 °C. The PXRD patterns display tetragonal ZrO₂ (t-ZrO₂) reflections, together with hexagonal ZnO (h-ZnO), reported with arrows in Figure 1a. During the thermal treatment no new reflections were observed, but a variation of unit cell volume and ZnO-ZrO₂ relative concentration. Indeed, up to 300 °C the unit cell volume increases following the same trend observed for a t-ZrO₂ reference (Figure 1b). Beyond 300 °C the volume increases at faster speed and then decreases. At the same time, h-ZnO concentration increases (Figure 1c) and it could explain the variation in the slope of unit cell volume rate (Figure 1b). The formation of h-ZnO could be related to the formation of a ZnO secondary phase.

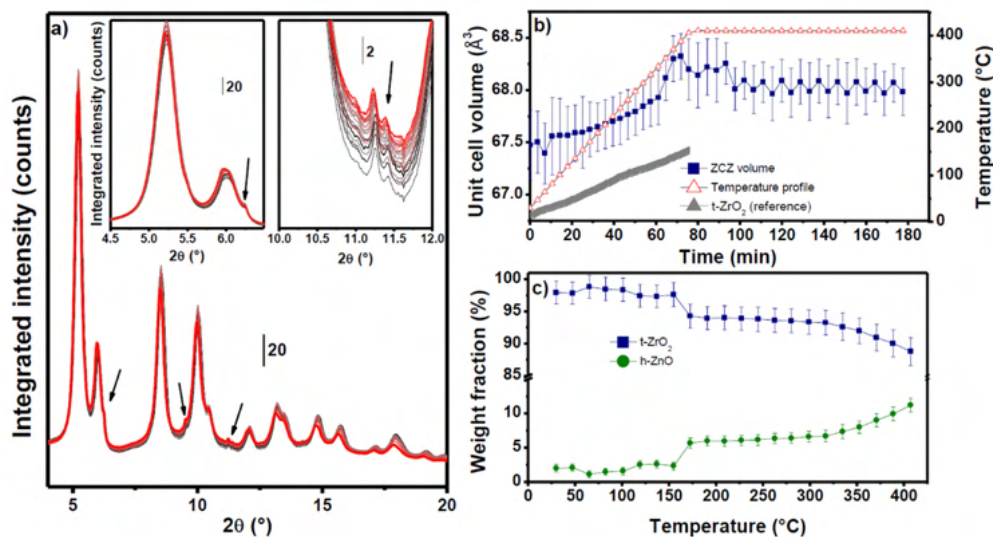


Figure 1 – a) In-situ PXRD pattern collected during activation under He:H₂ (1:1) from RT (black line) to 400 °C (red line). Arrows indicate h-ZnO reflections. b) Unit cell volume variation during the temperature ramp. c) ZnO- ZrO₂ relative concentration determined with Sequential Rietveld Refinement of the experimental diffractograms.

5.2 Spectroscopic characterization

The present section only deals with the spectroscopic characterization of stand-alone ZnCeZrO_x and stand-alone RUB-13 because of two main reasons: the first concerns the catalytic activity of the samples which highlighted the high instability of the zeotype (RUB-13) which was observed a loss of activity over time, due to structure disruption, and that lead COZMOS project to put this sample aside; the second is more related to the information coming from infrared spectroscopy. As for this last point, ZnCeZrO_x bands lie in the same region of the zeolite and RUB-13 larger specific surface area, compared to the oxidic

counterpart, so that CO absorption bands on RUB-13 predominate and do not help to characterize both the phases. Indeed, no further information there could have been obtained from FT-IR analysis, but the absorption band related to the pure RUB-13 (*vide infra*). Hence, for the sake of brevity, I decided to keep it out from this chapter and only focusing on the stand-alone oxidic phase.

5.2.1 FT-IR: H₂ interaction with stand-alone ZnCeZrO_x

Both ZnO and CeO₂ are well known in literature for their semiconducting properties. According to XAS (*vide infra*), ZnCeZrO_x is a mixed oxide, but both Zn and Ce could segregate and leave the ZrO₂ lattice, giving rise to specific spectroscopic features. Hence, to study these properties, ZnCeZrO_x was investigated by means of FT-IR to follow a temperature programmed analysis in static H₂ atmosphere, moving from 50 °C up to 400 °C (Figure 2). In order to observe the formation of oxygen vacancies, after having reached 400 °C, the H₂ gas phase was evacuated and substituted with fresh H₂ admission, before a second acquisition (400 °C II). All the spectra reported in Figure 2 are difference spectra obtained by subtracting spectra in O₂ from those in H₂ at each temperature. As illustrated in Figure 2, there are no significant differences between the spectrum at 50 °C and the first acquired spectrum at 400 °C, but a slight variation in the slope of the spectrum (400 °C I, orange line). A much more remarkable difference was observed after a fresh H₂ addition (400 °C II, red line). The new band can be

ascribed to a combination of both “free” electron absorption in the conduction band (C.B.) and electrons entrapped in oxygen vacancies.

According to the nature of a semiconducting oxide the electrons could occupy levels in the band gap more or less distant from the bottom of the C.B. When electronic levels are less than 0.05 eV distant from the C.B., a transition could easily occur to the C.B., even at room temperature. The presence of electrons in the C.B. is evidenced by a monotonic absorption, whose common pattern is illustrated by dashed grey line in Figure 2. When the absorption is induced by IR radiation, it concerns mono-ionized oxygen vacancies (V_{O}^{+}) and the transition of the electrons from V_{O}^{+} to the C.B. is featured by a “hump” and broad band, with a maximum that corresponds to the deepness in the band gap of the energy levels related to the mono-ionized oxygen vacancies. This absorption pattern is illustrated in Figure 2 with a dashed blue line. The maximum is centered at about 1200 cm^{-1} , $\sim 0.15\text{ eV}$, which is very close to the V_{O}^{+} ionization energy of ZnO (0.18 eV) [1,2]. Hence, it could reflect the presence of a secondary ZnO phase responsible for the absorption. However, CeO_2 is a semiconductor as well, but it is well-known to form Ce^{3+} [3]. When oxygen vacancies are formed, some electrons could be associated to Ce^{4+} leading to reduction to Ce^{3+} , while others can contribute to the above-mentioned absorption related to Figure 2.

To explain why the infrared absorption became visible after evacuation and substitution of the gas phase with fresh hydrogen is not straightforward. A possible hypothesis could be linked to the fact that the first reduction treatment

was not strong enough, and some hydrogen was consumed by some “*parasite*” reactions, so that a second admission of hydrogen was necessary to drive the formation oxygen vacancies.

The negative band around 1500 cm⁻¹ were already discussed in the previous chapter for ZnZrO_x. Using a continuum model of a phonon term and free electron term, a similar phenomenon could be observed for plasmon absorption of conductors and semiconductors. In particular, when plasmon frequency overcomes the phonon frequency, a coupling could occur together with a decreasing of pure vibrational bands [4–6]. In this case study, the vibrational bands are related to carbonate species adsorbed on the surface of ZnCeZrO_x.

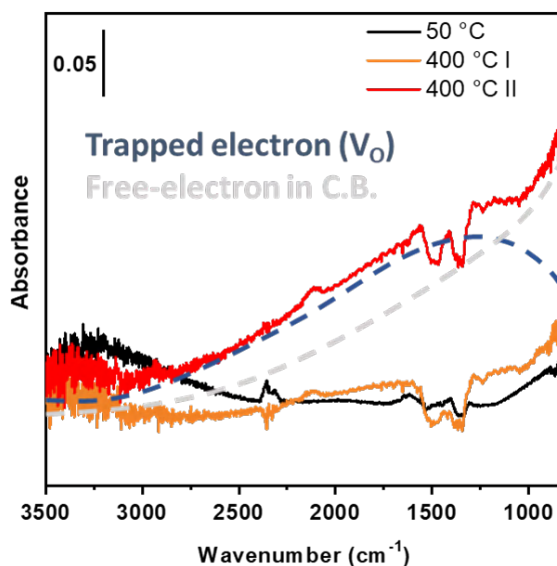


Figure 2 – FT-IR spectra acquired in H₂ at 50°C (black) and 400 °C (red and orange). Subtrahend spectra in O₂ were subtracted to spectra in H₂ at each temperature. Grey and blue dashed line indicate the absorption pattern related to free electron in the C.B. and entrapped in oxygen vacancies, respectively.

5.2.2 *FT-IR: CO adsorption on stand-alone ZnCeZrO_x*

Aiming at studying cationic sites, such as Zn²⁺, Zr⁴⁺, and Ce^{4+/3+}, FT-IR experiments on ZnCeZrO_x were carried out upon adsorption of CO at both room (RT) and liquid-nitrogen (LNT) temperature on oxidized, activated (reduced) and re-oxidized catalyst, in order to compare all the findings.

Comparing the spectra of the sample after the different treatments (Figure 3) there is no significant variation for the infrared absorption profile, except a broad band at 2127 cm⁻¹ ascribable to Ce³⁺ forbidden electronic transition $^2F_{5/2} \rightarrow ^2F_{7/2}$ [7,8]. Reasonably, Ce³⁺ is only observable on the reduced sample, since its formation is related to the formation of oxygen vacancies.

In addition, below 1750 cm⁻¹ there are some bands related to presence of nitrates originating from the synthesis of the sample. Their intensity is not related to the oxidation/reduction of the sample, but it progressively decreases with the thermal treatments, suggesting a progressive decomposition.

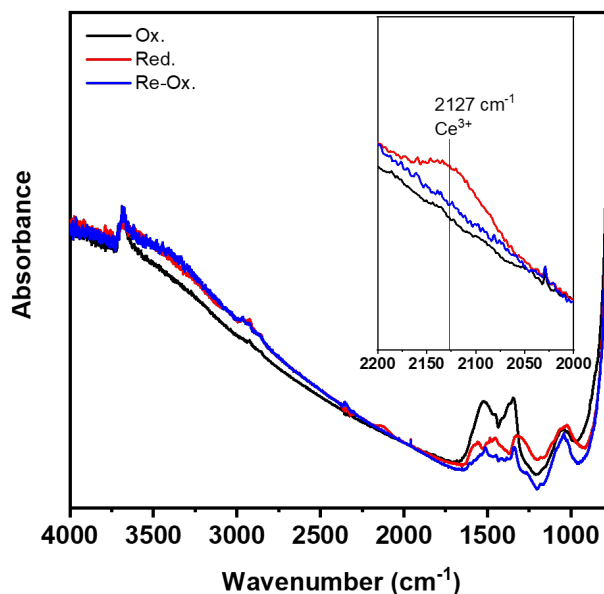


Figure 3 – FTIR spectra of oxidized (black), activated (red) and re-oxidized (blue) ZnCeZrO_x.

Adsorbed CO is known to absorb infrared radiation, thus in order to follow the adsorption at different CO doses and coverages (θ_{CO}), from now on all the spectra reported will be difference spectra.

Figure 4 reports all the spectra obtained after all thermal treatments at decreasing θ_{CO} from 50 mbar to complete evacuation (10^{-3} mbar). Figure 4a includes the spectra obtained on oxidized ZnCeZrO_x and shows a broad band constituted by two main components. The former lies in the range from 2189 to 2165 cm⁻¹ and can be ascribed to both Zr⁴⁺ and Ce⁴⁺ with a coordinative unsaturation. Hence, we are referring to them as *cus*-Zr⁴⁺ and *cus*-Ce⁴⁺. The latter is an absorption centered

at 2150 cm^{-1} . This component can include CO on both Zr^{4+} and Ce^{4+} with lower coordinative unsaturation, but also CO interacting via hydrogen bonds with surface OH groups [7–12].

As for activated/reduced ZnCeZrO_x (Figure 4b) CO adsorption leads to several bands, whose assignment is not straightforward. Even in this case we can define two main regions being separated by an “crossover” point around 2100 cm^{-1} .

Beyond 2100 cm^{-1} , it is possible to identify carbonyls ascribable to *cus*- Zr^{4+} and *cus*- Ce^{4+} from 2189 to 2162 cm^{-1} ; the absorption band at 2145 cm^{-1} can be the result of several contributions such as OH-CO, Zr^{4+} -CO and Ce^{4+} -CO. However, after outgas, two peaks at 2145 and 2129 cm^{-1} are stable at very low ϑ_{CO} and in dynamic vacuum (last red curve). As already mentioned in the previous section, the activated sample is featured by the presence of Ce^{3+} , hence on the basis of literature data [13,14], these two components can be related to Ce^{3+} -CO, in particular to Ce^{3+} sites with high (2145 cm^{-1}) and low (2129 cm^{-1}) coordinative unsaturation.

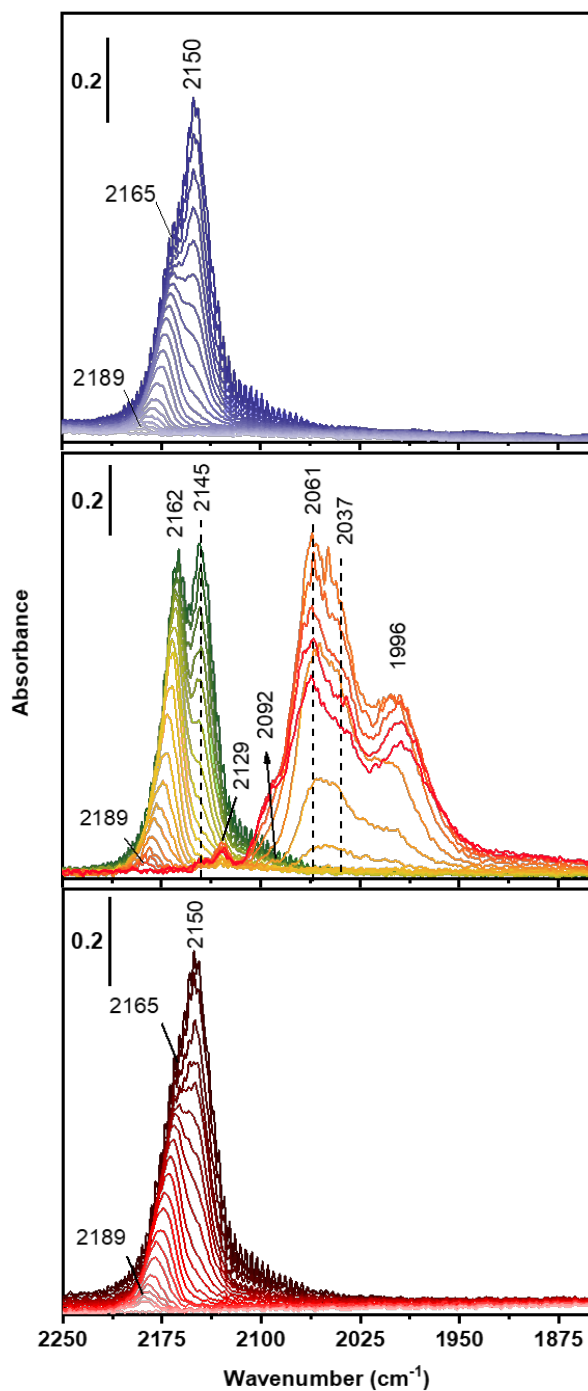


Figure 4 – CO adsorption at decreasing doses on a) oxidized ZnCeZrO_x (from dark blue to light blue spectrum), b) activated ZnCeZrO_x (from green to red spectrum) and c) re-oxidized ZnCeZrO_x (from dark red to light red spectrum).

Below 2100 cm^{-1} the assignment reported in this work, to the best of our research group knowledge, has not been presented in scientific literature yet. In the light of XAS findings (*vide infra*), it is noteworthy to highlight that the possibility cerium and zinc generate one or more alloys cannot be excluded. CeZn alloys have been already presented in several past works [15–21]. However, by FTIR and XAS it was not possible to determine which kind of alloy is formed, but both the techniques helped us to show specific features.

CO adsorption leads to several absorption bands observable at low θ_{CO} . It is quite interesting that all the features were observed by decreasing CO coverage. For the sake of clarity, spectra obtained at increasing CO doses were excluded, but no peaks below 2100 cm^{-1} were present.

The strangest peculiarity of these bands is that their intensity rises upon decreasing θ_{CO} followed by their intensity decline. While this last part could be easily explained by the CO molecule removal, on the other hand explaining their increase is not simple at all and it is very counter-intuitive. Zn is not prone to bind CO when reduced to the metallic state, thus that the presence/amount of Zn^0 is often determined by intensity difference of the Zn^{2+} -CO peak, between oxidized and reduced Zn-containing samples [22]. Hence, in the hypothesis of a CeZn alloy, it is reasonable that CO is adsorbed on Ce sites.

The very low temperature should hinder every possible reaction or migration. At the same time, low temperature reduces diffusion and could facilitate CO molecule stacking on specific sites, thus promoting the adsorption on these sites

upon outgassing. However, why this behavior was only observed during step outgassing, and not during adsorption, it is still difficult to explain. A hypothesis could be linked to a different organization of CO adsorbed on all the sites at hand: during adsorption, the catalyst surface is clean, and CO could directly be adsorbed on Zr⁴⁺, Ce⁴⁺ and Ce³⁺; during outgassing, due to the very low temperature, CO molecules are not easily desorbed, so that when a single CO molecule leaves the surface its adsorption on other sites could be driven by other adsorbed CO molecule, in a sort of “*solvation effect*”. This results in a sort of transfer of CO molecule from higher-frequency sites (> 2100 cm⁻¹) to lower-frequency sites (< 2100 cm⁻¹). It is noteworthy that this intensity modulation concerns both the region below 2100 cm⁻¹ and Ce³⁺ peaks, as reported in the inset of Figure 4b. Upon outgassing, the intensity of the peaks decreases without a complete loss, but it reaches a stability in dynamic vacuum.

Figure 4c reports all the spectra related to decreasing doses of CO on re-oxidized ZnCeZrO_x. Comparing all the figures, re-oxidized ZnCeZrO_x leads almost to the same absorption observed on the oxidized catalyst. No peaks below 2100 cm⁻¹ are present, this means that the complete cycle induces no significant variation on the catalyst surface sites, i.e. it is a completely reversible process.

In the light of all the findings, we reasonably assigned the entire region below 2100 cm⁻¹ to a CeZn alloy after the following considerations: i) no peaks below 2100 cm⁻¹ are observable on both oxidized and re-oxidized sample, which means this region is related to reduced species; ii) $\nu(\text{C}\equiv\text{O})$ is quite lower than the gaseous

CO stretching frequency (2143 cm^{-1}) and lies in the typical region of metallic atoms with oxidation state equals to 0. Nonetheless, no literature data could confirm the assignment of those bands. In order to have an eventual confirmation about this hypothesis, more experiments were performed: i) activation in CO at $400\text{ }^{\circ}\text{C}$ and CO adsorption at LNT; ii) activation in H_2 at $400\text{ }^{\circ}\text{C}$ and CO dosing with two consecutive adsorptions after partial outgassing; iii) activation in H_2 at 400°C and CO adsorption at room temperature. In all the cases we reproduced the same experiment following the same protocol discussed in the experimental section.

i) Activation in CO and CO adsorption at 77K

This kind of treatment was conceived in order to exclude the formation of hydrides, which typically lie in the same region, and that could have eventually influenced CO adsorption and, thus, the generation of the bands below the *crossover* point.

FT-IR measurement (Figure 5) shows almost for same spectroscopic features observed on the activated sample in pure H_2 , except a slight variation in frequency of some component. Besides the peaks related to Zr^{4+} and Ce^{4+} in the range $2200\text{-}2140\text{ cm}^{-1}$, which are as intense as those reported in Figure 4, the reduction process in CO seems to be less effective on those sites responsible for the absorption below 2100 cm^{-1} . In fact, comparing the relative intensity of both the

regions on either sides of the *crossover* point, both Ce³⁺ (2150-2120 cm⁻¹) and CeZn alloy carbonyls are not as intense as the peaks observed in Figure 4b. The only “new component” lies at 2044 cm⁻¹. This peak rose upon decreasing θ_{CO} , as observed for the catalyst reduced in pure H₂. In particular, the band at 2044 cm⁻¹ increases and then decreases in intensity, when both the bands at 2061 and 2037 cm⁻¹ compare and stand out over the band at 2044 cm⁻¹.

Upon outgassing (Figure 5 black line) CO remains only adsorbed on those sites with frequency ≤ 2100 cm⁻¹.

This analysis confirmed that the bands below the *crossover* point are not related to the presence of hydrides adsorbed on those surface sites. On the contrary, all bands are clearly related to the adsorption of CO.

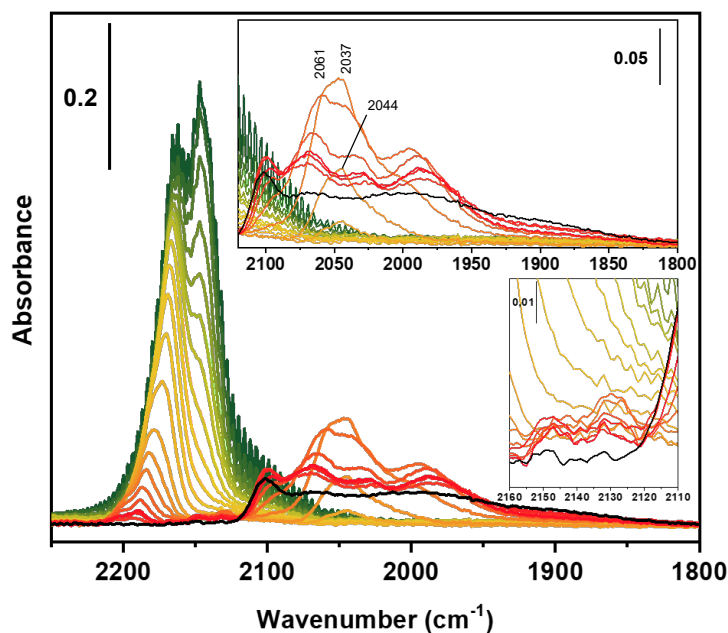


Figure 5 – CO adsorption at LNT on ZnCeZrO_x after reduction in pure CO at 400 °C at decreasing coverage of CO (from green to red line)

ii) *Activation in H₂ and double consecutive CO dosing at 77K*

FTIR spectra were also acquired on activated ZnCeZrO_x by decreasing θ_{CO} and sending back the same maximum pressure of CO (50 mbar) when the components below 2100 cm⁻¹ reached the maximum intensity. By means of this procedure the aim was to study the behavior of all the sites generating peaks below 2100 cm⁻¹.

This experiment was based on two hypotheses:

- i) if the second dose of CO had not increased the intensity of the peaks, the phenomenon could have been associated to physical/weak interaction of CO with the surface upon outgassing;
- ii) if the second dose of CO had either increased the intensity or generated new absorption bands, then the absorption could have been related to some surface species specifically formed during CO outgassing and able to bind CO during the second admission.

Figure 6 reports two figures. Figure 6a includes all the spectra acquired at decreasing CO coverage from 50 mbar to about 0.07 mbar (from dark to light red line) when the bands below 2100 cm⁻¹ reach the maximum intensity. All the spectra show the usual peaks at 2162 and 2145 cm⁻¹, which decreased in intensity upon outgassing, while new components below the *crossover* point increased (as already discussed for Figure 4b). Figure 6b includes all the spectra obtained after the second dose of CO on the sample (from 0.07 mbar to 50 mbar) and then slowly outgassed (from red to blue line). When CO pressure increased, the peaks at 2162 and 2145 cm⁻¹ grew up again, but at the same time a component at 2047 cm⁻¹ and

a shoulder at 2027 cm⁻¹ increased. This phenomenon evidenced the adsorption of CO on specific sites which we already attributed to CeZn alloy. Upon a second outgassing, the intensity of the peaks in the higher frequency region (> 2100 cm⁻¹) decreased and Ce³⁺-CO peaks at 2145 and 2129 cm⁻¹ showed up again. As for the absorption bands below 2100 cm⁻¹ new components were observed. Moving from red to blue line, the peak at 2047 cm⁻¹ decreases in intensity, while new bands at 2097, 2066 and 1991 cm⁻¹ started growing, despite ϑ_{CO} was reducing. Indeed, all the peaks reached a maximum at very low ϑ_{CO} and are stable upon dynamic vacuum (last spectra).

These findings are in line with what has been already shown for CO adsorbed on reduced ZnCeZrO_x after reduction in pure H₂ (Figure 4b). Indeed, when fresh CO is introduced the peak at 2047 cm⁻¹ increases as a very sharp band, like all the CO molecules are adsorbed in the same way on very similar sites. When CO is desorbed, upon outgassing, molecules spread over different surface sites. Trying to give an assignment to all the bands observed, the band at 2047 cm⁻¹ could be assigned to linear (Zn)Ce-CO. Upon outgassing, CO molecules could have redistributed on the surface, binding on less defective sites (2097 and 2066 cm⁻¹) and multiple sites, giving rise to bridged carbonyls (1991 cm⁻¹). Then the intensity reduces to very stable peak under dynamic vacuum. As already mentioned, the assignment is based on hypotheses that have not find any confirmation on literature data.

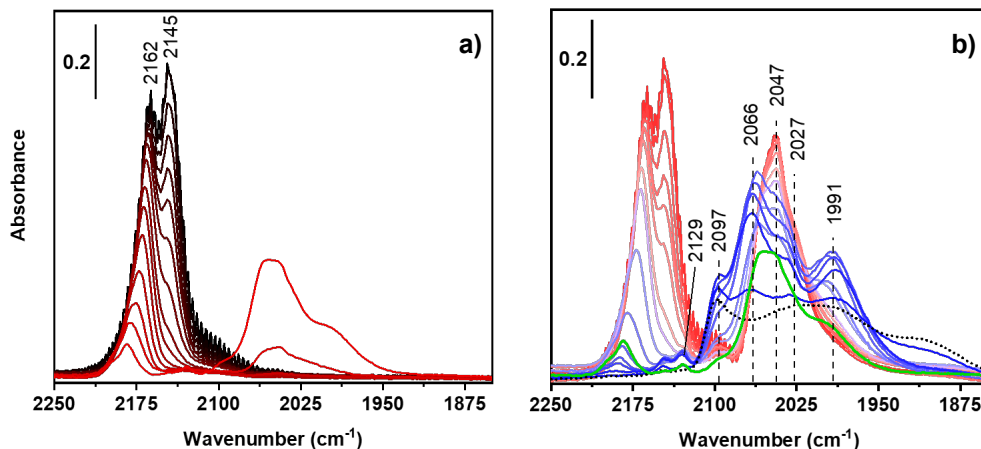


Figure 6 – CO adsorption at LNT on ZnCeZrO_x after activation in pure H_2 at 400°C at: a) decreasing coverage of CO (from dark to light red line) until maximum intensity of the adsorption band below 2100 cm^{-1} ; b) decreasing coverage of CO (from red to blue line), after a second dose of CO (up to 50 mbar). The green curve indicates the last spectrum of panel a), while the black dashed curve is the last spectrum acquired upon outgassing.

iii) *Activation in H_2 at 400°C and CO adsorption at room temperature*

CO adsorption at RT was performed on both oxidized and activated ZnCeZrO_x and reported in Figure 7. Comparing both the figures, except the band at 2129 cm^{-1} (Figure 7b) related to the presence of Ce^{3+} , four bands are in common: 2097, 2066, 2006 and 1984 cm^{-1} . As a matter of fact, these peaks can only be visible on the oxidized sample when the adsorption occurs at RT, because at this temperature CO is able to reduce Ce^{4+} to Ce^{3+} sites. This confirms that they formed upon reduction, in this case induced by CO adsorption at RT on the oxidized ZnCeZrO_x . The only remarkable difference between the absorption bands reported in Figure 7a and Figure 7b lies in their stability upon outgassing in dynamic vacuum. Indeed, all the carbonyls formed on the activated ZnCeZrO_x

are significantly more stable (Figure 7b, red line), while in the oxidized sample all the peaks disappear upon complete outgassing. This could mean that these species are related to reduced species obtained after activation in pure H₂ or by CO reduction on the oxidized sample, but in this last case it is not as reductive as the thermal treatment in H₂, leading to less stable species.

Hence, we reasonably assigned all the above-mentioned spectroscopic features to carbonyls of Ce⁰ sites in a CeZn alloy. Indeed, all these bands are also visible after adsorption at LNT, except those observed in the range between 2050 and 2010 cm⁻¹ (already discussed for Figure 4 and Figure 6), which could be related to less stable species and, thus, not present at room temperature.

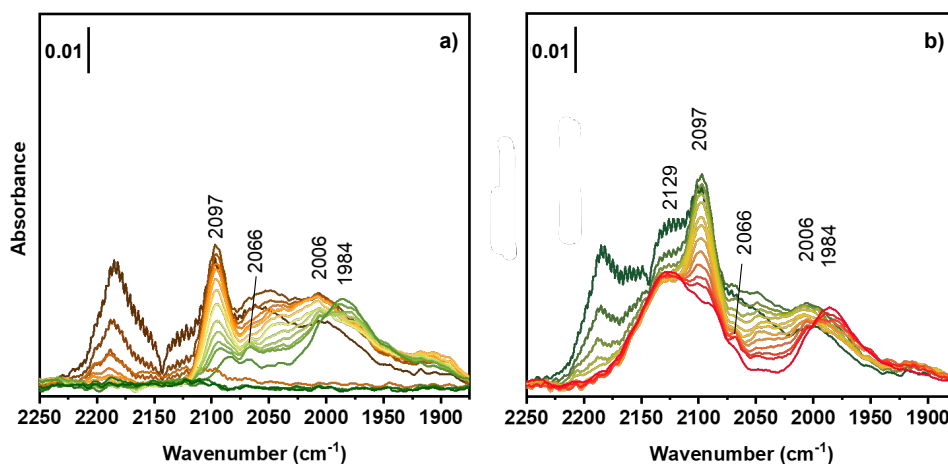


Figure 7 – FTIR spectra at decreasing θ_{CO} at RT on a) oxidized (from brown to green line) and b) activated (from green to red line) ZnCeZrO_x.

5.2.3 *FT-IR: CO₂ adsorption on stand-alone ZnCeZrO_x*

Figure 8 reports FTIR spectra collected after CO₂ adsorption at increasing doses up to 20 mbar. Both the panels (a and b) present common spectroscopic features related to carbonate produced on catalyst surface, in particular bands at 1563, 1414, 1344, 1223, 1058 and 844 cm⁻¹. On the oxidized sample, CO₂ adsorption generates two more evident components at 1635 and 1454 cm⁻¹.

Some bands are so large due to the presence of several components of carbonate families, so that we reported the frequency of the most predominant components. More specifically, basing the assignment to the literature [9,23–30], the bands at 1635 and 1414 cm⁻¹ and the peak at 1223 cm⁻¹ can be assigned to $\nu(\text{C=O})$, $\nu(\text{C-OH})$ and $\delta(\text{COH})$ of bicarbonates species, respectively. Hence, we confidently assigned these bands to bidentate and monodentate carbonates, in particular [31,32]:

- 1563, 1344 and 1058 cm⁻¹ can be assigned to $\nu(\text{C=O})$, $\nu_{\text{asym}}(\text{O-C-O})$ and $\nu_{\text{sym}}(\text{O-C-O})$ mode of bidentate carbonates, respectively;
- 1454 and 1058 cm⁻¹ can be related to $\nu_{\text{asym}}(\text{O-C-O})$ and $\nu(\text{C-O})$ modes of monodentate carbonates, respectively;
- 844 cm⁻¹ can be associated to $\delta(\text{O-C-O})$ as reported by other works.

Considering that ZnO, CeO₂ and ZrO₂ can all adsorb CO₂ to generate carbonates, it cannot be excluded that all the cations (e.g. Zr⁴⁺, Zr³⁺, Ce⁴⁺, Ce³⁺ and Zn²⁺) can synergically contribute to carbonates formation on both oxidized and activated

catalyst. Figure 8b exhibited a lack of two components at 1635 and 1454 cm⁻¹. As just mentioned, the first one is related to bicarbonate species, furtherly confirmed by the presence of two more absorption bands at 1414 and 1223 cm⁻¹, suggesting that the bands at 1635 and 1454 cm⁻¹ are covered by the bands related to bidentate carbonates. Indeed, the reduced sample shows a higher contribution of bidentate and less monodentate than the oxidized sample.

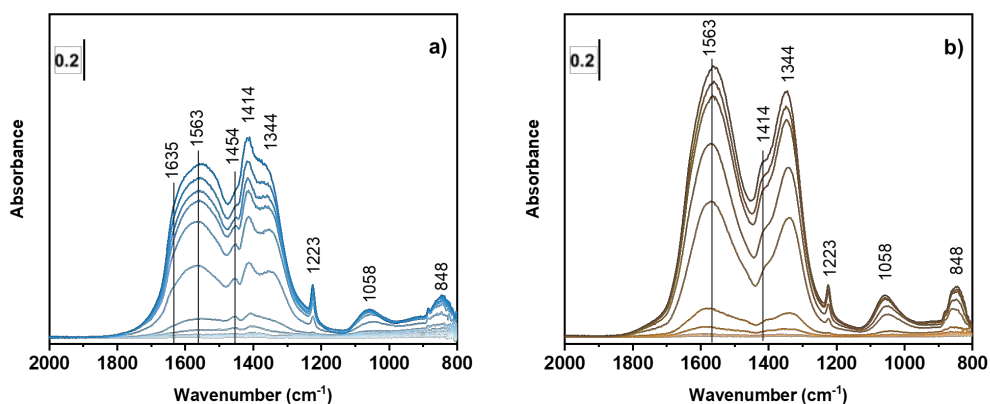


Figure 8 – CO₂ adsorption (from lighter to darker colors) at room temperature on a) oxidized and b) activated ZnCeZrO_x.

5.2.4 FT-IR: CO adsorption at LNT on RUB-13

CO adsorption on RUB-13 highlighted the presence of typical components of zeolites/zeotype featured by peaks at 2155 cm⁻¹, 2140 cm⁻¹ and 2134 cm⁻¹.

The highest component in frequency is ascribable to CO adsorbed on Brønsted acid sites (OH-CO), while the last two are related to CO entrapped in the pores of

RUB-13. Both the frequencies could be associated to CO entrapped in two different pore channels [33–35].

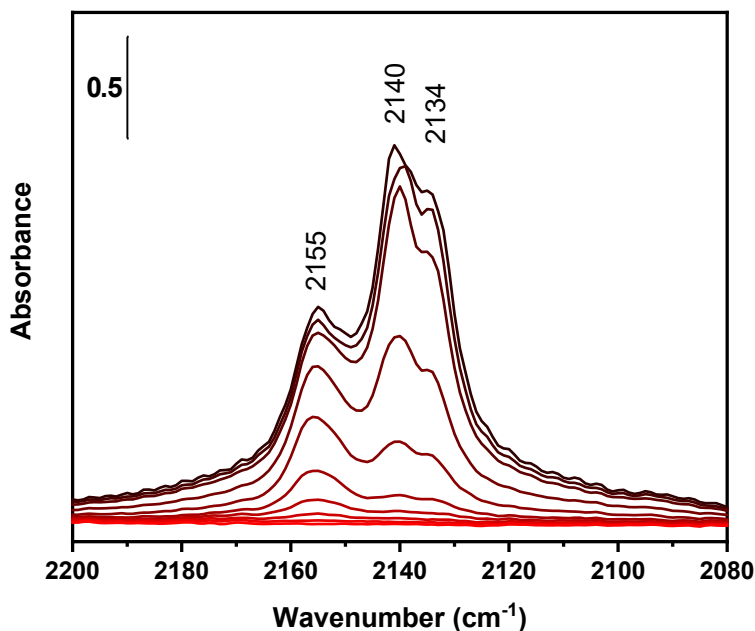


Figure 9 – CO adsorption at LNT on activated RUB-13 at 400 °C in pure H₂. CO coverage from light to dark red line.

5.2.5 XAS: Ce K-edge on stand-alone ZnCeZrO_x

XAS measurements were performed by Dr. Davide Salusso at ESRF (BM31 beamline) synchrotron. Differently from what has been discussed for the other systems, described in the previous chapters, the following section only deals with the stand-alone ZnCeZrO_x.

Figure 10a and b illustrate XANES spectra acquired at both Zn and Ce K-edge, respectively, at different temperature from RT to 400 °C in H₂. The as-prepared

catalyst has a ZnO-like and CeO₂-like environment, suggesting that both the metals present their higher oxidation state. Upon temperature increase, at Zn K-edge, the white-line reduced its intensity and slightly shifted to lower energy. The intensity reduction could be related to an increase of the ZnO particle size, also due to the segregation of a h-ZnO as shown by PXRD results, while the shift could be linked to a partial reduction of zinc, from Zn²⁺ to Zn^{δ+} (0 < δ < 2) (Figure 10a, inset).

As for Ce, a shift to lower frequency, to almost match a Ce(NO₃)₃ reference spectrum, suggests a reduction to Ce³⁺. This is highlighted by the inset reported in Figure 10a, but a little shoulder at lower energy than the one related to the maximum of Ce(NO₃)₃ reference first derivative spectrum suggests that there are some cerium sites with an oxidation state lower than 3+.

A further analysis involving a Principal Component Analysis (PCA) and Multivariate Curve Resolution – Alternating Least Squares (MCR-ALS), which protocol has been described in Dr. Salusso's PhD thesis [36], allowed to extract three components reported in Figure 10c. The red and green spectra resembled CeO₂ and Ce(NO₃)₃ reference spectra, thus Ce⁴⁺ and Ce³⁺ states. The blue spectrum was assigned to Ce^{δ+}. Unfortunately, due to the lack of a Ce⁰ foil reference, it was not possible to give a clear association to δ+ state.

Moreover, from the further analyses it was possible to determine a concentration profile for all three components, illustrated in Figure 10d. The figure highlights that at about 300 °C, Ce⁴⁺ concentration started to significantly decrease, and

beyond 320 °C both Ce^{3+} and $\text{Ce}^{\delta+}$ became more abundant. In particular, $\text{Ce}^{\delta+}$ is the dominant species at $T > 350$ °C.

Since a partial reduction of Zn was observed in concomitance with Ce reduction, we hypothesize the formation of a CeZn alloy, of undefined composition.

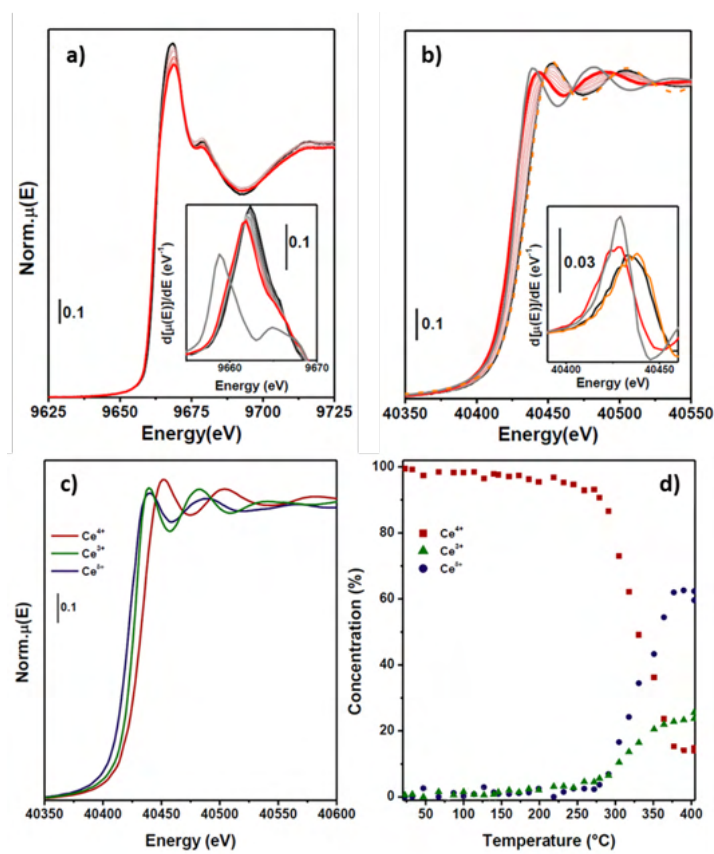


Figure 10 – a) Zn and b) Ce K-edges spectra collected at increasing temperature, from black to red line. Inset: XANES first derivative. Zn⁰ foil and Ce(NO₃)₃ reference spectra are reported with a grey line, while CeO₂ reference is reported with an orange line, respectively. c) Spectra principal component obtained from PCA and d) profile evolution obtained by Multivariate Curve Resolution – Alternating Least Squares (MCR-ALS).

5.3 Catalytic tests

Very preliminary catalytic results related to a different ZnCeZrO_x + H-RUB-13 bifunctional catalysts were reported by Wang et al. [37], from ICC, but performed on differently-synthesized materials. Unfortunately, no significant results related to COZMOS project have been published on this system, because of its C₃ productivity mismatch to the targets of the project itself. Hence, the catalyst characterized and discussed in this work was put aside and the attention was focused on a different system.

As reported by Wang and co-workers [37], at 350 °C, 1.0 MPa and 3:1 H₂/CO₂ ratio, CO₂ conversion was around 10%, CO selectivity around 30%, but almost 35% of selectivity for C₂⁻-C₄⁻. At 350 °C, 3.5 MPa and 3:1 H₂/CO₂ the catalyst reached 72.7% for C₂⁻-C₄⁻ selectivity, with a CO selectivity of 26.5% and around 30% of CO₂ conversion. Among the olefins, propene and butene accounted for ca. 90%.

However, the C₃ total productivity obtained was not suitable for COZMOS goals, hence this catalyst was excluded and no longer furtherly studied in the project.

REFERENCES

- [1] Ü. Özgür, Y.I. Alivov, C. Liu, A. Teke, M.A. Reshchikov, S. Doğan, V. Avrutin, S.J. Cho, H. Morkoç, A comprehensive review of ZnO materials and devices, *J. Appl. Phys.* 98 (2005) 1–103.
<https://doi.org/10.1063/1.1992666>.
- [2] W. Göpel, U. Lampe, Influence of defects on the electronic structure of zinc oxide surfaces, *Phys. Rev. B.* 22 (1980) 6447–6462.
<https://doi.org/10.1103/PhysRevB.22.6447>.
- [3] E. Kusmierek, A CeO₂ Semiconductor as a Photocatalytic and Photoelectrocatalytic Material for the Remediation of Pollutants in Industrial Wastewater: A Review, *Catal.* 2020, Vol. 10, Page 1435. 10 (2020) 1435. <https://doi.org/10.3390/CATAL10121435>.
- [4] G. Ghiotti, A. Chiorino, F. Prinetto, Chemical and electronic characterization of pure SnO₂ and Cr-doped SnO₂ pellets through their different response to NO, *Sensors Actuators B. Chem.* 25 (1995) 564–567. [https://doi.org/10.1016/0925-4005\(95\)85123-2](https://doi.org/10.1016/0925-4005(95)85123-2).
- [5] S. Morandi, M.C. Paganini, E. Giamello, M. Bini, D. Capsoni, V. Massarotti, G. Ghiotti, Structural and spectroscopic characterization of Mo_{1-x}W_xO_{3-δ} mixed oxides, *J. Solid State Chem.* 182 (2009) 3342–3352. <https://doi.org/10.1016/j.jssc.2009.09.025>.

- [6] L. Genzel, T.P. Martin, Infrared absorption by surface phonons and surface plasmons in small crystals, *Surf. Sci.* 34 (1973) 33–49. [https://doi.org/10.1016/0039-6028\(73\)90185-4](https://doi.org/10.1016/0039-6028(73)90185-4).
- [7] F. Bozon-Verduraz, A. Bensalem, IR studies of cerium dioxide: Influence of impurities and defects, *J. Chem. Soc. Faraday Trans.* 90 (1994) 653–657. <https://doi.org/10.1039/FT9949000653>.
- [8] C. Binet, A. Badri, J.C. Lavalley, A spectroscopic characterization of the reduction of ceria from electronic transitions of intrinsic point defects, *J. Phys. Chem.* 98 (1994) 6392–6398. <https://doi.org/10.1021/j100076a025>.
- [9] P. Ticali, D. Salusso, R. Ahmad, C. Ahoba-Sam, A. Ramirez, G. Shterk, K.A. Lomachenko, E. Borfecchia, S. Morandi, L. Cavallo, J. Gascon, S. Bordiga, U. Olsbye, CO₂ hydrogenation to methanol and hydrocarbons over bifunctional Zn-doped ZrO₂/zeolite catalysts, *Catal. Sci. Technol.* 11 (2021) 1249–1268. <https://doi.org/10.1039/D0CY01550D>.
- [10] A. Ramirez, P. Ticali, D. Salusso, T. Cordero-Lanzac, S. Ould-Chikh, C. Ahoba-Sam, A.L. Bugaev, E. Borfecchia, S. Morandi, M. Signorile, S. Bordiga, J. Gascon, U. Olsbye, Multifunctional Catalyst Combination for the Direct Conversion of CO₂ to Propane, *JACS Au.* 1 (2021) 1719–1732. <https://doi.org/10.1021/jacsau.1c00302>.
- [11] C. Morterra, G. Cerrato, L. Ferroni, A. Negro, L. Montanaro, *Surface*

- characterization of tetragonal ZrO₂, *Appl. Surf. Sci.* 65–66 (1993) 257–264. [https://doi.org/10.1016/0169-4332\(93\)90668-2](https://doi.org/10.1016/0169-4332(93)90668-2).
- [12] C. Binet, M. Daturi, J.C. Lavalley, IR study of polycrystalline ceria properties in oxidised and reduced states, *Catal. Today.* 50 (1999) 207–225. [https://doi.org/10.1016/S0920-5861\(98\)00504-5](https://doi.org/10.1016/S0920-5861(98)00504-5).
- [13] T. Tabakova, F. Boccuzzi, M. Manzoli, D. Andreeva, FTIR study of low-temperature water-gas shift reaction on gold/ceria catalyst, *Appl. Catal. A Gen.* 252 (2003) 385–397. [https://doi.org/10.1016/S0926-860X\(03\)00493-9](https://doi.org/10.1016/S0926-860X(03)00493-9).
- [14] K.I. Hadjiivanov, G.N. Vayssilov, Characterization of oxide surfaces and zeolites by carbon monoxide as an IR probe molecule, *Adv. Catal.* 47 (2002) 307–511. [https://doi.org/10.1016/S0360-0564\(02\)47008-3](https://doi.org/10.1016/S0360-0564(02)47008-3).
- [15] K.H.J. Buschow, Rare earth compounds, *Handb. Ferromagn. Mater.* 1 (1980) 297–414. [https://doi.org/10.1016/S1574-9304\(05\)80119-1](https://doi.org/10.1016/S1574-9304(05)80119-1).
- [16] E. Veleckis, C.L. Rosen, H.M. Feder, A recording effusion balance for phase diagram investigations: U-Cd, U-Zn and Ce-Zn systems, *J. Phys. Chem.* 65 (1961) 2127–2131. <https://doi.org/10.1021/j100829a004>.
- [17] C.P. Wang, X. Chen, X.J. Liu, F.S. Pan, K. Ishida, Thermodynamic modeling of the Ce-Zn and Pr-Zn systems, *J. Alloys Compd.* 458 (2008) 166–173. <https://doi.org/10.1016/j.jallcom.2007.03.120>.

- [18] M. Aljarrah, J. Alnahas, M. Alhartomi, Thermodynamic Modeling and Mechanical Properties of Mg-Zn-{Y, Ce} Alloys: Review, *Crystals*. 11 (2021). <https://doi.org/10.3390/cryst11121592>.
- [19] G. Bruzzone, M.L. Fornasini, F. Merlo, Rare-earth intermediate phases with zinc, *J. Less-Common Met.* 22 (1970) 253–264. [https://doi.org/10.1016/0022-5088\(70\)90074-3](https://doi.org/10.1016/0022-5088(70)90074-3).
- [20] O. Zelinska, M. Conrad, B. Harbrecht, Refinement of the crystal structure of cerium zinc (1:11), CeZn₁₁, *Zeitschrift Fur Krist. - New Cryst. Struct.* 219 (2004) 389–390. <https://doi.org/10.1524/ncrs.2004.219.14.389>.
- [21] B.G. Lott, P. Chiotti, Crystallographic data for cerium–zinc compounds, *Acta Crystallogr.* 20 (1966) 733–738. <https://doi.org/10.1107/s0365110x66001774>.
- [22] A.I. Serykh, Y.A. Agafonov, On the nature of active sites in alumina-supported zinc propane dehydrogenation catalysts, *Mol. Catal.* 493 (2020) 111055. <https://doi.org/https://doi.org/10.1016/j.mcat.2020.111055>.
- [23] J. Saussey, J.-C. Lavalley, C. Bovet, Infrared study of CO₂ adsorption on ZnO. Adsorption sites, *J. Chem. Soc. Faraday Trans. 1 Phys. Chem. Condens. Phases.* 78 (1982) 1457. <https://doi.org/10.1039/f19827801457>.
- [24] C. Li, Y. Sakata, T. Arai, K. Domen, K. Maruya, Adsorption of Carbon Monoxide and Carbon Dioxide on Cerium Oxide studied by Fourier-

- transform Infrared Spectroscopy, *J. Chem. Soc., Faraday Trans.* 85 (1989) 1451–1461.
- [25] G. Busca, V. Lorenzelli, *Materials Chemistry* 7 (1982) 89–126
INFRARED SPECTROSCOPIC IDENTIFICATION OF SPECIES
ARISING FROM REACTIVE ADSORPTION OF CARBON OXIDES
ON METAL OXIDE SURFACES G BUSCA, V LORENZELLI, *Mater.*
Chem. 7 (1982) 89–126.
- [26] J.C. Lavalley, Infrared spectrometric studies of the surface basicity of metal oxides and zeolites using adsorbed probe molecules, *Catal. Today.* 27 (1996) 377–401.
- [27] E.-M. Köck, M. Kogler, T. Bielz, B. Klötzer, S. Penner, In Situ FT-IR Spectroscopic Study of CO(2) and CO Adsorption on Y(2)O(3), ZrO(2), and Ytria-Stabilized ZrO(2), *J. Phys. Chem. C. Nanomater. Interfaces.* 117 (2013) 17666–17673. <https://doi.org/10.1021/jp405625x>.
- [28] K. Pokrovski, K.T. Jung, A.T. Bell, Investigation of CO and CO₂ Adsorption on Tetragonal and Monoclinic Zirconia, (2001) 4297–4303.
- [29] T. Akune, Y. Morita, S. Shirakawa, K. Katagiri, K. Inumaru, ZrO₂ Nanocrystals As Catalyst for Synthesis of Dimethylcarbonate from Methanol and Carbon Dioxide: Catalytic Activity and Elucidation of Active Sites, *Langmuir.* 34 (2018) 23–29.

<https://doi.org/10.1021/acs.langmuir.7b01294>.

- [30] B. Bachiller-Baeza, I. Rodriguez-Ramos, A. Guerrero-Ruiz, Interaction of carbon dioxide with the surface of zirconia polymorphs, *Langmuir*. 14 (1998) 3556–3564. <https://doi.org/10.1021/la970856q>.
- [31] H.J. Freund, M.W. Robert, Surface chemistry of carbon dioxide, *Surf. Sci. Rep.* 25 (1996) 225–273.
- [32] G. Ramis, G. Busca, V. Lorenzelli, Low-temperature CO₂ adsorption on metal oxides: spectroscopic characterization of some weakly adsorbed species, *Mater. Chem. Phys.* 29 (1991) 425–435.
[https://doi.org/10.1016/0254-0584\(91\)90037-U](https://doi.org/10.1016/0254-0584(91)90037-U).
- [33] S. Bordiga, D. Scarano, G. Spoto, A. Zecchina, C. Lamberti, C. Otero Areán, Infrared study of carbon monoxide adsorption at 77 K on faujasites and ZSM-5 zeolites, *Vib. Spectrosc.* 5 (1993) 69–74.
[https://doi.org/10.1016/0924-2031\(93\)87056-Y](https://doi.org/10.1016/0924-2031(93)87056-Y).
- [34] S. Bordiga, E. Escalona Platero, C. Otero Areán, C. Lamberti, A. Zecchina, Low temperature CO adsorption on Na-ZSM-5 zeolites: An FTIR investigation, *J. Catal.* 137 (1992) 179–185.
[https://doi.org/10.1016/0021-9517\(92\)90147-A](https://doi.org/10.1016/0021-9517(92)90147-A).
- [35] K. Hadjiivanov, A. Penkova, M.A. Centeno, FTIR indication of CO interaction with O₂⁻ ions: A new adsorption form in the gap between

chemi- and physisorbed CO, *Catal. Commun.* 8 (2007) 1715–1718.

<https://doi.org/10.1016/J.CATCOM.2007.02.002>.

[36] D. Salusso, ZrO₂/CeO₂-based catalysts: understanding their structural and chemical role towards CO₂ valorisation reactions, University of Turin, 2022.

[37] S. Wang, L. Zhang, W. Zhang, P. Wang, Z. Qin, W. Yan, Selective conversion of CO₂ into propene and butene, (n.d.) 1–38.

CHAPTER VI

GaZrO_x: from lab to technical scale

6.1 Lab scale: structural characterization

The following section is based on data elaboration and analysis performed by Dr. Davide Salusso.

The structural characterization was carried out comparing GaZrO_x with a pure ZrO₂ reference (Figure 1a), composed almost completely by a tetragonal phase. GaZrO_x pattern (Figure 1b) shows the presence of the same peaks reported for the ZrO₂ reference, suggesting that the lattice is stabilized in the tetragonal phase. Indeed, no reflections of monoclinic ZrO₂ can be observed, which are indicated only in Figure 1a by three arrows.

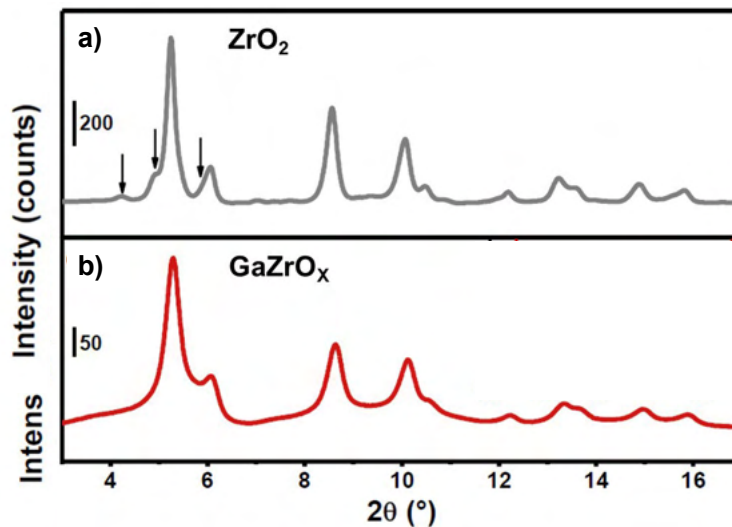


Figure 1 – PXRD pattern of a) ZrO₂ (arrows: monoclinic reflections), and b) GaZrO_x.

6.2 Lab scale: spectroscopic characterization of stand-alone

GaZrO_x

According to the catalytic tests performed on this material by ICC group (partner of COZMOS project) [1] and reported in paragraph 6.3, gallium seems to play a key role in enhancing CO₂ adsorption and hydrogenation. In order to study Ga active sites, the following first section focuses on FT-IR measurements performed on GaZrO_x and a reference of β-Ga₂O₃ at both liquid nitrogen and room temperature, after reduction/activation in pure H₂ at 400 °C. In particular, H₂ and CO adsorption was performed at both liquid nitrogen and room temperature, whereas CO₂ adsorption was performed at room temperature in order to study the carbonate formation. Differently from the other samples, GaZrO_x did not show any semiconductive properties, thus for the sake of clarity I will not discuss those results. However, GaZrO_x showed the formation of hydrides.

The last section illustrates XAS measurements regarding Ga K-edge in order to complete the structural information related to this sample. All XAS data were acquired and elaborated by Dr. Davide Salusso.

6.2.1 FT-IR: CO adsorption

In order to investigate the surface properties of GaZrO_x responsible for the catalytic activity, CO adsorption (up to 20 mbar) was carried out on both GaZrO_x and Ga₂O₃, being this last used as a reference. To have a complete overview of all

Lewis acid sites, i.e. gallium and zirconium sites, CO adsorption was performed at liquid-nitrogen temperature (LNT) first and then at room temperature (RT) to evaluate the most stable species.

Figure 2 reports CO adsorption at LNT on both reduced/activated samples. All the spectra show a very wide band in the range from 2220 to 2080 cm^{-1} . Focusing on Figure 2a, i.e. Ga_2O_3 , four main components can be identified (from higher to lower frequency): 2185, 2170, 2150 and 2137 cm^{-1} .

According to several authors [4–7], absorption bands in the range between 2200 and 2160 cm^{-1} are ascribed to Ga^{3+} ions, in particular to tetrahedral Ga sites ($\text{Ga}_{\text{Td}}^{3+}$). In this region, it is possible to identify two main bands. The first one shifts from 2200 to 2185 cm^{-1} upon CO adsorption and it is clearly visible at very low CO coverage (θ_{CO}). Whereas the second absorption is centered at 2170 cm^{-1} and it is only visible at very high CO doses. This behavior suggests a higher stability and a stronger interaction with CO for the first component.

Focusing on the highest frequency peak of Ga_2O_3 spectra, its continuous shift towards lower frequencies (red shift) upon increasing θ_{CO} can be related to the “chemical effect” [8–10]. As already mentioned in the previous chapters, when CO binds ionic surface sites, such as Ga^{3+} ions, the electron density flows from CO molecule to the surface. However, the electron donation from σ -acceptor sites to CO becomes smaller and smaller upon increasing CO pressure, so that the higher the CO coverage the lower the CO stretching observed. This behavior is observable for several oxidic material, like ZrO_2 [8,11].

On the other side, the same phenomenon cannot be observed for the second component at 2170 cm^{-1} . In the light of these features, we agree with some authors [12,13] to assign the highest frequency band to coordinatively unsaturated tetrahedral Ga^{3+} carbonyls (*cus*- $\text{Ga}_{\text{Td}}^{3+}$ -CO), while the component at 2170 cm^{-1} can be ascribed to tetrahedral Ga^{3+} sites with higher coordination.

Moving to lower frequencies, the assignment of all the peaks is not straightforward. In fact, the peak at 2150 cm^{-1} can result as a combination of CO adsorption on hydroxyls groups and octahedral Ga^{3+} sites ($\text{Ga}_{\text{Oh}}^{3+}$) [12–14].

Another confirmation of the dislocation of some lattice oxygen ions induced by the reduction/activation and following coordination change of gallium atoms in Ga_2O_3 comes from the peak at 2137 cm^{-1} . According to some authors [7], this peak could be assigned to Ga^+ -CO.

As for GaZrO_x , CO adsorption gives rise to the same main components, but there are some variations in comparison to the adsorption on pure gallia. Future analyses, regarding XAS data elaboration, will deal with the determination if GaZrO_x is a solid solution or just mixed oxides, but in both cases CO adsorption on Zr sites cannot be excluded at liquid-nitrogen temperature [8,15,16]. In fact, the band at 2200 cm^{-1} can be ascribed to both *cus*- Ga^{3+} and *cus*- Zr^{4+} carbonyls, which are characterized by a red-shift to $2185\text{-}2170\text{ cm}^{-1}$ at higher θ_{CO} .

Furthermore, the peak at 2150 cm^{-1} cannot be only ascribed to octahedral Ga^{3+} sites, because of the strong contribution of Zr^{4+} -CO in this range [8,15,16].

Finally, the component at 2137 cm⁻¹ it is not well distinguishable as shown on pure gallia (Figure 2a), so that it is plausible that gallium(I) sites (Ga⁺) are under the instrumental limit of detection or the formation of Ga⁺ is hindered and not observed due to a stabilization of gallium in a +3 oxidation state in GaZrO_x solid solution.

In order to confirm the assignment of all the above-mentioned bands, FT-IR measurements were repeated at room temperature. Figure 2 displays CO adsorption spectra for both Ga₂O₃ and GaZrO_x at RT.

As shown in Figure 2b, CO can only adsorb on *cus*-Ga_{Td}³⁺ sites on GaZrO_x surface. Indeed, as already mentioned in the previous chapters, ZrO₂ is not capable of adsorbing CO at RT (see, for instance, CO adsorption at RT on PdZn/ZrO₂), thus all the species observed at RT after CO adsorption could only be ascribed to gallium sites.

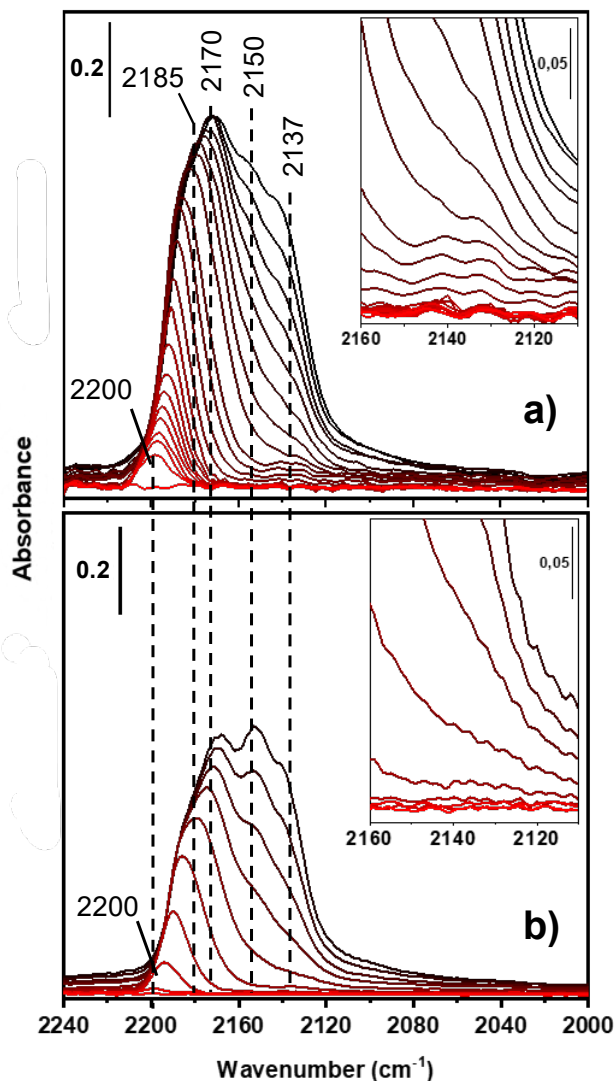


Figure 2 – CO adsorption on reduced/activated (a) Ga₂O₃ (b) GaZrO_x at liquid nitrogen temperature.

Differently from what has been described for Figure 2a, reduced gallium oxide reference does not show any CO molecule adsorbed at room temperature on the surface and it could be related to the unavailability of Ga sites to coordinate CO. A possible reason can be the presence of surface hydrides that hinder CO

adsorption at room temperature (*vide infra*). In the light of this hypothesis, CO adsorption at liquid-nitrogen temperature allowed also to observe less-stable sites which were probably not bound to hydrides. These “hydride-free” sites could be not catalytically active, since not involved in hydrogen splitting. This assumption would confirm why CO can only be adsorbed on gallia surface at LNT. Hydrides formation has been already observed and documented on several gallium-based materials [7,17–19] and it has also been observed on the same gallia sample dealt with in this work, after activation in pure H₂ (*vide infra*).

Differently from Ga₂O₃, CO adsorption at room temperature on GaZrO_x gives rise to adsorbed species. The inclusion of gallium inside the ZrO₂ lattice could create more defects on the surface, hence more sites prone to bind CO. In the light of the above-mentioned hypothesis related to absence of Ga-carbonyls on activated Ga₂O₃, it is feasible that the hydrides species are also present on activated GaZrO_x, but this catalyst might be featured by the presence of more Ga sites with less stable hydrides covering the surface and available for CO adsorption.

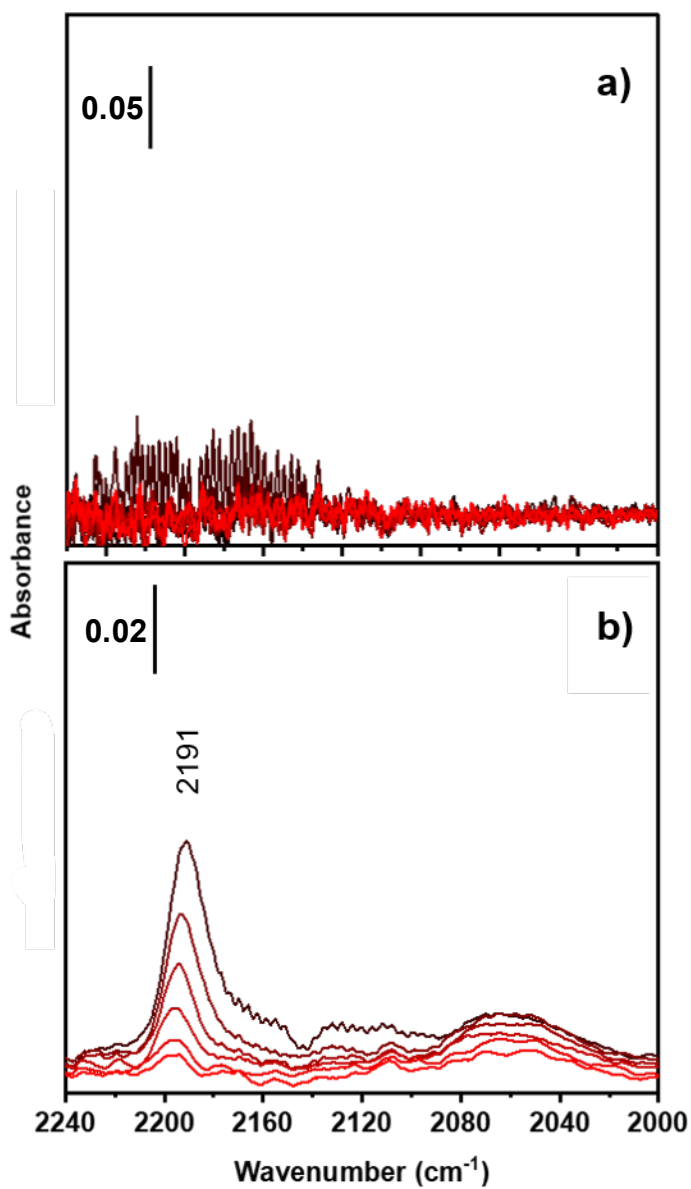


Figure 3 – CO adsorption on reduced/activated (a) Ga₂O₃ and (b) GaZrO_x at room temperature.

6.2.2 FT-IR: H₂ adsorption

CO₂ hydrogenation is strictly connected to the capability of a catalyst to adsorb and split H₂ in order to induce the reduction of CO₂ to methanol. By means of FT-IR spectroscopy it is possible to follow the adsorption of H₂ and its splitting to produce hydride species.

According to the literature [17,19,20], Ga₂O₃ can adsorb hydrogen as gallium hydrides. In particular, gallium hydrides lie in the region between 2010 and 1980 cm⁻¹ [17,19]. In order to have a reference sample to compare, FT-IR measurements were carried out on both GaZrO_x and β-Ga₂O₃.

Figure 4 reports two spectra related to the Ga₂O₃ reference and GaZrO_x sample at RT in 40 mbar H₂ atmosphere. The absorption band centered at about 2000 cm⁻¹ is related to gallium hydrides (Ga-H). Before describing the spectra, it is worth to point out that all the observed hydrides species are obtained after activation at 400 °C in pure H₂. The infrared measurements were performed both in H₂ atmosphere at RT and after outgassing at 400 °C and cooling at RT: in order to show intense peaks with a good signal-to-noise ratio, only the spectra acquired in H₂ atmosphere at RT are reported in Figure 4.

These species are also likely formed on Ga_{Td}³⁺ sites which strongly interact with hydrogen, leading to the unavailability to bind CO at RT, as already mentioned. On the other hand, less-interacting gallium sites with hydrogen are free to bind CO.

The explanation about the origin of this band can rely upon the same explanation given for CO adsorption. In particular, as described by Collins et al. [17] two main regions can be identified. The highest in frequency, $\geq 2000 \text{ cm}^{-1}$, can be attributed to $\text{Ga}_{\text{Td}}\text{-H}$ stretching. In analogy to CO adsorption, it is ascribable to coordinatively unsaturated tetrahedral Ga^{3+} sites (*cus*- $\text{Ga}_{\text{Td}}^{3+}$), whereas a component centered at 2000 cm^{-1} is related to non-coordinatively unsaturated ones ($\text{Ga}_{\text{Td}}^{3+}$). The region below 2000 cm^{-1} can be related to $\text{GaOH}^{3+}\text{-H}$ stretching mode.

According to the literature [17–19], by means of X-ray photoelectron spectroscopy, the authors determined that the observed hydrides species can be ascribed to $\text{Ga}^{\delta+}\text{-H}$ species (with $\delta < 2$). On that basis, they postulated that hydrogen is dissociatively chemisorbed over the gallium oxide surface.

In line with these findings on the Ga_2O_3 , a similar assignment was given to GaZrO_x hydrides (Figure 4, black line). The spectra reported in Figure 4 are normalized on pellet weight, but the lower intensity of the absorption band can be ascribed to Ga concentration. Indeed, GaZrO_x has Ga/Zr ratio equals to 0.5, hence Ga quantity is lower than pure gallium oxide.

The similarity in hydrides formation between Ga_2O_3 and GaZrO_x highlights that there is significant variation on the surface of both the oxides, hence it is likely that Ga sites in GaZrO_x are very similar to the one observed on pure gallia.

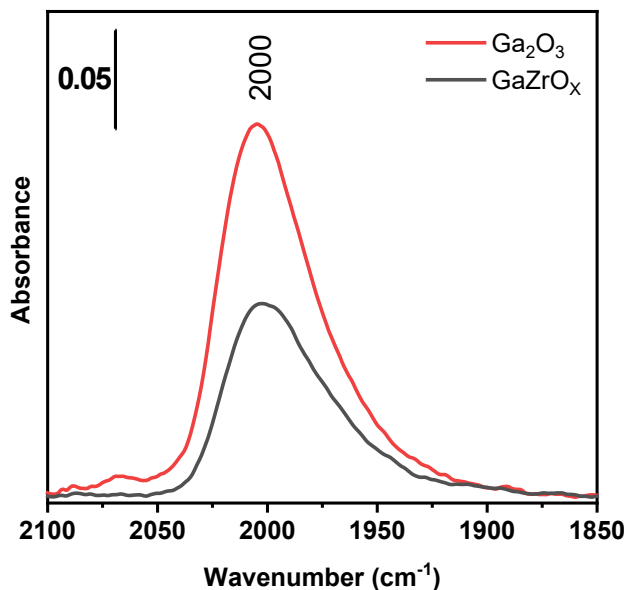


Figure 4 – Comparison of FT-IR spectra of Ga₂O₃ and GaZrO_x in H₂ atmosphere (40 mbar) acquired at RT.

6.2.3 FT-IR: CO₂ adsorption

FT-IR measurements were also performed after CO₂ adsorption. As already done in the previous section, CO₂ adsorption was carried out on both GaZrO_x and Ga₂O₃. Figure 5 shows the spectra obtained after an admission of 20 mbar of CO₂. CO₂ adsorption on Ga₂O₃ leads to bicarbonate (HCO₃⁻) species identified by IR frequency at 1628, 1426 and 1225 cm⁻¹ as reported in Figure 5. The presence of bicarbonates suggests the existence of remaining OH species on the surface. Besides the HCO₃⁻ species, all the other components reported in Figure 5 are related to different carbonate species, as follows [21–23]:

- 1802 and 1728 cm^{-1} modes are related to $\nu(\text{C}=\text{O})$ of bridged “organic-like” carbonates (which is typically accompanied by $\nu_{\text{asym}}(\text{O}-\text{C}-\text{O})$ that is not observable);
- 1588 and 1339 cm^{-1} modes are related to $\nu(\text{C}=\text{O})$ and $\nu_{\text{asym}}(\text{O}-\text{C}-\text{O})$ of bidentate carbonates, respectively;
- 1450 cm^{-1} is ascribable to $\nu_{\text{asym}}(\text{CO}_3)$ of highly-symmetric carbonates, interacting with all three O atoms;
- the modes in the range 1070-1000 cm^{-1} are assigned to $\nu_{\text{sym}}(\text{O}-\text{C}-\text{O})$ of bidentate carbonates and $\nu(\text{C}-\text{O})$ of monodentate carbonates, respectively.

In contrast, CO_2 adsorption on GaZrO_x leads to the same species observed on the gallia reference, but with different intensities (Figure 5). According to the elemental analysis of the GaZrO_x , Ga/Zr ratio is equal to 0.5, so less gallium is present in this sample than Ga_2O_3 , but ZrO_2 is well known to bind CO_2 [24] and it could contribute to CO_2 adsorption. Hence, it is likely that GaZrO_x exhibits a lower basicity than Ga_2O_3 [25]. The lower basic properties of the solid solution surface can be related to the presence of zirconium. However, considering the huge similarity of both spectra reported in Figure 5, we assumed CO_2 is predominant on Ga sites, but the basicity of the sites is surely influenced by the presence of zirconium oxide. Upon activation, surface OH groups can be lost due to either the treatment or the coordinative variation of Ga to Ga_{Td} . According to Lavalley et al.[25], who compared three gallium oxide polymorphs, the highest

basicity was observed on the samples with lower amount of tetrahedral gallium sites. Tetrahedral coordination is induced by a stronger polarization of the anions due to Ga³⁺, leading to larger covalent properties of the Ga-O bond [26]. In the light of this hypothesis, it is feasible that gallium is stabilized inside the ZrO₂ lattice in a +3 oxidation state, with tetrahedral coordination, inducing less basicity to the sample and less CO₂ adsorption.

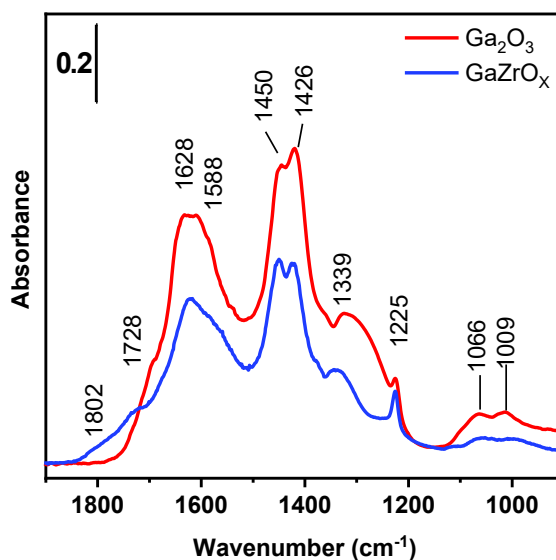


Figure 5 – FT-IR spectra of CO₂ adsorbed (20 mbar) on activated Ga₂O₃ and GaZrO_x.

6.2.4 XAS: Ga K-edge

Ga K-edge XANES spectra were acquired at both room temperature (RT) and 400 °C in H₂. Figure 6 illustrates the results and highlights the presence of two coordinations: tetrahedral and octahedral.

In both XANES spectra at RT and 400 °C, the broad white-line was elaborated using a fit procedure, employing the available literature [2,3] to determine that the majority of gallium atoms already has a tetrahedral coordination in the as-prepared catalyst. However, at the expense of the octahedral coordination, Ga_{Td} abundance further increases upon reduction and this could be translated into an intensity loss and energy shift of the white-line.

At the moment, the results shown are preliminary and they will need further investigation and data analysis.

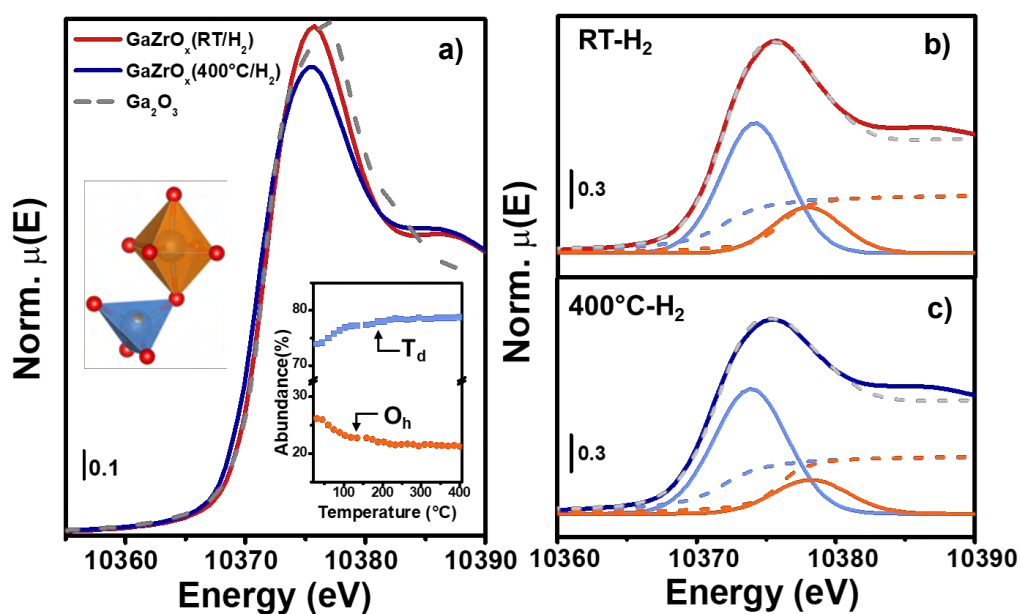


Figure 6 – a) Ga K-edge XANES spectra at RT (red line) and 400°C (blue line) under H_2 , and a reference of Ga_2O_3 (dark grey line). Inset: abundance evolution of Ga_{Td} (light blue) and Ga_{Oh} (orange) during activation in H_2 . b) experimental (solid red and dark blue line) and best fit (dashed light grey line) Ga K-edge XANES acquired at b) RT and c) 400°C.

6.3 Lab scale: catalytic tests

All the tests regarding the GaZrO_x + H-SSZ-13 were performed by Wang et al. [1] comparing several GaZrO_x with different Ga/Zr ratios with H-SSZ-13 at different Si/Al ratios. Catalytic results performed at 350°C, H₂/CO₂ equals to 3, 3.0 MPa and 2400 mL g⁻¹ h⁻¹ are summarized in Figure 7 that reports CO₂ conversion performances over GaZrO_x catalysts and same SSZ-13 (Si/Al=6, namely H-SSZ-13(6.0)), and the best GaZrO_x catalyst (Ga/Zr=0.5, namely, GaZrO_x (0.5)) with several SSZ-13 zeolites.

According to the work, bare ZrO₂ combined with H-SSZ-13 leads to propane selectivity of about 73.6% (with overall LPG – propane + butane – selectivity of 81.3% considering all the hydrocarbons and oxygenates), CO selectivity of 19.5% and CO₂ conversion of 5.3%. When Ga/Zr is 0.5 and GaZrO_x is combined with H-SSZ-13, the results show a propane selectivity in hydrocarbon of 79.5% (9.9% for butane, leading to almost 90% selectivity for LPG), CO selectivity of 31.8% and CO₂ conversion of 43.4%. The catalyst is stable up to 500 h.

The choice of using an SSZ-13 zeolite with Si/Al ratio (SAR) equal to 6 is not a coincidence. The study was performed using a wide batch of sample with different Si/Al ratio and keeping Ga/Zr ratio equals to 0.5. By increasing the Al content and moving from SAR=22 to SAR=6, after optimization of catalyst preparation and reaction conditions, the selectivity towards propane increased from 75.8% to 79.5% and LPG selectivity from 87.6% to 89.4%. However, as shown in Figure 7c, a drastic reduction of SAR to 3, reduces both propane and LPG selectivity to

40.1% and 42.3%, respectively, due to a larger amount of C₂⁼-C₄⁼ olefins.

According to the authors, after having performed a NH₃-TPD, the decrease of SAR from 6 to 3 reduces both amount and strength of strong acid sites, suggesting that stronger acid sites induce more alkenes hydrogenation, enhancing alkanes.

In conclusion, the catalytic tests showed that both acid sites amount and gallium inclusion in ZrO₂ lattice synergically contribute to the very good performances of the catalyst. On this basis, COZMOS project chose to select GaZrO_x as the new generation of catalyst to be scaled up.

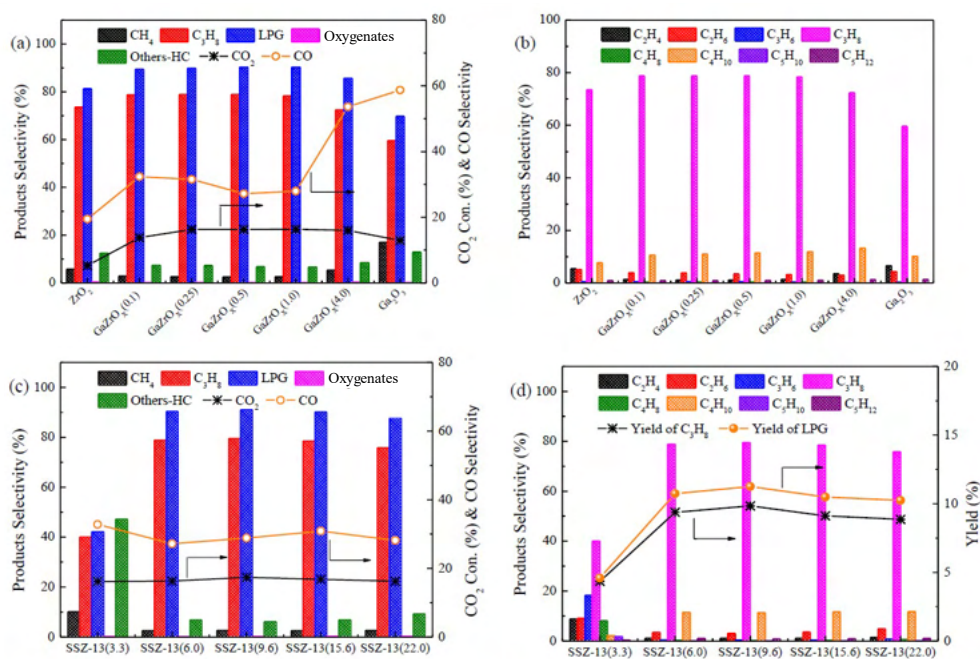


Figure 7 – Catalytic performance for CO₂ conversion. Catalytic performance for CO₂ conversion into propane over various GaZrO_x + H-SSZ-13(6.0) catalysts (a) and detailed product distribution (b). Influence of H-SSZ-13 zeolite Si/Al ratio on CO₂ conversion (c) and product distribution (d) over different GaZrO_x(0.5) + H-SSZ-13 catalysts. Others-HC represents the selectivity towards hydrocarbons, except methane, propane and butane. Reaction conditions: 3.0 MPa, 350 °C, H₂/CO₂ = 3:1 and 2400 mL g⁻¹ h⁻¹.

6.4 Scale up: spectroscopic characterization of stand-alone

GaZrO_x

As already reported in Chapter II, no information about the synthesis of this sample have been disseminated. Hence, the section herein reported is only a summary of preliminary FT-IR characterization results determined on two stand-alone GaZrO_x samples, calcined at two different temperatures (the number indicates the calcination temperature): GaZrO_x-350 and GaZrO_x-500.

The protocol used for the activation is almost the same reported for the lab scale sample, but the activation temperature has been changed, according to the calcination temperature. In particular, as for GaZrO_x-350, since the calcination was performed at 350 °C, the activation in pure H₂ was performed at that temperature. GaZrO_x-500 was activated, as usual, at 400 °C.

Figure 8 displays CO adsorption spectra acquired at LNT on both GaZrO_x-350 and GaZrO_x-500, panel *a* and *b*, respectively.

Both the samples show the same absorption bands and all of them lies in the same frequency range as those reported for the lab scale catalyst, and the assignment of the bands is the same: the band at 2192 could be assigned at both *cus*-Ga³⁺ and *cus*-Zr⁴⁺ carbonyls. Both the sites could lead to a red-shift of the band towards 2172 cm⁻¹. Similarly, the band at 2150 cm⁻¹ could be assigned to OH-CO and both less defective Ga³⁺ and Zr⁴⁺ sites.

Compared to Figure 2, the absorption bands observed on these scaled-up catalyst are more distinguishable. In addition, the lower intensity ratio between the band at 2172 cm^{-1} and that at 2150 cm^{-1} , could be related to two main reasons: i) higher amount of OH groups and ii) lower amount of coordinatively unsaturated sites. Both assumptions may be valid.

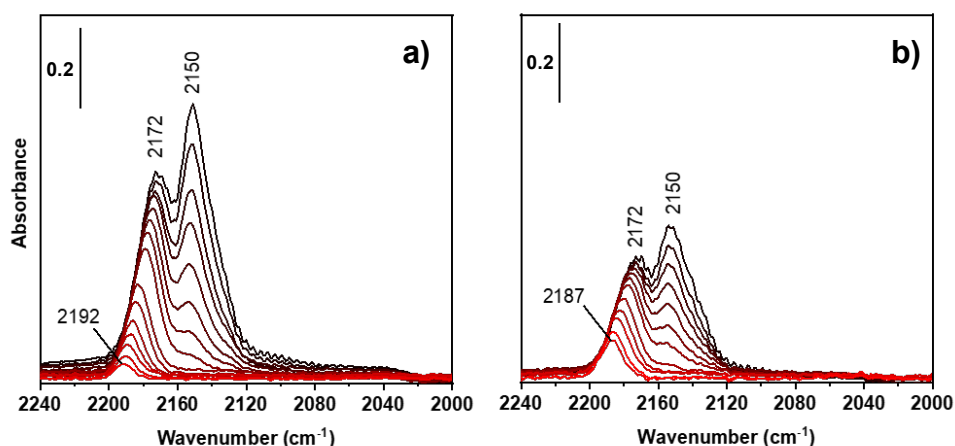


Figure 8 – CO adsorption spectra at LNT of GaZrO_x-350 (a) and GaZrO_x-500 (b).

The presence of *cus*-Ga³⁺ sites can be confirmed by CO adsorption at RT. As already mentioned, ZrO₂ is not capable of adsorbing CO at RT, hence only gallium could be responsible of adsorption bands at RT. Figure 9 shows CO adsorption spectra on both GaZrO_x-350 (Figure 9a) and GaZrO_x-500 (Figure 9b) at RT.

The observed adsorption features lie in the same frequency range of that reported in Figure 3, for the lab scale catalyst, despite a slight variation in frequency that

could be led to a weak influence of the *chemical effect* to the position of the band at high θ_{CO} . Both the bands at 2186 cm⁻¹ in Figure 9a and 2191 cm⁻¹ in Figure 9b confirm the presence of *cus*-Ga³⁺-CO.

Similarly to the spectra acquired at LNT, the intensity of the band of GaZrO_x-500 is less than that of GaZrO_x-350, confirming the trend. A possible reason why the intensity of all the bands of GaZrO_x-500 is less intense can be ascribed to the low surface area: as a matter of fact, as reported in Chapter II, GaZrO_x-500 has a lower BET surface area than GaZrO_x-350. It is reasonable that higher particle dimension induced by the higher calcination temperature, which could explain both the lower surface area and CO adsorption.

To conclude, for this scaled-up catalyst no catalytic test have been conducted yet. However, considering the very good performances observed for the lab scale catalyst and the lower costs compared to PdZn/ZrO₂, this catalyst could be a good candidate to be implemented at large scale.

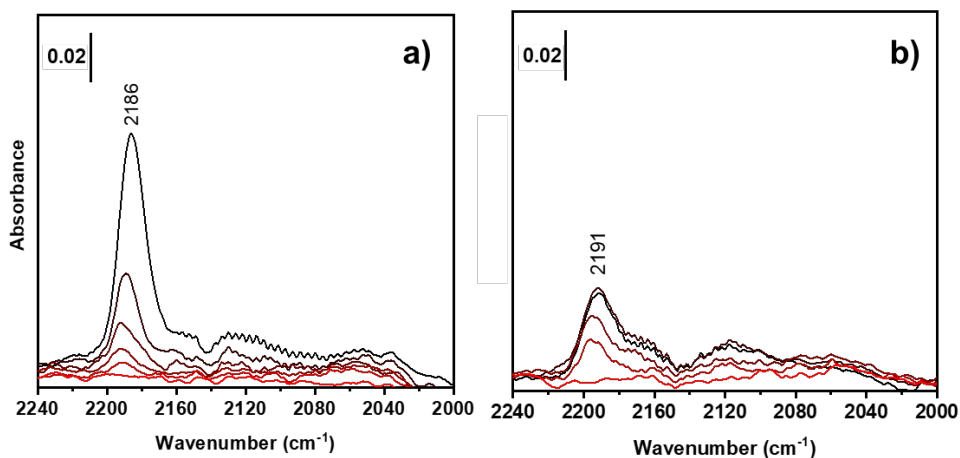


Figure 9 – CO adsorption spectra at RT of GaZrO_x-350 (a) and GaZrO_x-500 (b).

REFERENCES

- [1] S. Wang, L. Zhang, P. Wang, W. Jiao, Z. Qin, M. Dong, J. Wang, U. Olsbye, W. Fan, Highly selective hydrogenation of CO₂ to propane over GaZrOx/H-SSZ-13 composite, *Nat. Catal.* 2022. (2022) 1–13.
<https://doi.org/10.1038/s41929-022-00871-7>.
- [2] M. Akatsuka, T. Yoshida, N. Yamamoto, M. Yamamoto, S. Ogawa, S. Yagi, XAFS analysis for quantification of the gallium coordinations in Al₂O₃-supported Ga₂O₃ photocatalysts, *J. Phys. Conf. Ser.* 712 (2016) 012056. <https://doi.org/10.1088/1742-6596/712/1/012056>.
- [3] K. Nishi, K.I. Shimizu, M. Takamatsu, H. Yoshida, A. Satsuma, T. Tanaka, S. Yoshida, T. Hattori, Deconvolution Analysis of Ga K-Edge XANES for Quantification of Gallium Coordinations in Oxide Environments, *J. Phys. Chem. B.* 102 (1998) 10190–10195.
<https://doi.org/10.1021/JP982704P>.
- [4] C.O. Areán, M.R. Delgado, V. Montouillout, D. Massiot, Synthesis and Characterization of Spinel-Type Gallia-Alumina Solid Solutions, *Zeitschrift Für Anorg. Und Allg. Chemie.* 631 (2005) 2121–2126.
<https://doi.org/10.1002/zaac.200570027>.
- [5] M. Rodríguez Delgado, C. Morterra, G. Cerrato, G. Magnacca, C. Otero Areán, Surface Characterization of γ -Ga₂O₃: A Microcalorimetric and IR Spectroscopic Study of CO Adsorption, *Langmuir.* 18 (2002) 10255–

10260. <https://doi.org/10.1021/la026362x>.
- [6] C. Otero Areán, A.L. Bellan, M.P. Mentrut, M.R. Delgado, G.T. Palomino, Preparation and characterization of mesoporous γ -Ga₂O₃, Microporous Mesoporous Mater. 40 (2000) 35–42. [https://doi.org/10.1016/S1387-1811\(00\)00240-7](https://doi.org/10.1016/S1387-1811(00)00240-7).
- [7] V.B. Kazansky, I.R. Subbotina, R.A. van Santen, E.J.M. Hensen, DRIFTS study of the chemical state of modifying gallium ifreeons in reduced Ga/ZSM-5 prepared by impregnation: I. Observation of gallium hydrides and application of CO adsorption as a molecular probe for reduced gallium ions, J. Catal. 227 (2004) 263–269. <https://doi.org/https://doi.org/10.1016/j.jcat.2004.07.021>.
- [8] P. Ticali, D. Salusso, R. Ahmad, C. Ahoba-Sam, A. Ramirez, G. Shterk, K.A. Lomachenko, E. Borfecchia, S. Morandi, L. Cavallo, J. Gascon, S. Bordiga, U. Olsbye, CO₂ hydrogenation to methanol and hydrocarbons over bifunctional Zn-doped ZrO₂/zeolite catalysts, Catal. Sci. Technol. 11 (2021) 1249–1268. <https://doi.org/10.1039/D0CY01550D>.
- [9] M. Moskovits, J.E. Hülse, Frequency shifts in the spectra of molecules adsorbed on metals, with emphasis on the infrared spectrum of adsorbed CO, Surf. Sci. 78 (1978) 397–418. [https://doi.org/10.1016/0039-6028\(78\)90088-2](https://doi.org/10.1016/0039-6028(78)90088-2).

- [10] G.D. Mahan, A.A. Lucas, Collective vibrational modes of adsorbed CO, *J. Chem. Phys.* 68 (1978) 1344–1348. <https://doi.org/10.1063/1.435952>.
- [11] C. Morterra, V. Bolis, B. Fubini, L. Orto, T.B. Williams, A FTIR and HREM study of some morphological and adsorptive properties of monoclinic ZrO₂ microcrystals, *Surf. Sci.* 251–252 (1991) 540–545. [https://doi.org/10.1016/0039-6028\(91\)91051-X](https://doi.org/10.1016/0039-6028(91)91051-X).
- [12] M. Rodríguez Delgado, C. Morterra, G. Cerrato, G. Magnacca, C. Otero Areán, Surface Characterization of γ -Ga₂O₃: A Microcalorimetric and IR Spectroscopic Study of CO Adsorption, *Langmuir*. 18 (2002) 10255–10260. <https://doi.org/10.1021/la026362x>.
- [13] C. Otero Areán, A.L. Bellan, M.P. Mentrut, M.R. Delgado, G.T. Palomino, Preparation and characterization of mesoporous γ -Ga₂O₃, *Microporous Mesoporous Mater.* 40 (2000) 35–42. [https://doi.org/10.1016/S1387-1811\(00\)00240-7](https://doi.org/10.1016/S1387-1811(00)00240-7).
- [14] C.O. Areán, M.R. Delgado, V. Montouillout, D. Massiot, Synthesis and Characterization of Spinel-Type Gallia-Alumina Solid Solutions, *Zeitschrift Für Anorg. Und Allg. Chemie.* 631 (2005) 2121–2126. <https://doi.org/10.1002/zaac.200570027>.
- [15] A. Ramirez, P. Ticali, D. Salusso, T. Cordero-Lanzac, S. Ould-Chikh, C. Ahoba-Sam, A.L. Bugaev, E. Borfecchia, S. Morandi, M. Signorile, S.

- Bordiga, J. Gascon, U. Olsbye, Multifunctional Catalyst Combination for the Direct Conversion of CO₂ to Propane, *JACS Au*. 1 (2021) 1719–1732. <https://doi.org/10.1021/jacsau.1c00302>.
- [16] C. Morterra, E. Giamello, L. Orio, M. Volante, Formation and reactivity of Zr³⁺ centers at the surface of vacuum-activated monoclinic zirconia, *J. Phys. Chem.* 94 (1990) 3111–3116. <https://doi.org/10.1021/j100370a067>.
- [17] S.E. Collins, M.A. Baltanás, A.L. Bonivardi, Hydrogen Chemisorption on Gallium Oxide Polymorphs, *Langmuir*. 21 (2005) 962–970. <https://doi.org/10.1021/la0481389>.
- [18] S.E. Collins, M.A. Baltanás, J.L. Garcia Fierro, A.L. Bonivardi, Gallium-hydrogen bond formation on gallium and gallium-palladium silica-supported catalysts, *J. Catal.* 211 (2002) 252–264. <https://doi.org/10.1006/jcat.2002.3734>.
- [19] E.A. Gonzalez, P. V. Jasen, A. Juan, S.E. Collins, M.A. Baltanás, A.L. Bonivardi, Hydrogen adsorption on β-Ga₂O₃(100) surface containing oxygen vacancies, *Surf. Sci.* 575 (2005) 171–180. <https://doi.org/10.1016/j.susc.2004.11.018>.
- [20] Z. Li, W. Huang, Hydride species on oxide catalysts, *J. Phys. Condens. Matter*. 33 (2021) 433001. <https://doi.org/10.1088/1361-648X/ac17ad>.
- [21] G. Busca, V. Lorenzelli, *Materials Chemistry* 7 (1982) 89- 126

INFRARED SPECTROSCOPIC IDENTIFICATION OF SPECIES
ARISING FROM REACTIVE ADSORPTION OF CARBON OXIDES
ON METAL OXIDE SURFACES G BUSCA, V LORENZELLI, *Mater.*
Chem. 7 (1982) 89–126.

- [22] S.E. Collins, M.A. Baltanás, A.L. Bonivardi, Infrared Spectroscopic Study of the Carbon Dioxide Adsorption on the Surface of Ga₂O₃ Polymorphs, *J. Phys. Chem. B.* 110 (2006) 5498–5507.
<https://doi.org/10.1021/jp055594c>.
- [23] S. COLLINS, M. BALTANAS, A. BONIVARDI, An infrared study of the intermediates of methanol synthesis from carbon dioxide over Pd/-GaO, *J. Catal.* 226 (2004) 410–421.
<https://doi.org/10.1016/j.jcat.2004.06.012>.
- [24] B. Bachiller-Baeza, I. Rodriguez-Ramos, A. Guerrero-Ruiz, Interaction of carbon dioxide with the surface of zirconia polymorphs, *Langmuir.* 14 (1998) 3556–3564. <https://doi.org/10.1021/la970856q>.
- [25] J.C. Lavalley, M. Daturi, V. Montouillout, G. Clet, C. Otero Areán, M. Rodríguez Delgado, A. Sahibed-dine, Unexpected similarities between the surface chemistry of cubic and hexagonal gallia polymorphs, *Phys. Chem. Chem. Phys.* 5 (2003) 1301–1305.
<https://doi.org/10.1039/b211767n>.

- [26] K. Fajans, Degrees of polarity and mutual polarization of ions in the molecules of alkali fluorides, SrO, and BaO, in: Struct. Bond., Springer Berlin Heidelberg, Berlin, Heidelberg, n.d.: pp. 88–105.
<https://doi.org/10.1007/BFb0118879>.

CONCLUSIONS AND PERSPECTIVES

Towards COZMOS-2

The entire work presented in this Ph.D. thesis summarizes the best results achieved during the last three years.

The Ph.D. research work is affiliated to COZMOS project. The aim of the project is to employ bifunctional catalysts to produce methanol from CO₂ hydrogenation and convert methanol to C₃ hydrocarbons. The bifunctional catalysts consist of a methanol-producing phase, constituted by a supported metal/oxidic phase, and methanol-converting phase, made up of a zeolite/zeotype phase, following either methanol-to-olefines or methanol-to-hydrocarbons reaction pathways.

In order to understand the role of each phase and to support the catalytic tests performed on the bifunctional catalysts, the present work focused the attention on the adsorption of specific molecules – such as CO, H₂ and CO₂ – followed by FT-IR spectroscopy. For sake of completeness, the supported metal/oxidic phase and the zeolitic phase were analyzed as both stand-alone phase and combined 1:1 mass ratio physical mixture.

The characterization of all the methanol-producing phases showed in this work evidenced that the presence of specific surfaces sites, able to split hydrogen (as assumed for PdZn/ZrO₂ and observed for GaZrO_x), and the generation of oxygen vacancies (as reported for PdZn/ZrO₂, ZnZrO_x and ZnCeZrO_x) play a key role in CO₂ hydrogenation. As a matter of fact, as for ZnZrO_x it was possible to follow

the catalytic activity of all the catalysts with different composition, i.e. Zn content. Indeed, ZnZr-30 was featured by higher Zn content and an extra-phase of ZnO, responsible for the formation of higher amount of oxygen vacancies that was linked to better catalytic performances of this material.

As for the zeolitic counterpart, the acidity drastically influences the yield of the process. In particular, AlPOs-derived zeotypes (such as SAPO-34) seem to be the best systems, compromising both the coke production, that leads to the deactivation of the catalyst, and the hydrocarbon selectivity.

Among the analyzed catalyst only PdZn/ZrO₂+SAPO-34 combined system and GaZrO_x oxidic phase have been chosen to be scaled up. In particular, the first catalyst was scaled-up in order to highlight both the advantages and drawbacks concerning the synthesis of the system. Unfortunately, the results collected and discussed in this thesis were not as expected. As for the second catalyst, the actual goal of the project is to scale up a bifunctional catalyst made up of GaZrO_x and MAPO-18 (Mg-APO-18). Both the characterization of the system and the catalytic tests are still on-going and will be completed by the end of the project.

Due to COVID-19 pandemics, the entire project has been extended until May 2023, but only in the last few months the pilot plant at Tüpraş became operative, and the next step will be testing the catalysts on larger scale.

In addition, falling outside my research work, I did not show any results regarding the Life Cycle Assessment of all the sample analyzed in this thesis, in particular those chosen to be scaled up. Indeed, on the *last generation* of catalysts before

Conclusions and perspectives

the project closure, a complete assessment must be done in order to demonstrate that the project met the goals proposed. On this side, more efforts should be implemented. In particular, some recent studies have been conducted on both kinetic models, process design and life cycle assessment for PdZn/ZrO₂+SAPO-34 system.

On this basis, the project might evolve into a *COZMOS-2* project, intended to include more industrial partners and focus on the application of scaled-up catalysts at larger scale than prototypal plants. A strict bond between academia and industry could be the key to speed up and enhance the research on the field of CO₂ hydrogenation catalysis, with a view to the Net Zero scenario proposed in 2050.

At the end of my doctoral activity, after having assisted at almost the entire evolution of the project, in my opinion a *COZMOS-2* project would be the best epilogue. To date, a great part of research is focused on carbon capture and utilization technology and I think that, with further financial support, the *COZMOS* project would play an important role in the fight against the global warming.

APPENDIX

A.1

Multifunctional Catalyst Combination for the Direct Conversion of CO₂ to Propane

Adrian Ramirez, Pierfrancesco Ticali, Davide Salusso, Tomas Cordero-Lanzac, Samy Ould-Chikh, Christian Ahoba-Sam, Aram L. Bugaev, Elisa Borfecchia, Sara Morandi, Matteo Signorile, Silvia Bordiga,* Jorge Gascon,* and Unni Olsbye*

Cite This: *JACS Au* 2021, 1, 1719–1732

Read Online

ACCESS |

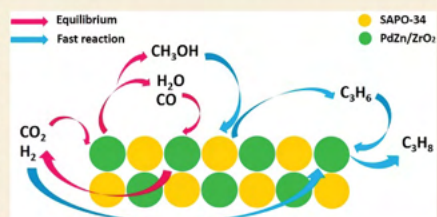
Metrics & More

Article Recommendations

Supporting Information

ABSTRACT: The production of carbon-rich hydrocarbons via CO₂ valorization is essential for the transition to renewable, non-fossil-fuel-based energy sources. However, most of the recent works in the state of the art are devoted to the formation of olefins and aromatics, ignoring the rest of the hydrocarbon commodities that, like propane, are essential to our economy. Hence, in this work, we have developed a highly active and selective PdZn/ZrO₂+SAPO-34 multifunctional catalyst for the direct conversion of CO₂ to propane. Our multifunctional system displays a total selectivity to propane higher than 50% (with 20% CO, 6% C₁, 13% C₂, 10% C₄, and 1% C₅) and a CO₂ conversion close to 40% at 350 °C, 50 bar, and 1500 mL g⁻¹ h⁻¹. We attribute these results to the synergy between the intimately mixed PdZn/ZrO₂ and SAPO-34 components that shifts the overall reaction equilibrium, boosting CO₂ conversion and minimizing CO selectivity. Comparison to a PdZn/ZrO₂+ZSM-5 system showed that propane selectivity is further boosted by the topology of SAPO-34. The presence of Pd in the catalyst drives paraffin production via hydrogenation, with more than 99.9% of the products being saturated hydrocarbons, offering very important advantages for the purification of the products.

KEYWORDS: CO₂ conversion, hydrogenation, propane, tandem catalysts, zeolites, kinetics, reaction mechanism



1. INTRODUCTION

Carbon capture and utilization (CCU) is critical to reducing CO₂ emissions and mitigating global warming.¹ Through the production of carbon-rich hydrocarbons via CO₂ valorization,^{2,3} CCU is expected to pave the route for the transition to renewable, non-fossil-fuel-based energy sources.⁴

One of the most promising approaches toward CO₂ valorization consists of the combination of conventional metallic catalysts with acidic zeolites.⁵ This combination can directly transform CO₂ to a great variety of chemicals with a selectivity above the limitation of the Anderson–Schulz–Flory distribution (ASF).⁶ However, most of the work to date has been limited to the production of either olefins or aromatics, with the rest of essential hydrocarbons being barely studied.⁷ This is of particular importance as, for a real circular carbon economy (CCE), other common hydrocarbons and fuels should be as well produced via CO₂.⁸ One example of essential hydrocarbon with high demand is propane.

Propane is nowadays produced as a byproduct in two other processes, natural gas processing and petroleum refining. The propane market is expected to grow at 5% per year, adding up to 350 million metric tons per year in 2025⁹ (with the potential therefore to account for 1050 million metric tons of CO₂),

being the industrial and residential sectors the two most relevant actors. In industrial processes, propane is used for large-scale applications such as furnaces and heaters. And in the residential sector, propane is widely used for air conditioning, heating, refrigeration, production of textiles, lighting, and other uses. However, despite the obvious importance of this hydrocarbon, propane formation from CO₂ has been barely touched in the available literature,^{10,11} and only a few prior papers targeted paraffin formation, mostly from syngas.^{12–17}

Hence, with propane production in mind, in this work we have developed a highly active and selective PdZn/ZrO₂+SAPO-34 multifunctional catalyst. In particular, we took advantage of the hydrogenation function of the Pd component and the high C₃ selectivity of the SAPO-34 to

Received: July 6, 2021

Published: September 2, 2021



develop a catalytic system with high selectivity toward propane. Zn and ZrO₂ were also included in the formulation because of the well-known ability of these elements to efficiently convert CO₂ to methanol,¹⁸ the first step in the overall multifunctional mechanism.⁶

The resulting PdZn/ZrO₂+SAPO-34 catalytic system displays a total selectivity to propane higher than 50% with a CO₂ conversion close to 40% and only 20% of CO selectivity at 350 °C, 50 bar, and 1500 mL g⁻¹ h⁻¹. To the best of our knowledge, this is the highest total selectivity per pass ever reported for a single C₃ hydrocarbon during CO₂ valorization.¹¹ We attribute these results to the intimate contact between the PdZn/ZrO₂ and SAPO-34 components that shifts the overall reaction equilibrium, ultimately boosting CO₂ conversion and minimizing CO selectivity. Kinetic modeling of the catalytic data alongside with thermodynamic equilibrium calculations fully support this hypothesis. Lastly, the presence of Pd in the catalyst drives paraffin production via hydrogenation, with more than 99.9% of the products being saturated hydrocarbons, offering very important advantages for the purification of the products.

2. EXPERIMENTAL SECTION

2.1. Catalyst Preparation

Pd(CH₃COO)₂ (>99.9%), Zn(CH₃COO)₂ (99.99%), Zr(OH)₄ PVP (Mwt 10000), DMF (99.8%), and ethylene glycol (99.8%) were purchased from Sigma-Aldrich and used as received. ZSM-5 (SiO₂/Al₂O₃ = 23) was purchased from Zeolyst. SAPO-34 (SiO₂/Al₂O₃ = 0.5) was purchased from ACS materials. All the zeolites were dried at 120 °C for 12 h and calcined at 550 °C for 2 h prior to testing.

The PdZn/ZrO₂ catalyst was obtained by a colloidal impregnation method. Briefly, 5 g L⁻¹ of Pd(CH₃COO)₂ was dissolved in DMF and 20 g L⁻¹ Zn(CH₃COO)₂ dissolved in ethylene glycol were prepared. Eight grams of PVP was added to 80 mL of the Zn precursor solution and heated to 80 °C to obtain a clear yellow solution. Fifty milliliters of the Pd precursor solution was added to the clear yellow zinc/PVP solution amidst stirring and heated to 100 °C under reflux for 2 h. The colloidal mixture was cooled, centrifuged, and washed with acetone and then dispersed in ethanol. The dispersed colloidal mixture in ethanol was added to 6 g of Zr(OH)₄ powder and stirred for 20 h at room temperature. The resulting mixture was oven-dried and calcined at 500 °C for 3 h. The multifunctional PdZn/ZrO₂+zeolite catalysts were prepared by mortar mixing of both components with a 1:1 mass ratio.

2.2. Catalytic Tests and Kinetic Modeling

Catalytic tests were executed in a 16 channel Flowence from Avantium. Fifty milligrams of the stand-alone PdZn/ZrO₂ catalyst and 100 mg of composite catalyst with PdZn/ZrO₂+zeolite with a mass ratio of 1/1 in a mixed bed configuration were typically used. Both functions were pelletized together in a 1/1 ratio, and then sieved to a particle size 150–250 μm. The mixed feed had 22.5 vol % of CO₂, 72.5 vol % of H₂, and 5% of He as internal standard. For the catalyst activity evaluation, we aimed at a gas hourly space velocity (GHSV) value of 12000 mL g⁻¹ h⁻¹ per channel. One of the 16 channels was always used without catalyst as blank. The reaction temperature was typically set at 350 °C. Prior to feeding the reaction mixture all samples were pretreated in situ with a pure H₂ atmosphere for 4 h at 400 °C. The tubes were then pressurized to 30 bar using a membrane-based pressure controller. Extra runs were also performed in order to evaluate the kinetics of the reactions using the stand-alone PdZn/ZrO₂ catalyst and the multifunctional catalytic system. For this purpose, operation conditions were ranged between 250 and 350 °C, 30–50 bar and 1500–30 000 mL g⁻¹ h⁻¹.

Reaction products were analyzed online in a gas chromatograph. The GC is an Agilent 7890B with three detectors, a TCD and 2 FIDs. TCD is equipped with 2 Haysep precolumn and a MSSA, where He,

H₂, CH₄, CO₂, and CO are separated. FIDs are equipped with Gaspro and an Innowax columns. Gaspro separates C₁–C₈ hydrocarbons and DME. Innowax separates oxygenates and aromatics.

Conversion (X, %) and selectivity (S_{C_n}, %) are defined as follow:

$$X_{\text{CO}_2} = \left(1 - \frac{C_{\text{He},\text{bl}} C_{\text{CO}_2,\text{R}}}{C_{\text{He},\text{R}} C_{\text{CO}_2,\text{bl}}} \right) 100 \quad (1)$$

$$S_{\text{C}_n} = \frac{\frac{n C_{\text{C}_n,\text{R}}}{C_{\text{He},\text{R}}}}{\left(\frac{C_{\text{CO}_2,\text{bl}}}{C_{\text{He},\text{bl}}} - \frac{C_{\text{CO}_2,\text{R}}}{C_{\text{He},\text{R}}} \right)} 100 \quad (2)$$

where C_{He,bl}, C_{He,R}, C_{CO₂,bl}, and C_{CO₂,R} are the concentrations determined by GC analysis of He in the blank, He in the reactor effluent, CO₂ in the blank, and CO₂ in the reactor effluent, respectively, and C_{C_n,R} is the concentration of the reactor effluent determined by GC analysis of a product with *n* carbon atoms. The error in carbon balance was better than 2.5% in all cases.

Experimental results collected with both the stand-alone PdZn/ZrO₂ catalyst and the multifunctional PdZn/ZrO₂+SAPO-34 catalytic system were fitted by means of kinetic modeling in order to estimate and compare the rates of the reactions. Because of the characteristics of the experimental setup, some assumptions can be made, thereby simplifying the system. More details can be found in the Supporting Information. Briefly, a steady-state plug flow model, working at isothermal and isobaric conditions, is assumed for the reactor. To avoid mathematical uncertainty and strictly compare reaction rates, we considered two equilibrium reactions: CO₂ hydrogenation to methanol and the reverse water–gas shift reaction. Equilibrium constants were considered with empirical correlations, and the results were contrasted with those obtained from the *FactSage* equilibrium database. For the multifunctional system where methanol is further transformed to hydrocarbons, a fast conversion of methanol to propane is assumed, with both methanol-to-propene and propene hydrogenation considered to be quite faster than CO₂/CO/MeOH equilibria.

2.3. Characterization of Catalysts

The powder X-ray diffraction (XRD) measurements were performed by using a Bruker D8 Discover, with a Cu Kα source and a Lynx Eye silicon detector. The diffractograms were scanned with step size of 0.02° in the 2θ range of 10–90°. The crystalline phase was identified by comparison with data from the inorganic crystal structure database, ICSD.

Nitrogen adsorption-desorption isotherms were recorded using a Micromeritics ASAP 2040 at –196 °C. Samples were previously evacuated at 100 °C for 16 h. The Brunauer–Emmett–Teller (BET) method was used to calculate the surface area. The *p/p₀* range for BET analysis was 0.067 < *p/p₀* < 0.249.

The temperature-programmed desorption (TPD) experiments were carried out in a Micromeritics ASAP 2020. The catalyst samples were first heated in helium flow at 350 °C for 4 h, followed by cooling to 50 °C. After cooling, the zeolites were saturated in ammonia and the temperature of the samples was increased linearly at a rate of 10 °C/min. Ammonia was fed at atmospheric pressure with a 5% vol. NH₃ concentration was diluted in Helium. The ammonia desorption was continuously monitored by a thermal conductivity detector.

Thermogravimetric analyses (TGA) of catalysts were carried out in a TGA/DSC1 STAR-e system apparatus (Mettler Toledo). Before TPO experiments, the catalyst was submitted to stripping under a N₂ stream (50 mL min⁻¹) up to the reaction temperature using a heating ramp of 10 °C min⁻¹. After that, the sample was cooled and stabilized at 100 °C. The temperature was then increased up to 850 °C using a heating ramp of 5 °C min⁻¹ under an air flow of 50 mL min⁻¹ to ensure the total combustion of coke.

XAS measurements were performed at the Quick-XAS ROCK¹⁹ beamline of the French synchrotron SOLEIL. K-edges of Pd and Zn were separately collected in transmission mode. Si(220) and Si(111) monochromators were employed to scan Pd and Zn absorption edges,

in the range 23.8–25.7 and 9.3–10.7 keV, respectively. The PdZn/ZrO₂ catalyst was physically mixed with zeolite ZSM-5 (1:1 weight ratio) and packed in a quartz capillary reactor. To optimize the signal quality in transmission mode, we chose a capillary of Ø 1 mm for the Zn K edge and 2.5 mm for the Pd K edge. The capillary was connected to a gas flow system while heating was provided by a heat gun. The measurement followed the catalyst activation protocol used for the catalytic tests, i.e. XAS spectra were recorded during a heating ramp (RT–400 °C) under H₂ gas flow (10 mL/min). The reported XAS spectra resulted from the average of 500 and 120 quick-EXAFS spectra (0.5 s/scan). Two ionization chambers were used to measure I_0 and I_{γ} while a third one measured a reference metal foil used for energy alignment. ZnO and PdO were also measured as reference compounds in the form of self-supporting pellets. XAS data analysis (XANES normalization and energy calibration, $\chi(k)$ EXAFS extraction, and Fourier transform (FT)-EXAFS calculation) were carried out using the *Athena* software from the *Demeter* package.²⁰ The EXAFS fitting of PdZn active phase was performed using the *ARTEMIS* code of the *Demeter* package.²⁰ Pd–Pd and Pd–Zn scattering paths were generated by the *FEFF6* code implemented in *ARTEMIS* using starting interatomic distances taken from literature.²¹ The passive amplitude reduction factor was obtained from EXAFS analysis of aPd reference foil. Pd–Pd and Pd–Zn coordination numbers were fixed to the bulk values (4 and 8, respectively), whereas the energy shift (E_0), radial distances (ΔR), and Debye–Waller factors (σ^2) were fit as free variables.

Absorption IR spectra were run using a PerkinElmer FTIR 2000 spectrophotometer equipped with a Hg–Cd–Te cryo-detector, in the range of wavenumbers 7200–580 cm⁻¹ at a resolution of 2 cm⁻¹. The powder of PdZn/ZrO₂ was compressed in self-supporting discs (~20 mg cm⁻²) and placed in quartz IR cells suitable for thermal treatments in controlled atmosphere and spectra recording at room temperature (RT). Moreover, a commercial stainless-steel cell (Aabspec), allowing thermal treatments in situ under vacuum or controlled atmosphere and the simultaneous registration of spectra at temperatures up to 600 °C, was employed. Before IR measurements, catalyst underwent oxidizing or reducing pretreatment: in both cases, it was outgassed at 400 °C for 30 min and then oxidized in dry oxygen (40 mbar) or reduced in hydrogen (40 mbar) at 400 °C for 30 min. Reduction treatment simulates the reduction step performed prior to the catalytic tests. Prereduced catalyst will be named activated catalyst. First of all, interaction with the reagents involved in the CO₂-to-methanol process, i.e., H₂ and CO₂, was investigated. In particular, interaction with H₂ (10 mbar) was performed in situ at increasing temperature on the preoxidized catalyst to study the effect of the activation step used for the catalytic tests. Interaction with CO₂ (20 mbar) was studied at RT on both preoxidized and activated catalyst. To characterize the supported metal phase, we carried out CO adsorption for increasing pressure up to 20 mbar at RT on the activated catalyst.

Transmission electron microscopy (TEM) of the samples was performed with a Cs-probe corrected Titan microscope from Thermo Fisher Scientific by operating it at an accelerating voltage of 300 kV and with a beam current of 0.5–0.8 nA. Dark-field imaging was performed by scanning TEM (STEM) coupled to a high-angle annular dark-field (HAADF) detector. The STEM-HAADF data were acquired with a convergence angle of 17.1 mrad and a HAADF inner angle of 50 mrad. Furthermore, a X-ray energy-dispersive spectrometer (FEI SuperX, ~0.7 sr collection angle) was also utilized in conjunction with DF-STEM imaging to acquire STEM-EDS spectrum-imaging data sets (image size: 512 × 512 pixels, dwell time 4 μs). During the acquisition of these data sets, at every image-pixel, a corresponding EDS spectrum was also acquired for generating simultaneously the elemental maps of Si, Al, Pd, Zn, Zr, and O atoms. It is also pertinent to note herein that spectrum-imaging data sets were acquired in the so-called frame mode, in which the electron beam was allowed to dwell at each pixel for only a time of few microseconds in order to keep a total frame time to 2 s or less. Both imaging and spectroscopy data sets for each sample were acquired as well as analyzed with a newly developed software package called *Velox*

from Thermo Fisher Scientific. The elemental maps for Si, Al, Pd, Zn, Zr, and O atoms were computed using the extracted intensity of their respective *K*α lines after background subtraction. The generated maps were slightly postfiltered by applying a Gaussian filter (sigma = 0.5). Because of the possible air sensitivity of the PdZn/ZrO₂ solid after H₂ activation and CO₂ hydrogenation, the sample was handled inside an Ar-filled glovebox. The specimen was prepared by simply shaking a small amount of dry powder and the TEM grid inside a 2 mL sample vial. The TEM grid was retrieved and mounted in a Gatan double-tilt vacuum transfer TEM holder, model 648 that was used for the transfer into the microscope.

UV-Raman spectra were collected with a Renishaw inVia Raman spectrometer, adopting a Coherent MotoFred 300C frequency doubled Ar⁺ laser emitting at 244 nm as excitation source. The spectrometer is equipped with a 15× objective, a 3600 lines/mm grating and a Peltier cooled CCD detector. To prevent sample decomposition, we kept samples under movement during the measurements with a specifically designed setup.²³

3. RESULTS AND DISCUSSION

3.1. Catalytic Tests for the CO₂ Hydrogenation to Propane

We first performed a catalytic screening over the stand-alone PdZn/ZrO₂ catalysts and their combination with SAPO-34 and ZSM-5, the two most common zeolites employed in multifunctional catalysts for CO₂ conversion.⁷ These control experiments were focused on monitoring MeOH selectivity for the stand-alone PdZn/ZrO₂ catalysts and that of propane for the multifunctional systems. In particular, the effect of reaction pressure (20, 30, and 40 bar) and temperature (250 °C, 300 and 350 °C) was evaluated. The results are summarized in Figure 1a. CO₂ conversion is similar for the three systems (filled symbols, left axis) and it increases with pressure and temperature, in agreement with the process thermodynamics.¹¹ On the other hand, selectivity follows a completely different trend (empty symbols, right axis). For the stand-alone PdZn/ZrO₂ catalysts, MeOH selectivity also follows the process thermodynamics, increasing with pressure and decreasing with temperature. A full picture of the allowed equilibrium selectivities (lines) and the obtained experimental data (dots) can be observed in Figure S1. Note that the orange lines indicate the maximum allowed methanol selectivity considering the CO₂ to methanol equilibrium. For the multifunctional systems, however, no propane is observed for temperatures lower than 350 °C, and SAPO-34 displays higher selectivity than ZSM-5 (16% vs 3%), in line with the typical methanol-to-hydrocarbons (MTH) mechanism.²³ Looking in detail at the PdZn/ZrO₂+SAPO-34 system, the achieved propane selectivity is higher than the MeOH one of the stand-alone PdZn/ZrO₂ catalysts at 350 °C (16% vs 7%). Interestingly, MeOH selectivity is overlapped with the equilibrium line, indicating that at these conditions the reaction is limited by the reaction thermodynamics (Figure S2a). Conversely, propane selectivity is substantially higher than MeOH equilibrium, suggesting an equilibrium displacement when the multifunctional system is assembled. Therefore, we can conclude that SAPO-34 seems to be a more promising candidate to produce propane than ZSM-5. Moreover, although there are thermodynamics restrictions at high temperature, it seems that an operation temperature of 350 °C is needed for the MeOH conversion to occur in both SAPO-34 and ZSM-5.

Next, the more promising PdZn/ZrO₂+SAPO-34 system was studied at 350 °C using different space velocity values (1500, 3000, 6000, and 12000 mL g⁻¹ h⁻¹) and pressures (30,

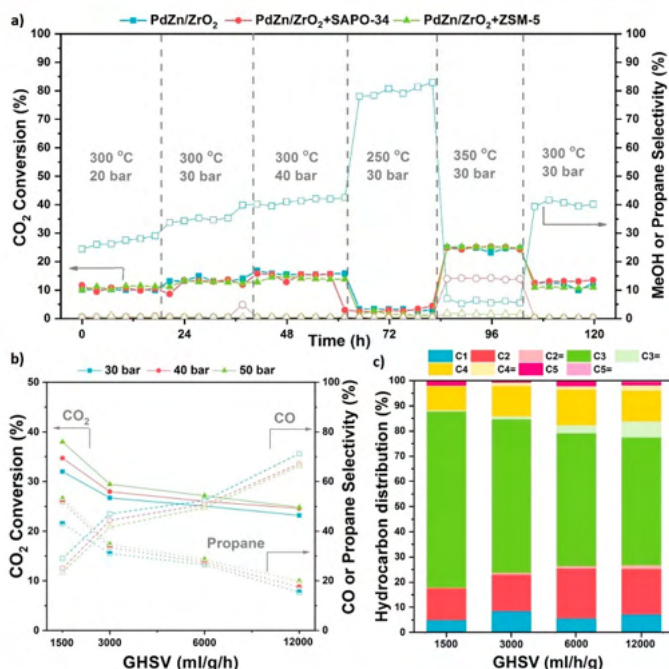


Figure 1. (a) CO₂ conversion (filled symbols) and MeOH (for PdZn/ZrO₂) or propane (for PdZn/ZrO₂+SAPO-34 and PdZn/ZrO₂+ZSM-5) selectivity (empty symbols) at several screening conditions. H₂/CO₂ = 3, 12 000 mL g⁻¹ h⁻¹. (b) CO₂ conversion (filled symbols) and CO (empty symbols) or propane (half empty symbols) selectivity for the PdZn/ZrO₂+SAPO-34 system at different space velocities and pressures. 350 °C, H₂/CO₂ = 3. MeOH selectivity was lower than 1% at all conditions. (c) Detailed hydrocarbon distribution (CO free) of the PdZn/ZrO₂+SAPO-34 combined system for the CO₂ conversion to hydrocarbons at different space velocities. CO₂:H₂ 1:3, 350 °C, 50 bar.

40, and 50 bar). The results are summarized in Figure 1b. As expected, CO₂ conversion increases with decreasing space velocity and increasing pressure. However, CO selectivity also decreases with space velocity, reaching a minimum value of 25% at 50 bar and 1500 mL g⁻¹ h⁻¹. This behavior is unexpected as, for most of the state-of-the-art CO₂ to MeOH catalysts, the opposite trend is observed and higher MeOH selectivity is usually obtained at higher space velocity value.²⁴ Hence, these data may suggest that CO-involving reactions play a key role using the PdZn/ZrO₂+SAPO-34 system, because of a limitation in its formation or a consumption of the formed CO to produce more methanol. Moreover, from the data at 50 bar and 1500 mL g⁻¹ h⁻¹, a total selectivity to propane higher than 50% can be observed, with a CO₂ conversion close to 40% and only 25% of CO selectivity. To the best of our knowledge, this is the highest total selectivity reported for a single C₂ hydrocarbon during CO₂ hydrogenation at meaningful conversion levels.¹¹ Additionally, thanks to the Pd hydrogenating effect and as intended, the paraffins account for more than 99.9% of the products, greatly facilitating the product separation in a potential industrial process. This later can be better observed if we look in detail at the CO free hydrocarbon distribution (Figure 1c). Figure S2 shows conversion/selectivity plots with these experiments

being compared with the above-discussed CO₂-to-methanol equilibrium. The presence of acid sites in SAPO-34, in close proximity to the methanol-forming PdZn/ZrO₂ catalyst, leads to rapid conversion of methanol into hydrocarbons (mainly propene). Consequently, the methanol concentration remains below the equilibrium limit, and the selectivity to propane (formed from the fast hydrogenation of propene) is significantly above the equilibrium line at 350 °C and 30 (Figure S2a), 40 (Figure S2b), and 50 bar (Figure S2c). Otherwise, the selectivity to methanol was clearly restricted by equilibrium under these conditions (Figure S2a, orange dot).

To shed light on the strikingly low CO selectivity and the CO role, additional experiments with both CO₂ and CO feeds were performed comparing the original PdZn/ZrO₂+SAPO-34 mixed system with the stand-alone PdZn/ZrO₂ catalyst and the multifunctional system in dual bed configuration. The results are summarized in Figure 2. Considering first the CO₂ feed (Figure 2a), the rather stable CO₂ conversion, and the huge decrease in CO selectivity (from 95% to 35%), only observed when mixing PdZn/ZrO₂ with SAPO-34, a lower CO formation rate in the presence of SAPO-34 is suggested. The similar CO selectivity with similar CO₂ conversion in the dual bed setup confirms that, indeed, the intimate mixture of both components is needed to displace equilibrium. Here, the CO-

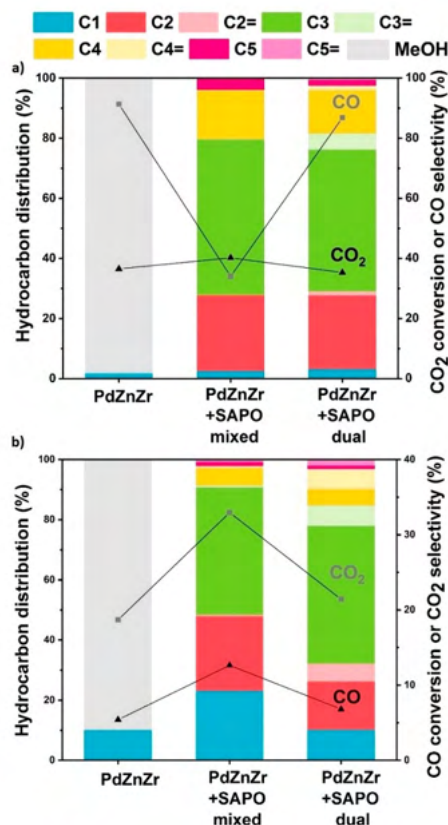


Figure 2. Catalytic performance of the PdZn/ZrO₂ catalyst and the PdZn/ZrO₂+SAPO-34 combined system: (a) CO₂ and (b) CO conversion to hydrocarbons. CO₂:H₂ 1:3, 350 °C, 30 bar, 3000 mL g⁻¹ h⁻¹.

forming PdZn/ZrO₂ will compete with the hydrocarbon-forming SAPO-34 for methanol and, due to the rapid transformation of methanol to hydrocarbons over SAPO-34, the CO₂/MeOH/CO equilibrium system would be shifted to minimize CO formation in the mixed bed case. The higher olefin-to-paraffin ratios in the dual bed configuration are the result of the higher hydrogenation ability of PdZn/ZrO₂ compared to SAPO-34 as we initially intended. At the same time, the dual bed data demonstrate that SAPO-34 has substantial hydrogenation activity in the presence of surplus H₂. This is well in line with prior literature over SAPO-34 in the presence of H₂.²⁵

Considering the CO feed (Figure 2b), CO conversion is substantially lower than that of CO₂, but with higher methanol selectivity compared to CO₂ over the PdZn/ZrO₂ alone. This is in line with process thermodynamics (the lower the conversion, the higher the MeOH selectivity) but also suggests that CO limits the rate of the reaction. Surprisingly, here the

CO₂ selectivity shows a different trend and it is maximized in the mixed bed PdZn/ZrO₂+SAPO-34 configuration. CO conversion is also increased in this mixed bed configuration. We attribute this result to another equilibrium displacement. This time, the water-gas shift (WGS) is promoted because of the water presence. Converting the MeOH generated on the PdZn/ZrO₂ to hydrocarbons on the SAPO-34 generates great amounts of water that can favor the WGS on the hydrogenating catalyst, thus increasing the CO conversion and selectivity to CO₂. Summing up, from these results, we can confirm the clear effect of CO and WGS in the mixed bed configuration when both catalytic functions are intimately mixed together and the equilibrium can be shifted.

3.2. Kinetic Modeling of the PdZn/ZrO₂+SAPO-34 System

Because of the relevant role of equilibrium and thermodynamics in the overall process and the observed advantages of intimate mixing both functions, a kinetic modeling study was carried out comparing the performances of the stand-alone PdZn/ZrO₂ catalyst and the PdZn/ZrO₂+SAPO-34 system. More details on the reaction network and kinetic equations can be found in the Supporting Information. Experimental data fitting at selected conditions can be observed in Figure 3a, b for both catalysts at the optimal conditions for the production of methanol and propane, respectively. Moreover, the fitting of all experimental data can be found in Figure S3. A clearly differentiated trend is observed. CO₂ is converted to CO and MeOH over the stand-alone catalyst, with the concentration of MeOH decreasing with space time and that of CO reaching a saturating trend at 350 °C (Figure S3c). Otherwise, in line with our previous claims, CO shows a maximum when both functions are mixed, accentuated at 50 bar (Figure 3b). As expected, the concentration of propane increases with space time. As propane is formed only from MeOH, this can only be explained by shifts on CO₂/CO/MeOH equilibria caused by the presence of SAPO-34. This can be more clearly understood when the estimated reaction rates for the CO₂-to-MeOH and rWGS reactions are compared (Figure 3c, d). The evolution with space time of the individual reactions rates at all tested temperatures and pressures are shown in Figures S4 and S5.

At low temperature and low CO₂ conversions (250 °C, Figure 3c), reactions are not limited by equilibrium, as was well-predicted by thermodynamics studies (Figure S4). Forward reactions are remarkably promoted but with low rate values. When temperature is increased, rate values increase but forward/reverse rates for CO₂/MeOH equilibrium are, in practice, the same, confirming the above-discussed thermodynamics constraint at this high temperature. A comparison of these rates with those calculated for the PdZn/ZrO₂+SAPO-34 multifunctional system at the same conditions and half GHSV (same CO₂-to-PdZn/ZrO₂ ratio, Figure 3d) shows a ten-times increase in MeOH formation (in equilibrium) because of its consumption to form propane, but also a significant increase in the reverse rate of CO formation (ca. 18 mol kg⁻¹ h⁻¹, the forward reaction, ca. 4 vs ca. 14 mol kg⁻¹ h⁻¹, the reverse reaction). The better performance at 50 bar is explained by the minimum formation of CO due to the CO₂/CO reaction being also in equilibrium, which is caused by the promotion of the propane formation rate. This result suggests a substantial modification of the CO₂/CO/MeOH equilibrium but also, as expected, a limitation in propane production due to the system thermodynamics.

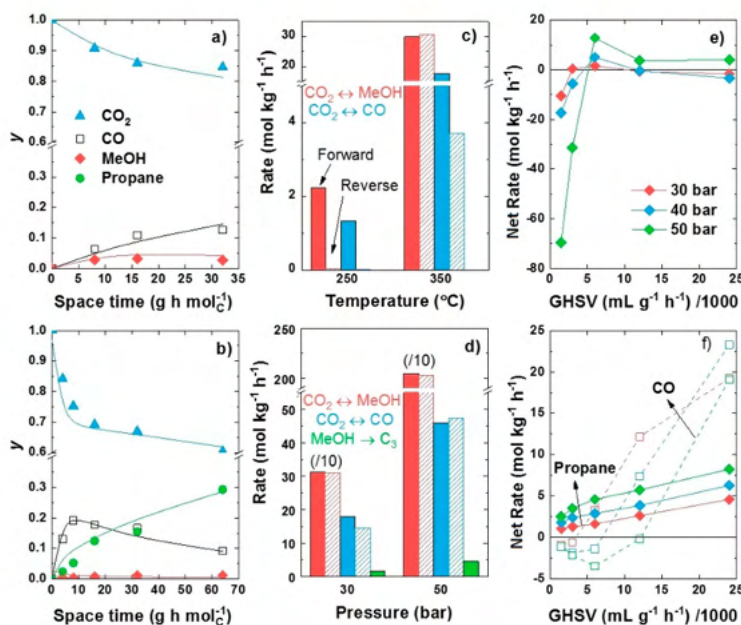


Figure 3. Experimental data fitting of (a) CO_2 to methanol over the PdZn/ZrO_2 catalyst at $300\text{ }^\circ\text{C}$ and 30 bar and (b) CO_2 to propane over the PdZn/ZrO_2 +SAPO-34 system at $350\text{ }^\circ\text{C}$ and 50 bar. (c) Comparison of reaction rates for methanol and CO formation over the PdZn/ZrO_2 catalyst at 250 and $350\text{ }^\circ\text{C}$ and 30 bar ($12000\text{ mL g}^{-1}\text{ h}^{-1}$), and (d) influence of propane formation on these rates over the PdZn/ZrO_2 +SAPO-34 system at $350\text{ }^\circ\text{C}$ and 30 and 50 bar ($6000\text{ mL g}^{-1}\text{ h}^{-1}$). Evolution with GHSV of the net formation rate of (e) methanol and (f) CO and propane over the PdZn/ZrO_2 +SAPO-34 system at $350\text{ }^\circ\text{C}$.

The selective methanol conversion can be better observed in the evolution with GHSV of MeOH (Figure 3e), CO, and propane (Figure 3f) net formation rates. Those corresponding to the stand-alone PdZn/ZrO_2 catalyst can be found in Figure S6. At high GHSV values, MeOH formation rate tends to zero, with maximum rates for CO and propane formation. This coincides with the lowest CO_2 conversion values shown in Figure 1b. At conditions of optimized CO_2 conversion with low GHSV values, the net rate of MeOH decreases to negative values, also leading to a significant decrease in CO net formation rate. As a consequence, the propane rate is selectively higher, explaining the highest selectivity to this product at these conditions (Figures 1b and 3f). Moreover, all these trends are maximized when the pressure is increased, with 50 bar being the optimal pressure to enhance propane selective formation.

As previously discussed, the conversion of MeOH into propane takes place through the dual-cycle mechanism and a fast hydrogenation of the formed olefins. This industrial process over SAPO-34 suffers a well-known fast deactivation due to the formation of coke within the zeotype cages. For this reason, deactivation can also play a role in the view of the industrial implementation of the tandem process presented herein. Therefore, the effect of in situ regeneration at $600\text{ }^\circ\text{C}$ was studied with a 5% O_2 in N_2 stream for 5 h (Figure S7). The catalytic system is rather stable for at least 48 h and only at

very high space velocity values ($24000\text{ mL g}^{-1}\text{ h}^{-1}$), deactivation is significant. In particular, after deactivation at $24000\text{ mL g}^{-1}\text{ h}^{-1}$, the products selectivity is mainly a mix of MeOH and DME with CO (73% MeOH, 26% DME and 1% CH_4), whereas the CO_2 conversion remains invariable, further corroborating that the SAPO-34 component is the one being deactivated. However, the in situ regeneration worked for all samples and the initial activity was regained after the regeneration cycle at $600\text{ }^\circ\text{C}$.

3.3. Characterization of the Multifunctional Catalysts

The powder X-ray diffraction (PXRD) pattern of the as prepared PdZn/ZrO_2 sample is shown in Figure S8. The sample shows a diffraction pattern of zincite (ZnO), PdO, and tetragonal/cubic ZrO_2 . Concerning the ZrO_2 structure, even if cubic and tetragonal polymorphs are not discernible because of crystallite-induced peak broadening, their distinction is out of the scope of the present work. Indeed, as shown hereafter, ZrO_2 's major role is to be an active support of PdZn alloy for CO_2 adsorption through carbonates formation, making the identification of a single phase/mixture of monoclinic/tetragonal (cubic) polymorphs the most relevant detail.²⁶ Energy-dispersive X-ray spectroscopy (EDS) shows a molar composition of 2% Pd, 13% Zn, and 85% Zr, close to the theoretical synthesis value (Table S2).

Nitrogen adsorption-desorption isotherms of both SAPO-34 and ZSM-5 zeolites are depicted in Figure S9. The detailed

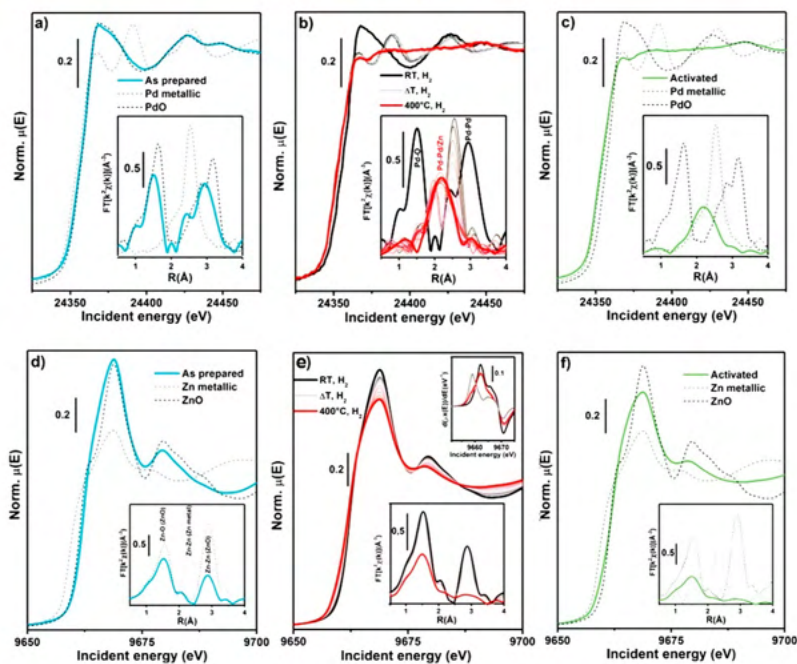


Figure 4. Pd K-edge, Zn K-edge XANES (main panels), and EXAFS (insets) spectra of PdZn/ZrO₂+ZSM-5 catalyst. XAS spectra for relevant reference compounds are also reported as dashed lines. (a) Pd K-edge for as prepared catalyst. (b) Pd K-edge for catalyst during activation (RT–400 °C) under H₂ gas flow. (c) Pd K-edge for catalyst after activation at 400 °C under H₂ atmosphere. (d) Zn K-edge for as prepared catalyst. (e) Zn K-edge for catalyst during activation (RT–400 °C) under a H₂ gas flow. Top right inset: first derivative of the XANES spectra for as prepared catalyst (black), activated catalyst (red), reference Zn(0) metal foil (light gray). (f) Zn K-edge for catalyst after activation at 400 °C under a H₂ gas flow. For clarity of comparison, the Pd metallic foil EXAFS signal was rescaled by a factor of 1/2. The EXAFS spectra reported in the bottom insets have been obtained by transforming the corresponding $k^2\chi(k)$ EXAFS function in the 2.5–11.0 Å⁻¹ range.

textural properties are summarized in Table S3. SAPO-34 displays a microporous type I isotherm and ZSM-5 a microporous type IV isotherm. The BET surface of SAPO-34 is estimated to be 770 m²/g with 762 m²/g of micropores, whereas for ZSM-5, it is estimated to be 417 m²/g with 296 m²/g of micropores. NH₃-TPD profiles of both zeolites are depicted in Figure S10. SAPO-34 displays only one peak at ca. 400 °C, whereas ZSM-5 displays the two characteristic peaks of weak (Lewis) and strong (Bronsted) acid sites at 225 and 425 °C, respectively.²⁷

3.3.1. Local Structure and Electronic Properties of Pd and Zn Species. X-ray absorption spectroscopy (XAS) was initially performed on the PdZn/ZrO₂ catalyst physically mixed with ZSM-5 aiming to characterize, in an element-selective way, Pd- and Zn-containing species formed in a model multifunctional system, in its as-prepared state and upon activation. The XAS spectra reported in Figure 4 show how electronic and structural features of both Pd and Zn change considerably when the catalyst is subjected to the activation treatment. Indeed, both XANES (main panels) and EXAFS spectra (insets) show substantial modifications at high temperature in the presence of H₂.

Considering the Pd K edge, the as-prepared catalyst (Figure 4a) presents the typical XANES (edge position, postedge resonances) and EXAFS (Pd–O bond in first coordination shell) features of the reference PdO, consistently with PXRD results (section 3.1). During activation (Figure 4b, from ca. 50 °C up to ca. 200 °C) Pd(II)-to-Pd(0) reduction is underlined by (i) shift of the absorption edge position to lower energy, (ii) rapid change of the oscillation in the XANES from PdO-like to those resembling metallic Pd (Figure 4a, b light gray line), and (iii) intensity loss of the Pd–O first coordination shell in the phase-uncorrected EXAFS (inset Figure 4b) and shift to lower R values of the Pd–Pd second coordination shell. As the temperature rises (300 °C), the oscillations in the XANES get flatter and EXAFS evolves into a single broad peak around 2.15 Å in the phase-uncorrected spectrum (Figure 4b red curve). These features were already observed and well reported in the case of other PdZn systems and ascribed to the formation of β₁-PdZn alloy.^{21,28–35} The EXAFS fit on the activated catalyst spectrum, reported in Figure S11, further confirmed the alloy formation. The fit obtained considering the simultaneous presence of Pd–Zn and Pd–Pd scattering paths well reproduced the experimental data. The magnitude and the

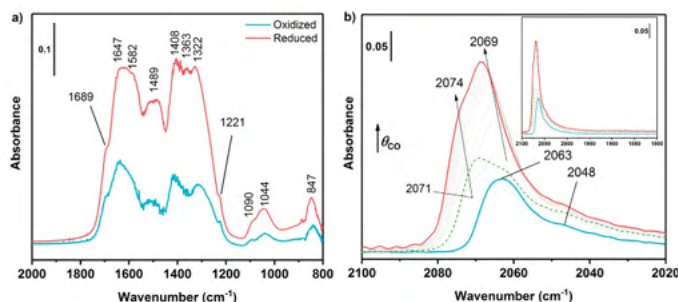


Figure 5. (a) FT-IR spectra of CO_2 adsorbed at RT on oxidized and activated PdZn/ZrO_2 at equilibrium pressure of 20 mbar. (b) FT-IR spectra of CO adsorbed at RT on activated PdZn/ZrO_2 . Spectra were acquired at increasing dosage of CO up to 20 mbar (from blue to red line) and after outgassing (green dashed line).

imaginary parts of the FT-EXAFS spectra (Figure S11a,b) presented a broad peak and a single oscillation, respectively. Analysis of the imaginary parts of the Pd–Pd and Pd–Zn scattering paths optimized in the fit (Figure S11c) highlighted a wide overlap of the two contributions, justifying the observed broadening in the experimental spectra (Figure S11a, b). Despite their overlap, Pd–Zn and Pd–Pd paths have a stronger contribution at lower and higher radial distances, respectively, leading to evaluation of a shorter Pd–Zn and a longer Pd–Pd path, the values of which are reported in Table S4 and confirmed the PdZn alloy formation.^{21,28} σ_2 values are consistent with the thermal contribution at 400 °C and are comparable with literature results obtained at similar temperatures.^{21,28}

Moving to the Zn K-edge, the as-prepared catalyst (Figure 4d) essentially presents the same XANES and EXAFS features of the reference ZnO , also in line with PXRD analysis of the as-prepared PdZn/ZrO_2 phase. A careful observation of the EXAFS data unveils a lower intensity of the second shell peak in the catalyst with respect to the reference oxide (inset Figure 4d), indicating a higher concentration of defects in the former. From the Zn perspective, the activation protocol causes (i) a pronounced decrease of the signal intensity in both the XANES and EXAFS region and (ii) a subtle red-shift of the edge energy position, better observed from the growth of a shoulder at low energy values in the XANES first derivative, matching the first maximum for Zn(0) metal foil (top right inset Figure 4e). Zn species are present in the activated sample (Figure 4f), and therefore they dominantly occur as a highly defective ZnO phase with a minor Zn(0) contribution ascribable to the fraction of Zn taking part to the formation of PdZn alloy. Despite its nature as a bulk-sensitive technique, in the case of ion-exchanged zeolite/zeotype systems, XAS becomes extremely sensitive to the absorber atom local environment.^{36–39} In the case of other PdZn/zeolite combined systems, Zn was observed to diffuse within the zeolite,²⁹ modifying the Zn local environment and leading to characteristic Zn K-edge spectra well reported in the literature.³⁸ In the case of the system here investigated, i.e., PdZn/ZrO_2 +zeolite, fingerprints of Zn-exchanged zeolite were not observed,³⁸ suggesting that impregnating Pd and Zn over ZrO_2 stabilizes the former atoms, avoiding their further diffusion into the zeolitic component.

3.3.2. Surface Interactions with Key Reactants and Molecular Probes.

Differently from XAS, which provided an element-selective view on Pd- and Zn-containing species in a representative combined system, FT-IR analysis was focused on the stand-alone PdZn/ZrO_2 system. Exploring its interaction with key reactants/molecular probes (H_2 , CO_2 , and CO), we aimed at confirming and further deepening two major issues related to the CO_2 -hydrogenation functionality, namely activation-driven oxygen vacancies formation and nature of the PdZn phase.

Zinc oxide phase plays a key role for both intermediate stabilization and H_2 heterolytic splitting thanks to its propensity to form stoichiometric defects (such as oxygen vacancies).^{40–42} In our case, the presence of a ZnO phase is shown by XAS and XRD results. Specifically, according to XAS, after the activation a highly defective ZnO phase is formed, together with the PdZn alloy. Hence, CO_2 hydrogenation can be due to the oxygen-vacancy formation in the defective ZnO phase. To investigate the formation of oxygen vacancies, different IR measurements were performed in H_2 at different temperatures, as well as under oxidizing conditions for comparison purposes.

To understand the IR results, it is important to underline that lattice defects, such as oxygen vacancies (V_{O}), make ZnO a semiconducting material.^{43–45} Neutral V_{O} shows two trapped electrons located in levels at 0.05 and 0.18 eV below the conduction band (C.B.). The first electronic level is very near to the bottom of the C.B., so that the majority of electrons can be moved to the C.B. at room temperature to produce monoionized oxygen vacancies (V_{O}^-). The second ionization of V_{O} can be promoted by IR, and thus it is possible to observe the photoionization of monoionized oxygen vacancies. Typically, pure ZnO shows a broad absorption band centered at about 1450 cm^{-1} , i.e. 0.18 eV, after reduction treatments.⁴⁵ Interaction with H_2 can create V_{O}^- following two main pathways: (i) the filling with an electron of pre-existing bionized V_{O} (V_{O}^{2+}) by consuming adsorbed oxygen species, such as O_2^- , O^- , O_2^{2-} ; (ii) the generation of new V_{O}^+ extracting lattice oxygen ions from the surface, but this route occurs only at high temperature. The IR method is not able to discriminate the two routes for V_{O}^- formation.

Figure S12 displays different spectra obtained in H_2 at different temperature from 50 to 400 °C. The broad absorption band related to monoionized oxygen vacancies is

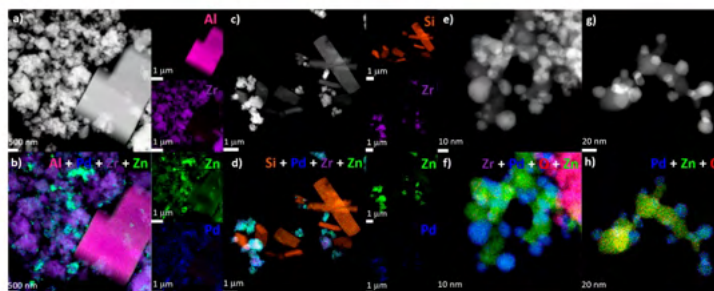


Figure 6. Low-magnification HAADF-STEM imaging of PdZn/ZrO₂ catalysts mixed either with (a) SAPO-34 and with (c) ZSM-5 crystals and (b, d) related elemental maps built with *K_α* emission lines provided by Al, Si, Pd, Zr, and Zn atoms. Magnification of the PdZn/ZnO nanoparticles observed at the edge of the ZrO₂ support when mixed either with (e) SAPO-34 and with (g) ZSM-5 crystals. (f, h) Associated overlaps of elemental maps.

well evident. The band increases in intensity up to 150 °C, losing intensity at higher temperature. The intensity loss can be ascribed to the PdZn alloy formation evidenced by XAS measurements (reduction of Zn²⁺ to Zn⁰ occurs at the expense of electrons trapped in V_O[•]). As a matter of fact, the formation of metallic Zn at this temperature is not expected, but it could be favored by Pd presence and alloy formation. The band is centered at about 1250 cm⁻¹, which corresponds to monoionized oxygen vacancies at about 0.15 eV under the C.B., very near to the ionization energy observed for pure ZnO. The obtained results, in agreement with XAS findings, demonstrate the presence of a highly defective ZnO-like phase.

To explore the interaction/adsorption of CO₂ with the catalyst surface, we followed adsorption at room temperature on both oxidized and H₂-activated PdZn/ZrO₂ by FT-IR spectroscopy and spectra, reported in Figure 5a. All the shown bands can be assigned to different carbonate species. These species could be formed on both the ZnO and ZrO₂ phase; however, CO₂ adsorption on ZnO^{46,47} and tetragonal ZrO₂⁴⁸ gives carbonates with spectral features different from those shown in Figure 5a. In particular, tetragonal zirconia gives an appreciable amount of polydentate bridging carbonates that are not present in our case. Bare ZnO gives an appreciable amount of bicarbonates that are present in very small amounts in our case. None of them forms the bridged and monodentate species that are present for the PdZn/ZrO₂ catalyst. More specifically, the following adsorbed species can be identified:^{47–53} (i) bicarbonates, weak bands at 1689 and 1221 cm⁻¹, assigned to $\nu(\text{C}=\text{O})$ and $\delta(\text{C}-\text{O}-\text{H})$ modes, respectively; (ii) bridged carbonates, bands at 1647, 1322, and 1044 cm⁻¹, assigned to $\nu(\text{C}=\text{O})$, $\nu_{\text{sym}}(\text{O}-\text{C}-\text{O})$, and $\nu_{\text{sym}}(\text{O}-\text{C}-\text{O})$ modes, respectively; (iii) bidentate carbonates, bands at 1582, 1363, and 1044 cm⁻¹, assigned to $\nu(\text{C}=\text{O})$, $\nu_{\text{sym}}(\text{O}-\text{C}-\text{O})$, and $\nu_{\text{sym}}(\text{O}-\text{C}-\text{O})$ modes, respectively; (iv) monodentate carbonates, bands at 1489, 1408, and 1090 cm⁻¹, assigned to $\nu_{\text{sym}}(\text{O}-\text{C}-\text{O})$, $\nu_{\text{sym}}(\text{O}-\text{C}-\text{O})$, and $\nu(\text{C}-\text{O})$, respectively. The band at 847 cm⁻¹ can be related to the $\delta(\text{O}-\text{C}-\text{O})$ mode of both monodentate and bidentate carbonates, as mentioned by some works on different oxides.^{54,55}

Spectral features obtained for the oxidized sample are the same obtained for the activated one, but the overall intensity of the bands in Figure 5a shows that there are much more carbonates on the activated sample when compared with the

oxidized one. The reason could reside in the stoichiometric defect formation: reduction generates oxygen vacancies on the surface of ZnO, giving a highly defective phase more suitable for carbonate formation. In light of this result, we reasonably ascribe the formation of carbonate species mainly to CO₂ adsorption on this phase. Different spectral features with respect to bare ZnO carbonates^{47,56} can be related to the fact that ZnO is a supported phase in our system. This causes the presence of huge amount of surface defects, such as edges, corners and kinks, beside stoichiometric defectiveness, which is characteristic of ZnO itself. Surface defects are able to create high heterogeneity of surface-adsorbed species. Moreover, the interaction with both ZrO₂ and Pd reasonably contributes to carbonate species heterogeneity.

CO adsorption at room temperature was also performed to characterize metallic Pd and explore its interaction to CO. The adsorption was carried out on activated PdZn/ZrO₂, i.e., after reduction in H₂ at 400 °C. Figure 5b reports several spectra obtained at increasing CO coverage (θ_{CO}) corresponding to increasing CO pressure up to 20 mbar: an asymmetric band in the region between 2080 and 2020 cm⁻¹ appears and increases in intensity upon increasing pressure. The band lies in the region of Pd⁰ linear carbonyls^{48,57} and more specifically, it appears constituted by different components: the main peak at 2063 cm⁻¹ that shifts to 2069 cm⁻¹ at the maximum CO coverage and two shoulders at 2071 cm⁻¹ (2074 cm⁻¹ for the maximum θ_{CO}) and 2048 cm⁻¹. As a matter of fact, the frequencies reached at the maximum coverage are quite lower with respect to the characteristic ones of Pd⁰ linear carbonyls. According to literature,^{58–60} the lower frequencies can be ascribed to CO on Pd sites in the PdZn alloy. Indeed, the dilution of Pd in the alloy deletes the dipolar coupling and changes in the electronic properties of Pd, induced by the alloying, can slightly increase π -backdonation.

To assign the different components, it is worth remembering that the Pd⁰-CO bond shows strong π -backdonation character; as a consequence, the lower the band frequency the more coordinatively unsaturated the site.⁶¹ Hence, the shoulder at 2048 cm⁻¹ is assigned to CO adsorbed on highly defective Pd⁰ sites, such as corners, the main band at 2063–2069 cm⁻¹ to less defective sites, such as edges, whereas the shoulder at the higher frequency can be related to terrace sites.

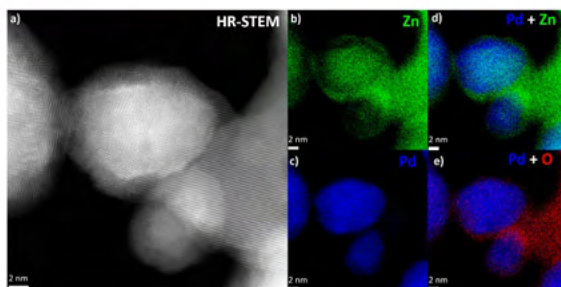


Figure 7. (a) High-resolution HAADF-STEM imaging of a PdZn alloy nanoparticle after CO₂ hydrogenation. Elemental maps of the same area built with *K α* emission lines: (b) Zn, (c) Pd, (d) overlap of Pd and Zn maps, and (e) overlap of Pd and O maps.

As for the blue shift observed by increasing coverage, it can be explained by two phenomena: the dipolar coupling and the “chemical effect”. The first one is predominant for terrace sites on regular facets but, in our case, it can be neglected due to the presence of Pd dilution by alloying with Zn, as evidenced by XAS measurements. The second one is caused by the decrease in π -backdonation as the number of adsorbed CO molecules increases, so that the higher the θ_{CO} , the lower the donated electron density per each adsorbed molecule. Therefore, upon increasing coverage, the π -backdonation contribution to all adsorbed CO molecules becomes weaker and weaker, and then an increase in $\nu(\text{C}\equiv\text{O})$ is observed.

After outgassing (dashed-green line in Figure 5b), the intensity of the peak is drastically reduced but not totally brought down, showing a certain stability of Pd⁰–CO at room temperature. It is important to note that the outgassing cancels out all of the effect due to the θ_{CO} . Hence, the peaks are shifted back to their original frequency, with slightly different relative intensities of the three main absorptions. Pd is also known to form a considerable amount of bridged carbonyls on different supports when reduced to metallic Pd.^{48,62} In our case, it is worth noting the absence of bridged Pd–carbonyls in the region between 2000 and 1800 cm⁻¹ (inset Figure 5b). This highlights the absence of neighboring Pd atoms, confirming the PdZn alloy formation, in agreement with XAS results.

3.3.3. Morphological/Chemical Insights on Used Multifunctional Catalysts. Imaging by high-angle annular dark-field scanning transmission electron microscopy (HAADF-STEM) was performed to investigate the morphological properties of the PdZn/ZrO₂ catalyst mixed either with SAPO-34 or with ZSM-5, recovered after catalytic testing for 24 h at 350 °C, 30 bar, and 12000 mL g⁻¹ h⁻¹. The low-magnification micrograph presented in Figure 6a shows a typical juxtaposition of large cubic SAPO-34 crystals with the PdZn/ZrO₂ function showing as nanoparticle agglomerates. Furthermore, Zr, Zn, and Pd elemental maps computed from X-ray fluorescence spectroscopy (STEM-EDX) reveal that most of the Pd and Zn atoms are distributed at the periphery of the ZrO₂ support (Figure 6b). Similar observations are also recorded when the PdZn/ZrO₂ catalyst is mixed with ZSM-5 (Figure 6c, d). Besides, there is no clear signal from the X-ray fluorescence spectra that would suggest a quantitative migration of Pd and Zr atoms over or into SAPO-34 and ZSM-5 crystals during CO₂ hydrogenation. However, a small X-ray emission from Zn atoms was detected in both case (<1

wt %). The nature of those Zn species was difficult to pinpoint given their low abundance and the thickness of the SAPO-34 and ZSM-5 crystals.

Magnification on the edge of the ZrO₂ support shows nanoparticles in 5–30 nm range (Figure 6e, g). Interestingly, some nanoparticles appear brighter, suggesting the presence of heavier atoms, e.g., Pd. The atomic composition shown on Figure 6f, h) reveals a mixture of ZnO and alloyed PdZn nanoparticles, as suggested by former HAADF imaging and consistently with the spectroscopy results presented in section 3.2. Quantification of the Pd and Zn atomic content at the core of the PdZn alloy by X-ray fluorescence provides a Pd/Zn molar ratio of 1.16 ± 0.15 and 1.27 ± 0.14 for SAPO-34 and ZSM-5, respectively (measurement performed on ca. 20 particles). All the observations described below are identical for both catalysts, mixed either with ZSM-5 or with SAPO-34.

High-resolution STEM images highlight a core–shell structure displaying clearly resolved lattice fringes (Figure 7a). The shell is polycrystalline as seen from the various orientation of lattice fringes and has a thickness of about 2 nm. In contrast, the core appears monocrystalline and composed of Pd and Zn atoms. Subsequent elemental mapping provides more details related to the shell composition, which is divided in two parts: (i) a main volume attached to the core where Zn is depleted and metallic Pd majorly remains (Figure 7b–d), (ii) an outer layer composed of zinc oxide (Figure 7b, d, and e). Those compositional characteristics were already reported by Armbrüster et al.^{63–65} for PdZn/ZnO catalysts used with methanol steam reforming (i.e., the inverse reaction: CH₃OH + H₂O → 3 H₂ + CO₂). They have shown that the oxidation of the PdZn alloy by the CO₂ gas causes the Zn atoms to leave the intermetallic phase and rise to the surface, forming ZnO patches.

Since a reoxidation of the metallic particles with O₂ from the air prior to TEM imaging cannot be univocally ruled out,⁶⁶ those results were completed with a imaging study handled without air exposure both after H₂ activation and CO₂ hydrogenation. Initially, the sample in its as-synthesized state displays grapes of PdO nanoparticles with a size in the 1–3 nm which are distributed between the ZnO nanoparticles (Figure S14). During H₂ activation, the PdO nanoparticles within the grapes merges and reduces into 10 to 30 nm metallic nanoparticles (Figure S15). The elemental composition as revealed by STEM-EDS shows clearly the formation of a Pd–Zn alloy at that stage. CO₂ hydrogenation is also confirmed to

induce the formation of the ZnO shell on the surface of the Pd–Zn alloy (Figures S16 and S17). The latter phenomenon was further established by multiple observations in several area of the sample (Figure S18).

To obtain deeper insight into deactivation pathways in bifunctional systems, UV-Raman spectroscopy was also used to characterize the multifunctional system. Figure S13 reports Raman spectra collected at RT on SAPO-34 alone and on the fresh and spent PdZn/ZrO₂+SAPO-34 combined catalyst. Spectra of the bare SAPO-34 and of fresh PdZn/ZrO₂+SAPO-34 are almost superimposable. The most intense signals are observed for the spent catalyst, i.e., two intense peaks at 1630 and 1384 cm⁻¹. The latter also presents an evident shoulder at higher Raman shifts, roughly centered at 1420 cm⁻¹. All these features relate to species trapped in the zeotype cages, identifiable as fingerprints of alkenes (1630 and 1420 cm⁻¹ modes)^{67–69} and polycyclic aromatic hydrocarbons (1383 cm⁻¹ peak, typical for naphthalene).⁷⁰ TGA analysis was further employed on the spent hybrid system to quantify the amount of coke, showing a 2.96 wt % weight loss in the 300–600 °C region that can be attributed to coke (see Figure 7b). This is evidence for an incipient catalyst deactivation by coking due to the condensation of methanol-to-hydrocarbon reaction intermediates and can justify the decrease in propane production (over SAPO-34) while constant CO₂ conversion (over the PdZn/ZrO₂ function) is observed at high GHSV values in Figure S7a.

3.4. Reaction Mechanism for the CO₂ Conversion to Propane

On the basis of the above results, we propose a reaction mechanism for the CO₂ conversion to propane on the PdZn/ZrO₂+SAPO-34 multifunctional systems (see Figure 8). First, a

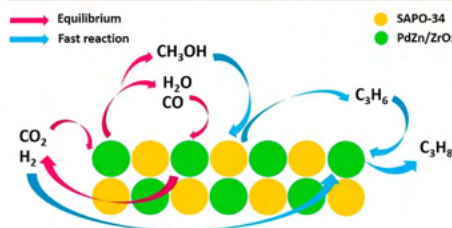


Figure 8. Reaction mechanism for the CO₂ conversion to propane over the PdZn/ZrO₂+SAPO-34 system.

PdZn alloy is formed during catalyst activation, in intimate contact with oxygen-vacancy rich ZnO particles over the ZrO₂ support, as demonstrated by XAS and FT-IR (see section 3.3). This alloy, once exposed to the CO₂-containing reaction feed, develops into a core–shell structure (see Figure 7) with a 2 nm polycrystalline ZnO shell and it is directly responsible of the MeOH formation in the PdZn/ZrO₂ component.^{71–75} This MeOH formed in the alloy instantly reacts over the SAPO-34 following a classical MTO mechanism with propene as the main product.^{76,77} The instant consumption of MeOH can be ascribed to the intimate mixture of both PdZn/ZrO₂ and SAPO-34 and ultimately causes a CO₂/CO/MeOH equilibria displacement, increasing the CO₂ conversion and reducing drastically the CO selectivity (from 95% to 35%, see Figure 2a). The rapid transformation of MeOH to hydrocarbons

(mainly propene) over SAPO-34 tends to minimize the formation rate of CO as a side product over the PdZn/ZrO₂ catalyst, which can be explained by a shift in the reverse WGS (Figure 3). Nevertheless, an avoided formation of CO via MeOH degradation in the PdZn/ZrO₂ due to its transformation to hydrocarbons cannot be discarded. This was suggested by the clear differences in the net formation rates of CO when SAPO-34 was added to the catalytic bed (Figure 3c, d). Moreover, the H₂O formed as byproduct over SAPO-34 can also displace the reverse WGS equilibrium (reaction 2 in Supporting Information, CO₂ + H₂ → CO + H₂O),⁷⁸ further reducing the CO selectivity. Lastly, the again intimately mixed PdZn/ZrO₂ rapidly hydrogenates the propene produced over SAPO-34, forming the resulting propane.

CONCLUSIONS

In conclusion, we have developed a highly active and selective PdZn/ZrO₂+SAPO-34 multifunctional catalyst for the direct conversion of CO₂ to propane that displays a total selectivity to propane higher than 50% (with 20% CO, 6% C₁, 13% C₂, 10% C₄, and 1% C₅) and a CO₂ conversion close to 40% at 350 °C, 50 bar, and 1500 mL g⁻¹ h⁻¹. These results can be rationalized as a consequence of the combined effects of each component of the multifunctional system. First, the alloy formed during catalyst activation is responsible for the formation of MeOH in the PdZn/ZrO₂ component. XAS and FT-IR, together with high-resolution HAADF-STEM imaging, demonstrate that this alloy is directly responsible for the initial high CO₂ conversion and evolves into a core–shell structure with a 2 nm polycrystalline ZnO shell. The MeOH formed in the PdZn/ZrO₂ component instantly reacts over the SAPO-34 forming propene as main product following a classic MTO mechanism. This rapid MeOH consumption triggers several reaction equilibrium shifts, ultimately boosting the initial CO₂ conversion and minimizing the CO selectivity. Lastly, the Pd component of the system hydrogenates all the propene formed over the intimately mixed SAPO-34, resulting in a paraffins hydrocarbon selectivity over 99.9%. Our results confirm the great importance of synergies in catalyst development for the production of individual hydrocarbons from CO₂ with the ultimate goal of facilitating the transition to renewable, non-fossil-fuel-based energy sources.

ASSOCIATED CONTENT

Supporting Information

The Supporting Information is available free of charge at <https://pubs.acs.org/doi/10.1021/jacsau.1c00302>.

CO₂ hydrogenation thermodynamics (Figures S1 and S2), kinetic model for CO₂ hydrogenation (Methodology, Table S1 and Figures S3–S6), regeneration of the PdZn/ZrO₂+SAPO-34 multifunctional catalyst (Figures S7), chemical and textural characterization of catalysts (Tables S2 and S3 and Figures S8–S10), spectroscopic characterization of the PdZn/ZrO₂ (Table S4 and Figures S11–S13), imaging of the PdZn/ZrO₂ and PdZn/ZrO₂+SAPO-34 catalysts (Figures S14–S18) (PDF)

AUTHOR INFORMATION

Corresponding Authors

Unni Olsbye – SMN Centre for Materials Science and Nanotechnology, Department of Chemistry, University of Oslo, Oslo N-0315, Norway; orcid.org/0000-0003-3693-2857; Email: unni.olsbye@kjemi.uio.no

Jorge Gascon – KAUST Catalysis Center (KCC), King Abdullah University of Science and Technology, Thuwal 23955, Saudi Arabia; orcid.org/0000-0001-7558-7123; Email: jorge.gascon@kaust.edu.sa

Silvia Bordiga – Department of Chemistry, NIS Center and INSTM Reference Center, University of Turin, Turin 10125, Italy; orcid.org/0000-0003-2371-4156; Email: silvia.bordiga@unito.it

Authors

Adrian Ramirez – KAUST Catalysis Center (KCC), King Abdullah University of Science and Technology, Thuwal 23955, Saudi Arabia

Pierfrancesco Ticali – Department of Chemistry, NIS Center and INSTM Reference Center, University of Turin, Turin 10125, Italy; orcid.org/0000-0003-3514-0196

Davide Salusso – Department of Chemistry, NIS Center and INSTM Reference Center, University of Turin, Turin 10125, Italy; orcid.org/0000-0001-7927-4001

Tomas Cordero-Lanzac – SMN Centre for Materials Science and Nanotechnology, Department of Chemistry, University of Oslo, Oslo N-0315, Norway

Samy Ould-Chikh – KAUST Catalysis Center (KCC), King Abdullah University of Science and Technology, Thuwal 23955, Saudi Arabia; orcid.org/0000-0002-3486-0944

Christian Ahoba-Sam – SMN Centre for Materials Science and Nanotechnology, Department of Chemistry, University of Oslo, Oslo N-0315, Norway

Aram L. Bugaev – The Smart Materials Research Institute, Southern Federal University, Rostov-on-Don 344090, Russian Federation; orcid.org/0000-0001-8273-2560

Elisa Borfecchia – Department of Chemistry, NIS Center and INSTM Reference Center, University of Turin, Turin 10125, Italy; orcid.org/0000-0001-8374-8329

Sara Morandi – Department of Chemistry, NIS Center and INSTM Reference Center, University of Turin, Turin 10125, Italy; orcid.org/0000-0003-0577-7911

Matteo Signorile – Department of Chemistry, NIS Center and INSTM Reference Center, University of Turin, Turin 10125, Italy; orcid.org/0000-0003-0521-3702

Complete contact information is available at: <https://pubs.acs.org/10.1021/jacsau.1c00302>

Notes

The authors declare no competing financial interest.

ACKNOWLEDGMENTS

This project has received funding from the European Union's Horizon 2020 research and innovation programme under grant agreement 837733. The XAS measurements were supported by a public grant overseen by the French National Research Agency (ANR) as part of the "Investissements d'Avenir" program (reference: ANR-10-EQPX-45). The authors are grateful to C. La Fontaine and V. Briosis, as well as to K. A. Lomachenko and A. Lazzarini for the help with the XAS experiment at ROCK, Soleil. Dr. Idoia Hita Del Olmo is

acknowledged for her help with the TGA measurements. A.R., S.O.C., and J.G. acknowledge financial support from King Abdullah University of Science and Technology (KAUST). C.A.S. acknowledges the Norwegian Research Council for financial support through project no. 288331 (CO2LO). A.L.B. acknowledges the President's Grant of Russian Federation MK-5853.2021.1.2.

REFERENCES

- (1) Markewitz, P.; Kuckshinrichs, W.; Leitner, W.; Linssen, J.; Zapp, P.; Bongartz, R.; Schreiber, A.; Müller, T. E. Worldwide Innovations in the Development of Carbon Capture Technologies and the Utilization of CO₂. *Energy Environ. Sci.* **2012**, *5* (6), 7281.
- (2) Centi, G.; Quadrelli, E. A.; Perathoner, S. Catalysis for CO₂ Conversion: A Key Technology for Rapid Introduction of Renewable Energy in the Value Chain of Chemical Industries. *Energy Environ. Sci.* **2013**, *6* (6), 1711.
- (3) Ojelade, O. A.; Zaman, S. F. A Review on CO₂ hydrogenation to Lower Olefins: Understanding the Structure-Property Relationships in Heterogeneous Catalytic Systems. *Journal of CO₂ Utilization* **2021**, *47*, 101506.
- (4) Dittmeyer, R.; Klumpp, M.; Kant, P.; Ozin, G. Crowd Oil Not Crude Oil. *Nat. Commun.* **2019**, *10* (1), 1818.
- (5) Zhou, W.; Cheng, K.; Kang, J.; Zhou, C.; Subramanian, V.; Zhang, Q.; Wang, Y. New Horizon in C1 Chemistry: Breaking the Selectivity Limitation in Transformation of Syngas and Hydrogenation of CO₂ into Hydrocarbon Chemicals and Fuels. *Chem. Soc. Rev.* **2019**, *48* (12), 3193–3228.
- (6) Ramirez, A.; Dutta Chowdhury, A.; Dokania, A.; Cnudde, P.; Caglayan, M.; Yarulina, I.; Abou-Hamad, E.; Gevers, L.; Ould-Chikh, S.; de Wispelaere, K.; van Speybroeck, V.; Gascon, J. Effect of Zeolite Topology and Reactor Configuration on the Direct Conversion of CO₂ to Light Olefins and Aromatics. *ACS Catal.* **2019**, *9* (7), 6320–6334.
- (7) Dokania, A.; Ramirez, A.; Bavykina, A.; Gascon, J. Heterogeneous Catalysis for the Valorization of CO₂: Role of Bifunctional Processes in the Production of Chemicals. *ACS Energy Letters* **2019**, *4* (1), 167–176.
- (8) Shih, C. F.; Zhang, T.; Li, J.; Bai, C. Powering the Future with Liquid Sunshine. *Joule* **2018**, *2* (10), 1925–1949.
- (9) *Propane Market—Growth, Trends, And Forecast (2020–2025)*; Report Linker, 2020.
- (10) Liu, Z.; Ni, Y.; Sun, T.; Zhu, W.; Liu, Z. Conversion of CO₂ and H₂ into Propane over InZrO and SSZ-13 Composite Catalyst. *J. Energy Chem.* **2021**, *54*, 111–117.
- (11) De, S.; Dokania, A.; Ramirez, A.; Gascon, J. Advances in the Design of Heterogeneous Catalysts and Thermocatalytic Processes for CO₂ Utilization. *ACS Catal.* **2020**, *10* (23), 14147–14185.
- (12) Ge, Q.; Li, X.; Kaneko, H.; Fujimoto, K. Direct Synthesis of LPG from Synthesis Gas over Pd-Zn-Cr/Pd-β Hybrid Catalysts. *J. Mol. Catal. A: Chem.* **2007**, *278* (1–2), 215–219.
- (13) Li, C.; Fujimoto, K. Selective Synthesis of Isobutane from CO₂-Containing Synthesis Gas. *Energy Fuels* **2014**, *28* (2), 1331–1337.
- (14) Li, G.; Jiao, F.; Miao, D.; Wang, Y.; Pan, X.; Yokoi, T.; Meng, X.; Xiao, F. S.; Parvulescu, A. N.; Müller, U.; Bao, X. Selective Conversion of Syngas to Propane over ZnCrOx-SSZ-39 OX-ZEO Catalysts. *J. Energy Chem.* **2019**, *36*, 141–147.
- (15) Li, C.; Fujimoto, K. Synthesis Gas Conversion to Isobutane-Rich Hydrocarbons over a Hybrid Catalyst Containing Beta Zeolite – Role of Doped Palladium and Influence of the SiO₂/Al₂O₃ Ratio. *Catal. Sci. Technol.* **2015**, *5* (9), 4501–4510.
- (16) Li, C.; Yuan, X.; Fujimoto, K. Direct Synthesis of LPG from Carbon Dioxide over Hybrid Catalysts Comprising Modified Methanol Synthesis Catalyst and β-Type Zeolite. *Appl. Catal., A* **2014**, *475*, 155–160.
- (17) Ge, Q.; Tomonobu, T.; Fujimoto, K.; Li, X. Influence of Pd Ion-Exchange Temperature on the Catalytic Performance of Cu-

- ZnO/Pd- β Zeolite Hybrid Catalyst for CO Hydrogenation to Light Hydrocarbons. *Catal. Commun.* **2008**, *9* (8), 1775–1778.
- (18) Ticali, P.; Salusso, D.; Ahmad, R.; Ahoba-Sam, C.; Ramirez, A.; Shterk, G.; Lomachenko, K. A.; Borfecchia, E.; Morandi, S.; Cavallo, L.; Gascon, J.; Bordiga, S.; Olsbye, U. CO₂ Hydrogenation to Methanol and Hydrocarbons over Bifunctional Zn-Doped ZrO₂/Zeolite Catalysts. *Catal. Sci. Technol.* **2021**, *11*, 1249.
- (19) La Fontaine, C.; Belin, S.; Barthe, L.; Roudenko, O.; Briois, V. ROCK: A Beamline Tailored for Catalysis and Energy-Related Materials from Ms Time Resolution to Mm Spatial Resolution. *Synchrotron Radiation News* **2020**, *33* (1), 20–25.
- (20) Ravel, B.; Newville, M. ATHENA, ARTEMIS, HEPHAESTUS: Data Analysis for X-Ray Absorption Spectroscopy Using IFEFFIT. *J. Synchrotron Radiat.* **2005**, *12*, 537–541.
- (21) Tew, M. W.; Emerich, H.; Van Bokhoven, J. A. Formation and Characterization of PdZn Alloy: A Very Selective Catalyst for Alkyne Semihydrogenation. *J. Phys. Chem. C* **2011**, *115* (17), 8457–8465.
- (22) Signorile, M.; Bonino, F.; Damin, A.; Bordiga, S. A Novel Raman Setup Based on Magnetic-Driven Rotation of Sample. *Top. Catal.* **2018**, *61* (14), 1491–1498.
- (23) Yarulina, L.; Chowdhury, A. D.; Meirer, F.; Weckhuysen, B. M.; Gascon, J. Recent Trends and Fundamental Insights in the Methanol-to-Hydrocarbons Process. *Nature Catalysis* **2018**, *1* (6), 398–411.
- (24) Bavykina, A.; Yarulina, L.; Al Abdughani, A. J.; Gevers, L.; Hechili, M. N.; Miao, X. H.; Galilea, A. R.; Pustovarenko, A.; Dikhtiarenko, A.; Cadiou, A.; Aguilera-Tapia, A.; Hazemann, J. L.; Kozlov, S. M.; Oud-Chikh, S.; Cavallo, L.; Gascon, J. Turning a Methanation Co Catalyst into an In-Co Methanol Producer. *ACS Catal.* **2019**, *9* (8), 6910–6918.
- (25) Arora, S. S.; Shi, Z.; Bhan, A. Mechanistic Basis for Effects of High-Pressure H₂ Cofeeds on Methanol-to-Hydrocarbons Catalysis over Zeolites. *ACS Catal.* **2019**, *9* (7), 6407–6414.
- (26) Bachiller-Baeza, B.; Rodriguez-Ramos, L.; Guerrero-Ruiz, A. Interaction of Carbon Dioxide with the Surface of Zirconia Polymorphs. *Langmuir* **1998**, *14* (13), 3556–3564.
- (27) Lónyi, F.; Vályon, J. On the Interpretation of the NH₃-TPD Patterns of H-ZSM-5 and H-Mordenite. *Microporous Mesoporous Mater.* **2001**, *47* (2–3), 293–301.
- (28) Gallagher, J. R.; Childers, D. J.; Zhao, H.; Winans, R. E.; Meyer, R. J.; Miller, J. T. Structural Evolution of an Intermetallic Pd-Zn Catalyst Selective for Propane Dehydrogenation. *Phys. Chem. Chem. Phys.* **2015**, *17* (42), 28144–28153.
- (29) Ahoba-Sam, C.; Borfecchia, E.; Lazzarini, A.; Bugaev, A.; Isah, A. A.; Taoufik, M.; Bordiga, S.; Olsbye, U. On the Conversion of CO₂ to Value Added Products over Composite PdZn and H-ZSM-5 Catalysts: Excess Zn over Pd, a Compromise or a Penalty? *Catal. Sci. Technol.* **2020**, *10*, 4373–4385.
- (30) Gentzen, M.; Doronkin, D. E.; Sheppard, T. L.; Zimina, A.; Li, H.; Jelic, J.; Stedt, F.; Grunwaldt, J. D.; Sauer, J.; Behrens, S. Supported Intermetallic PdZn Nanoparticles as Bifunctional Catalysts for the Direct Synthesis of Dimethyl Ether from CO-Rich Synthesis Gas. *Angew. Chem., Int. Ed.* **2019**, *58* (44), 15655–15659.
- (31) Kast, P.; Friedrich, M.; Girgsdies, F.; Kröhnert, J.; Teschner, D.; Lunkenbein, T.; Behrens, M.; Schlögl, R. Strong Metal-Support Interaction and Alloying in Pd/ZnO Catalysts for CO Oxidation. *Catal. Today* **2016**, *260*, 21–31.
- (32) Jerero, E.; Lebarbier, V.; Datye, A.; Wang, Y.; Vohs, J. M. Interaction of CO with Surface PdZn Alloys. *Surf. Sci.* **2007**, *601* (23), 5546–5554.
- (33) Johnson, R. S.; DeLaRiva, A.; Ashbacher, V.; Halevi, B.; Villanueva, C. J.; Smith, G. K.; Lin, S.; Datye, A. K.; Guo, H. The CO Oxidation Mechanism and Reactivity on PdZn Alloys. *Phys. Chem. Chem. Phys.* **2013**, *15* (20), 7768–7776.
- (34) Bollmann, L.; Ratts, J. L.; Joshi, A. M.; Williams, W. D.; Pazzino, F.; Joshi, Y. V.; Miller, J. T.; Kropf, A. J.; Delgass, W. N.; Ribeiro, F. H. Effect of Zn Addition on the Water-Gas Shift Reaction over Supported Palladium Catalysts. *J. Catal.* **2008**, *257* (1), 43–54.
- (35) Kattel, S.; Ramirez, P. J.; Chen, J. G.; Rodriguez, J. A.; Liu, P. Active Sites for CO₂ Hydrogenation to Methanol on Cu/ZnO Catalysts. *Science* **2017**, *355* (6354), 1296–1299.
- (36) Bordiga, S.; Groppo, E.; Agostini, G.; Van Bokhoven, J. A.; Lamberti, C. Reactivity of Surface Species in Heterogeneous Catalysts Probed by in Situ X-Ray Absorption Techniques. *Chem. Rev.* **2013**, *113* (3), 1736–1850.
- (37) Martini, A.; Borfecchia, E.; Lomachenko, K. A.; Pankin, I. A.; Negri, C.; Berlier, G.; Beato, P.; Falsig, H.; Bordiga, S.; Lamberti, C. Composition-Driven Cu-Speciation and Reducibility in Cu-CHA Zeolite Catalysts: A Multivariate XAS/FTIR Approach to Complexity. *Chemical Science* **2017**, *8* (10), 6836–6851.
- (38) Pinilla-herrero, I.; Borfecchia, E.; Holzinger, J.; Mentzel, U. V.; Joensen, F.; Lomachenko, K. A.; Bordiga, S.; Lamberti, C.; Berlier, G.; Olsbye, U.; Svelle, S.; Skibsted, J.; Beato, P. High Zn/Al Ratios Enhance Dehydrogenation vs Hydrogen Transfer Reactions of Zn-ZSM-5 Catalytic Systems in Methanol Conversion to Aromatics. *J. Catal.* **2018**, *362*, 146–163.
- (39) Pinilla-herrero, I.; Borfecchia, E.; Cordero-Lanzac, T.; Mentzel, U. V.; Joensen, F.; Lomachenko, K. A.; Bordiga, S.; Olsbye, U.; Beato, P.; Svelle, S. Finding the Active Species: The Conversion of Methanol to Aromatics over Zn-ZSM-5/Alumina Shaped Catalysts. *J. Catal.* **2021**, *394*, 416–428.
- (40) Rozanov, V. V.; Krylov, O. V. Hydrogen Spillover in Heterogeneous Catalysis. *Russ. Chem. Rev.* **1997**, *66* (2), 107–119.
- (41) Conner, W. C.; Falconer, J. L. Spillover in Heterogeneous Catalysis. *Chem. Rev.* **1995**, *95* (3), 759.
- (42) Ye, J.; Liu, C.; Mei, D.; Ge, Q. Active Oxygen Vacancy Site for Methanol Synthesis from CO₂ Hydrogenation on In₂O₃(110): A DFT Study. *ACS Catal.* **2013**, *3* (6), 1296–1306.
- (43) Ogur, U.; Alivov, Y. I.; Liu, C.; Teke, A.; Reshchikov, M. A.; Dogan, S.; Avrutin, V.; Cho, S.-J.; Morkoc, H. A Comprehensive Review of ZnO Materials and Devices. *J. Appl. Phys.* **2005**, *98* (4), 041301.
- (44) Göpel, W.; Lampe, U. Influence of Defects on the Electronic Structure of Zinc Oxide Surfaces. *Phys. Rev. B: Condens. Matter Mater. Phys.* **1980**, *22* (12), 6447–6462.
- (45) Morandi, S.; Fioravanti, A.; Cerrato, G.; Lettieri, S.; Sacerdoti, M.; Carotta, M. C. Facile Synthesis of ZnO Nano-Structures: Morphology Influence on Electronic Properties. *Sens. Actuators, B* **2017**, *249* (3), 581–589.
- (46) Esken, D.; Noei, H.; Wang, Y.; Wiktor, C.; Turner, S.; Van Tendeloo, G.; Fischer, R. A. ZnO@ZIF-8: Stabilization of Quantum Confined ZnO Nanoparticles by a Zinc Methylimidazolate Framework and Their Surface Structural Characterization Probed by CO₂ Adsorption. *J. Mater. Chem.* **2011**, *21* (16), 5907–5915.
- (47) Busca, G.; Lorenzelli, V. Infrared Spectroscopic Identification of Species arising from Reactive Adsorption of Carbon Oxides on Metal Oxide Surfaces. *Mater. Chem.* **1982**, *7*, 89–126.
- (48) Föttinger, K.; Emhofer, W.; Lennow, D.; Ruppelcher, G. Adsorption and Reaction of CO on PdAl₂O₄ and PdZrO₂: Vibrational Spectroscopy of Carbonate Formation. *Top. Catal.* **2017**, *60* (19–20), 1722–1734.
- (49) Lavalley, J. C. Infrared Spectrometric Studies of the Surface Basicity of Metal Oxides and Zeolites Using Adsorbed Probe Molecules. *Catal. Today* **1996**, *27* (3–4), 377–401.
- (50) Köck, E.-M.; Kogler, M.; Biele, T.; Klötzer, B.; Penner, S. In Situ FT-IR Spectroscopic Study of CO₂ and CO Adsorption on Y₂O₃, ZrO₂, and Yttria-Stabilized ZrO₂. *J. Phys. Chem. C* **2013**, *117* (34), 17666–17673.
- (51) Pokrovski, K.; Jung, K. T.; Bell, A. T. Investigation of CO and CO₂ Adsorption on Tetragonal and Monoclinic Zirconia. *Langmuir* **2001**, *17*, 4297–4303.
- (52) Akune, T.; Morita, Y.; Shirakawa, S.; Katagiri, K.; Inumaru, K. ZrO₂ Nanocrystals As Catalyst for Synthesis of Dimethylcarbonate from Methanol and Carbon Dioxide: Catalytic Activity and Elucidation of Active Sites. *Langmuir* **2018**, *34* (1), 23–29.

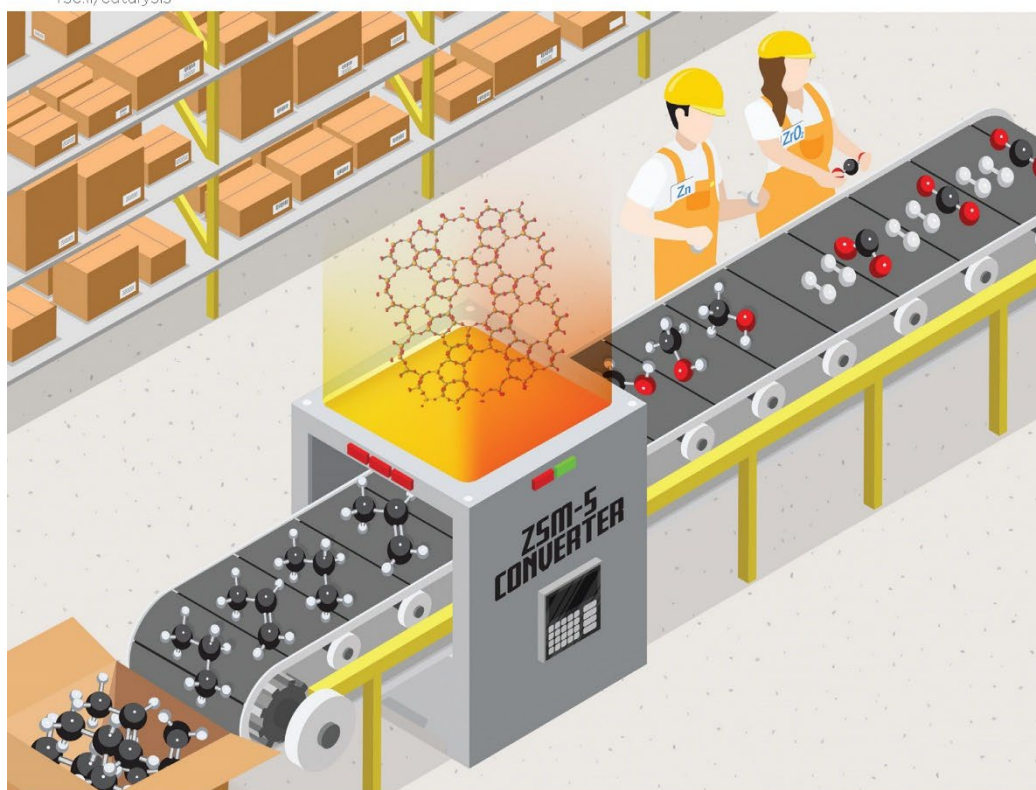
- (53) Bachiller-Baeza, B.; Rodríguez-Ramos, L.; Guerrero-Ruiz, A. Interaction of Carbon Dioxide with the Surface of Zirconia Polymorphs. *Langmuir* **1998**, *14* (13), 3556–3564.
- (54) Freund, H.-J.; Roberts, M. W. Surface Chemistry of Carbon Dioxide. *Surf. Sci. Rep.* **1996**, *25*, 225–273.
- (55) Ramis, G.; Busca, G.; Lorenzelli, V. Low-Temperature CO₂ Adsorption on Metal Oxides: Spectroscopic Characterization of Some Weakly Adsorbed Species. *Mater. Chem. Phys.* **1991**, *29* (1–4), 425–435.
- (56) Esken, D.; Noei, H.; Wang, Y.; Wiktor, C.; Turner, S.; Van Tendeloo, G.; Fischer, R. A. ZnO@ZIF-8: Stabilization of Quantum Confined ZnO Nanoparticles by a Zinc Methylimidazolate Framework and Their Surface Structural Characterization Probed by CO₂ Adsorption. *J. Mater. Chem.* **2011**, *21* (16), 5907–5915.
- (57) Groppo, E.; Bertarione, S.; Rotunno, F.; Agostini, G.; Scarano, D.; Pellegrini, R.; Leofanti, G.; Zecchina, A.; Lamberti, C. Role of the Support in Determining the Vibrational Properties of Carbonyls Formed on Pd Supported on SiO₂-Al₂O₃, Al₂O₃, and MgO. *J. Phys. Chem. C* **2007**, *111* (19), 7021–7028.
- (58) Föttinger, K. The Effect of CO on Intermetallic PdZn/ZnO and Pd₂Ga/Ga₂O₃ Methanol Steam Reforming Catalysts: A Comparative Study. *Catal. Today* **2013**, *208*, 106–112.
- (59) Conant, T.; Karim, A. M.; Lebarbier, V.; Wang, Y.; Girgsdies, F.; Schlögl, R.; Datye, A. Stability of Bimetallic Pd-Zn Catalysts for the Steam Reforming of Methanol. *J. Catal.* **2008**, *257* (1), 64–70.
- (60) Rameshan, C.; Stadlmayr, W.; Weilach, C.; Penner, S.; Lorenz, H.; Havelcker, M.; Blume, R.; Rocha, T.; Teschner, D.; Knop-Gericke, A.; Schlögl, R.; Memmel, N.; Zemlyanov, D.; Rupprechter, G.; Klötzer, B. Subsurface-Controlled CO₂ Selectivity of PdZn near-Surface Alloys in H₂ Generation by Methanol Steam Reforming. *Angew. Chem., Int. Ed.* **2010**, *49* (18), 3224–3227.
- (61) Hollins, P. The Influence of Surface Defects on the Infrared Spectra of Adsorbed Species. *Surf. Sci. Rep.* **1992**, *16* (2), 51–94.
- (62) Khivantsev, K.; Jaegers, N. R.; Kovarik, L.; Hanson, J. C.; Tao, F.; Tang, Y.; Zhang, X.; Koleva, L. Z.; Aleksandrov, H. A.; Vayssilov, G. N.; Wang, Y.; Gao, F.; Szanyi, J. Achieving Atomic Dispersion of Highly Loaded Transition Metals in Small-Pore Zeolite SSZ-13: High-Capacity and High-Efficiency Low-Temperature CO and Passive NO_x Adsorbers. *Angew. Chem., Int. Ed.* **2018**, *57* (51), 16672–16677.
- (63) Nowicka, E.; Althabban, S. M.; Luo, Y.; Krieger, R.; Shaw, G.; Morgan, D. J.; He, Q.; Watanabe, M.; Armbrüster, M.; Kiely, C. J.; Hutchings, G. J. Highly Selective PdZn/ZnO Catalysts for the Methanol Steam Reforming Reaction. *Catal. Sci. Technol.* **2018**, *8* (22), 5848–5857.
- (64) Friedrich, M.; Penner, S.; Heggen, M.; Armbrüster, M. High CO₂ Selectivity in Methanol Steam Reforming through ZnPd/ZnO Teamwork. *Angew. Chem., Int. Ed.* **2013**, *52* (16), 4389–4392.
- (65) Heggen, M.; Penner, S.; Friedrich, M.; Dunin-Borkowski, R. E.; Armbrüster, M. Formation of ZnO Patches on ZnPd/ZnO during Methanol Steam Reforming: A Strong Metal–Support Interaction Effect? *J. Phys. Chem. C* **2016**, *120* (19), 10460–10465.
- (66) Föttinger, K.; Van Bokhoven, J. A.; Nachtegaal, M.; Rupprechter, G. Dynamic Structure of a Working Methanol Steam Reforming Catalyst: In Situ Quick-EXAFS on Pd/ZnO Nanoparticles. *J. Phys. Chem. Lett.* **2011**, *2* (5), 428–433.
- (67) Signorile, M.; Rojo Gama, D.; Bonino, F.; Svelle, S.; Beato, P.; Bordiga, S. Operando UV-Raman Study of the Methanol to Olefins Reaction over SAPO-34: Spatiotemporal Evolution Monitored by Different Reactor Approaches. *Catal. Today* **2019**, *336*, 203–209.
- (68) Signorile, M.; Rojo-Gama, D.; Bonino, F.; Beato, P.; Svelle, S.; Bordiga, S. Topology-Dependent Hydrocarbon Transformations in the Methanol-to-Hydrocarbons Reaction Studied by Operando UV-Raman Spectroscopy. *Phys. Chem. Chem. Phys.* **2018**, *20* (41), 26580–26590.
- (69) Sheppard, N.; Simpson, D. M. The Infra-Red and Raman Spectra of Hydrocarbons. Part I. Acetylenes and Olefins. *Q. Rev., Chem. Soc.* **1952**, *6* (1), 1–33.
- (70) Signorile, M.; Bonino, F.; Damin, A.; Bordiga, S. In Situ Resonant UV-Raman Spectroscopy of Polycyclic Aromatic Hydrocarbons. *J. Phys. Chem. C* **2015**, *119* (21), 11694–11698.
- (71) Bahruji, H.; Bowker, M.; Jones, W.; Hayward, J.; Ruiz Esquius, J.; Morgan, D. J.; Hutchings, G. J. PdZn Catalysts for CO₂ Hydrogenation to Methanol Using Chemical Vapour Impregnation (CVI). *Faraday Discuss.* **2017**, *197*, 309–324.
- (72) Malik, A. S.; Zaman, S. F.; Al-Zahrani, A. A.; Daous, M. A.; Driss, H.; Petrov, L. A. Development of Highly Selective PdZn/CeO₂ and Ca-Doped PdZn/CeO₂ Catalysts for Methanol Synthesis from CO₂ Hydrogenation. *Appl. Catal., A* **2018**, *560* (April), 42–53.
- (73) Malik, A. S.; Zaman, S. F.; Al-Zahrani, A. A.; Daous, M. A.; Driss, H.; Petrov, L. A. Selective Hydrogenation of CO₂ to CH₃OH and In-Depth DRIFT Analysis for PdZn/ZrO₂ and CaPdZn/ZrO₂ Catalysts. *Catal. Today* **2020**, *357*, 573.
- (74) Ojelade, O. A.; Zaman, S. F.; Daous, M. A.; Al-Zahrani, A. A.; Malik, A. S.; Driss, H.; Shterk, G.; Gascon, J. Optimizing Pd:Zn Molar Ratio in PdZn/CeO₂ for CO₂ Hydrogenation to Methanol. *Appl. Catal., A* **2019**, *584* (May), 117185.
- (75) Ojelade, O. A.; Zaman, S. F. A Review on Pd Based Catalysts for CO₂ Hydrogenation to Methanol: In-Depth Activity and DRIFTS Mechanistic Study. *Catal. Surv. Asia* **2020**, *24* (1), 11–37.
- (76) Hereijgers, B. P. C.; Bleken, F.; Nilsen, M. H.; Svelle, S.; Lillerud, K.-P.; Bjorgen, M.; Weckhuysen, B. M.; Olsbye, U. Product Shape Selectivity Dominates the Methanol-to-Olefins (MTO) Reaction over H-SAPO-34 Catalysts. *J. Catal.* **2009**, *264* (1), 77–87.
- (77) Dahl, L. M.; Kolboe, S. On the Reaction Mechanism for Propene Formation in the MTO Reaction over SAPO-34. *Catal. Lett.* **1993**, *20* (3–4), 329–336.
- (78) Daza, Y. A.; Kuhn, J. N. CO₂ Conversion by Reverse Water Gas Shift Catalysis: Comparison of Catalysts, Mechanisms and Their Consequences for CO₂ Conversion to Liquid Fuels. *RSC Adv.* **2016**, *6* (55), 49675–49691.

A.2

Catalysis Science & Technology

Volume 11
Number 4
21 February 2021
Pages 1143–1640

rsc.li/catalysis

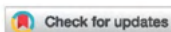


ISSN 2044-4761



PAPER

Jorge Gascon, Silvia Bordiga, Unni Olsbye *et al.*
CO₂ hydrogenation to methanol and hydrocarbons over
bifunctional Zn-doped ZrO₂/zeolite catalysts

Cite this: *Catal. Sci. Technol.*, 2021,
11, 1249**CO₂ hydrogenation to methanol and hydrocarbons over bifunctional Zn-doped ZrO₂/zeolite catalysts†**Pierfrancesco Ticali,^a Davide Salusso,^{†a} Rafia Ahmad,^b Christian Ahoba-Sam,^b Adrian Ramirez,^b Genrikh Shterk,^d Kirill A. Lomachenko,^{b,d} Elisa Borfecchia,^{b,a} Sara Morandi,^b Luigi Cavallo,^b Jorge Gascon,^b Silvia Bordiga,^{a*} and Unni Olsbye^{b,c*}

The tandem process of carbon dioxide hydrogenation to methanol and its conversion to hydrocarbons over mixed metal/metal oxide-zeolite catalysts is a promising path to CO₂ valorization. Herein, we report three Zn-doped ZrO₂ catalysts prepared by co-precipitation of Zn- and Zr-containing salts to obtain three different loadings of Zn (5, 15 and 30 wt%). In the context of bifunctional catalysts, we combined ZrZnO_x with two of the most performing zeolite/zeotype catalysts for the methanol-to-hydrocarbons (MTH) reaction: H-ZSM-5 and H-SAPO-34. Catalytic testing at 250–350 °C and 20–40 bar revealed that H-ZSM-5 is more stable and more capable of converting methanol at low temperature, whereas H-SAPO-34 shows the highest C₃ selectivity. The best performance was observed for the ZrZnO_x sample with 30% Zn, combined with ZSM-5 at 350 °C, 30 bar and H₂/CO₂/N₂ = 6/2/1. Under these conditions, the equilibrium methanol yield was observed after 0.4 s g⁻¹ ml⁻¹ over ZrZnO_x alone. Mixing with ZSM-5 in a 1:1 weight ratio, methanol was rapidly converted to hydrocarbons, with an optimum C₃ productivity of 1.5 mol kg⁻¹ h⁻¹ at 24 000 ml h⁻¹ g⁻¹. An extensive surficial, textural and structural characterization of ZrZnO_x alone was carried out by FT-IR spectroscopy, N₂ adsorption/desorption at liquid nitrogen temperature, PXRD and XAS. Formation of a ZrZnO_x tetragonal solid solution was confirmed for all the samples (PXRD, XAS). The amount of Zr⁴⁺ sites at the surface was found to decrease, while the number of oxygen vacancies increased after H₂ treatment at 400 °C, coherent with an increase of Zn loading (FT-IR). DFT modelling pointed out that once a stoichiometric oxygen vacancy is induced by the presence of Zn, the formation of extra oxygen vacancies during activation is thermodynamically favored. Moreover, i) the oxygen vacancies were found to play an active role in CO₂ hydrogenation, in accordance with experimental data, and ii) methanol is most likely formed via the formate pathway, and is energetically favored compared to CO formation, in agreement with the high methanol selectivity observed experimentally at low CO₂ conversion. Importantly, *operando*-XAS, XPS, TEM and PXRD studies of the as-prepared, pretreated and tested catalysts showed that the structure and composition of the catalyst is not affected by the reaction. Indeed, a final catalytic test carried out on the regenerated ZrZnO_x/H-ZSM-5 catalyst showed that the initial performances were completely restored and no Zn exchange in the zeolite was observed neither before nor after testing.

Received 3rd August 2020.
Accepted 22nd November 2020

DOI: 10.1039/d0cy01550d

rsc.li/catalysis

^a Department of Chemistry, NIS Center and INSTM Reference Center, University of Turin, 10125, Turin, Italy. E-mail: silvia.bordiga@unito.it^b King Abdullah University of Science and Technology, KAUST Catalysis Center (KCC), Thuwal 23955, Saudi Arabia. E-mail: jorge.gascon@kaust.edu.sa^c SMN Centre for Materials Science and Nanotechnology, Department of Chemistry, University of Oslo, N-0315 Oslo, Norway. E-mail: unni.olsbye@kjemi.uio.no^d European Synchrotron Radiation Facility, CS 40320, 38043 Grenoble Cedex 9, France

† Electronic supplementary information (ESI) available. See DOI: 10.1039/d0cy01550d

* Authors equally contributed.

1. Introduction

Today, the use of fossil fuels, coal, oil and natural gas represents the main source of carbon dioxide, which is principally responsible for the increment of global temperature. Its concentration in the atmosphere already overtook planetary boundary estimates and is expected to keep rising, reaching 570 ppm at the end of the century.¹

The single carbon atom that CO₂ possesses can be recovered and eventually added to other organic chemicals to obtain useful products. Technologies to recover and convert

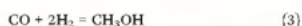
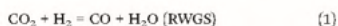


CO₂ have been known since the mid-19th century, however, only from the 1970s, CO₂ found its first industrial application in the synthesis of methanol from CO₂-enriched syngas (CO and H₂).² To date, CO₂ capture and utilization represents a promising route to control its emission while limiting fossil fuel extraction. Currently, biological, electrochemical and catalytic processes are all exploited for CO₂ valorization. Concerning the catalytic processes, carbon capture and storage (CCS) technologies² can be coupled with utilization of CO₂ as a feedstock in: i) low energy processes³ such as production of urea, carbonates, carbamates and ii) high-energy processes where high-value chemicals (CH₄, HCOOH, and CH₃OH) are obtained.^{2,4}

High-energy processes mostly exploit the capability of certain materials to reduce carbon dioxide to hydrocarbons and/or olefins. However, as CO₂ is the most oxidized form of carbon, it is located in a thermodynamic well, which makes its chemical reduction challenging,⁵ such that high temperature and pressure are required, increasing the total cost of the process.

CO₂ reduction can be achieved by using H₂: both academic and industrial research efforts are today focused on using renewable sources of H₂ to reduce the environmental impact of these processes.^{6,7} Hydrogenation is industrially exploited for the production of methanol, massively employed as a solvent, alternative fuel and feedstock for the chemical industry. To date, industrial-scale methanol production is still carried out from syngas over Cu/ZnO/Al₂O₃ catalysts developed by Imperial Chemical Industries (ICI).⁸ Partial substitution of the feed with CO₂ causes a drastic catalyst selectivity decreases⁸ due to the reverse water gas shift (RWGS) reaction (eqn (1)).

Another approach is to convert methanol to hydrocarbons in the same reaction batch. For this purpose, bifunctional catalysts play a key role in carbon dioxide hydrogenation and conversion to organic compounds, but the main challenge consists of compromising the catalyst performances, such as activity, selectivity and conversion, with the energy cost of the total reaction, *i.e.* low pressure and temperature (1 bar, <400 °C). The main reactions involved in this process are:



Recently, several groups^{9–14} investigated bifunctional catalysts obtained by combining a metal or metal oxide phase employed in CO₂ conversion to methanol with a selective zeolite/zeotype for the methanol-to-hydrocarbons process (MTH). However, the coexistence of two catalysts under the same reaction conditions is challenging. As a matter of fact, each catalyst should be the most appropriate for each

reaction and, simultaneously, the two active phases must not poison each other, *e.g.* water production in the second step of the reaction may induce sintering of the catalyst dedicated to methanol synthesis.¹⁵ Moreover, at high temperature, the possibility that the two materials undergo mutual interactions (*e.g.* inter-phase ion-exchange phenomena) altering their physico-chemical properties must be considered.¹⁰

Starting from the first step involved in CO₂ hydrogenation to methanol, it is important to compromise the thermodynamics of the reaction,¹⁶ *i.e.* methanol formation at low temperature and high pressure. From a global point of view, low temperature favors methanol production on the first catalyst while high temperature enhances methanol dehydration and C-C coupling in the zeolite. With this respect, high temperature moves the equilibrium of the first catalyst towards the endothermic RWGS reaction (eqn (1)).

In recent years, different research studies^{6,7,17–22} have been focused on using the same types of catalysts involved in the RWGS reaction but trying to promote: i) stabilization of intermediates for hydrogenation to methanol or other hydrocarbons instead of RWGS ones; ii) H₂ dissociation by heterolytic splitting; and iii) inhibition of the water poisoning effect, which hampers the catalytic hydrogenation activity.²¹

ZrO₂ has been investigated as a support material in many binary and ternary systems for CO/CO₂ hydrogenation to methanol.^{23–29} IR and TPD studies over pristine zirconia conducted by Pokrowski *et al.*³⁰ showed that CO and CO₂ are mainly adsorbed as HCO⁺, CO₃²⁻ and HCO₃⁻, m/b-CO₃²⁻, respectively. The CO₂ adsorption capacity increases with the strength of Zr⁴⁺ Lewis acid sites, O²⁻ Lewis basic sites and higher concentration and basicity of hydroxyl groups. However former studies showed that the main CO₂/ZrO₂ interaction occurs through the oxide basic sites;^{28,31} in particular with the formation of bicarbonate b-HCO₃-Zr,³⁰ which following hydrogenation is promoted from the weak hydrophilic character of the support.³² Recent NAP-XPS and IRAS studies by Li *et al.*³³ showed that the presence of hydroxyl groups on the ZrO₂ surface is essential for the bicarbonate species formation. Doping of ZrO₂ with an aliovalent cation (*e.g.* Zn²⁺) induces the formation of oxygen vacancies (V_O) and, as a direct consequence, generates defects featured by coordinatively unsaturated Zr⁴⁺ sites (*cus*-Zr⁴⁺) which can act as strong basic and acid sites respectively.³⁴

Carbon mono- and di-oxide activation was reported to be facilitated by the presence of neighbouring *cus*-Zr⁴⁺ ion sites and V_O.^{25,35–37} Thus, V_O enhance the Bronsted acidity of Zr-OH groups adjacent to *cus*-Zr⁴⁺ cations.³⁸ Between the potential dopants, Zn²⁺ has been investigated in the formation of ZnZrO_x solid solutions. CO₂ adsorption and methanol selectivity are enhanced by the increase of basic sites^{21,28,34} while H₂ activation is influenced by the synergy of Zn-Zr sites.³¹ Therefore, the simultaneous presence of *cus*-sites, V_O and surface hydroxyl groups seems to be a key combination to improve CO₂ adsorption, activation and hydrogenation to methanol.



Hence, both Zn and ZrO₂ seem to promote several reactions related to environmental concerns. To date, a major fraction of recent works based on Zn-Zr systems deals with syngas conversion^{13,36,37} whereas another fraction is devoted to Zn-Zr systems involved in CO₂ hydrogenation aiming for different products, such as methanol. In the case of Zn-doped ZrO₂ studied by Wang *et al.*,³¹ CO₂ conversion increases up to 20% at high temperatures (>320 °C) while methanol selectivity drops to less than 30%. These findings highlight that operation at high temperature thermodynamically favors side reactions, such as RWGS.¹⁶

In another recent contribution, Li *et al.*²⁹ used a metal-organic approach to prepare the catalysts by means of a Schiff base, yielding a Zn-doped ZrO₂ solid solution (with a 1 : 1 ratio). This catalyst showed a methanol selectivity of 70% with 5.7% CO₂ conversion at 320 °C, $V(\text{CO}_2)/V(\text{H}_2)/V(\text{N}_2) = 24/72/4\%$ and GHSV = 18 000 mL g⁻¹ h⁻¹. XRD and TEM/EDS analysis confirmed the doping of Zn in the ZrO₂ system, without any segregated phases. DRIFT spectroscopy was employed to investigate the produced species after CO₂ hydrogenation, highlighting the formation of CH₃O species on the ZnO-ZrO₂ phase, confirming that methanol is one of the main products obtained by this class of catalysts.

As for the zeolite/zeotype material for a selective MTH process, in recent years many acidic catalysts have been proposed focusing on features, such as pore and channel dimensions or reaction intermediates; recalling some examples, H-ZSM-5 has been proven to favor C₃ alkenes.^{13,39} Ongoing research efforts principally aim at: i) improving catalyst performance, *e.g.* by evaluating and optimizing Al dispersion in the zeolitic framework;^{40,41} ii) reducing coke and aromatic species formation, by understanding the influence of pore and channel dimensions in the search for optimized zeolite/zeotypes; iii) pushing temperature and pressure to a thermodynamically-favored range.

The Zn-Zr binary oxide has been combined with H-SAPO-34/H-ZSM-5/H-SSZ-13 to exploit hydrocarbon synthesis from syngas.^{13,36} Coupling a metal oxide for methanol production with a porous catalyst dedicated to MTH/MTO allows precise control of the elementary steps involved in the reaction (CO/CO₂ chemisorption, C-C coupling and C-C cleavage).⁴² The weak hydrogenating nature of ZnZrO₂ allows selective hydrogenation of CO/CO₂ but not the eventual production of olefins/hydrocarbons.

More recent works started to investigate tandem catalysts (ZnO-ZrO₂/zeolite and zeotype) for CO₂ hydrogenation. Li *et al.*¹⁴ studied a ZnO-ZrO₂ mixed metal oxide system, similar to those studied in this manuscript coupled with H-SAPO-34. A CO₂ conversion of 12.6% was found at 380 °C and 3600 mL g⁻¹ h⁻¹, with 80% selectivity to C₂-C₄. According to their XRD and HAADF-STEM findings, the sample is a solid solution with no trace of segregated phases. By means of DRIFT spectroscopy, they studied the reaction products adsorbed on the surface of the catalyst, concluding that CH_xO species are generated on the oxidic ZnZrO phase and then transferred onto SAPO zeolite for lower olefins production.

Similarly, Zhou *et al.* studied a ZnO-ZrO₂ solid solution in tandem with ZSM-5 zeolite and reported high selectivity towards aromatic products.⁴³

Choosing what kind of zeolite/zeotype material should be used in this reaction is not straightforward. Park *et al.*⁴⁴ compared two systems: CuZnO-ZrO₂/H-ZSM-5 and CuZnO-ZrO₂/H-SAPO-34. They found that the hydrocarbon distribution is strictly related to the nature of the zeolite. However, the interplay between the two catalytic functions is still not fully understood.

In this work, we investigated the catalytic properties of bifunctional catalysts obtained by physically mixing three different Zn-doped ZrO₂ (ZrZnO_x) with MTH-active zeolite/zeotype catalysts, H-ZSM-5 and H-SAPO-34. As such, our contribution represents a side-by-side comparison of these two materials combined with ZnZrO_x.

Firstly, we thoroughly characterized the oxidic phase by infrared spectroscopy (IR), powder X-ray diffraction (PXRD), N₂ adsorption/desorption and density functional theory (DFT) modelling, ultimately aiming at understanding its role in CO₂ hydrogenation. Specifically, our integrated characterization approach targeted: i) the role of Zn in creating defects; ii) the detailed properties of Zn and Zr sites as revealed by IR of adsorbed CO; iii) the response of the catalyst to high-temperature treatment under model oxidative and reducing conditions. Experimental findings were corroborated by theoretical modelling, which were also used to explore different reaction pathways for CO₂ hydrogenation over ZrZnO_x.

Secondly, we studied both the oxidic phase alone and the combined systems by catalytic test runs under different conditions, space times and after regeneration. For all the investigated cases, we determined the CO₂ conversion as well as methanol and hydrocarbon product distributions, highlighting the role of Zn in influencing the catalytic properties of the investigated systems.

Finally, we employed *operando* X-ray absorption spectroscopy (XAS) at Zr and Zn K-edges to directly probe the local structure and electronic properties of the ZrZnO_x/ZSM-5 system before and after activation in H₂, as well as to assess its stability under reaction conditions, *i.e.* high temperature (300 °C) and pressure (10 bar) under a CO₂/H₂ feed.

In this work, we aim to give a significant contribution to the understanding of the oxygen vacancy formation and its role in the CO₂ hydrogenation pathway, elucidating the synergy between cations in ZnZrO_x solid solutions. We also critically evaluated the relationship between experimental conditions (*i.e.* contact time) and catalyst activity towards value-added hydrocarbons at lower temperature than those usually reported in the literature.^{45,46}

2. Experimental

2.1. Materials

Three Zn-containing ZrO₂ samples were prepared by coprecipitation starting from solutions of zirconium and zinc



inorganic salts following the recipe from Wang *et al.*³¹ The samples were named ZrZn-*X*, where *X* is the Zn loading determined by ICP-AES analysis (*vide infra*) and reported in Table 1. The typical procedure for making sample ZrZn-30, taken as an example, was by mixing 0.6 g Zn(NO₃)₂·6H₂O and 2.15 g ZrN₂O₇·*x*H₂O in 100 ml of type 2 H₂O in a round bottom flask. The mixtures prepared for the three samples were then heated to 70 °C in an oil bath under reflux amidst stirring. 3.06 g (NH₄)₂CO₃ was dissolved in 100 ml of type 2 H₂O and then added to the warm precursor solutions dropwise: white precipitates immediately formed. The mixtures were further stirred at 70 °C for 2 h, cooled at ambient temperature, centrifuged and the precipitates were washed twice with type 2 H₂O. The wet powders were oven-dried at 110 °C and then calcined at 500 °C for 3 h.

Combined systems were obtained by mechanical mixing of the ZrZn-*X* catalysts with a commercial H-ZSM-5 zeolite with a mass ratio of 1:1. For comparison purposes, combined systems using commercial H-SAPO-34 were also prepared by the same mechanical mixing protocol. Commercial H-ZSM-5 and H-SAPO-34 characteristics are reported in the ESI†

2.2. Methods

2.2.1. Chemical, textural and structural characterization of the ZrZn-*X* catalysts. Zirconium and zinc contents in the ZrZn-*X* specimens were determined using a Perkin Elmer Optima 7000 DV (Perkin Elmer, Norwalk, Connecticut, USA) inductively coupled plasma-atomic emission spectrometer (ICP-AES) equipped with a PEEK Mira Mist nebulizer, a cyclonic spray chamber and an Echelle monochromator. The wavelengths used for Zr and Zn determination were $\lambda_{Zr} = 339.197$ nm and $\lambda_{Zn} = 213.857$ nm. For the analyses, a pre-treatment of the samples was required. Acid digestion of the oxides was carried out using a Milestone MLS-1200 MEGA microwave laboratory unit (Milestone, Sorisole, Italy). Aliquots of 200 mg of each sample were transferred in tetrafluoromethoxyl (TFM) bombs and digested with 2 mL of hydrofluoric acid and 5 mL of *aqua regia* before the analysis. Four heating steps of 5 min each (250, 400, 600, and 250 W power, respectively), followed by a ventilation step of 25 min,

were applied. Then 0.7 g of boric acid was added, and the bombs were further heated for 5 min at 250 W and again cooled by a ventilation step of 15 min. At the end of the full treatment, the samples appeared completely dissolved. The digested solutions were diluted to 20 mL with high purity water. Each sample was analysed in duplicate and each concentration value was averaged on the basis of three instrumental measurements. Blanks were simultaneously run. It is well-known that Hf, chemically similar to Zr, is a common natural contaminant in every Zr compound. For this reason, using $\lambda_{Hf} = 277.336$ nm the presence of Hf was determined to be less than 2 wt% for each sample, but there is no evidence about its influence on our results.

Specific surface areas (SSAs) and pore size distributions (PSDs) of the ZrZn-*X* samples were determined by applying the Brunauer-Emmett-Teller (BET) method and the DFT method, respectively, to the adsorption/desorption isotherms of N₂ at liquid nitrogen temperature obtained with a Micromeritics ASAP 2010 physisorption analyzer. PSDs were obtained applying the DFT method on cylindrical pores, using the Tarazona NLDFT approach. The adsorption/desorption isotherms were determined over a wide range of relative pressures ($10^{-6} < p/p_0 < 1$). All the samples underwent an activation step to remove physisorbed species from the surface while avoiding irreversible changes of the surface or the solid structure. Each sample was studied after outgassing under vacuum at 120 °C (heating ramp of 5 °C min⁻¹) for 5 h (residual pressure of 10⁻² mbar).

Powder X-ray diffraction (PXRD) patterns of the as-prepared ZrZn-*X* catalysts were collected at room temperature (RT) using a glass capillary ($\sigma = 0.3$ mm) in a PW3050/60 X'Pert PRO MPD diffractometer from PANalytical working with the Bragg-Brentano geometry. Patterns from the Cu K $\alpha_{1,2}$ X-ray source were recorded from 10 to 90° 2 θ with a step size of 0.0156° and an integration time of 150 s. The Rietveld refinement method implemented in the FullProf software package⁴⁷ was used to extract lattice parameters and average crystallite size from all the three samples. The PXRD patterns of ZrZn-30 alone and that physically mixed with the ZSM-5 zeolite recovered after catalytic tests (referred to as 'tested' in the following) were measured and refined following the same procedure mentioned above. We refer to the ESI† for the complete procedure description.

2.2.2. Spectroscopic characterization of the ZrZn-*X* catalysts. Absorption/transmission IR spectra were run on a Perkin-Elmer FTIR 2000 spectrophotometer equipped with a Hg-Cd-Te cryo-detector, working in the range of wavenumbers 7200–580 cm⁻¹ at a resolution of 2 cm⁻¹. For IR analysis, the ZrZn-*X* powders were compressed in self-supporting discs (~20 mg cm⁻²) and placed in IR cells suitable for different kinds of measurements. In particular, a commercial stainless steel cell (Aabspec), allowing thermal treatments *in situ* under vacuum or a controlled atmosphere and the simultaneous registration of spectra at temperatures up to 600 °C, was employed to study H₂ interaction at 400 °C on the pre-oxidized catalysts. IR measurements in hydrogen

Table 1 Chemical, textural and structural features of ZrZn-*X* catalysts. In order: Zn loading, specific surface area (SSA), pore volume, lattice parameter (*a* = *b*), and average crystallite size (*d*)

	ZrZn-5	ZrZn-15	ZrZn-30
Zn loading (wt%)	5	15	30
SSA (m ² g ⁻¹)	47	46	37
DFT cumulative pore volume (cm ³ g ⁻¹)	0.24	0.21	0.49
Space group	<i>P4₁/nmc</i>	<i>P4₁/nmc</i>	<i>P4₁/nmc</i>
<i>a</i> (= <i>b</i>) (Å)	3.6049 ± 0.0008	3.58900 ± 0.00018	3.59440 ± 0.0008
<i>c</i> (Å)	5.0980 ± 0.0015	5.1020 ± 0.0005	5.082 ± 0.002
Crystallite size (nm)	55 ± 1	20 ± 1	12 ± 1



were performed to study the effect of the activation step used for the catalytic tests (*vide infra*).

In order to characterize the Lewis acid sites, *i.e.* Zn²⁺ and Zr⁴⁺, at the surface of both pre-oxidized and pre-reduced samples, the catalysts were placed in a quartz IR cell, allowing thermal treatments and *ex situ* measurements of CO adsorption at liquid nitrogen temperature (LNT).

Before the IR measurements, the samples were outgassed under vacuum at 400 °C for 30 min and then oxidized or reduced. The oxidation pre-treatment was performed in dry oxygen (40 mbar) for 30 min at 400 °C. Finally, the samples were cooled to room temperature (RT) in O₂.

The reduction pre-treatment was performed in the same way using H₂. In this case, the hydrogen was outgassed at 400 °C and then the samples were cooled at RT under vacuum.

2.2.3. Molecular modelling of the ZrZn-X catalysts. Periodic cells were optimized with spin-polarized DFT calculations using the Vienna *ab initio* simulation package (VASP 5.4.4).^{48,49} Projector augmented wave (PAW)⁵⁰ potentials were used to describe the core electrons with the generalized gradient approximation (GGA) using the PBE⁵¹ functional including the Becke-Johnson damped D3 dispersion correction⁵² as implemented in VASP. The Kohn-Sham one-electron wave functions were expanded by using a plane wave basis set with a kinetic energy cutoff of 450 eV. The Brillouin zone of the structures was sampled using the Γ point. An energy convergence criterion of 10⁻⁶ eV and a force convergence criterion of 0.05 eV Å⁻¹ were used.

The unit lattice vectors and atoms of tetragonal ZrO₂ were fully optimized in the beginning. We began the geometry optimization with the experimental lattice parameter values, which were optimized to $a = b = 3.646$ Å, and $c = 5.275$ Å. The most stable surface of the tetragonal ZrO₂ phase was simulated by a 2 × 2 × 1 supercell model. To eliminate the artificial dipole moments within the slab model, we constructed a symmetric slab of at least 5 layers of Zr atoms. The slab was separated from its periodic image by 15 Å to avoid spurious interactions between the periodic slab models. The adsorption energy of the reactants and reaction intermediates was calculated as:

$$\Delta E[\text{adsorption}] = E[\text{adsorbate} + \text{surface}] - E[\text{adsorbate}] - E[\text{clean surface}]$$

2.2.4. Catalytic tests on the ZrZn-X catalysts and the combined ZrZn-X/zeolite systems. Catalytic tests were executed in a 16 channel Flowence® from Avantium. 50 mg of the stand-alone MeOH catalyst (ZrZn-X samples) or 100 mg of the combined catalyst with a ZrZn-X/zeolite mass ratio of 1:1 in a mixed bed configuration was typically used. The attention was focused on the systems with H-ZSM-5 zeolite; however, for comparison purposes, combined systems with H-SAPO-34 were also tested and the results are reported in the ESI† The gas feed composition was: 23 vol% of CO₂, 69 vol% of H₂ and 8 vol% of He as the internal standard. We

typically aimed to have 12 000 ml h⁻¹ g⁻¹ per channel. One of the 16 channels was always used without a catalyst as the blank. Prior to feeding the reaction mixture, all the samples were reduced *in situ* with a pure H₂ atmosphere for 4 hours at 400 °C. The tubes were then pressurized to 30 bar using a membrane-based pressure controller. Regeneration tests were carried out *in situ* at atmospheric pressure and 600 °C with a 5% O₂ in N₂ stream for 6 hours. In some cases, the reacted gas was diluted with N₂ (20 mL min⁻¹ per reactor) in the reactor outlet and automatically supplied for online gas chromatographic (GC) analysis.

The GC is an Agilent 7890B with two sample loops. After flushing the loops for 24 min, the content is injected. One sample loop goes to the TCD channel with 2 Haysep pre-columns and MS5A, where He, H₂, CH₄ and CO are separated. Gases that have longer retention times than CO₂ on the Haysep column (column 4 Haysep Q 0.5 m G3591-80023) are back-flushed. Further separation of permanent gases is done on another Haysep column (column 5 Haysep Q 6 Ft G3591-80013) to separate CO₂ before going to MS5A. Another sample loop goes to an Innowax pre-column (5 m, 0.20 mm OD, 0.4 μm film); in the first 0.5 min of the method, the gases coming from the pre-column are sent to the Gaspro column (Gaspro 30 M, 0.32 mm OD) followed by FID. After 0.5 min, the valve is switched and gases are sent to the Innowax column (45 m, 0.2 mm OD, 0.4 μm) followed by FID. The Gaspro column separates C₁-C₆ paraffins and olefins, while the Innowax column separates oxygenates and aromatics.

Conversions, CO selectivity, MeOH selectivity, hydrocarbon distribution selectivity (CO free) and C₃ productivity are reported on the C₁ basis and are defined as follows:

$$\text{Conv}_{\text{CO}_2} (\%) = \frac{\text{CO}_{2\text{bl}}/\text{He}_{\text{bl}} - \text{CO}_{2\text{r}}/\text{He}_{\text{r}}}{\text{CO}_{2\text{bl}}/\text{He}_{\text{bl}}} \times 100$$

$$S_{\text{CO}} (\%) = \frac{\frac{\text{CO}_{\text{bl}}}{\text{He}_{\text{bl}}}}{\left(\frac{\text{CO}_{2\text{bl}}}{\text{He}_{\text{bl}}} - \frac{\text{CO}_{2\text{r}}}{\text{He}_{\text{r}}}\right)} \cdot 100$$

$$S_{\text{MeOH}} (\%) = \frac{\frac{\text{C}_{\text{MeOH}}}{\text{C}_{\text{He}}}}{\left(\frac{\text{CO}_{2\text{bl}}}{\text{He}_{\text{bl}}} - \frac{\text{CO}_{2\text{r}}}{\text{He}_{\text{r}}}\right)} \cdot 100$$

$$C_n \text{ Hydrocarbon Sel} (\%) = \frac{n \cdot (C_n)}{\sum n \cdot C_n} \times 100$$

$$\text{Product}_{\text{C}_3} (\text{mol Kg}_{\text{cat}}^{-1} \text{ h}^{-1}) = \frac{\text{Yield} (\text{C}_3 + \text{C}_3^-) / 100 \cdot \text{GHSV}_{\text{CO}_2}}{22.4}$$

where C_{bl} and C_{r} are the concentrations determined by GC analysis in the blank and in the reactor outlet, respectively. Carbon balance closure was better than 2.5% in all cases.



2.2.5. XAS measurements on the combined ZrZn-X/ZSM-5 systems. Zn and Zr K-edge *operando* XAS experiments in transmission mode were performed at the Quick-XAS ROCK beamline⁵³ (Rocking Optics for Chemical Kinetics) of the French Synchrotron SOLEIL. A quasi-simultaneous scanning of Zr (17.7–19 keV) and Zn (9.3–10.7 keV) K-edges was possible thanks to the quick edge-jump feature of the ROCK beamline.⁵³ However, jumping between two absorption edges dictated to find a compromise between the sample thickness and the absorption length of both edges. Hard X-ray XAS allows monitoring with element-selectivity of the bulk properties of the combined systems and the ZrZn-X/zeolite interaction under *operando* conditions. For this purpose, around 5 mg of ZrZn-X: H-ZSM-5 = 1:1 physical mixture was mortar-grounded, sieved down to 40 μm and loaded in a quartz capillary reactor ($\phi = 1 \text{ mm}$). The capillary reactor was then connected to an appropriate gas-flow setup for the CO_2 hydrogenation reaction, supporting operation at high gas pressure. The temperature at the measurement position was controlled by a heat gun. The gas total flux was maintained constant (10 ml min^{-1}) during all the measurements. The measurement protocol for the three combined systems consisted of two main parts: 1. activation: heating (RT to $400 \text{ }^\circ\text{C}$, $5 \text{ }^\circ\text{C min}^{-1}$) at 1 bar in pure H_2 flow; 2. reaction: feed of $\text{CO}_2:\text{H}_2:\text{He} = 1.25:7.5:1 \text{ (mL min}^{-1}\text{)}$ at $300 \text{ }^\circ\text{C}$ (temperature showing the highest performance from the catalytic test) and 15 bar pressure.

Incident X-ray energy at both Zr and Zn K-edges was scanned by two quick-XAS monochromators, each mounted on a cam-driven tilt table that oscillates periodically around a fixed Bragg angle. A Si(111) monochromator was used to measure the Zn K-edge (9659 eV) while Si(220) was employed for the Zr K-edge (17 998 eV). Time-resolved data throughout the applied protocol were initially obtained as the average of 50 scans for an exposure time of 12.5 s and a total time/scan of 25 seconds. The reported XAS spectra representative of the as-prepared and activated catalysts, as well as of the catalysts under reaction conditions, are obtained upon further averaging of the time-resolved spectra obtained in the last 10 min of acquisition for each protocol step, after checking for the complete stabilization of the spectral features. Incident (I_0) and transmitted (I_t) beams were measured by two sets of ionization chambers. An energy step of 2 eV was used for the two edges. The energy sampling was intensified using a step of 0.2 eV in the main edge region for Zn (range: 9530–9780 eV) and of 0.4 eV for Zr (range: 17 970–18 120 eV). A third set of ionization chambers (I_t) was employed to measure simultaneously the transmitted intensity after Zr and Zn metal foils, for energy calibration purposes. Pure hexagonal ZnO and tetragonal ZrO_2 powders, used as reference compounds, were measured at the same beamline, in the form of self-supporting pellets with optimized mass for transmission XAS at Zn and Zr K-edge, respectively. For the sake of comparison, a reference monoclinic ZrO_2 was also measured in the form of an optimized self-supporting pellet at the BM23 beamline of the European Synchrotron Radiation Facility (ESRF).⁵⁴

The Athena software from the Demeter package⁵⁵ was used to align in energy and normalize the XAS spectra to unity edge jump, as well as to extract the $\chi(k)$ EXAFS function and calculate its Fourier transform.

2.2.6. Transmission electron microscopy characterization. High-angle annular dark-field imaging (HAADF) in conjunction with energy-dispersive X-ray spectroscopy (EDXS) was carried out with a Cs-corrected Titan G² 80-300 ST Mono (Thermo-Fisher Scientific). The microscope was equipped with a GIF Quantum (Gatan Inc.) and a Super-X EDXS detector (Thermo-Fisher Scientific). STEM-EDXS analysis was performed with an accelerating voltage of 300 kV, a beam current of 0.10 nA and a dwell time of ~ 1 second per picture with a total acquisition time of 10 minutes per elemental map. Acquisition and processing of the obtained data were performed with the Velox (Thermo-Fisher Scientific) software package. Dry sample preparation was used for all of the samples.

2.2.7. X-ray photoelectron spectroscopy (XPS) characterization. XPS studies were carried out using a Kratos Axis Ultra DLD spectrometer (Kratos Analytical Ltd) equipped with a monochromatic AlK α X-ray source ($h\nu = 1486.6 \text{ eV}$) operating at 150 W; acquisition of spectra was performed under ultra-high vacuum conditions (10^{-8} – 10^{-9} mbar). Measurements were carried out in hybrid mode using electrostatic and magnetic lenses. The high-resolution spectra were collected at a fixed analyzer pass energy of 20 eV. Charge neutralization with low energy electrons was applied for all the samples. The spectrum line of C1s (284.8 eV for adventitious carbon) was used for binding energy correction. The Zn LMM Auger peak was used for zinc chemical state identification ($KE_{\text{ZnO}} \sim 988 \text{ eV}$). Typically, powder samples were immobilized on Cu conductive tape (SPI supplies, Structure Probe, Inc.), placed on the sample holder and evacuated overnight until ultra-high vacuum was reached.

3. Results and discussion

3.1. Chemical, textural and structural characterization of the ZrZn-X catalysts

As for zirconium and zinc contents in the ZrZn-X samples determined by ICP-AES analysis, the approximate compositions were calculated as weight percentage of Zn and reported in Table 1 along with specific surface areas (SSA) and pore volumes. As already mentioned in the Experimental section, the samples were named ZrZn-X, where X is the Zn loading.

The SSAs of ZrZn-5 and ZrZn-15 are approximately the same, whereas that of ZrZn-30 is about 20% lower. The adsorption/desorption isotherms^{56,57} and the pore size distributions (PSDs) of the as-prepared ZrZn-X catalysts are displayed in the ESI† Fig. S1 and S2† respectively.

All the samples exhibit the hysteresis loop characteristic of mesoporous materials with similar PSDs with a maximum at about 3 nm. However, all these samples show a broad PSD



covering a wide range of pore widths from 3 to 12 nm. Moreover, the pore volumes are comparable for ZrZn-5 and ZrZn-15, whereas it is twice as high for ZrZn-30.

The PXRD patterns of the as-prepared ZrZn-*X* samples are reported in Fig. 1. Intensities were not rescaled but only offset-shifted. All the three samples show a diffraction pattern typical of crystalline zirconia, but the diffractograms of cubic and tetragonal ZrO₂ are not distinguishable between each other. However, XAS measurements discussed in the following (see section 3.5) evidenced features characteristic of tetragonal zirconia. Moreover, reflections of monoclinic ZrO₂ are absent, also at $2\theta < 20^\circ$ as shown in Fig. S3†

The inset in Fig. 1 underlines a shift to higher 2θ values of the (101) reflection with respect to a pure ZrO₂ reference. This shift was previously observed by Wang *et al.*³¹ and explained considering a shrinking of the ZrO₂ unit cell when the largest Zr⁴⁺ (0.82 Å)⁵⁸ is substituted by Zn²⁺ (0.74 Å).

The peak shift trend is consistent with the Zn concentration found from ICP analysis (*i.e.*, the higher the Zn loading, the more pronounced the shift results). Moreover, comparison of the diffractograms highlights a peak broadening effect, slightly enhanced as the Zn loading increases. The three samples were measured with the same instrumental parameters and the background position was the same for the three diffractograms (Fig. S3†). Hence, we can safely verify that the amorphous fraction is the same. The crystallite size obtained from Rietveld refinement decreases as the loading of Zn increases.

However, the SSA value does not reflect this trend (Table 1). The SEM images of the catalysts (Fig. S17†) show that they consist of particles with small aggregated crystallites. Therefore, the area exposed is correlated to the dimensions of these aggregates rather than to the crystallite size.

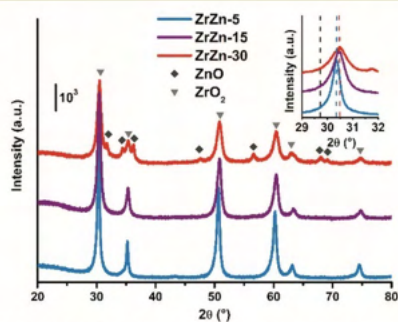


Fig. 1 PXRD patterns of the as-prepared ZrZn-*X* samples. Triangles and diamonds indicate respectively peak positions of cubic/tetragonal ZrO₂ and hexagonal ZnO. Inset: Magnification of the ZrO₂ (101) reflection with the peak position for a pure ZrO₂ (ref. 60) (dashed black line) compared to that observed for the ZrZn-*X* samples (dashed coloured lines).

Extra reflections are present only in sample ZrZn-30 (diamond symbols in Fig. 1). They are indexed considering an additional ZnO (ref. 59) wurtzite phase. The ZrO₂:ZnO phase ratio was extracted by Rietveld refinement. Using hexagonal ZnO (*P6₃mc*) and tetragonal ZrO₂ (*P4₂/nmc*)⁶⁰ as input parameters, we found that ZrZn-30 is composed of 85 wt% of ZrO₂ and 15 wt% of ZnO (Table S1†). Consequently, part of Zn is not incorporated in the host lattice but is segregated as a second phase, justifying also why the (101) reflection for ZrZn-30 is very close to the one for ZrZn-15. Nonetheless, as evidenced by EXAFS results presented in section 3.5, a slightly higher amount of Zn is expected to enter the ZrO₂ lattice in ZrZn-30 with respect to ZrZn-15. With our co-precipitation technique, we could therefore achieve a maximum Zn doping of ZrO₂ of about 15 wt%. Finally, the decreased area and the increased pore volume observed for ZrZn-30 could be also correlated to the presence of segregated ZnO.

3.2. Spectroscopic characterization of the ZrZn-*X* catalysts

3.2.1. H₂ interaction with the oxidized samples at 400 °C. The activity of these catalysts in CO₂ hydrogenation can be related to the peculiar property of ZnO to form oxygen vacancies under reducing conditions.¹⁷ Moreover, the presence of Zn in the ZrO₂ lattice can induce the formation of oxygen vacancies for the ZrZn-*X* catalysts. IR spectroscopy is suitable for revealing features characteristic of the presence of oxygen vacancies.

Fig. S4† compares the spectra recorded in oxygen and in hydrogen at 400 °C for the three catalysts. For all the samples under both conditions, absorption bands in the regions 4000–3000 cm⁻¹, 2500–2000 cm⁻¹ and 1700–1000 cm⁻¹ are present. These bands are related to surface hydroxyls, CO₂ encapsulated in closed pores and carbonate/nitrate species, respectively. Encapsulated CO₂ and carbonates/nitrates stem directly from the precursors used for the synthesis. More detailed discussion about these species is reported in the ESI.†

Focusing on the effect of the interaction with H₂, in Fig. S4† an increase of the sample absorbance in a large spectroscopic region passing from oxygen to hydrogen is evident, in particular for ZrZn-15 and ZrZn-30. This is due to the increase of a very broad absorption band, whose shape is discernable by subtracting the spectrum recorded in oxygen from the spectrum recorded in hydrogen. The result of this subtraction for the different samples is reported in Fig. 2. The very broad bands evidenced by the grey dotted lines are related to the photo-ionization of mono-ionized oxygen vacancies.^{61–63} On these electronic absorption bands, negative vibrational peaks that complicate the shape of the spectra are superimposed.

Before discussing the origin of the negative peaks, we focus on the broad electronic absorption. It is well known that ZnO is a semiconducting material due to the presence of lattice defects, *i.e.* oxygen vacancies (V_O).^{61,62} The two



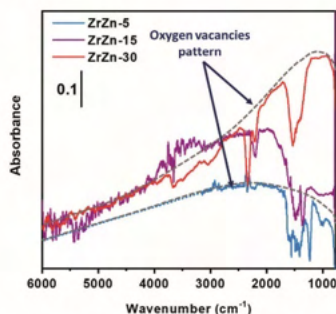


Fig. 2 FT-IR difference spectra of ZrZn-X catalysts at 400 °C in H₂ (subtrahend spectrum is that recorded in oxygen at 400 °C). The ZrZn-5 spectrum is cut at 3155 cm⁻¹ because, beyond that frequency, data are affected by the low signal-to-noise ratio; the cut part has been substituted with a dotted blue line, which aims to reproduce the trend.

electronic levels at 0.05 and 0.18 eV below the conduction band (C.B.) are associated with the V_O of ZnO. Neutral vacancies show two trapped electrons that occupy the above-mentioned levels. The first ionization energy is so low that the major part of V_O are mono-ionized (V_O⁺), being the excited electrons in the C.B. The second ionization of V_O can be promoted by IR radiation (photo-ionization of mono-ionized oxygen vacancies): in the spectrum of pure ZnO, a broad absorption band appears centered at the energy corresponding to 0.18 eV, *i.e.* at about 1450 cm⁻¹, after reduction treatments. Interaction with hydrogen can create V_O⁻ following two routes: i) the filling with an electron of the pre-existing bi-ionized V_O (V_O²⁺) by consuming adsorbed oxygen species, such as O₂⁻, O⁻, and O₂²⁻; ii) the creation of new V_O⁻ extracting lattice oxygen ions from the surface. This last pathway occurs only at high temperature, with the temperature threshold depending on the specific material. The IR technique is not able to distinguish the two routes to V_O⁻ formation.

Concerning our case, the V_O⁻ absorption bands reported in Fig. 2 for ZrZn-30 and ZrZn-5 show a maximum centered at about 1100 and 2200 cm⁻¹, respectively, which can be associated with mono-ionized oxygen vacancies at 0.14 and 0.27 eV under the C.B.^{61–63} This result evidences the influence of the different Zn loadings on the associated energy level of the mono-ionized oxygen vacancies with respect to the C.B. In particular, ZrZn-30 shows a V_O⁺ ionization energy (0.14 eV) very close to that of pure ZnO (0.18 eV), being the sample with the highest Zn content in the ZrO₂ lattice, as evidenced by the EXAFS results presented in section 3.5.

We cannot exclude that the presence of a segregated ZnO extra-phase, as shown by PXRD (Fig. 1), could also slightly influence the position of the oxygen vacancy band. As for ZrZn-5, the V_O⁺ ionization energy (0.27 eV) is higher than that

of pure ZnO: the effect of the ZrO₂ lattice and the low amount of Zn induce the formation of V_O⁺ with electronic levels deeper in the band gap.

The identification of the correct position of the maximum absorption related to V_O⁺ for ZrZn-15 is complicated by the superimposed, above mentioned “negative vibrational peaks”. These peaks are well visible for all the samples, but only for ZrZn-15 their presence hamper the identification of the actual shape of the V_O⁺ absorption. The negative peaks are related to the vibrational modes of encapsulated CO₂ and carbonate/nitrate species and they arose from the subtraction operation, since these vibrational bands show lower intensity in hydrogen than in oxygen. It is important to underline that their intensities return to the original ones when the samples were exposed to oxygen after interaction with hydrogen. So, carbonates/nitrates and, even more reasonably, encapsulated CO₂ are not partially removed from the samples by the interaction with H₂, but their intensity loss has another origin. In particular, it is possible to consider a coupling process occurring between the electronic absorption of V_O⁺ and the surface species vibrations. Genzel and Martin,⁶⁴ using a continuum model made up of a phonon term and a free electron term, provided an explanation for a similar phenomenon when plasmon absorptions occurred in small particles of conducting and semiconducting materials. When the concentration of the free carriers is high enough to cause the plasmon frequency to overcome the phonon frequency, a plasmon-phonon coupling process occurs leading to the decrease/disappearance of any band of a purely vibrational nature. In our case, the coupling process occurs between vibrational modes of surface species and IR absorption of electrons trapped in mono-ionized oxygen vacancies, as already observed and reported in the literature for semiconducting oxides, such as SnO₂, ZnO, WO₃, and MoO₃.^{65,66}

As for the intensity of the electronic band, ZrZn-30 and ZrZn-15 show a significant absorption related to V_O⁻, whereas ZrZn-5 does not, due to the different amount of V_O⁻ generated. As demonstrated by quantitative analysis, the Zn loading decreases in the order: ZrZn-30 > ZrZn-15 > ZrZn-5, so that the infrared absorption shown in Fig. 2 is in line with the chemical composition and with the Zn content in the ZrO₂ lattice shown by PXRD and EXAFS results. These results are corroborated by modelling calculations (see section 3.3). Moreover, the highest amount of V_O⁻ observed for ZrZn-30 can be correlated to the best catalytic performances of this catalyst among all the samples (see section 3.4). Finally, these IR results highlight the importance of pre-reducing the samples before the catalytic run in order to create a high concentration of reactive oxygen vacancies.

3.2.2. CO adsorption at LNT. CO dosage was performed at liquid-nitrogen temperature (LNT) because of its weak adsorption on Zr⁴⁺ and Zr²⁺ cations. Fig. 3 reports the spectra collected at increasing CO coverage (θ_{CO}) on oxidized and reduced ZrZn-X catalysts.



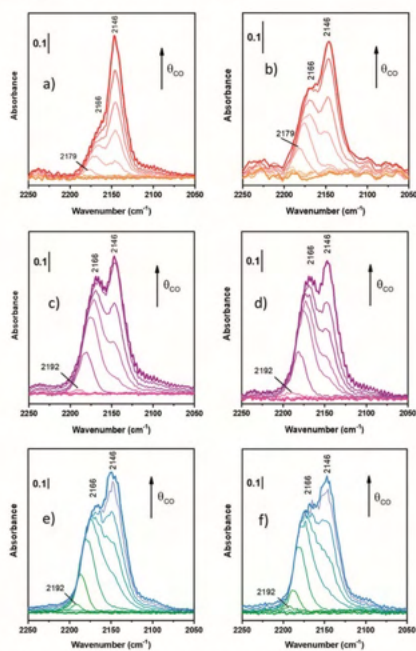


Fig. 3 FT-IR spectra of CO adsorption at LNT on oxidized ZrZn-30 (a), ZrZn-15 (c), and ZrZn-5 (e) and reduced ZrZn-30 (b), ZrZn-15 (d), and ZrZn-5 (f) at increasing doses up to 20 mbar.

Starting from the oxidized samples (Fig. 3a, c and e), two main peaks are highlighted between 2200 and 2100 cm^{-1} . The first peak at 2166 cm^{-1} can be related to coordinatively unsaturated Zr^{4+} carbonyls⁶⁷ (*cus*- Zr^{4+} -CO), i.e. Zr atoms located on edges or steps. Zr^{4+} carbonyls on regular facets should show absorption bands between 2148 and 2142 cm^{-1} .⁶⁷ However, when CO is adsorbed on metal cations with a dominant σ -donation, the higher the unsaturation of the adsorption site, the higher the $\nu(\text{C}=\text{O})$. In particular, Zr^{4+} is a $4d^0$ cation, thus it lacks π -backdonation and σ -bonding is the only contribution to the bond with CO.

The peak related to *cus*- Zr^{4+} -CO also features a red-shift from 2179–2192 cm^{-1} (according to the sample) to 2166 cm^{-1} . Different explanations can be proposed for the frequency shift vs. θ_{CO} , but the most observed are usually four: i) “through space” dipole–dipole interaction between parallel vibrating molecules;⁶⁸ ii) “through solid” via the vibrational coupling mechanism across binding electrons;⁶⁹ iii) the “chemical effect”, another “through solid” phenomenon due to adsorbed molecules;^{69,70} and iv) the “electrostatic” or

“solvent” effect caused by adsorbed molecules perturbing each other.⁷¹ The first and the second effect are dynamic, whereas the third and the fourth ones are static. Typically, among dynamic effects, the second one is negligible when adsorption is characterized by small adsorption enthalpy, or in general when $\nu(\text{C}=\text{O})$ is very close to that of free CO (2143 cm^{-1}). Among the static effects, the fourth one is often small or negligible⁷² and it usually appears at higher pressures or for densely packed CO, where it assumes a solvent-like behavior, hence not in this case, since we observed this effect at low pressures.

Among the remaining effects, in our case we can exclude the dipole–dipole coupling since it is the dominant factor for CO adsorbed on sites on extended regular facets (dipolar coupling occurs between “equal” oscillators, i.e. CO molecules, and defects interrupt dipole–dipole coupling) and it causes in all cases a blue-shift on increasing coverage. Hence, the observed red-shift is due to the “chemical effect”, as a result of the reduction of CO σ -donation on increasing coverage. As a matter of fact, for metal cations with dominant σ -donation, the higher the θ_{CO} , the higher the electron density on the binding sites. As a consequence, on increasing coverage the σ -donation contribution of all adsorbed CO molecules becomes smaller and smaller and thereby a decrease of $\nu(\text{C}=\text{O})$ is observed.⁷³

The second peak at 2146 cm^{-1} is assigned to CO adsorbed on Zr^{4+} with a lower coordinative unsaturation.^{67,74} This band does not show any shift on increasing CO coverage: this is reasonably due to the compensation between the dipole–dipole coupling effect (blue shift) and the chemical one (red-shift). As a consequence, the peak remains stationary and this observation confirms its assignment to CO on Zr^{4+} sites of regular facets.

Differently from Zr^{4+} sites, Zn^{2+} sites are not visible. Zinc is in a lower amount and, reasonably, its carbonyl band can be totally hidden by Zr^{4+} -CO bands. Indeed, according to some authors,^{74,75} Zn^{2+} -CO is characterized by peaks between 2190 and 2160 cm^{-1} , where the absorption frequency changes according to the chemical environment. For the sake of clarity, it is possible that all peaks at 2192 (Fig. 3c and e) and 2179 cm^{-1} (Fig. 3a) observed as first peaks during CO adsorption can be associated with Zn^{2+} -CO, but there is neither evidence nor references to prove it in systems like the ZrZn-X samples studied in this work.

On the reduced samples (Fig. 3b, d and f), all peaks can be assigned as reported for the oxidized ones.

Nevertheless, comparing the spectra of all the samples, normalized for the specific surface area and pellet thickness, many features are evident (Fig. 4). First of all, for the oxidized samples, the markedly lower intensity of the band at 2166 cm^{-1} , related to coordinatively unsaturated Zr^{4+} , is well evident for ZrZn-30 with respect to the other samples. The lower amount of defect sites for ZrZn-30 can be related to the BET results: the lower surface area of this sample with respect to ZrZn-5 and ZrZn-15 is reasonably reflected in a minor amount of *cus*- Zr^{4+} sites. Moreover, by comparing the



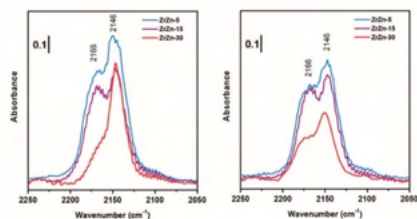


Fig. 4 Comparison between FT-IR spectra collected at the highest CO coverage for oxidized (left) and reduced (right) ZrZn-X catalysts.

total integrated intensity of the bands in the region 2200–2100 cm^{-1} , it decreases in the order: ZrZn-5 > ZrZn-15 > ZrZn-30. This is in agreement with the chemical analysis and the EXAFS results (*vide infra*) on the Zn content in the ZrO_2 lattice: on increasing the Zn loading, the amount of surface Zr^{4+} sites decreases.

After reduction, there is not a significant variation in spectra except for $\nu(\text{C}=\text{O})$ at 2166 cm^{-1} on ZrZn-30. Comparing CO adsorption on oxidized and reduced ZrZn-30, the intensity of the band at 2166 cm^{-1} appears significantly increased after reduction. This phenomenon can be ascribed to oxygen vacancy formation: after reduction at $400 \text{ }^\circ\text{C}$ in H_2 the presence of oxygen vacancies is responsible for an increased surface disorder, which causes a growth of *cus*- Zr^{4+} concentration (2166 cm^{-1}) and thereby a correlated reduction in the amount of Zr^{4+} on facets (2146 cm^{-1}).

3.3. Molecular modelling of the ZrZn-X catalysts

We performed DFT calculations to characterize the catalyst structure and the involved reaction mechanism for CO_2 hydrogenation on a ZnZrO_x solid solution. For the sake of simplicity, we model the system as a five layered ZrO_2 slab presenting variable ZnO– ZrO_2 composition on the surface. Beginning with a tetragonal unit cell of ZrO_2 , we constructed low index facets (100), (101), and (111). The surface energies of the slabs were computed as $\gamma = \frac{\Delta E[\text{surface}]}{2A}$, with $\Delta E[\text{surface}]$ defined in eqn (5):

$$\Delta E[\text{surface}] = E[\text{slab}] - N_{\text{ZrO}_2} \times E[\text{bulk}] \quad (5)$$

where $E[\text{slab}]$ is the DFT calculated energy of the whole slab, $E[\text{unit}]$ is the energy per formula unit of bulk ZrO_2 , N_{ZrO_2} is the number of ZrO_2 formula units in the slab, and A is the area of the slab surface.

According to calculations, the (101) surface has the lowest surface energy, 0.1 J m^{-2} , followed by the (100) and (111) surfaces, 0.7 and 2.8 J m^{-2} (see Fig. S5†). We thus focused on the (101) surface to investigate the formation energy of O vacancies in the presence of H_2 , as thermal O vacancies are

highly unlikely on ZrO_2 , on ZnZrO_x solid solutions using eqn (6):

$$E[\text{vac}] = E[\text{pristine}] - E[\text{system with O vacancy}] + E_{\text{H}_2\text{O}} - E_{\text{H}_2} \quad (6)$$

where $E[\text{pristine}]$, $E[\text{system with O vacancy}]$, $E_{\text{H}_2\text{O}}$, and E_{H_2} are the DFT calculated energies of the pristine slab, the slab with oxygen vacancies, and isolated water and hydrogen molecules, respectively.

Using eqn (6), we first calculated the energy required to form an O vacancy on a pristine ZrO_2 (101) surface, 3.28 eV . In line with earlier reports,^{76,77} this indicates that no O vacancy can be expected at thermodynamic equilibrium on the pristine (101) facets of ZrO_2 under the reactivity conditions used in this work. To include the effect of Zn doping, we replaced one ZrO_2 unit on the surface with one ZnO unit and a “stoichiometric” O vacancy, which is a vacancy introduced to balance the charge difference created by replacing one Zr^{4+} with one Zn^{2+} in the lattice. To quantify the formation energy of stoichiometric O vacancies, we computed the substitution energy of ZrO_2 units by ZnO units, $E[\text{sub}]$, using eqn (7):

$$E[\text{sub}] = E_{\text{slab}}[x\text{ZnO}/\text{ZrO}_2] - E_{\text{slab}}[\text{ZrO}_2] - xE_{\text{bulk}}[\text{ZnO}] + \frac{1}{2}E_{\text{O}_2} \quad (7)$$

where x is the number of Zn atoms doped on the surface, and $E_{\text{slab}}[x\text{ZnO}/\text{ZrO}_2]$, $E_{\text{slab}}[\text{ZrO}_2]$, $E_{\text{bulk}}[\text{ZnO}]$ and E_{O_2} are the DFT calculated energies of a ZrO_2 (101) slab doped with x ZnO units, a pristine ZrO_2 (101) slab, a bulk ZnO unit, and an isolated oxygen molecule, respectively. Once a ZnO doped surface with a stoichiometric number of O vacancies is generated, the formation energy of additional O vacancies,

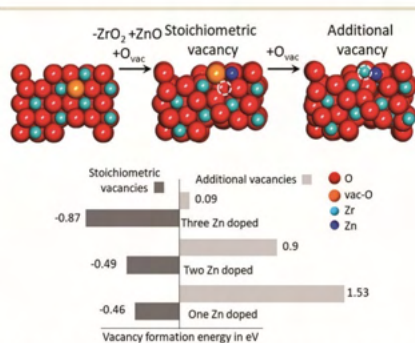


Fig. 5 The O vacancy formation energy trend with increasing number of Zn atoms on the surface of ZrO_2 (101). The schematic illustrates the way “stoichiometric” and additional vacancies are modeled. The red, blue and dark blue colors represent oxygen, zirconium and zinc atoms, respectively. The orange atom and dashed circle show the O atom to be removed and the O vacancy formed, respectively.

Catalysis Science & Technology

with the assistance of H_2 , can be calculated using an approach similar to that of eqn (6).

Fig. 5 summarizes the formation energies of stoichiometric and additional O vacancies for x ranging from 1 to 3. Considering that the ZrO_2 supercell we used has 8 Zr atoms, the doping we considered corresponds to 12.5, 25.0 and 37.5% Zn atoms on the surface. Calculations indicate that substitution of a single ZrO_2 unit by ZnO, with creation of a vacancy, is thermodynamically favored by -0.46 eV, a value that reduces slightly to -0.29 eV per ZnO unit and -0.87 eV when 3 ZrO_2 units are replaced with 3 ZnO. This indicates that ZrO_2 can tolerate high amounts of Zn substitution at the surface. As for the formation of O vacancies, in addition to the stoichiometric ones, our calculations indicate that the system with just one Zn doped on the surface is not prone to further O vacancy formation, with an $E[\text{vac}] - 1.53$ eV, although this value is remarkably lower than that calculated on a pristine ZrO_2 surface, 3.28 eV. However, the chances of formation of additional O vacancies increase with increasing number of Zn atoms on the surface, with an $E[\text{vac}] = 0.9$ eV only, when 3 out of the 8 ZrO_2 units on the surface are replaced with ZnO. Overall, this is in qualitative agreement with the experimental evidence that increasing amounts of O vacancies are experimentally observed at increasing Zn content.

To investigate the catalytic behavior, we used the model composed of one ZnO unit replacing a surface ZrO_2 unit, with generation of a stoichiometric O vacancy. We first calculated CO_2 adsorption on the O vacancy near the Zn atom, which resulted in an adsorption energy of -0.50 eV. Dissociation of the adsorbed CO_2 molecule with release of a CO molecule is thermodynamically unfavored by 0.71 eV, indicating that these surface O vacancies cannot be CO_2 traps generating CO (Fig. S6†).

We were not able to locate any other energetically favored CO_2 adsorption geometry. Adsorption of molecular hydrogen occurs at the Zn atom, with an adsorption energy of -0.20 eV. However, dissociation of molecular hydrogen into $2H^*$ is favored, with an energy gain of 0.39 eV. The dissociated hydrogen is present as H^{+} and H^{-} species on the O and Zn sites, respectively. Simultaneous adsorption of CO_2 and $2H^*$ is favored by -0.73 eV, which is slightly less than the sum of the adsorption energies of isolated CO_2 and $2H^*$, -1.09 eV. The completely optimized geometries of the Zn-doped ZrO_2 (101) with CO_2 , H_2 , $2H^*$ and $CO_2 + 2H^*$ are shown in Fig. S7†.

Possible thermodynamic profiles for the conversion of adsorbed CO_2 and dissociated H_2 on the ZnO/ ZrO_2 surface are reported in Fig. 6. Considering that the formate and CO pathways have been proposed to be involved in methanol formation,¹⁷ we evaluated the free energies of the most important intermediates involved in the two pathways. The starting point is CO_2 adsorbed on the O vacancy near the Zn site, and dissociated H_2 adsorbed on the Zn site and on a nearby O atom.

View Article Online

Paper

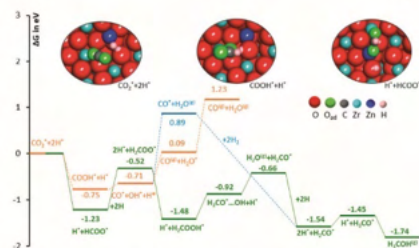


Fig. 6 Free energy diagram for comparing the intermediates involved in CO_2 hydrogenation to methanol via the formate and CO pathway. The three insets represent the completely optimized structures of reactants and intermediates with $HCOO^*$ and $COOH^*$, respectively. The red, grey, pink, blue, green and dark blue colors represent oxygen, carbon, hydrogen, zirconium, O atom of the adsorbate and zinc atoms, respectively.

The first possibility we examined is the transfer of the H^* on Zn to the C atom of *CO_2 along the formate pathway, leading to formation of $HCOO^*$ through a highly exergonic step, by -1.23 eV. Subsequent hydrogenation of $HCOO^*$ leads first to an adsorbed formaldehyde molecule with liberation of a water molecule, $H_2CO^* + H_2O(\text{gas})$, and finally to adsorbed methoxide, CH_3O^* . All intermediates along the formate pathway are at free energies below the starting $CO_2^* + 2H^*$ species, and the overall energy span between the

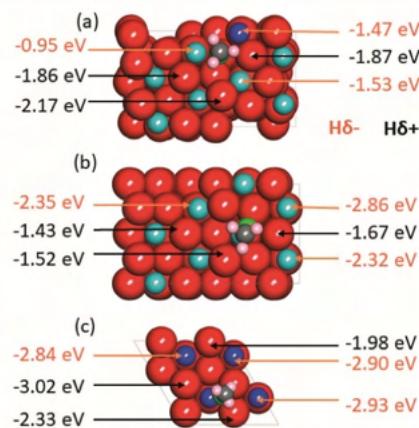


Fig. 7 A top view of the space filling atom model, with adsorbed CH_3O^* , of (a) Zn doped ZrO_2 (101), (b) ZrO_2 (101), and (c) ZnO (111) surface comparing the adsorption energies of H^{+} and H^{-} species. The red, grey, pink, blue, green and dark blue colors represent oxygen, carbon, hydrogen, zirconium, O atom of the adsorbate and zinc atoms, respectively.



Paper

highest and the lowest energy intermediates is smaller than 1.22 eV, indicating a viable reaction pathway under the reaction conditions used in this work. The second possibility we examined is reactivity along the carbon monoxide pathway, which starts with conversion of CO_2^* to CO^* , followed by its hydrogenation to form methanol.³¹ As shown in Fig. 7, the first intermediate along this pathway, COOH^* , at -0.75 eV, is less stable than the first intermediate along the formate pathway, HCOO^* , resting at -1.23 eV.

Evolution of this intermediate to $\text{CO}^* + \text{H}_2\text{O}^*$ first, followed by CO dissociation to $\text{CO}(\text{gas}) + \text{H}_2\text{O}^*$, is an endergonic sequence, with $\text{CO}(\text{gas}) + \text{H}_2\text{O}^*$ above the starting $\text{CO}_2^* - 2\text{H}^*$ species. Similarly, H_2O dissociation leaving CO^* , from which hydrogenation to CH_3O^* can occur, is even more expensive, with $\text{CO}^* + \text{H}_2\text{O}(\text{gas})$ at 0.89 eV above the starting $\text{CO}_2^* - 2\text{H}^*$ species.

Furthermore, all intermediates involved in dissociation of CO_2 to CO are less stable than the intermediates formed by subsequent hydrogenation of formate species. This is consistent with the experimental CH_3OH selectivity (*vide infra*) and it suggests that the formate reaction pathway is operative.

Having clarified the pathway leading to CH_3O^* , we investigate methanol *versus* methane selectivity, which has been shown to depend on a competition between the transfer of a H^+ to the O atom of CH_3O^* , liberating methanol, and the transfer of a H^+ species to the C atom of CH_3O^* , dissociating the C–O bond and liberating methane.^{78,79} To shed light on this point, we explored the relative stabilities of H^{O^*} and H^{C^*} species on Zn doped ZrO_2 , and pristine ZrO_2 and ZnO (Fig. 7). According to calculations, in the presence of CH_3O^* on Zn doped ZrO_2 , H^{O^*} species have stronger binding energies compared to H^{C^*} species, which can explain the catalyst selectivity towards methanol production.⁷⁸ On the other hand, on pristine ZrO_2 (101) and ZnO (111), H^{C^*} species have stronger binding energies than H^{O^*} species, which should imply that Zn doped ZrO_2 has better selectivity towards methanol formation than both its pristine counterparts.

3.4. Catalytic tests on the ZrZn-X catalysts and the combined ZrZn-X/zeolite systems

We first studied the stand-alone ZrZn-X catalysts with different Zn-loadings (ZrZn-5, ZrZn-15 and ZrZn-30) in the CO_2 conversion to methanol (MeOH), the initial step in the CO_2 'cascade' conversion over the bifunctional catalysts. In particular, we screened the effect of reaction pressure (20, 30 and 40 bar), temperature (250 °C, 300 °C and 350 °C) and CO addition (10% in the feed), as this gas is likely to be recycled with the unreacted CO_2 and H_2 in a perspective process.^{80,81} The results are summarized in Fig. 8.

We can observe that increasing the pressure results in higher conversion and methanol selectivity for the three catalysts, in good agreement with the process thermodynamics.^{78,82} The main product in all cases is CO

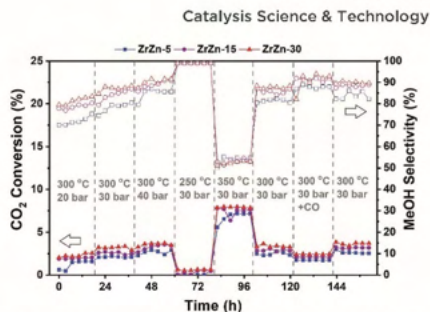


Fig. 8 Catalytic performance of all ZrZn-X stand-alone samples for the CO_2 conversion to MeOH. $\text{CO}_2:\text{H}_2$ 1:3, 12 000 $\text{mL h}^{-1} \text{g}^{-1}$.

with small traces of CH_4 (selectivity <1%) being as well detected. Similarly, decreasing the temperature increases the methanol selectivity to almost 100% with the CO_2 conversion being drastically reduced. On the other hand, increasing the temperature to 350 °C significantly increases the conversion with the MeOH selectivity being reduced to ca. 50%. CO addition slightly increases MeOH selectivity, again in line with previous observations.⁸² Interestingly, despite the multiple conditions tested, no deactivation was observed for any of the samples after more than 150 hours under reaction conditions. From the reported results, ZrZn-30 appears as the optimal catalyst composition, displaying the highest activity and selectivity regardless of the reaction conditions. We attribute this superior performance of the ZrZn-30 sample to the already discussed higher amount of oxygen vacancies in the sample.^{17,83}

Afterwards, we studied the combination of ZrZn-X catalysts with the two most common zeolites for the CO_2 cascade conversion:^{84,85} ZSM-5 and H-SAPO-34. Similar to the above tests, we evaluated the effect of reaction pressure,

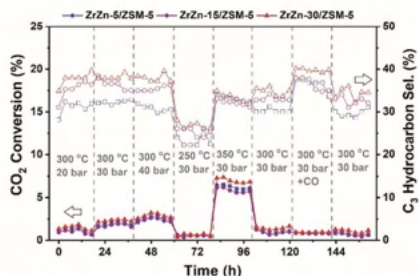


Fig. 9 Catalytic performance of the combined ZrZn-X/ZSM-5 systems for CO_2 conversion to hydrocarbons. $\text{CO}_2:\text{H}_2$ 1:3, 12 000 $\text{mL h}^{-1} \text{g}^{-1}$. Please note that the secondary Y axis refers to the C_3 selectivity among hydrocarbons (CO free).

temperature and CO addition. The results are summarized in Fig. 9 for ZSM-5 and in Fig. S8† for H-SAPO-34. We can observe that the CO₂ conversion for these bifunctional catalysts goes in line with the one observed for the stand-alone ZrZn-*X* samples, increasing with both pressure and temperature. Similar conversion values and CO selectivity are also obtained regardless of the reaction conditions or zeolite component (see Fig. S9† for a detailed comparison). However, when looking at the hydrocarbon distribution, we can observe that the zeolite component plays a critical role. In particular, the H-SAPO-34 based catalyst displayed a higher C₃ selectivity among hydrocarbons (up to 60%) but it is rapidly deactivated, especially at 350 °C where it lost almost all activity in less than 20 hours and unreacted methanol became the main reaction product (see Fig. S8 and S9†). Moreover, it seems that an operation temperature of 250 °C is too low for MeOH conversion to occur in H-SAPO-34.^{45,66} This catalytic behavior is consistent with the fast deactivation and higher selectivity observed for H-SAPO-34 in the MTH reaction.^{87,88} On the other hand, the ZSM-5 based catalyst displayed a more stable performance, with a C₃ selectivity of ca. 40%. However, we need to point out that a slight deactivation is also observed at 350 °C for the ZSM-5 based catalysts. Finally, CO addition seems to slightly enhance the C₃ selectivity, in line with the recent results by Tan *et al.*⁸⁹ who observed an increase in the hydrocarbon selectivity by CO co-feeding. Altogether, we can consider the ZrZn-30/ZSM-5 combined system, tested at 350 °C and 30 bar, as the most promising candidate/reaction conditions, displaying the highest conversion and stability with a C₃ selectivity close to 35% among hydrocarbons.

Further catalyst studies were performed under these optimal reaction conditions (350 °C, 30 bar), using two other ZSM-5 samples with Si/Al = 25 and 360 (ESI† section 5.3). When testing the ZrZn-30 catalyst alone, methanol and CO were the only carbon-containing products (Fig. S10†). Product selectivity favored methanol at the shortest contact times, suggesting that the rate of CO₂ conversion to methanol (eqn (2)) is faster than the reverse water gas shift reaction (eqn (1)), in agreement with the results of the computational study (section 3.3). The methanol yield reached equilibrium after 0.4 s g⁻¹ ml⁻¹ contact time. The CO₂ conversion and hence, CO selectivity increased with a further increase in contact time. Due to water formed in the reverse water gas shift reaction, the methanol equilibrium yield decreased with increasing contact time.

When mixing ZrZn-30 with the two H-ZSM-5 catalysts in a 1:1 ratio, a range of hydrocarbon products, as well as dimethyl ether (DME) were observed, in addition to CO and methanol (Fig. S11†). The methanol yield was low, substantially below equilibrium, and decreased with increasing acid site density in H-ZSM-5. This result suggests that CO₂ hydrogenation to methanol is the rate-limiting step of hydrocarbon formation in the bifunctional ZrZn-30:H-ZSM-5 = 1:1 mixed catalysts.

Considering next CO₂ conversion *versus* contact time, it did not change significantly with the addition of H-ZSM-5, as already observed in Fig. 8 and 9. However, the CO selectivity decreased with the addition of H-ZSM-5, and decreased further with an increase in the acid site density of H-ZSM-5 (Fig. S12†). This result may suggest that CO, like the hydrocarbons, is a (competing) secondary product from methanol, or that CO, like methanol, is converted to hydrocarbons over H-ZSM-5. The recent literature suggests that both hypotheses are plausible.^{90,91}

Surprisingly, when considering next the hydrocarbon distribution over mixed catalysts, the aromatics selectivity is typically below 10% and only at 6000 ml h⁻¹ g⁻¹ is a significant fraction observed for the main ZSM-5 catalyst tested here (Fig. 10).

We attribute these results to the high space time employed in this work that suppresses the aromatization cycle, in line with the results by Cui *et al.* who observed an increase of aromatics selectivity from ca. 20% to 75% by reducing the space time by one order of magnitude.²² These results are supported by testing other ZSM-5 catalysts mixed with ZrZn-30 (section 5.3). A higher acid site density in H-ZSM-5 led to more saturated aliphatic products, and less aromatic products, compared to a lower acid site density (Fig. S13 and S14†). These results suggest an intricate, joint behavior of the two catalyst functions that warrants further investigations in future contributions.

Additionally, if we look in detail at the CO free hydrocarbon distribution (Table S4† and Fig. 11), we can observe that, apart from the above-mentioned aromatics influence, the space time also affects the olefin/paraffin ratio. At high space times, paraffins are the predominant fraction, while at lower space times the olefins start to increase. These trends can be counter-intuitive and the opposite trend should be expected since olefins are the primary products of the HC pool reaction and the thermodynamic equilibrium of alkane

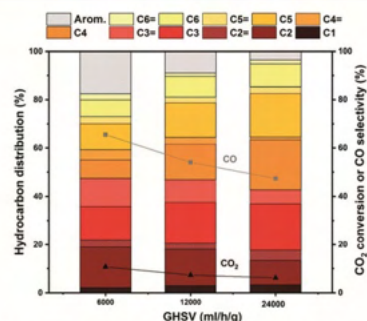


Fig. 10 Hydrocarbon distribution of the ZrZn-30/ZSM-5 combined system for CO₂ conversion to hydrocarbons at different space times. CO₂:H₂ 1:3, 350 °C, 30 bar.



Paper

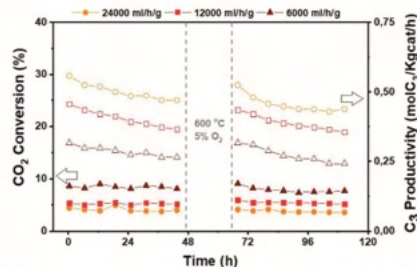


Fig. 11 Catalytic performance of the ZrZn-30/ZSM-5 combined system before and after regeneration for CO₂ conversion to hydrocarbons at different space times. CO₂:H₂ 1:3, 350 °C, 30 bar.

dehydrogenation reactions lies far to the alkane side for C₂ and C₃. However, if we look in detail at the reaction kinetics over ZSM-5,^{33,34} we can observe that at very high space times (like the ones in our study) the slope of olefin increase is higher than the ones for paraffins plus C₃₊ hydrocarbons, therefore in line with our experimental observations. Last but not least, the productivities displayed here are among the highest reported for state-of-the-art catalysts⁸⁴ despite the low conversion, probably owing to the high space times employed in our study and the associated absence of aromatics.

Finally, since deactivation can play a role especially in view of industrial implementation of the investigated bifunctional catalysts, we studied the effect of *in situ* regeneration at 600 °C with a 5% O₂ in N₂ stream for the ZrZn-30/ZSM-5 combined system at different space times. The results are summarized in Fig. 11. We can observe that the *in situ* regeneration worked for all the samples and the initial activity was regained after the regeneration cycle at 600 °C. Moreover, increasing the space time drastically increases the C₃ productivity despite the CO₂ conversion decrease, achieving a maximum of 1.5 mol kg⁻¹ h⁻¹ at 24 000 ml h⁻¹ g⁻¹.

3.5. XAS measurements on the combined ZrZn-X/ZSM-5 systems

Focusing on ZrZn-X/ZSM-5 combined systems, we finally applied *in situ* and *operando* XAS to monitor the average electronic properties and local structure of Zr and Zn metal centres, in the presence of the zeolite functionality and under realistic activation and process conditions. This becomes especially relevant, in view of recent findings highlighting inter-phase ion exchange phenomena in combined systems obtained by physically mixing acid zeolites and Zn-containing hydrogenation catalysts.¹⁰ To obtain fully comparable information at Zr and Zn K-edges, we measured the two absorption edges quasi-simultaneously during the same experiment, exploiting the unique capability of the ROCK

Catalysis Science & Technology

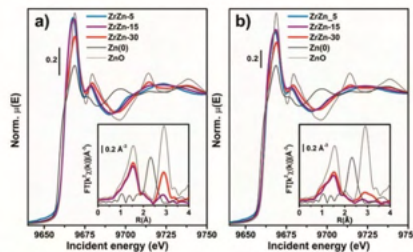


Fig. 12 K-edge XANES (main panel) and phase-uncorrected FT-EXAFS (bottom inset) spectra of the three samples and of Zn metal and ZnO model compounds, collected at (a) RT under He flux and (b) after the activation process (400 °C, H₂). The EXAFS spectra reported in the bottom insets have been obtained transforming the corresponding k²χ(k) EXAFS function in the 2.5–13.0 Å⁻¹ range.

beamline⁵³ of the SOLEIL synchrotron (see section 2.2.5 for details).

Considering the Zn K-edge XAS spectra in Fig. 12a, we observe how the as-prepared samples exclusively contain Zn²⁺ species. Indeed, the edge energy position is substantially equivalent for the three ZrZn-X/ZSM-5 combined systems and overlapped with that of the ZnO model compound. Notably, ZrZn-30/ZSM-5 shows an overall XANES line-shape and specific post-edge features characteristic of ZnO (e.g. peaks at 9714 and 9738 eV), which are instead not detected in the other samples. This is explained considering the presence of the ZnO extra phase unveiled by PXRD in the ZrZn-30 catalyst. The inset of Fig. 12a shows the FT-EXAFS spectra of the two combined systems featuring the higher Zn-loadings, whereas for the lowest-loading ZrZn-5/ZSM-5 system, the low S/N ratio in the EXAFS region unfortunately prevented a reliable data interpretation. Both the samples show a very similar first coordination shell peak stemming from O nearest neighbours (NNs). The first-shell peaks are comparable with that of the reference ZnO in terms of the *R*-space position, while they display slightly lower intensity, consistent with distortions in the local coordination environment of substitutional Zn ions in the ZrO₂ lattice. The two samples show more pronounced differences in the second-shell region of the EXAFS spectra. In particular, for ZrZn-30/ZSM-5 we recognize a well-defined peak matching the position of the second-shell feature in ZnO, arising from Zn next nearest neighbour (NNN) atoms. The lower peak intensity with respect to what is observed for the model compound can be connected with the simultaneous presence of substitutional Zn ions in the ZrO₂ lattice, as well as with possible defectiveness of the segregated ZnO particles. Conversely, only a broad and much weaker peak is observed for ZrZn-15/ZSM-5 in the second-shell region, pointing to rather high structural disorder in the NNN distribution for substitutional Zn ions in ZrO₂.



During activation (Fig. 12b) the Zn K-edge XANES features are substantially unchanged, underpinning two important facts: i) the average oxidation state of Zn does not change (no edge-shift is observed nor any evidence for the formation of Zn⁰ phases) and ii) Zn²⁺ does not diffuse in the zeolite (typical spectral features of Zn-exchanged zeolites⁹³ are not observed). Considering the corresponding FT-EXAFS spectra (Fig. 12b, inset), the first-shell peak undergoes a slight intensity decrease, consistent with the increased thermal contribution to Debye-Waller factors at 400 °C. The second shell peaks, connected with NNN contributions, appear more strongly affected. The two samples maintain the same intensity trend as in their as-prepared state, with ZrZn-30/ZSM-5 showing the highest intensity; however, in both cases an important dampening/broadening effect is observed. Also in this case, increased Debye-Waller factors at 400 °C contribute to EXAFS signal dampening. However, it is clear that activation also triggered an increase in the local disorder around Zn²⁺ sites – both those hosted in the ZrO₂ lattice and those segregated as ZnO extra-phases, in agreement with IR results demonstrating oxygen vacancy formation during thermal treatment in H₂ up to 400 °C.

Under quasi-simultaneous acquisition conditions, Zr K-edge XAS (Fig. 13a) allowed us to obtain structural insights on the ZrO₂ matrix complementary to the ones accessed by PXRD analysis (see section 3.1). In particular, we were able to discriminate tetragonal from cubic and monoclinic structures, as the XANES features for the two configurations are strongly influenced by the ZrO₄ polyhedron distortion. Li *et al.*⁹⁶ reported three important features in the spectra ascribable to tetragonal ZrO₂: i) the pre-edge peak associated with the 1s → 4d transition, ii) white-line peak splitting, absent in the monoclinic ZrO₂ and iii) broad post-edge resonance around 35 eV after the edge. All these spectroscopic fingerprints, further corroborated by the Zr K-edge XAS spectra of reference monoclinic and tetragonal

ZrO₂ reported in Fig. 13, are observable in the XANES of the three investigated ZrZn-X/ZSM-5 combined systems, pointing to the presence of a tetragonal ZrO₂ phase. In particular the 1s → 4d pre-edge feature, which is very evident in the XANES first derivative (Fig. S15†), is a fingerprint of t-ZrO₂ where Zr is eight-fold coordinated. In the perfect ZrO₈ pyrochlore-like structure, this s-d transition would not be detectable, as it is dipole forbidden.

However, it is well documented^{97,98} that in t-ZrO₂ four oxygens are closer while four are farther from the Zr cation. This leads to visualization of the Zr atom as coordinated with two different tetrahedra of oxygen atoms.^{96,99} Since the centrosymmetry is broken, the dipole forbidden 1s → 4d transition gains in intensity being observable in the Zr K pre-edge.^{96,100} Moreover, two features in the FT-EXAFS, highlighted by dashed lines in Fig. S15† can be ascribed to t-ZrO₂: i) the Zr-Zr second shell position and ii) the relatively intense high-R peak in the 6–7 Å range in the phase-uncorrected spectra. As shown by Li *et al.*^{96,100} with careful EXAFS fit of various ZrO₂ polymorphs, in c-ZrO₂ the average Zr-Zr distance is almost 0.1 Å shorter than that in t-ZrO₂. Therefore, the Zr-Zr second feature of c-ZrO₂ should be located at a lower R value than that of the reference t-ZrO₂. Besides, the intense feature around 6.7 Å (Fig. S15† inset) is related to collinear multiple scattering between Zr atoms which is present in t-ZrO₂ but absent in c-ZrO₂.^{96,101}

Previous works explained the stabilization of tetragonal ZrO₂ considering the substitution of the Zr atom with either Zn (ref. 31) or Hf.¹⁰² For clarity, we outline that a trace of Hf L₃-edge (9561 eV) was observed during the Zn K-edge XAS measurements, in line with chemical analysis results: the small amount of Hf present in the investigated samples plausibly also contributes to promoting the tetragonal ZrO₂ structure. Phase-uncorrected FT-EXAFS, reported in the inset of Fig. 13a, show a first-shell peak stemming from O NN, consistent for all the three samples with the one observed for the ZrO₂ model compound.

Conversely, with the increase of Zn content (ZrZn-30 > ZrZn-15 > ZrZn-5) the intensity of the second-shell peak is progressively attenuated, while its position is substantially unaltered, always closely resembling the one observed for the tetragonal ZrO₂ model compound. In agreement with PXRD results, this intensity trend stems from Zn entering the ZrO₂ lattice, causing destructive interference among scattering paths involving Zr and Zn NNs. We note a pronounced intensity decrease while moving from ZrZn-5 to ZrZn-15, while a further increase of Zn-loading in ZrZn-30 only results in a slight additional attenuation of the second-shell peak. This observation further supports that in ZrZn-15 we are close to the upper threshold for the incorporation of Zn in the ZrO₂ lattice.

However, in ZrZn-30, a slightly higher amount of Zn still enters the ZrO₂ matrix, as proven by the additional weakening of the second-shell peak. Afterwards, excess Zn segregates as hexagonal ZnO, silent in Zr K-edge XAS but detectable in Zn K-edge XAS and PXRD. Activation (Fig. 13b)

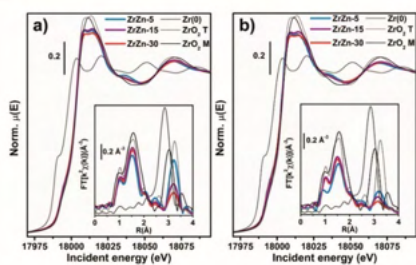


Fig. 13 K-edge XANES (main panel) and phase-uncorrected FT-EXAFS (bottom inset) spectra of the three samples and of Zr metal and ZrO₂ model compounds, collected at (a) RT under He flux and (b) after the activation process (400 °C, H₂). The EXAFS spectra reported in the bottom insets have been obtained transforming the corresponding $k^2\chi(k)$ EXAFS function in the 2.5–13.0 Å⁻¹ range.



does not cause substantial modifications in the ZrO_2 structure, nor detectable reduction phenomena involving Zr atoms. Tetragonal features of ZrO_2 are still evident, while the structural disorder in the NNN distribution around Zr centres further increases, translating into an abatement of the second-shell peaks, as observed under the same conditions in Zn K-edge FT-EXAFS.

Under reaction conditions (Fig. S16†), XAS data collected at both absorption edges showed that the catalyst structural stability is preserved. In particular: i) the ZrO_2 matrix maintains the tetragonal structure; ii) Zn does not exchange in the zeolite; iii) both Zr^{4+} and Zn^{2+} do not undergo detectable reduction phenomena. The absence of structural changes after the reaction was also observed from the PXRD measurement of the tested catalysts, reported in the following section. Structural modifications possibly involving surface metal sites upon interaction with the CO_2/H_2 feed are not detectable, as the measured XAS signal includes mainly bulk information.

3.6. Structural characterization of the fresh/tested ZrZn-30/ZSM-5 combined system

In order to investigate possible structural modification induced by the physical mixing and the reaction conditions, we measured the PXRD pattern of the ZrZn-30/ZSM-5 physical mixture before and after 120 hours of catalytic test. Each reflection was ascribed to the corresponding crystalline phase by measuring the PXRD for the single components: i) ZrZn-30 catalyst alone after a reaction cycle and ii) commercial ZSM-

5. The diffraction pattern of the ZrZn-30/ZSM-5 combined system in Fig. 14, measured before and after the catalytic test, does not present any differences related to potential structural changes, *i.e.* crystallite defects such as dimensions, stress or strain related to peak broadening. We can clearly distinguish the reflections from each crystal phase, *i.e.* orthorhombic zeolite, tetragonal zirconia and hexagonal zinc oxide. Rietveld refinement was conducted only on the diffraction pattern of the ZrZn-30 catalyst measured after the reaction (Fig. 14 inset). The same refinement strategy used for the fresh catalyst was applied. Taking into account the error of the technique, the results in Fig. 14 and Table S2† evidence structural features very similar to those observed for the fresh sample, while the zeolite crystallinity is preserved as the peaks show similar FWHM (Fig. 14 inset). The increase of the intensity between ZrZn-30 alone and its physical mixture with the zeolite is related to the decrease of the total absorption coefficient as in the second case, half of the capillary contains the zeolite.

We further investigated the possible surface composition changes before and after the reaction by performing XPS analysis on both fresh and tested samples (Fig. S18 and S19†). We can observe that there are no appreciable shifts in the binding energies of both Zn and Zr after 48 hours of catalytic test. Furthermore, the binding energy of Zr at the $\text{Zr}3p_{3/2}$ level is 182.37 eV, lower than the 182.7 eV assigned to the pure ZrO_2 .¹⁰³ This shift has already been reported in the presence of oxygen vacancies due to the substitution of Zn^{4+} by Zn^{2+} ,¹⁰⁴ in line with our FT-IR observations. We also need to remark that, similar to the PXRD in Fig. 14, the intensity difference between ZrZn-30 alone and its physical mixture with the zeolite is related to the decrease of loading.

We next investigated the possible morphological changes in our system *via* high-angle annular dark-field transmission microscopy (HAADF) in conjunction with energy-dispersive X-ray spectroscopy (EDXS). We can observe that in the fresh

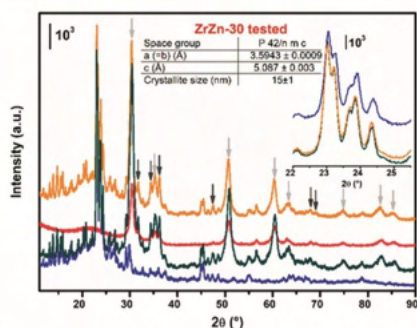


Fig. 14 Stacked representation of the PXRD measured for i) commercial ZSM-5 zeolite alone, in blue; ii) fresh physical mixture ZrZn-30/ZSM-5, in dark-green; iii) ZrZn-30 catalyst after 120 hours of catalytic test, in red; iv) physical mixture of ZrZn-30/ZSM-5 after 120 hours of catalytic test, in orange. For the sake of clarity in the latter pattern, the reflections corresponding to tetragonal ZrO_2 and hexagonal ZnO are indicated by light and dark grey arrows, respectively. Structure results obtained from Rietveld refinement of the tested ZrZn-30 catalyst alone are reported in the table. A detail of the zeolite Bragg peaks is reported in the inset.

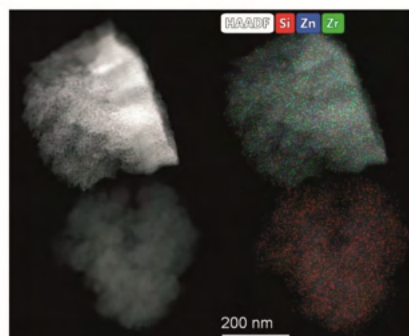


Fig. 15 HAADF STEM-EDXS images of the tested ZrZn-30/ZSM-5 catalyst after 48 hours of catalytic test.



ZrZn-30 sample both Zn and Zr elements are closely incorporated and that an excess of Zn segregates as ZnO, in line again with the above XANES and PXRD characterization. (Fig. S20†). Similarly, imaging of the tested sample (Fig. 15) shows no structural changes after the reaction with an intimate mixture of both ZrZn-30 and ZSM-5 components in the final bifunctional system. However, we need to point out that a small migration of Zn was observed in some of the zeolite particles (~0.2 wt%, Fig. S21†).

Conclusions

In this work we have synergized catalytic tests under different conditions, multi-technique characterization and computational modelling to advance the understanding of bifunctional Zn-doped-ZrO₂/zeolite catalysts for CO₂ hydrogenation to methanol and conversion to value-added hydrocarbons.

Three Zn-containing ZrO₂ samples were prepared by co-precipitation (ZrZn-*X*, *X* = Zn wt%, *i.e.* 5, 15, 30). The formation of the expected ZrZnO_{*X*} solid solution was confirmed by both XAS characteristic features and powder diffractograms. In particular, the crystalline structure of tetragonal zirconia was recognized with diffraction peak shifts consistent with the Zn loading in the structure. A ZnO extra phase is present for the ZrZn-30 sample, evidencing that the co-precipitation technique employed allows achievement of a maximum Zn doping of ZrO₂ of about 15 wt%, even though EXAFS results show that a slightly higher amount of Zn enters the ZrO₂ lattice in ZrZn-30 with respect to ZrZn-15. CO adsorption (at LNT) followed by FT-IR spectroscopy shows that the amount of Zr²⁺ sites at the surface decreases coherently with the increase of Zn loading found from chemical composition and X-ray results.

Interaction with hydrogen at increasing temperature causes the formation of mono-ionized oxygen vacancies, as evidenced by FT-IR spectroscopy. In agreement with FT-IR results, DFT calculations show that chances of oxygen vacancy formation with the assistance of hydrogen increase with increasing Zn content. In particular, DFT modelling points out that once a stoichiometric oxygen vacancy is induced by the presence of Zn, the formation of extra oxygen vacancies during activation is thermodynamically favored. Moreover, DFT modelling points out that i) the oxygen vacancies play an active role in CO₂ hydrogenation, ii) the presence of neighboring Zn and Zr sites enhances methanol selectivity thanks to the proximity of CH₃O* and H⁺, strongly bonded than H⁺, and iii) methanol is most likely formed via the formate pathway.

Coherently, the catalytic performances of the stand-alone ZrZn-*X* samples showed the same trend shown by the oxygen vacancy amount, *i.e.* CO₂ conversion and CH₃OH selectivity increases with the Zn loading. While we cannot exclude that segregated ZnO in the most active catalyst (ZrZn-30) also plays a role, the reported characterization, modelling and testing results consistently suggest that the main

contribution to the catalyst activity comes from the ZrZnO_{*X*} solid solution. Combined systems were obtained by mechanical mixing of the ZrZn-*X* catalysts with a commercial zeolite (H-ZSM-5 and H-SAPO-34) with a mass ratio of 1:1. Comparing ZrZn-30/ZSM-5 and ZrZn-30/H-SAPO-34 combined systems, we pointed out that the ZSM-5-containing system is more promising than the one with H-SAPO-34. Indeed, the highest conversion and stability with *circa* 30% C₃ selectivity among hydrocarbons were found testing ZrZn-30/ZSM-5 at 350 °C and 30 bar. At *T* < 350 °C, alkylbenzene dealkylation is unlikely to occur.^{45,46} However, in this work we highlight an unusual aliphatics selectivity (and stability) at lower temperature and shorter contact time, more favored with H-ZSM-5 than H-SAPO-34 as the zeotype has lower activity/stability at low temperature.

Finally, the structure of the catalysts is not affected by the reaction conditions as shown by the *operando* XAS and the structural/textural characterization of the tested samples; indeed a final catalytic test carried out on the regenerated catalyst shows that the initial performances are completely restored.

In conclusion, in the light of our findings, we can affirm that, for a bifunctional catalyst, both chemical (oxidic phase composition, Brønsted acid site density, and pore dimensions) and kinetic factors (temperature, pressure and space time velocity) must be considered in order to drive the reaction towards the desired products and, therefore, to achieve a good reaction yield.

Conflicts of interest

There are no conflicts to declare.


Acknowledgements

This project has received funding from the European Union's Horizon 2020 Research and Innovation Programme under grant agreement No. 837733. This work was supported by a public grant overseen by the French National Research Agency (ANR) as part of the "Investissements d'Avenir" program (reference: ANR-10-EQPX-45). The authors are grateful to C. La Fontaine, V. Briois, A. L. Bugaev and A. Lazzarini for the help with the XAS experiment at ROCK, Soleil.

References

- 1 J. Rockström, W. Steffen, K. Noone, Å. Persson, F. S. Chapin, E. F. Lambin, T. M. Lenton, M. Scheffer, C. Folke, H. J. Schellnhuber, B. Nykvist, C. A. de Wit, T. Hughes, S. van der Leeuw, H. Rodhe, S. Sörlin, P. K. Snyder, R. Costanza, U. Svedin, M. Falkenmark, L. Karlberg, R. W. Corell, V. J. Fabry, J. Hansen, B. Walker, D. Liverman, K. Richardson, P. Crutzen and J. A. Foley, *Nature*, 2009, **461**, 472–475.
- 2 M. Aresta, A. Dibenedetto and A. Angelini, *J. CO₂ Util.*, 2013, **3–4**, 65–73.



- Open Access Article. Published on 18 January 2021. Downloaded on 11/28/2022 3:05:56 PM.
This article is licensed under a Creative Commons Attribution-NonCommercial 3.0 Unported Licence.
- 
- 29 T. Sakakura, J. C. Choi and H. Yasuda, *Chem. Rev.*, 2007, **107**, 2365–2387.
- 30 S. Saedi, N. A. S. Amin and M. R. Rahimpour, *J. CO₂ Util.*, 2014, **5**, 66–81.
- 31 Z. Jiang, T. Xiao, V. L. Kuznetsov and P. P. Edwards, *Philos. Trans. R. Soc., A*, 2010, **368**, 3343–3364.
- 32 S. Kattel, P. Liu and J. G. Chen, *J. Am. Chem. Soc.*, 2017, **139**, 9739–9754.
- 33 W. Wang, S. Wang, X. Ma and J. Gong, *Chem. Soc. Rev.*, 2011, **40**, 3703–3727.
- 34 J. B. Hansen and P. E. Højlund Nielsen, Methanol Synthesis, in *Handbook of Heterogeneous Catalysis*, ed. G. Ertl, H. Knözinger, F. Schüth and J. Weitkamp, Wiley, Germany, 2008.
- 35 J. R. Gallagher, D. J. Childers, H. Zhao, R. E. Winans, R. J. Meyer and J. T. Miller, *Phys. Chem. Chem. Phys.*, 2015, **17**, 28144–28153.
- 36 C. Ahoba-Sam, E. Borfecchia, A. Lazzarini, A. Bugaev, A. A. Isah, M. Taoufik, S. Bordiga and U. Olsbye, *Catal. Sci. Technol.*, 2020, **10**, 4373–4385.
- 37 M. Gentzen, D. E. Doronkin, T. L. Sheppard, A. Zimina, H. Li, J. Jelic, F. Studt, J. D. Grunwaldt, J. Sauer and S. Behrens, *Angew. Chem., Int. Ed.*, 2019, **58**, 15655–15659.
- 38 M. W. Tew, H. Emerich and J. A. Van Bokhoven, *J. Phys. Chem. C*, 2011, **115**, 8457–8465.
- 39 K. Cheng, B. Gu, X. Liu, J. Kang, Q. Zhang and Y. Wang, *Angew. Chem., Int. Ed.*, 2016, **55**, 4725–4728.
- 40 Z. Li, J. Wang, Y. Qu, H. Liu, C. Tang, S. Miao, Z. Feng, H. An and C. Li, *ACS Catal.*, 2017, **7**, 8544–8548.
- 41 G. Bonura, M. Migliori, L. Frusteri, C. Cannilla, E. Catizzone, G. Giordano and F. Frusteri, *J. CO₂ Util.*, 2018, **24**, 398–406.
- 42 W. J. Thomas and S. Portalski, *Ind. Eng. Chem.*, 1958, **50**, 967–970.
- 43 J. Ye, C. Liu, D. Mei and Q. Ge, *ACS Catal.*, 2013, **3**, 1296–1306.
- 44 A. S. Malik, S. F. Zaman, A. A. Al-Zahrani, M. A. Daous, H. Driss and L. A. Petrov, *Appl. Catal., A*, 2018, **560**, 42–53.
- 45 A. S. Malik, S. F. Zaman, A. A. Al-Zahrani, M. A. Daous, H. Driss and L. A. Petrov, *Catal. Today*, 2020, **357**, 573–582.
- 46 H. Bahruji, M. Bowker, W. Jones, J. Hayward, J. Ruiz Esquius, D. J. Morgan and G. J. Hutchings, *Faraday Discuss.*, 2017, **197**, 309–324.
- 47 K. Li and J. G. Chen, *ACS Catal.*, 2019, **9**, 7840–7861.
- 48 S. Kattel, P. J. Ramirez, J. G. Chen, J. A. Rodriguez and P. Liu, *Science*, 2017, **357**, 1296–1299.
- 49 Y. Amenomiya, *Appl. Catal., A*, 1987, **30**, 57–68.
- 50 X. Dong, F. Li, N. Zhao, F. Xiao, J. Wang and Y. Tan, *Appl. Catal., B*, 2016, **191**, 8–17.
- 51 H. Gu, J. Ding, Q. Zhong, Y. Zeng and F. Song, *Int. J. Hydrogen Energy*, 2019, **44**, 11808–11816.
- 52 I. A. Fisher and A. T. Bell, *J. Catal.*, 1999, **184**, 144–156.
- 53 G. Wang, D. Mao, X. Guo and J. Yu, *Int. J. Hydrogen Energy*, 2019, **44**, 4197–4207.
- 54 F. Arena, G. Italiano, K. Barbera, S. Bordiga, G. Bonura, L. Spadaro and F. Frusteri, *Appl. Catal., A*, 2008, **350**, 16–23.
- 55 W. Li, K. Wang, J. Huang, X. Liu, D. Fu, J. Huang, Q. Li and G. Zhan, *ACS Appl. Mater. Interfaces*, 2019, **11**, 33263–33272.
- 56 K. Pokrovski, K. T. Jung and A. T. Bell, *Langmuir*, 2001, **17**, 4297–4303.
- 57 J. Wang, G. Li, Z. Li, C. Tang, Z. Feng, H. An, H. Liu, T. Liu and C. Li, *Sci. Adv.*, 2017, **3**, 1–11.
- 58 A. Wokaun, *Phys. Chem. Chem. Phys.*, 1999, **1**, 5071–5080.
- 59 H. Li, C. Rameshan, A. V. Bukhtiyarov, I. P. Prosvirin, V. I. Bukhtiyarov and G. Rupprechter, *Surf. Sci.*, 2019, **679**, 139–146.
- 60 L. H. Chagas, P. C. Zonetti, C. R. V. Matheus, C. R. K. Rabello, O. C. Alves and L. G. Appel, *ChemCatChem*, 2019, **11**, 5625–5632.
- 61 O. E. Everett, P. C. Zonetti, O. C. Alves, R. R. de Avillez and L. G. Appel, *Int. J. Hydrogen Energy*, 2020, **45**, 6352–6359.
- 62 X. Liu, W. Zhou, Y. Yang, K. Cheng, J. Kang, L. Zhang, G. Zhang, X. Min, Q. Zhang and Y. Wang, *Chem. Sci.*, 2018, **9**, 4708–4718.
- 63 A. V. Kirilin, J. F. Dewilde, V. Santos, A. Chojecki, K. Scieranka and A. Malek, *Ind. Eng. Chem. Res.*, 2017, **56**, 13392–13401.
- 64 M. D. Rhodes, K. A. Pokrovski and A. T. Bell, *J. Catal.*, 2005, **233**, 210–220.
- 65 F. Jiao, J. Li, X. Pan, J. Xiao, H. Li, H. Ma, M. Wei, Y. Pan, Z. Zhou, M. Li, S. Miao, J. Li, Y. Zhu, D. Xiao, T. He, J. Yang, F. Qi, Q. Fu and X. Bao, *Science*, 2016, **351**, 1065–1068.
- 66 S. Wang, P. Wang, Z. Qin, Y. Chen, M. Dong, J. Li, K. Zhang, P. Liu, J. Wang and W. Fan, *ACS Catal.*, 2018, **8**, 5485–5505.
- 67 T. Liang, J. Chen, Z. Qin, J. Li, P. Wang, S. Wang, G. Wang, M. Dong, W. Fan and J. Wang, *ACS Catal.*, 2016, **6**, 7311–7325.
- 68 K. Cheng, J. Kang, Q. Zhang and Y. Wang, *Sci. China Chem.*, 2017, **60**, 1382–1385.
- 69 C. Zhou, J. Shi, W. Zhou, K. Cheng, Q. Zhang, J. Kang and Y. Wang, *ACS Catal.*, 2020, **10**, 302–310.
- 70 Y. K. Park, K. C. Park and S. K. Ihm, *Catal. Today*, 1998, **44**, 165–173.
- 71 H. Schulz, *Catal. Today*, 2010, **154**, 183–194.
- 72 F. Bleken, M. Bjørgen, L. Palumbo, S. Bordiga, S. Svelle, K. P. Lillerud and U. Olsbye, *Top. Catal.*, 2009, **52**, 218–228.
- 73 J. Rodriguez-Carvajal, *Newsl. Comm. Powder Diffr. IUCr*, 2001, vol. 26, pp. 12–19.
- 74 P. Hohenberg and W. Kohn, *Phys. Rev.*, 1964, **136**, B864–B871.
- 75 W. Kohn and L. J. Sham, *Phys. Rev.*, 1965, **140**, A1133–A1138.
- 76 P. E. Blöchl, *Phys. Rev. B: Condens. Matter Phys.*, 1994, **50**, 17953–17979.
- 77 J. Klimeš, D. R. Bowler and A. Michaelides, *Phys. Rev. B: Condens. Matter Phys.*, 2011, **83**, 1–13.
- 78 S. Grimme, S. Ehrlich and L. Goerigk, *J. Comput. Chem.*, 2011, **32**, 1456–1465.
- 79 C. La Fontaine, S. Belin, L. Barthe, O. Roudenko and V. Briois, *Synchrotron Radiat. News*, 2020, **33**, 20–25.
- 80 O. Mathon, A. Beteva, J. Borrel, D. Bugnazet, S. Gatha, R. Hino, I. Kantor, T. Mairs, M. Munoz, S. Pasternak, F. Perrin and S. Pascarelli, *J. Synchrotron Radiat.*, 2015, **22**, 1548–1554.

- 55 B. Ravel and M. Newville, *J. Synchrotron Radiat.*, 2005, **12**, 537–541.
- 56 K. S. W. Sing and R. T. Williams, *Adsorpt. Sci. Technol.*, 2004, **22**, 773–782.
- 57 K. S. W. Sing, D. H. Everett, R. A. W. Haul, L. Moscou, R. A. Pierotti, J. Rouquerol and T. Siemienińska, *Pure Appl. Chem.*, 1985, **57**, 603–619.
- 58 B. Y. R. D. Shannon, M. H. N. H. Baur, O. H. Gibbs, M. Eu and V. Cu, *Acta Crystallogr., Sect. A: Cryst. Phys., Diff., Theor. Gen. Crystallogr.*, 1976, **32**, 751–767.
- 59 S. C. Abrahams and J. L. Bernstein, *Acta Crystallogr., Sect. B: Struct. Crystallogr. Cryst. Chem.*, 1969, **25**, 1233–1236.
- 60 G. Teufer, *Acta Crystallogr.*, 1962, **15**, 1187.
- 61 U. Özgür, Y. I. Alivov, C. Liu, A. Teke, M. A. Reshchikov, S. Doğan, V. Avrutin, S. J. Cho and H. Morkoç, *J. Appl. Phys.*, 2005, **98**, 1–103.
- 62 W. Göpel and U. Lampe, *Phys. Rev. B: Condens. Matter Mater. Phys.*, 1980, **22**, 6447–6462.
- 63 S. Morandi, A. Fioravanti, G. Cerrato, S. Lettieri, M. Sacerdoti and M. C. Carotta, *Sens. Actuators, B*, 2017, **249**, 581–589.
- 64 L. Genzel and T. P. Martin, *Surf. Sci.*, 1973, **34**, 33–49.
- 65 G. Ghiotti, A. Chiorino and F. Pinnetto, *Sens. Actuators, B*, 1995, **25**, 564–567.
- 66 S. Morandi, M. C. Paganini, E. Giamello, M. Bini, D. Capsoni, V. Massarotti and G. Ghiotti, *J. Solid State Chem.*, 2009, **182**, 3342–3352.
- 67 C. Morterra, E. Giamello, L. Orto and M. Volante, *J. Phys. Chem.*, 1990, **94**, 3111–3116.
- 68 B. N. J. Persson and R. Ryberg, *Phys. Rev. B: Condens. Matter Mater. Phys.*, 1981, **24**, 6954–6970.
- 69 M. Moskovits and J. E. Hülse, *Surf. Sci.*, 1978, **78**, 397–418.
- 70 G. D. Mahan and A. A. Lucas, *J. Chem. Phys.*, 1978, **68**, 1344–1348.
- 71 G. L. Griffin and J. T. Yates, *J. Chem. Phys.*, 1982, **77**, 3744–3750.
- 72 D. Scarano and A. Zecchina, *J. Chem. Soc., Faraday Trans. 1*, 1986, **82**, 3611–3624.
- 73 C. Morterra, V. Bolis, B. Fubini, L. Orto and T. B. Williams, *Surf. Sci.*, 1991, **251–252**, 540–545.
- 74 K. I. Hadjiivanov and G. N. Vayssilov, *Adv. Catal.*, 2002, **47**, 307–511.
- 75 D. Scarano, S. Bertarione, G. Spoto, A. Zecchina and C. Otero Areán, *Thin Solid Films*, 2001, **400**, 50–55.
- 76 L. R. del Silva-Calpa, P. C. Zonetti, C. P. Rodrigues, O. C. Alves, L. G. Appel and R. R. de Avillez, *J. Mol. Catal. A: Chem.*, 2016, **425**, 166–173.
- 77 A. A. Safonov, A. A. Bagatur'yants and A. A. Korokin, *Microelectron. Eng.*, 2003, **69**, 629–632.
- 78 A. Bavykina, I. Yarulina, A. J. Al Abdulghani, L. Gevers, M. N. Hedhili, X. H. Miao, A. R. Galilea, A. Pustovarenko, A. Dikhtiarenko, A. Cadiou, A. Aguilar-Tapia, J. L. Hazemann, S. M. Kozlov, S. Oud-Chikh, L. Cavallo and J. Gascon, *ACS Catal.*, 2019, **9**, 6910–6918.
- 79 J. L. Snider, V. Streibel, M. A. Hubert, T. S. Choksi, E. Valle, D. C. Upham, J. Schumann, M. S. Dtyar, A. Gallo, F. Abild-Pedersen and T. F. Jaramillo, *ACS Catal.*, 2019, **9**, 3399–3412.
- 80 E. S. Van-Dal and C. Bouallou, *J. Cleaner Prod.*, 2013, **57**, 38–45.
- 81 D. Milani, R. Khalilpour, G. Zahedi and A. Abbas, *J. CO2 Util.*, 2015, **10**, 12–22.
- 82 Y. Slotboom, M. J. Bos, J. Pieper, V. Vrieswijk, B. Likozar, S. R. A. Kersten and D. W. F. Brilman, *Chem. Eng. J.*, 2020, **389**, 124181.
- 83 N. Rui, Z. Wang, K. Sun, J. Ye, Q. Ge and C. J. Liu, *Appl. Catal., B*, 2017, **218**, 488–497.
- 84 A. Dokania, A. Ramirez, A. Bavykina and J. Gascon, *ACS Energy Lett.*, 2019, **4**, 167–176.
- 85 Z. Q. Ma and M. D. Porosoff, *ACS Catal.*, 2019, **9**, 2639–2656.
- 86 H. Schulz, *Catal. Lett.*, 2018, **148**, 1263–1280.
- 87 I. Yarulina, A. D. Chowdhury, F. Meirer, B. M. Weckhuysen and J. Gascon, *Nat. Catal.*, 2018, **1**, 398–411.
- 88 U. Olsbye, S. Svelle, M. Bjorgen, P. Beato, T. V. W. Janssens, F. Joensen, S. Bordiga and K. P. Lillerud, *Angew. Chem., Int. Ed.*, 2012, **51**, 5810–5831.
- 89 L. Tan, P. P. Zhang, Y. Cui, Y. Suzuki, H. J. Li, L. S. Guo, G. H. Yang and N. Tsubaki, *Fuel Process. Technol.*, 2019, **196**, 106174.
- 90 K. Cheng, W. Zhou, J. Kang, S. He, S. Shi, Q. Zhang, Y. Pan, W. Wen and Y. Wang, *Chem*, 2017, **3**, 334–347.
- 91 Q. Song, Y. Men, J. Wang, S. Liu, S. Chai, W. An, K. Wang, Y. Li and Y. Tang, *Int. J. Hydrogen Energy*, 2020, **45**, 9592–9602.
- 92 X. Cui, P. Gao, S. G. Li, C. G. Yang, Z. Y. Liu, H. Wang, L. S. Zhong and Y. H. Sun, *ACS Catal.*, 2019, **9**, 3866–3876.
- 93 J. S. Martínez-Espin, M. Mortén, T. V. W. Janssens, S. Svelle, P. Beato and U. Olsbye, *Catal. Sci. Technol.*, 2017, **7**, 2700–2716.
- 94 T. Cordero-Lanzac, A. Ateka, P. Pérez-Uriarte, P. Castaño, A. T. Aguayo and J. Bilbao, *Ind. Eng. Chem. Res.*, 2018, **57**, 13689–13702.
- 95 I. Pinilla-herrero, E. Borfecchia, J. Holzinger, U. V. Mentzel, F. Joensen, K. A. Lomachenko, S. Bordiga, C. Lamberti, G. Berlier, U. Olsbye, S. Svelle, J. Skibsted and P. Beato, *J. Catal.*, 2018, **362**, 146–163.
- 96 P. Li, I. W. Chen and J. E. Penner-Hahn, *Phys. Rev. B: Condens. Matter Mater. Phys.*, 1993, **48**, 10063–10073.
- 97 P. Li, I. W. Chen and J. E. Penner-Hahn, *Phys. Rev. B: Condens. Matter Mater. Phys.*, 1993, **48**, 10082–10089.
- 98 C. J. Howard, R. J. Hill and B. E. Reichert, *Acta Crystallogr., Sect. B: Struct. Sci.*, 1988, **44**, 116–120.
- 99 P. Li, I.-W. Chen and J. E. Penner-Hahn, *J. Am. Ceram. Soc.*, 1994, **77**, 1281–1288.
- 100 P. Li, I. W. Chen and J. E. Penner-Hahn, *Phys. Rev. B: Condens. Matter Mater. Phys.*, 1993, **48**, 10074–10081.
- 101 B. W. Veal, A. G. McKale, A. P. Paulikas, S. J. Rothman and L. J. Nowicki, *Physica B+C*, 1988, **150**, 234–240.
- 102 D. Y. Cho, H. S. Jung and C. S. Hwang, *Phys. Rev. B: Condens. Matter Mater. Phys.*, 2010, **82**, 1–7.



[View Article Online](#)

Paper

Catalysis Science & Technology

- 103 Y. Liu, C. Xia, Q. Wang, L. Zhang, A. Huang, M. Ke and Z. Song, *Catal. Sci. Technol.*, 2018, 8, 4916–4924.
- 104 C. Wang, G. Garbarino, L. F. Allard, F. Wilson, G. Busca and M. Flytzani-Stephanopoulos, *ACS Catal.*, 2016, 6, 210–218.

Open Access Article. Published on 18 January 2021. Downloaded on 11/28/2022 3:05:56 PM.
This article is licensed under a Creative Commons Attribution-NonCommercial 3.0 Unported Licence.



A.3 (not published – submitted)**Applied Catalysis A, General****PdZn/ZrO₂ + SAPO-34 bifunctional catalyst for CO₂ conversion: further insights by spectroscopic characterization**

--Manuscript Draft--

Manuscript Number:	
Article Type:	Research Paper
Keywords:	CO ₂ hydrogenation; PdZn alloy; SAPO-34; FT-IR spectroscopy of CO adsorption; NAP-XPS; solid-state NMR.
Corresponding Author:	Sara Morandi Università degli Studi di Torino Torino, Piemonte ITALY
First Author:	Pierfrancesco Ticali
Order of Authors:	Pierfrancesco Ticali Sara Morandi Genrikh Shterk Samy Ould-Chikh Adrian Ramirez Jorge Gascon Sang-Ho Chung Javier Ruiz-Martinez Silvia Bordiga
Abstract:	<p>The present work aims at further investigating a previously studied PdZn/ZrO₂+SAPO-34 bifunctional catalyst for CO₂ conversion. High activity and selectivity for propane was proved and the results obtained by NAP-XPS measurements and CO adsorption at liquid-nitrogen temperature (LNT) followed by FT-IR spectroscopy are shown. After reduction, we confirmed the formation of PdZn alloy. At LNT Pd carbonyl band shows a peculiar behavior linked to an intimate interaction between PdZn particles, ZnO and ZrO₂.</p> <p>The combined system was characterized as fresh, used and regenerated. On the fresh PdZn/ZrO₂+SAPO-34 the characteristic features of the two components do not appear perturbed by the mixing. As for the used system, the absence of Pd carbonyls and the decrease of CO on SAPO-34 Brønsted acid sites are correlated to organic species revealed by ssNMR. Regeneration in oxygen restores catalytic sites, although new Pd carbonyls appear due to Pd²⁺ ionic exchange into SAPO-34 framework.</p>
Suggested Reviewers:	<p>Jeroen van Bokhoven jeroen.vanbokhoven@chem.ethz.ch</p> <p>Sharif Zaman sfzaman@kau.edu.sa</p> <p>Davide Ferri davide.ferri@psi.ch</p>

PdZn/ZrO₂ + SAPO-34 bifunctional catalyst for CO₂ conversion: further insights by spectroscopic characterization

Pierfrancesco Ticali¹, Sara Morandi^{1*}, Genrikh Shterk², Samy Ould-Chikh²,
Adrian Ramirez^{2,3}, Jorge Gascon², Sang-Ho Chung², Javier Ruiz-Martinez² and
Silvia Bordiga¹

¹*Department of Chemistry, NIS Center and INSTM Reference Center, University of Turin, 10125, Turin, Italy.*

²*KAUST Catalysis Center (KCC), King Abdullah University of Science and Technology, Thuwal 23955, Saudi Arabia.*

³*SwissCAT+ East, ETH Zurich, Zurich 8093, Switzerland.*

**Corresponding author: Tel. +390116707539, Fax: +390116707855; e-mail address: sara.morandi@unito.it*

ABSTRACT

The present work aims to further investigate a previously studied PdZn/ZrO₂ + SAPO-34 bifunctional catalyst for CO₂ conversion. In our previous work, high activity and selectivity for propane was proved, but the spectroscopic characterization was only focused at room temperature on the PdZn/ZrO₂ component alone. Here, the results obtained by FT-IR spectroscopy used to follow CO adsorption at liquid-nitrogen temperature on PdZn/ZrO₂ alone, SAPO-34 alone and mechanical mixture are shown. Moreover, near ambient pressure XPS measurements were performed to further investigate the PdZn/ZrO₂ component. We confirm that after reduction a PdZn alloy is formed. At liquid-nitrogen temperature, Pd carbonyl band shows a peculiar behavior that can be reasonably linked to a strong and intimate interaction between the PdZn particles and the oxidic ZnO and ZrO₂ phases.

The PdZn/ZrO₂ + SAPO-34 combined system was characterized as fresh, after catalytic testing and after the subsequent regeneration. On the fresh PdZn/ZrO₂ + SAPO-34 the characteristic features of the two components do not appear perturbed by the mixing. As for the used system, the absence of the band related to Pd carbonyls and the decrease of CO interacting with Brønsted acid sites of SAPO-34 are correlated with aromatic and olefinic species, covering the surface, confirmed by ssNMR. Finally, we have proved that regeneration in pure oxygen is able to restore the catalytic sites of the system, even if new Pd carbonyl bands

appear as a possible migration of small amount of Pd²⁺ ions into the zeotype micropores.

KEYWORDS. CO₂ conversion, Hydrogenation, Propane, PdZn alloy, Zeolites, CO adsorption, FT-IR spectroscopy, XPS, solid-state NMR

1. INTRODUCTION

Climate change is the most difficult challenge that humanity is trying to combat. The incessantly increase of carbon dioxide concentration reaches a new record year by year since the industrial revolution and the average of CO₂ concentration reached 418 ppm in January 2022[1]. To date, limiting the increase of global temperature to 1.5 °C, as established by the Paris Agreement, is the real challenge. Hence, Carbon Capture Utilization and Storage (CCUS) represents the only way to reduce the CO₂ concentration and to contain the greenhouse effect.

To achieve an efficient way for the capture, conversion, transportation, and storage is economically challenging. Indeed, CCUS is not technologically ready to be applied on a global scale, demonstrating how difficult it is to find an economic way to solve global environmental issues.

One option is represented by the chemical reduction of CO₂ to obtain C1 products[2], like methanol, and to convert methanol into hydrocarbons.

According to several works[3,4], metal/oxide systems are a good choice to perform CO₂ adsorption and conversion into methanol. Usually investigated metals[5,6] are Zn, Pt, Cu[7] and Pd[8] whereas, among supports, several oxides such as SiO₂, ZnO and ZrO₂ are used[9]. In particular, zinc plays a key role for both intermediate stabilization and H₂ heterolytic splitting thanks to its activity in inducing defects (such as oxygen vacancies)[10–13]. Moreover, ZrO₂ is weakly hydrophilic and avoids water-poisoning (iii)[2,5] and it is largely reported as an

excellent metal support. This oxide has unique surface properties: Brønsted basic sites, Lewis acidic-basic $\text{Zr}^{+4}\text{O}^{2-}$ pairs and redox activity[14,15]. All these properties are largely discussed in Li et al.[2], which exhaustively describes how ZrO_2 can be a promising candidate for CO_2 -to-methanol reaction.

According to some articles[16–22], Pd-based catalysts are active for CO_2 hydrogenation to methanol with high CO_2 conversion, methanol selectivity, yield, turnover frequency and stability with a minimal composition of Pd (≤ 5 wt%) and, by alloying with zinc, it seems to play a key role in hydrogen splitting, and it leads to a good conversion of CO_2 into methanol.

However, metal or oxidic phases are not capable of converting methanol into hydrocarbons. Hence, different authors[23,24] proposed bifunctional catalysts, which are made up of an oxidic phase on a zeolitic support. The acidity of zeolite is capable of binding and hydrogenating methanol molecules to produce hydrocarbons with different yield and different number of carbon atoms according to the type of the zeolite involved in the reaction[25,26]. Defining a possible route involved for the generation of different hydrocarbons is not straightforward. Over the years, three main pathways have been proposed. Chronologically, the first theorized mechanism was the one proposed by Dessau and LaPierre[27], founded on consecutive methylation and cracking, to produce ethylene and other higher alkenes over ZSM-5. The second mechanism was theorized by Dahl and Kolboe[28], based on the low reactivity of propene and ethylene when co-reacting with methanol over SAPO-34. This mechanism is

based on a hydrocarbon-pool concept[29]. The most recent mechanism is represented by the dual-cycle concept, which is founded on the interconnection between an olefinic and an aromatic cycle.

To date, one of the most demanding hydrocarbons is propane. By 2025, propane will represent one of the most used hydrocarbons for industrial purposes, with a market growth of 5% per year[30].

We have recently published interesting results about PdZn/ZrO₂ catalyst in combination with SAPO-34 exploited in the CO₂ adsorption and conversion with propane as the main product[31]. According to our previous work and to the best of our knowledge, this system shows very good propane yields, which have never been reported about CO₂ valorization with a meaningful C₂₊ hydrocarbon conversion[32]. In particular, we demonstrated by XAS and FT-IR spectroscopy that a PdZn alloy is formed during catalyst activation. The alloy is in intimate contact with oxygen-vacancy rich ZnO particles over the ZrO₂ support and, when it is exposed to the CO₂-containing reaction feed, develops into a core-shell structure with a PdZn alloy surrounded by a polycrystalline ZnO shell. PdZn alloy is directly responsible for the MeOH formation on the PdZn/ZrO₂ component. MeOH reacts over the SAPO-34 following a classical MTO mechanism with propane as the main product[31]. The intimate mixture of both PdZn/ZrO₂ and SAPO-34 causes an instant MeOH consumption, increasing the CO₂ conversion and reducing drastically the CO selectivity. In the previous work, the

characterization of the PdZn/ZrO₂ phase was reported, but the paper lacks the spectroscopic characterization of the PdZn/ZrO₂ + SAPO-34 combined system. Hence, in this work, we are going to present some new catalytic results, which are in line with those already presented in our former work, in any case. In order to achieve a more comprehensive understanding of the bifunctional system, using CO as probe molecule, we are going to focus on the spectroscopic characterization of the combined system, taking the moves from a more detailed FT-IR characterization of the PdZn/ZrO₂ component, which was also further investigated by near ambient pressure X-ray photoelectron spectroscopy. By means of solid-state nuclear magnetic resonance, we proposed an elucidation of the organic species trapped inside the SAPO-34 during catalytic runs.

2. EXPERIMENTAL SECTION

2.1 Catalyst preparation

Catalyst preparation steps are described in details in our former paper[31]. Summarizing in brief, the PdZn/ZrO₂ catalyst was prepared by a colloidal impregnation method starting from palladium and zinc acetate solutions in DMF and ethylene glycol, respectively. The obtained colloidal mixture, after washing and dispersion in ethanol, was added with zirconium hydroxide, Zr(OH)₄, in order to obtain a molar composition of 2% Pd, 13% Zn and 85% Zr, verified by Energy-dispersive X-ray spectroscopy (EDS). The final catalyst was obtained after drying

and calcination at 500 °C. As for SAPO-34, it was purchased from ACS materials ($\text{SiO}_2/\text{Al}_2\text{O}_3=0.5$).

The combined system was produced by mixing the oxidic phase with the zeotype by mortar and pestle in a 1:1 weight ratio.

2.2 Catalytic tests

Catalytic tests were executed in a 4 channel Flowrence® from Avantium. 50 mg of the stand-alone PdZn/ZrO₂ catalyst or 100 mg of the combined PdZn/ZrO₂+SAPO-34 catalyst was typically used. The gas feed composition was: 24vol% of CO₂, 72vol% of H₂ and 4vol% of He as internal standard. Before feeding the reaction mixture, all samples were reduced in situ with a pure H₂ atmosphere for 4 hours at 400 °C. The tubes were then pressurized to 30 bar using a membrane-based pressure controller.

GC is an Agilent 7890B with two sample loops. One sample loop goes to TCD channel with 2 Haysep pre-column and MS5A, where He, H₂, CH₄ and CO are separated. Another sample loop goes to an FID with an Innowax pre-column, a Gaspro column and another Innowax column. Gaspro column separates C₁-C₈, paraffins and olefins, while Innowax column separates oxygenated and aromatics.

Conversion and selectivity are reported on C₁ basis and are defined as follows:

$$\text{Conv}_{\text{CO}_2} (\%) = \frac{\text{CO}_{2\text{blk}}/\text{He}_{\text{blk}} - \text{CO}_{2\text{R}}/\text{He}_{\text{R}}}{\text{CO}_{2\text{blk}}/\text{He}_{\text{blk}}} \times 100$$

$$S_{Cn}(\%) = \frac{n \cdot \frac{C_{Cn,R}}{C_{He,R}}}{\left(\frac{C_{CO_2,blk}}{C_{He,blk}} - \frac{C_{CO_2,R}}{C_{He,R}} \right)} \cdot 100$$

where $C_{i_{blk}}$ and C_{i_R} are the concentrations determined by GC analysis in the blank and in the reactor outlet, respectively. Carbon balance closure was better than 2.5% in all cases.

For the ^{13}C labeled tests aimed at ssNMR measurements (vide infra) the same Flowrence® set up was used. The labeled $^{13}\text{CO}_2/\text{H}_2$ mixture (100 bar lecture bottle) was provided by CK Isotopes Limited.

2.3 Spectroscopic characterization

Absorption IR spectra were collected using a Perkin-Elmer FTIR 2000 spectrophotometer equipped with a Hg-Cd-Te cryo-detector, at a resolution of 2 cm^{-1} in the range of 7200-580 cm^{-1} . All sample powders were compressed in self-supporting discs ($\sim 20 \text{ mg cm}^{-2}$) and placed in a quartz IR cell suitable for thermal treatments in controlled atmosphere and spectra recording at room and liquid-nitrogen temperature (RT and LNT, respectively).

Before IR measurements, all the samples were outgassed at 400 °C for 30 mins and then reduced with 40 mbar of dry hydrogen at 400 °C for 30 mins. The reduction treatment aims at simulating the reduction step performed before the catalytic tests. From now on, we will name all the pre-reduced catalysts as “activated” catalysts.

After activation, FT-IR spectra were run at increasing CO pressure up to 20 mbar at RT and LNT on PdZn/ZrO₂ catalyst and at LNT on SAPO-34 and PdZn/ZrO₂ + SAPO-34 combined system. CO was used as probe molecule in order to characterize surface sites, such as Pd sites, Lewis acid sites (Zr⁴⁺ and Zn²⁺) and Brønsted acid sites of SAPO-34. Moreover, CO adsorption was performed on PdZn/ZrO₂ + SAPO-34 combined system after catalytic tests performed at 350 °C for 48 h, at 30 bar, with space velocity of 12000 mL·g⁻¹·h⁻¹. The used bifunctional system was characterized before and after a regeneration step. The used catalyst was activated as already mentioned for the fresh one, while the regeneration step was performed via oxidation in dry oxygen at 600 °C (for 30 mins) and then activation in hydrogen at 400 °C (for 30 mins), in order to simulate the regeneration conditions carried out before the catalytic tests reported in the previous work[31].

Near Ambient Pressure (NAP)-XPS measurements were carried out using an EnviroESCA spectrometer (SPECS GmbH) equipped with a monochromatic Al K α X-ray source ($h\nu = 1486.71$ eV) operating at 42 W and X-ray emission of 3.00 mA. Typically, the PdZn/ZrO₂ catalyst was mixed with carbon black powder in ratio 10:1 to avoid an excessive charging of the surface and then pressed into a pellet ($d=2$ mm, $h=0.5$ mm) within the central cavity of a steel plate. Resistive heating was carried out by a button heater (SPECS GmbH). Temperature setpoints for degassing and reduction of 400 °C were reached through manual ramping over a period of 30 minutes. High resolution spectra were obtained at energy pass of

10 eV; dwell time of 0.5 second per point and step of 0.1 eV were used for all regions (Zr(3d), C(1s), Pd(3d), O(1s) and Zr(2p)).

PdZn/ZrO₂ sample was measured with HR-XPS before NAP experiments. The sample was outgassed in the loading chamber for 1h at 400 °C under UHV conditions. Subsequently, to obtain the activated sample, a flow of 40 ml/min of H₂ at 20 mbar was applied for 2h. After reduction, the sample was transferred to the analysis chamber for further HR-XPS measurement.

All ¹H and ¹³C related (both 1D and 2D) MAS ssNMR spectroscopic experiments were performed on Bruker AVANCE III spectrometers operating at 600 MHz frequency for ¹H using a conventional double resonance 3.2 mm MAS HXY probe. ¹H and ¹³C NMR chemical shifts are reported with respect to the external reference adamantane. All NMR measurements were performed at room temperature (298 K) and MAS frequency of 20 kHz. Herein, samples were prepared using fully enriched ¹³CO₂ at experimental conditions (30 bar, 375 °C, H₂:¹³CO₂ = 3, and 10000 mL·g⁻¹·h⁻¹, 60 h) suitable to increase the ssNMR sensitivity. A dual-bed configuration was used, instead of a mechanical mixture of the standard catalytic tests, in order to be able to perform measurements on used SAPO-34 alone. The 1D direct excitation (DE) 1H-13C cross-polarization (CP) spectra were recorded using a 4 s recycle delay. The 1D insensitive nuclei enhanced by polarization transfer (INEPT) spectrum was recorded using a 2 s recycle delay, a 20 ms acquisition time, and accumulation of 4 k scans. 1H and 13C pulses were applied with a field strength of 70 and 50 kHz, respectively. 2D

^{13}C - ^{13}C spectra were recorded using a 2 s recycle delay, 10 ms (F2) and 1.3 ms (F1) acquisition time and an accumulation of 256 scans. ^{13}C - ^{13}C mixing was achieved through proton driven spin-diffusion (PDS) using phase-alternated-recoupling-irradiation-schemes (PARIS) for 120 ms (CP). 70 kHz SPINAL64 ^1H decoupling was applied during both direct and indirect dimensions. To probe mobile molecules, 2D ^1H - ^{13}C INEPT-based heteronuclear correlation (HETCOR) was applied with 1.5 s recycle delay, 17 ms (^{13}C , F2) and 4 ms (^1H , F1) acquisition time and an accumulation of 512 scans. To probe rigid molecules, dipolar based ^1H - ^{13}C - ^1H HETCOR correlation spectra were obtained using a fixed 0.5 ms contact time for both ^1H - ^{13}C CP and ^{13}C - ^1H CP periods. Background signals were suppressed by an 8 kHz MISSISSIPPI block ($\tau = 5$ ms, $N = 2$) before the last CP period. ^{13}C PISSARRO (phase inverted supercycled sequence for attenuation of rotary resonance) decoupling was applied during acquisition. The recycle delay was 2 s, acquisition times 10 ms (F2, ^1H) and 2 ms (F1, ^{13}C) ms and number of scans 64. All NMR spectra were processed and analyzed using Bruker TopSpin version 3.6.3.

3. RESULTS AND DISCUSSION

3.1 Catalytic performance of the PdZn/ZrO₂ and PdZn/ZrO₂+SAPO-34 catalysts

In our previous work[31], we reported a catalytic screening over the stand-alone PdZn/ZrO₂ catalyst and its combination with SAPO-34, focusing these control

experiments on monitoring MeOH selectivity for PdZn/ZrO₂ and that of propane for the bifunctional system at different reaction pressures and temperatures. Moreover, for the bifunctional system, detailed hydrocarbon distribution for the CO₂ conversion was reported as a function of space velocity. Here we focus on CO, MeOH and CH₄ selectivity for PdZn/ZrO₂ at constant pressure and different temperatures and space velocities and on the detailed hydrocarbon distribution as a function of time for the bifunctional system.

An overview of the catalytic performance of the stand-alone PdZn/ZrO₂ catalyst at different reaction conditions is shown in Table 1. We can observe that CO₂ conversion and MeOH/CO selectivity are in clear agreement with the process thermodynamics[32]. In particular, increasing the temperature or decreasing the gas hourly space velocity (GHSV) increases the CO₂ conversion. On the other hand, this conversion increase is accompanied by a MeOH selectivity decrease and the subsequent CO selectivity increase. The highest methanol selectivity was therefore obtained at the lowest temperature and highest GHSV (74.1%, 250 °C and 12000 ml/g/h). Looking at the methanol yield, the best condition was found at 250 °C, 30 bar and 3000 ml/g/h (5.1% yield). Lastly, methane selectivity is negligible (below 0.1-0.5%) at all tested conditions.

Table 1. Overview of the catalytic performance of the stand-alone PdZn/ZrO₂ catalyst at different reaction conditions. H₂/CO₂ ratio of 3, 30 bar and 24 hours T.O.S.

Temp (°C)	GHSV (ml/g/h)	Conversion (%)	Sel CO (%)	Sel MeOH (%)	Sel CH ₄ (%)	MeOH Yield (%)
250	12000	3.8	25.7	74.1	0.2	2.8
300	12000	9.2	68.3	31.6	0.1	2.9
350	12000	20.8	83.2	16.7	0.1	3.5
400	12000	28.2	96.5	3.4	0.2	1.0
250	6000	6.9	34.6	65.3	0.1	4.5
300	6000	14.1	76.7	23.2	0.0	3.3
350	6000	21.7	89.2	10.8	0.1	2.3
400	6000	28.2	96.8	3.1	0.2	0.9
250	3000	9.0	42.8	57.1	0.1	5.1
300	3000	15.4	82.1	17.8	0.1	2.7
350	3000	21.7	90.8	9.2	0.2	2.0
400	3000	28.2	96.8	3.0	0.5	0.8

An overview of the catalytic performance of the combined PdZn/ZrO₂ + SAPO-34 system is shown in Figure 1. We can observe that the addition of SAPO-34 successfully converts the MeOH produced on the first PdZn/ZrO₂ component into a series of hydrocarbons, with the C₃ family dominating the distribution, in line with the expected behavior of the system[31]. CO₂ conversion and CO selectivity remains in similar levels of the stand-alone PdZn/ZrO₂. With the evolution of the reaction with time, we can observe that deactivation starts to occur and, at around 38 hours on stream, DME starts being produced. This DME formation is a clear sign of the SAPO-34 component deactivation, and it fully dominates the hydrocarbon distribution after 50 hours on stream.

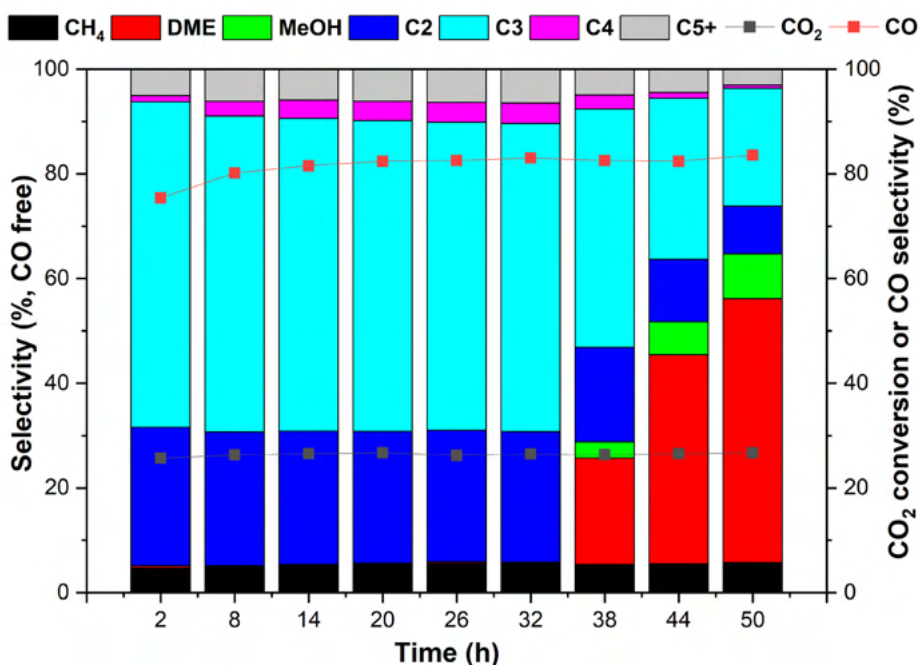


Figure 1. Overview of the catalytic performance of the combined PdZn/ZrO₂ + SAPO-34 system. H₂/CO₂ ratio of 3, 350 °C 12000 ml/g/h.

3.2 CO adsorption on PdZn/ZrO₂ catalyst

Figure 2-a reports FT-IR spectra of CO adsorbed at RT and at increasing pressure on the activated PdZn/ZrO₂ catalyst: an asymmetric band in the region between 2080 and 2020 cm⁻¹ appears and increases in intensity upon CO pressure increase. For sake of clarity, we opted to show the FT-IR spectra related to CO adsorption at RT, despite they have been already displayed in our previous work[31], in order to compare them with those obtained at LNT.

As described in our previous work[31], the band is ascribed to Pd⁰ linear carbonyls[33]. However, the frequency of the maximum, quite lower with respect

to that characteristic of linear carbonyls on reduced Pd supported particles, and the absence of bridged CO species in the region 2000-1970 cm^{-1} prove the presence of PdZn alloy[34–36]. Since Zn is markedly more abundant than Pd, PdZn particles are in intimate contact with ZnO particles over the ZrO_2 support, as well evidenced by high-resolution HAADF-STEM images in our previous work[31]. More in details, the linear carbonyl band is constituted by several components (see inset of Figure 2-a): the most intense one lies at 2063 cm^{-1} and shifts to 2069 cm^{-1} at the maximum CO coverage (θ_{CO} , from blue to red line), whereas two shoulders are evident at 2071 cm^{-1} (2074 cm^{-1} for the maximum θ_{CO} , red line) and 2048 cm^{-1} .

As just mentioned in our former work[31], Pd^0 -CO bond shows strong π -backdonation character, thus the lower the band frequency the more coordinatively unsaturated the site[37]. That being said, we assign the shoulder at 2048 cm^{-1} to carbonyls of highly defective Pd^0 sites, e.g. corners, the main component at 2063-2069 cm^{-1} to carbonyls of less defective sites, e.g. edges, whereas the shoulder at 2071-2074 cm^{-1} can be related to terrace sites.

The blue-shift of the main peak and shoulders is explained taking into account the dipolar coupling and the “*chemical effect*”[38]. The first one can be neglected in our case due to the presence of Pd dilution by alloying with Zn, which lowers the dipole-dipole interaction between neighboring CO molecules adsorbed on Pd. The second one is related with the decrease of π -backdonation as the number of

adsorbed CO molecules increases, so that the CO bond strength and, consequently, the stretching frequency increases upon increasing θ_{CO} .

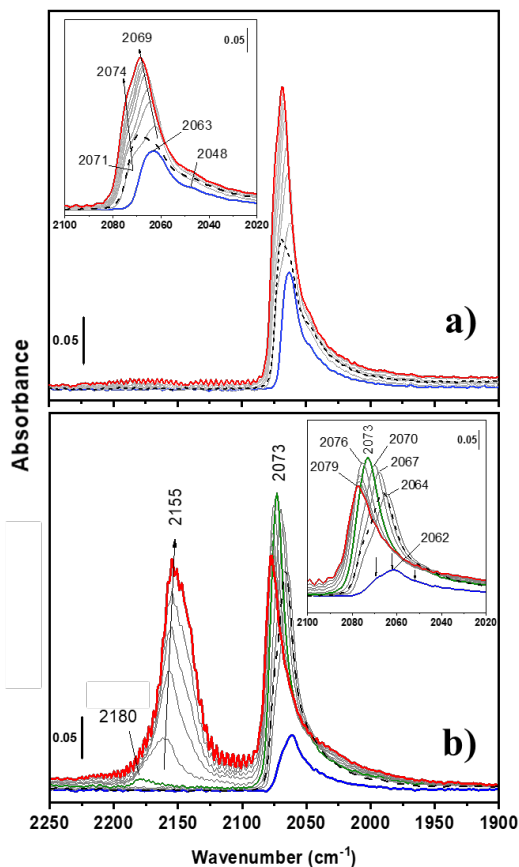


Figure 2. a) FT-IR spectra of CO adsorbed at RT on activated PdZn/ZrO₂ catalyst. Spectra were acquired at increasing CO pressure up to 20 mbar (from blue to red line) and after outgassing (black dashed line). b) FT-IR spectra of CO adsorbed at LNT on activated PdZn/ZrO₂ catalyst. Spectra were acquired at increasing CO pressure up to 20 mbar (from blue to red line) and after outgassing (black dashed line). The green line represents the CO pressure (“breakdown” pressure) beyond which Zn²⁺-CO and Zr⁴⁺-CO bands pop up and Pd⁰-CO band starts decreasing.

After outgassing (dashed-black line in Figure 2-a), the intensities of the main peak and shoulders are drastically reduced but not totally brought down, evidencing a certain stability of Pd⁰-CO at room temperature. The outgassing decreases the

effect due to the θ_{CO} , i.e. the “*chemical effect*”, shifting back the absorptions to their former positions.

In order to characterize Lewis acid sites (i.e. Zr^{4+} and Zn^{2+}) and eventually Zn^0 , CO adsorption was performed at liquid-nitrogen temperature on the activated PdZn/ZrO₂ catalyst (Figure 2-b). Two bands are present: the former in the range 2080-2020 cm⁻¹ is related to CO linearly adsorbed on metallic palladium sites in the PdZn alloy, the latter in the range 2190-2120 cm⁻¹ is related to CO adsorption on Zr^{4+} and Zn^{2+} sites.

As for the high-frequency region, the first appearing band at 2180 cm⁻¹ (Figure 2-b, green line) could be related to zinc(II)-carbonyls[33,39]: this very weak band is completely covered by the Zr^{4+} -CO band at higher CO doses. Zr^{4+} -CO band exhibits a red-shift up to 2155 cm⁻¹ due to the “*chemical effect*”: Zr^{4+} is a σ -donor center, hence the frequency of the peak red-shifts as the CO coverage increases[33,40]. These findings are in line with those reported by Ticali et al.[41] for ZnZrO_x systems: among the three samples analyzed, the one with the highest concentration of Zn was featured by the formation of a ZnO extra-phase that could be looked at as a Zn/ZrO₂ system. As reported, the authors highlighted that the same spectroscopic features could be mainly assigned to Zr^{4+} with different coordination, while Zn^{2+} could only give a minor contribution to the band.

As for Zn^0 sites, to the best of our knowledge no literature data are available about the Zn^0 -CO species, reasonably because d-orbitals of Zn^0 are not suitable to form stable carbonyl species. For this reason, some authors used bands related to Zn^{2+}

carbonyls on oxidized and reduced supported zinc to evaluate, by subtraction, the amount of Zn^0 formed in the reduction process[42]. These literature data highlight that Zn^0 carbonyls are not observable species.

Focusing on the Pd^0 region, as observed at RT, the carbonyl band show at least three components (evidenced by arrows in the inset of Figure 2-b), which put in evidence the different Pd sites in the alloy, as just discussed for Figure 2-a. Differently from CO adsorption at RT, it is worth to note a peculiar behavior when CO is adsorbed at increasing doses: from the blue line, through the green line, to the red line, the spectra highlight an increasing and then a decreasing intensity of Pd carbonyl band along with a continuous shift to higher frequencies. From now on we will call this behavior '*bell-shaped shift*'. This shift is featured by a maximum reached by the Pd carbonyl band (green line) at a pressure that we call '*breakdown pressure*'. After the *breakdown pressure*, as CO coverage increases, the band of CO on cationic sites in the region $2190-2120\text{ cm}^{-1}$ suddenly increases becoming well evident, but the absorption of CO on Pd^0 atoms decreases in intensity.

After outgassing (dashed line in Figure 2-b), Pd^0 -CO band goes back to the position and intensity of the spectrum collected after the second CO admission, just like their analogous in Figure 2-a. The intensity of the Pd^0 -CO band after outgassing is nearly the same reached for the maximum CO pressure (red line), while CO molecules on Zr^{4+} and Zn^{2+} are completely desorbed.

The comprehension of the intensity modulation that causes the *bell-shaped shift* is not straightforward. The blue-shift of the Pd⁰-CO band upon increasing CO pressure is similar to that observed at RT. The different behavior of this band at LNT is related to the loss of intensity that starts when CO is adsorbed on ZnO and zirconia support. This loss could be related to a diminution of the amount of CO molecules adsorbed on Pd; however, due to the lowering of the “*chemical effect*” upon decreasing CO coverage, this should cause a red-shift of the band. Alternatively, the intensity loss could be explained by a decrease of the absorption coefficient of Pd carbonyls, possibly induced by CO adsorption on ZnO and zirconia support; as a consequence, the absorption intensity decreases even if the amount of CO molecules on Pd increases. This last hypothesis is coherent with the behavior observed after the outgassing: by removing CO from Zr⁴⁺ and Zn²⁺ sites, the absorption coefficient increases again and the partial desorption of CO also from Pd causes the band red-shift. This hypothesis could be corroborated by the model describing the dipolar coupling obtained by Hammaker, Francis and Eischens (HFE) in 1965[43] and subsequently modified[37,44]. As a matter of fact, the modified HFE model predicts that the dipolar coupling causes two effects observable upon increasing interacting adsorbed molecules: a shift of the absorption band at higher frequency and a reduction of the absorption coefficient. The dipolar coupling and, thus, these effects occur when adsorbed molecules belong to the same surface species, i.e. adsorbed molecules with the same singleton frequency. As a consequence, CO molecules adsorbed on ZnO and

zirconia support cannot directly be responsible for the observed behavior. Moreover, due to the presence of the alloy, the dipolar coupling for CO adsorbed on Pd was previously excluded. However, the adsorption at LNT leads, reasonably, to the adsorption of a much higher amount of CO on Pd with respect to RT, which is hidden by the intensity loss. This could make the dipolar coupling to occur also for Pd in the alloy, and this is proved by the frequency at maximum coverage that is 10 cm^{-1} higher at LNT (2079 cm^{-1}) than at RT (2069 cm^{-1}). In addition, an effect of the presence of CO adsorbed on ZnO and zirconia support on the molecule proximity in the Pd carbonyl adlayer cannot be ruled out. This last should imply a strong interaction between PdZn alloy particles and the oxidic phases. Actually, HAADF-STEM images reported in our previous work[31] showed PdZn particles in intimate contact with ZnO over the ZrO_2 support.

3.3 Near Ambient Pressure X-ray photoelectron spectroscopy on PdZn/ZrO₂

In an attempt to determine the different Pd and Zn chemical species on the surface of the activated PdZn/ZrO₂ catalyst, a set of NAP-XPS experiments was performed (see Figure 3).

The formation of PdZn alloys has been previously studied using model systems[45–48]. These studies demonstrated a shift in the Pd⁰(3d_{5/2}) peak towards higher binding energies (from 335 to 336.1 eV) as a result of alloy formation[45,49]. The nature of such energy shifts in PdZn alloys and the effect of the alloying upon CO adsorption was studied by Rodriguez[50]. A combination

of MO-SCF calculations and XPS showed that Pd(4d)→Zn(4p) charge transfer and Pd(4d)→Pd(5s,5p) rehybridization during alloy formation are responsible for the binding energy shift and for a weakening of Pd(4d)→CO(2π) bonding interactions[50]. More recent studies on Pd-Zn interaction reported that the charge transfer induces a negative charge over Pd and a positive charge over Zn, which should imply a reverse shift with respect to that observed[46,51,52]. However, the shift of Pd(3d) and Zn(2p) bands to higher and lower binding energies, respectively, are largely accepted as fingerprints for PdZn alloying also in more recent literature[46,47,53,54]. In the pristine PdZn/ZrO₂ catalyst (Figure 2 (a,c)), the presence of native PdO (Pd 3d_{5/2} 337.4 eV) and ZnO (Zn 2p_{3/2} 1022.5(6) eV)[55] with an atomic ratio Pd/Zn of 1.1 (Table S1), in good agreement with previous paper[31], is observed. The calculated binding energies for the Pd(3d) region are slightly higher (0.4 - 0.2 eV) than previously reported in literature[55–57] for Pd²⁺.

This is probably due to charging of the sample surface and uncertainty of fitting due to overlapping with Zr(3p). The feature at ~1024 eV present in the Zn(2p_{3/2}) region can either be attributed to Zn attached to hydroxyl groups of the ZrO₂ surface[58] or to a differential charging effect that would result in an asymmetry of the ZnO peak.

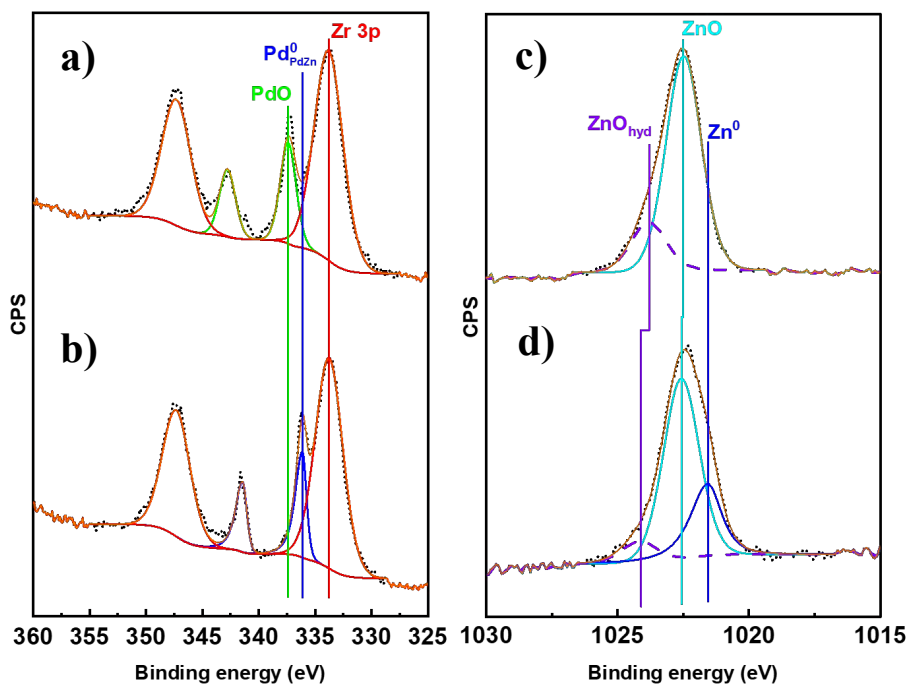


Figure 3. NAP-XPS spectra of Pd(3d) and Zn(2p_{3/2}) regions of PdZn/ZrO₂ catalyst as prepared (a, c) and after activation in H₂ (b, d).

After activation at 400 °C under 20 mbar of hydrogen (Figure 2 (b, d)), full and partial reduction of Pd and Zn, respectively, are observed, with binding energies of 336.1 eV and 1021.5 eV. In contrast, when a reference sample based on Pd foil was submitted to similar conditions (Figure S1), analysis of the XPS spectrum of the sample revealed a Pd(3d_{5/2}) binding energy of 335.1 eV, 1 eV lower than that observed for the PdZn/ZrO₂ catalyst after reduction. These results demonstrate the formation of the aforementioned alloy and are in good agreement with the literature[36,45,46,48,49,58]. The partial reduction of Zn is in good agreement with the results reported in our previous paper, in which XAS measurements

demonstrated the presence of a defective ZnO phase after reduction[31]. In addition, the Pd/Zn atomic ratio remains almost unchanged upon reduction (Table S1).

3.4. CO adsorption on SAPO-34 and PdZn/ZrO₂ + SAPO-34 combined system

In order to characterize the combined bifunctional system, FT-IR measurements of CO adsorption at LNT on both fresh and used PdZn/ZrO₂ + SAPO-34 system were performed after activation and reported in Figure 4 (sections b and c, respectively). For comparison purposes, the same measurement was performed on SAPO-34 alone (section a). In all the spectra, two main peaks at 2170 and 2140 cm⁻¹ are evident. The former is related to CO adsorbed on Brønsted acid sites of the zeotype material, and it grows first. The latter is assigned to liquid-like CO entrapped inside the pores of SAPO-34[59]. When a high fraction of Brønsted sites is engaged in interaction with CO, the band representing liquid like CO entrapped inside the cavities starts to increase. Another band at about 2090 cm⁻¹, which was observed in some works[60,61] for Ca-Y and Na-ZSM-5, is present. This band changes frequency according to the nature of coordinated metal or cation. Indeed, the σ -coordinated CO through the C-end could interact with the lattice *via* the O-end with a guest cation (e.g. Ca[60] and Na[61] ions) or any other Lewis acid site on the surface. Another hypothesis assign this band to CO in interaction with framework oxygen atoms[62].

When SAPO-34 is mixed with PdZn/ZrO₂, nothing seems to change for the previously mentioned peaks, except a slight change in their relative intensities. Moreover, Figure 4-b shows that the spectra of the fresh physical mixture still present the characteristic “*bell-shaped shift*” pattern in the region related to Pd⁰ carbonyls (see zoom in the inset). However, Pd⁰-CO pattern is no more evident on the used system (Figure 4-c), reasonably due to the presence of coke and some other products obtained during the catalytic tests. In order to verify the possibility of having PdZn/ZrO₂ surface covered by reaction products, we performed UV-Raman characterization, which was reported in our previous manuscript[31]. UV-Raman results obtained for the combined system showed the presence of alkenes and polycyclic aromatic hydrocarbons, which is a typical feature for an initial deactivation of the catalyst. Indeed, the presence of hydrocarbon residues decreases the amount of Brønsted acid sites of SAPO-34 as evidenced by the lower intensity of the band at 2170 cm⁻¹ with respect to that observed for the fresh combined system (compare Figure 4-c and 4-b).

In the light of the just mentioned findings, we performed a regeneration of the used combined system at 600 °C in O₂, in order to “clean” the surface from hydrocarbon residues, and then a reduction in H₂ at 400 °C to obtain the activated system. Figure 4-d displays that Pd is available again for CO adsorption, as evidenced by the *bell-shaped shift* pattern in the inset, and that Brønsted acid sites of SAPO-34 are restored, as evidenced by the increased intensity of the band at 2170 cm⁻¹. Hence, we can assure that regeneration is mandatory to restore the

catalytic activity of the combined system. Indeed, the catalytic tests on the regenerated sample reported in our previous paper showed a complete regained activity[31]. However, after having regenerated (i.e. oxidized) and reduced the sample, spectra are not the same as those in Figure 4-b for the fresh combined system. Indeed, at first look the intensity ratio of the main two peaks at 2170 and 2140 cm^{-1} is changed, and they look almost equally high. Moreover, two more peaks are visible at 2220 and 2195 cm^{-1} , which can be assigned to Pd^{2+} carbonyls[33], in particular to dicarbonyls of isolated Pd^{2+} [33,63,64]. This last assignment is consistent with the possibility that some Pd^{2+} ions have exchanged a little fraction of Brønsted acid sites in the SAPO-34. It is reasonable that this exchange occurs during the regeneration treatment in oxygen and that these isolated Pd^{2+} cations are stabilized by the zeotype framework, which prevents their reduction during the subsequent treatment in hydrogen.

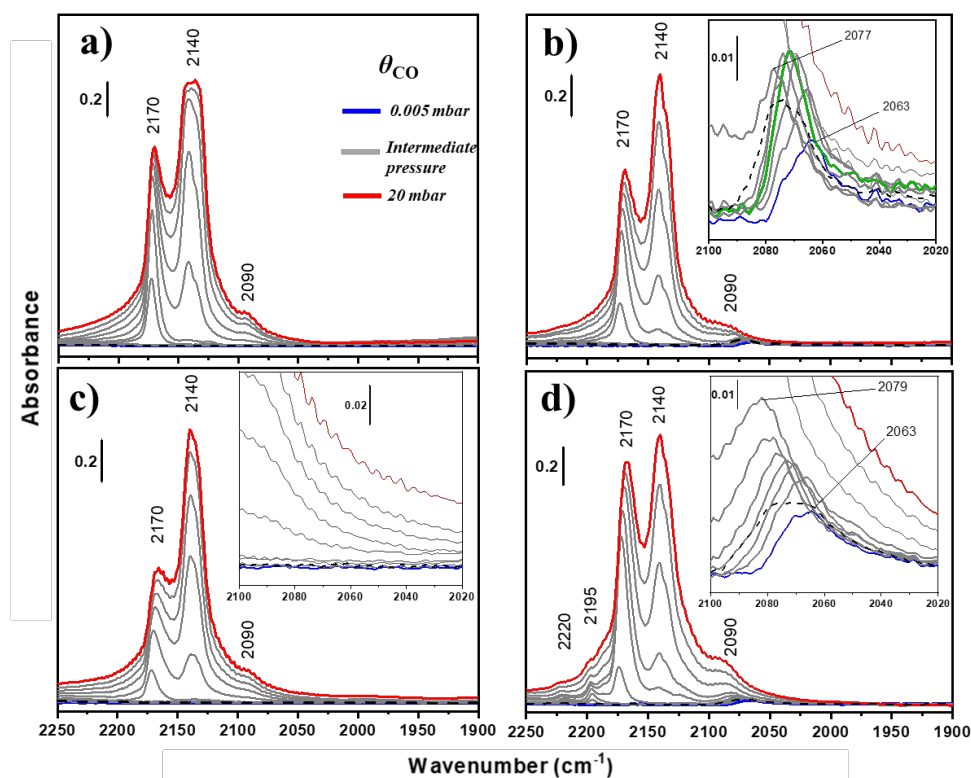


Figure 4. FT-IR spectra of CO adsorbed at LNT on the following activated systems: SAPO-34 (a), fresh PdZn/ZrO₂ + SAPO-34 (b), used PdZn/ZrO₂ + SAPO-34 (c) and used PdZn/ZrO₂ + SAPO-34 after regeneration in O₂ at 600 °C and activation step (d). Spectra were acquired at increasing CO pressure up to 20 mbar (from blue to red line) and after outgassing (black dashed line). Green line in section b): CO “breakdown” pressure for Pd carbonyls.

3.4. Elucidation of molecular structure of organic species trapped in SAPO-34

To elucidate the molecular structure of zeotype-trapped organic species, we performed solid-state NMR spectroscopy (ssNMR) on the post-reacted zeotype (SAPO-34) after 60 h under reaction conditions (30 bar, 375°C, H₂/CO = 3) using ¹³C isotope-enriched CO₂ (Figure 5). ¹³CO₂ high-pressure gas is cost intensive and the experiment was carried out as a model test to measure the SAPO-34 by

^{13}C ssNMR on a dual bed configuration. Generally, one-dimensional (1D) ssNMR spectra of the post-reacted zeotype show the following three features: (i) 5-50 ppm (aliphatic), (ii) 110-150 ppm (olefinic/methylated aromatic), and (iii) 180-220 ppm (carbonyl moieties)[65–68]. We applied a series of magnetization transfer schemes based on the mobility of trapped molecules, which had been previously developed to elucidate molecular structures in zeolites[65,69,70]. For example, ^{13}C direct excitation (DE) pulse sequence has been applied to detect all chemical species in quantitative analysis, while mobile and rigid organic species can be differentiated by applying scalar-based through-bond (insensitive nuclei enhanced by polarization transfer, INEPT) and dipolar-based thorough-space (cross-polarization based, CP) magnetization transfer schemes, respectively. Such technique allowed us to distinguish between species with either weak interaction or adsorbed on the zeotype.

The 1D ^{13}C DE MAS ssNMR spectra show high amounts of aromatics-related species in spent SAPO-34. Moreover, the species typically observed in the initial and steady-state stages during methanol-to-hydrocarbons, such as methoxy (13C, 1H = 57.7, 3.5 ppm), methanediol (93.1, 4.9 ppm), dimethoxymethane (100, 4.7 ppm), and DME (62.4, 3.46 ppm) are not observed, which again indicates this spent sample was obtained at the deactivation stage, which is in line with the activity test results (Figure 1). By applying ^1H - ^{13}C CP magnetization transfer scheme, alkane species can be enhanced due to higher proton density around ^{13}C nuclei of interest (H/C ratio of alkane = *ca.* 1.7; aromatics = 1 (benzene), 1.25

(xylene), respectively)[69]. Most of the observed species in INEPT based pulse are confidently assigned as terminal alkyl groups from methylated aromatics or polyaromatics, *i.e.*, most of the trapped aromatics are rigid aromatic species. This is confirmed by applying 2D ^{13}C - ^{13}C and ^1H - ^{13}C - ^1H correlation spectra, which was achieved through proton-driven spin diffusion using phase alternated recoupling irradiations schemes (PDS PARIS) and proton detected CP-based hetero-nuclear correlation spectroscopy (double CP-HETCOR) (Figure 5-b, c). For example, methylated aromatic species is readily observed at 135.2/20.0 and 131.3/19.9 ($^{13}\text{C}/^{13}\text{C}$), showing their correlation with ^1H at 7.2 ppm[71]. According to the hydrocarbon pool mechanism[29], the C3 families are mostly produced by two competing cycles governed by olefinic and aromatic cycles[72]. Although the sample was obtained at deactivation stage, we could see the traces of methylated olefinic species, indicating SAPO-34 has experienced dual-cycle mechanism, responsible for high C3 selectivity. The methylated poly-ene species are previously reported as rigid compounds, showing ^{13}C and ^1H chemical shift ranges at 130-160 and 1-3 ppm[69], respectively. In spent SAPO-34, we could observe the cross-peaks at 136.5/2.3 and 131.4/2.4 ($^{13}\text{C}/^1\text{H}$) ppm by 2D ^1H - ^{13}C CP-HETCOR but not by INEPT-HETCOR, indicating the presence of less-mobile methylated alkene species, which are presumably adsorbed in the zeotype framework (Figure 5-d, e).

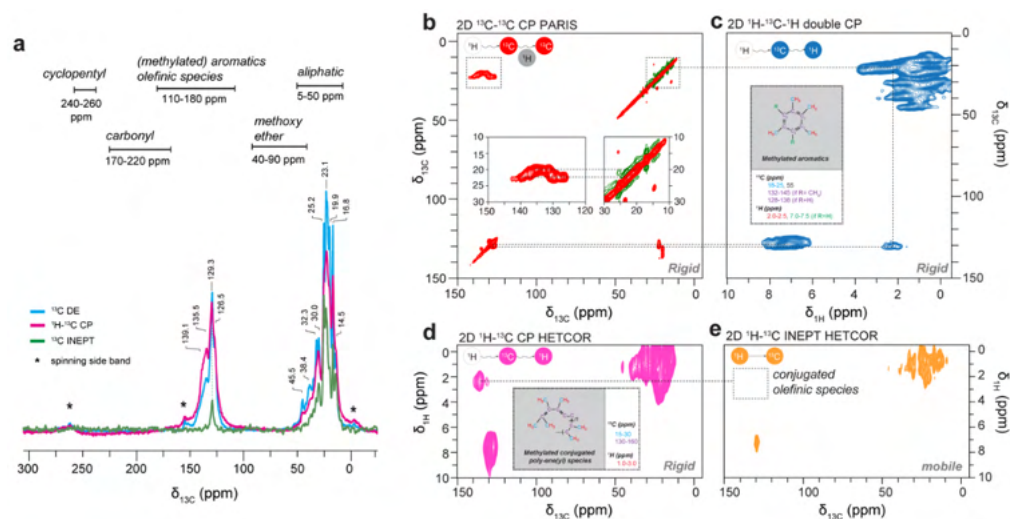


Figure 5. (a) 1D ^{13}C DE, ^1H - ^{13}C CP, ^1H - ^{13}C INEPT ssNMR MAS spectra of post-reacted SAPO-34 zeotype after hydrogenation of CO_2 of fully isotope-enriched $^{13}\text{CO}_2$ in the reactant feed ($^{13}\text{CO}_2$ at 30 bar, 375°C , $\text{H}_2/^{13}\text{CO}_2 = 3$, and 10000 mL/g/h at a time-on-stream of 60 h). 2D ssNMR correlation spectra acquired using (b) 2D ^{13}C - ^{13}C , (c) 2D ^1H - ^{13}C - ^1H , (d) ^1H - ^{13}C CP HETCOR, and (e) ^1H - ^{13}C INEPT HETCOR. MAS spinning rate at 20 kHz and the spinning side bands are noted with asterisk.

4. CONCLUSIONS

In this work, we have focused on the characterization of a combined system eligible as candidate for carbon dioxide hydrogenation into methanol and conversion to hydrocarbons. This system has shown to be highly active and selective for C_3 hydrocarbon production, in particular propane[31]. This attitude can be directly correlated to the formation of a PdZn alloy on the PdZn/ ZrO_2 component that has been confirmed in our previous paper[31] and well demonstrated by FT-IR findings. Indeed, using CO as a probe molecule on the lone PdZn/ ZrO_2 catalyst, the position of the IR band related to Pd^0 linear carbonyls

and the absence of bridged carbonyls are ascribable to the formation of the alloy. NAP-XPS study of PdZn/ZrO₂ catalyst, as prepared and after reduction, confirms the formation of a PdZn alloy. Indeed, in good agreement with the literature data[45,46,48], we observe a shift of 1 eV in binding energy after reduction when comparing the PdZn/ZrO₂ catalyst to a model of Pd foil submitted to similar conditions. Moreover, FT-IR spectra of CO adsorbed at LNT show a particular behavior of Pd⁰ carbonyl band, which we named ‘*bell-shaped shift*’, due to the CO adsorption onto Zn²⁺ and Zr⁴⁺ sites of the oxidic phases in intimate contact with the PdZn alloy particles. The presence of a residual ZnO phase after reduction is demonstrated by NAP-XPS measurements that confirm previously obtained results[31].

When the metal-oxide phase is mechanically mixed with the zeotype SAPO-34, the characteristic spectroscopic features of the two components obtained after CO adsorption at LNT do not appear perturbed by the mixing. Nevertheless, after catalytic testing, aromatic and aliphatic compounds cover Pd sites and decrease the amount of Brønsted acid sites of SAPO-34. Indeed, as confirmed by ssNMR results, high amount of aromatic and olefinic species are present, indicating that SAPO-34 underwent a dual-cycle mechanism, responsible for high C₃ selectivity. Regeneration (i.e. oxidation at 600 °C) is mandatory to restore the catalytic sites of the combined system; however, after the regeneration, a small fraction of Pd²⁺ exchanges some Brønsted acid sites inside the zeotype, which, after repeated

regeneration cycles, could be one of the causes of the reduction of the catalytic activity in propane formation.

ACKNOWLEDGEMENTS

This project has received funding from the European Union's Horizon 2020 Research and Innovation Programme under grant agreement No. 837733. The authors are grateful to Dr. Christian Ahoba-Sam for the synthesis of the PdZn/ZrO₂ sample.

REFERENCES

- [1] NOAA ESRL Global Monitoring Laboratory, Trends in Atmospheric Carbon Dioxide, . <https://gml.noaa.gov/ccgg/trends/mlo.html>, 2020.
- [2] K. Li, J.G. Chen, ACS Catal. 9 (2019) 7840–7861.
<https://doi.org/10.1021/acscatal.9b01943>.
- [3] S. Kattel, P. Liu, J.G. Chen, J. Am. Chem. Soc. 139 (2017) 9739–9754.
<https://doi.org/10.1021/jacs.7b05362>.
- [4] J.A. Rodriguez, P. Liu, D.J. Stacchiola, S.D. Senanayake, M.G. White, J.G. Chen, ACS Catal. 5 (2015) 6696–6706.
<https://doi.org/10.1021/acscatal.5b01755>.

- [5] J. Wambach, A. Baiker, A. Wokaun, *Phys. Chem. Chem. Phys.* 1 (1999) 5071–5080. <https://doi.org/10.1039/A904923A>.
- [6] W. Wang, S. Wang, X. Ma, J. Gong, *Chem. Soc. Rev.* 40 (2011) 3703–3727. <https://doi.org/10.1039/c1cs15008a>.
- [7] Y. Amenomiya, *Appl. Catal. A Gen.* 30 (1987) 57–68.
- [8] T. Fujitani, I. Nakamura, *Bull. Chem. Soc. Jpn.* 75 (2002) 1393–1398. <https://doi.org/10.1246/bcsj.75.1393>.
- [9] J. Wang, G. Li, Z. Li, C. Tang, Z. Feng, H. An, H. Liu, T. Liu, C. Li, *Sci. Adv.* 3 (2017) 1–11. <https://doi.org/10.1126/sciadv.1701290>.
- [10] S. Kattel, P.J. Ramírez, J.G. Chen, J.A. Rodriguez, P. Liu, *Science* (80-.). 357 (2017) 1296–1299. <https://doi.org/10.1126/science.aal3573>.
- [11] V. V. Rozanov, O. V. Krylov, *Usp. Khim.* 66 (1997) 127–130. <https://doi.org/10.1070/rc1997v066n02abeh000308>.
- [12] W.C. Conner, J.L. Falconer, *Chem. Rev.* 95 (1995).
- [13] J. Ye, C. Liu, D. Mei, Q. Ge, *ACS Catal.* 3 (2013) 1296–1306. <https://doi.org/10.1021/cs400132a>.
- [14] G. Cerrato, S. Bordiga, S. Barbera, C. Morterra, *Surf. Sci.* 377–379 (1997) 50–55. [https://doi.org/10.1016/S0039-6028\(96\)01348-9](https://doi.org/10.1016/S0039-6028(96)01348-9).

- [15] K. Tanabe, *Mater. Chem. Phys.* 13 (1985) 347–364.
[https://doi.org/10.1016/0254-0584\(85\)90064-1](https://doi.org/10.1016/0254-0584(85)90064-1).
- [16] O.A. Ojelade, S.F. Zaman, *J. CO2 Util.* 47 (2021) 101506.
<https://doi.org/10.1016/j.jcou.2021.101506>.
- [17] O.A. Ojelade, S.F. Zaman, *Catal. Surv. from Asia* 24 (2020) 11–37.
<https://doi.org/10.1007/s10563-019-09287-z>.
- [18] O.A. Ojelade, S.F. Zaman, M.A. Daous, A.A. Al-Zahrani, A.S. Malik, H. Driss, G. Shterk, J. Gascon, *Appl. Catal. A Gen.* 584 (2019).
<https://doi.org/10.1016/j.apcata.2019.117185>.
- [19] A.S. Malik, S.F. Zaman, A.A. Al-Zahrani, M.A. Daous, *J. Ind. Eng. Chem.* 103 (2021) 67–79. <https://doi.org/10.1016/J.JIEC.2021.07.019>.
- [20] S. Fakhruz Zaman, A. Shan Malik, A. Ahmed Alzahrani, M.A. Daous, L.A. Petrov, (2018).
- [21] O.A. Ojelade, S.F. Zaman, *Comptes Rendus l’Académie Bulg. Des Sci.* 72 (2019).
- [22] A.S. Malik, S.F. Zaman, A.A. Al-Zahrani, M.A. Daous, H. Driss, L.A. Petrov, *Catal. Today* 357 (2020) 573–582.
<https://doi.org/10.1016/j.cattod.2019.05.040>.

- [23] K. Cheng, B. Gu, X. Liu, J. Kang, Q. Zhang, Y. Wang, *Angew. Chemie - Int. Ed.* 55 (2016) 4725–4728. <https://doi.org/10.1002/anie.201601208>.
- [24] F. Jiao, J. Li, X. Pan, J. Xiao, H. Li, H. Ma, M. Wei, Y. Pan, Z. Zhou, M. Li, S. Miao, J. Li, Y. Zhu, D. Xiao, T. He, J. Yang, F. Qi, Q. Fu, X. Bao, *Science* (80-.). 351 (2016) 1065–1068. <https://doi.org/10.1126/science.aaf1835>.
- [25] S. Wang, P. Wang, Z. Qin, Y. Chen, M. Dong, J. Li, K. Zhang, P. Liu, J. Wang, W. Fan, *ACS Catal.* 8 (2018) 5485–5505. <https://doi.org/10.1021/acscatal.8b01054>.
- [26] T. Liang, J. Chen, Z. Qin, J. Li, P. Wang, S. Wang, G. Wang, M. Dong, W. Fan, J. Wang, *ACS Catal.* 6 (2016) 7311–7325. <https://doi.org/10.1021/acscatal.6b01771>.
- [27] R.M. Dessau, R.B. LaPierre, *J. Catal.* 78 (1982) 136–141. [https://doi.org/https://doi.org/10.1016/0021-9517\(82\)90292-5](https://doi.org/https://doi.org/10.1016/0021-9517(82)90292-5).
- [28] I.M. Dahl, S. Kolboe, *Catal. Letters* 20 (1993) 329–336. <https://doi.org/10.1007/BF00769305>.
- [29] W. Wang, Y. Jiang, M. Hunger, *Catal. Today* 113 (2006) 102–114. <https://doi.org/10.1016/J.CATTOD.2005.11.015>.
- [30] PROPANE MARKET - GROWTH, TRENDS, AND FORECAST (2020

- 2025), n.d.

- [31] A. Ramirez, P. Ticali, D. Salusso, T. Cordero-Lanzac, S. Ould-Chikh, C. Ahoba-Sam, A.L. Bugaev, E. Borfecchia, S. Morandi, M. Signorile, S. Bordiga, J. Gascon, U. Olsbye, *JACS Au* 1 (2021) 1719–1732.
<https://doi.org/10.1021/jacsau.1c00302>.
- [32] S. De, A. Dokania, A. Ramirez, J. Gascon, *ACS Catal.* 10 (2020) 14147–14185. <https://doi.org/10.1021/acscatal.0c04273>.
- [33] K.I. Hadjiivanov, G.N. Vayssilov, *Adv. Catal.* 47 (2002) 307–511.
[https://doi.org/10.1016/S0360-0564\(02\)47008-3](https://doi.org/10.1016/S0360-0564(02)47008-3).
- [34] K. Föttinger, *Catal. Today* 208 (2013) 106–112.
<https://doi.org/10.1016/j.cattod.2012.12.004>.
- [35] T. Conant, A.M. Karim, V. Lebarbier, Y. Wang, F. Girgsdies, R. Schlögl, A. Datye, *J. Catal.* 257 (2008) 64–70.
<https://doi.org/10.1016/j.jcat.2008.04.018>.
- [36] C. Rameshan, W. Stadlmayr, C. Weilach, S. Penner, H. Lorenz, M. Hävecker, R. Blume, T. Rocha, D. Teschner, A. Knop-Gericke, R. Schlögl, N. Memmel, D. Zemlyanov, G. Rupprechter, B. Klötzer, *Angew. Chemie - Int. Ed.* 49 (2010) 3224–3227.
<https://doi.org/10.1002/anie.200905815>.

- [37] P. Hollins, *Surf. Sci. Rep.* 16 (1992) 51–94. [https://doi.org/10.1016/0167-5729\(92\)90008-Y](https://doi.org/10.1016/0167-5729(92)90008-Y).
- [38] P. Hollins, J. Pritchard, *Surf. Sci.* 89 (1979) 486–495.
[https://doi.org/10.1016/0039-6028\(79\)90633-2](https://doi.org/10.1016/0039-6028(79)90633-2).
- [39] D. Scarano, S. Bertarione, G. Spoto, A. Zecchina, C. Otero Areán, *Thin Solid Films* 400 (2001) 50–55. [https://doi.org/10.1016/S0040-6090\(01\)01472-9](https://doi.org/10.1016/S0040-6090(01)01472-9).
- [40] C. Morterra, V. Bolis, B. Fubini, L. Orto, T.B. Williams, *Surf. Sci.* 251–252 (1991) 540–545. [https://doi.org/10.1016/0039-6028\(91\)91051-X](https://doi.org/10.1016/0039-6028(91)91051-X).
- [41] P. Ticali, D. Salusso, R. Ahmad, C. Ahoba-Sam, A. Ramirez, G. Shterk, K.A. Lomachenko, E. Borfecchia, S. Morandi, L. Cavallo, J. Gascon, S. Bordiga, U. Olsbye, *Catal. Sci. Technol.* 11 (2021) 1249–1268.
<https://doi.org/10.1039/D0CY01550D>.
- [42] A.I. Serykh, Y.A. Agafonov, *Mol. Catal.* 493 (2020) 111055.
<https://doi.org/https://doi.org/10.1016/j.mcat.2020.111055>.
- [43] R.M. Hammaker, S.A. Francis, E. R.P., *Spectrochim. Acta* 21 (1965) 1295–1309.
- [44] B.N.J. Persson, R. Ryberg, *Phys. Rev. B* 24 (1981) 6954–6970.
<https://doi.org/10.1103/PhysRevB.24.6954>.

- [45] A. Bayer, K. Flechtner, R. Denecke, H.-P. Steinrück, K.M. Neyman, N. Rösch, *Surf. Sci.* 600 (2006) 78–94.
<https://doi.org/10.1016/j.susc.2005.09.049>.
- [46] H.H. Holzapfel, A. Wolfbeisser, C. Rameshan, C. Weilach, G. Rupprechter, *Top. Catal.* 57 (2014) 1218–1228.
<https://doi.org/10.1007/s11244-014-0295-3>.
- [47] C. Rameshan, C. Weilach, W. Stadlmayr, S. Penner, H. Lorenz, M. Hävecker, R. Blume, T. Rocha, D. Teschner, A. Knop-Gericke, *J. Catal.* 276 (2010) 101–113. <https://doi.org/10.1016/j.jcat.2010.09.006>.
- [48] C. Rameshan, W. Stadlmayr, C. Weilach, S. Penner, H. Lorenz, M. Hävecker, R. Blume, T. Rocha, D. Teschner, A. Knop-Gericke, R. Schlögl, N. Memmel, D. Zemlyanov, G. Rupprechter, B. Klötzer, *Angew. Chemie Int. Ed.* 49 (2010) 3224–3227.
<https://doi.org/10.1002/anie.200905815>.
- [49] N. Iwasa, S. Masuda, N. Ogawa, N. Takezawa, *Appl. Catal. A Gen.* 125 (1995) 145–157. [https://doi.org/10.1016/0926-860X\(95\)00004-6](https://doi.org/10.1016/0926-860X(95)00004-6).
- [50] J.A. Rodriguez, *J. Phys. Chem.* 98 (1994) 5758–5764.
<https://doi.org/10.1021/j100073a031>.
- [51] K.M. Neyman, R. Sahnoun, C. Inntam, S. Hengrasmee, N. Rösch, J.

- Phys. Chem. B 108 (2004) 5424–5430.
<https://doi.org/10.1021/jp049830f>.
- [52] Z.-X. Chen, K.M. Neyman, A.B. Gordienko, N. Rösch, Phys. Rev. B 68 (2003) 075417. <https://doi.org/10.1103/PhysRevB.68.075417>.
- [53] K.M. Neyman, K.H. Lim, Z.-X. Chen, L. V. Moskaleva, A. Bayer, A. Reindl, D. Borgmann, R. Denecke, H.-P. Steinrück, N. Rösch, Phys. Chem. Chem. Phys. 9 (2007) 3470–3482.
<https://doi.org/10.1039/B700548B>.
- [54] M. Friedrich, A. Ormeci, Y. Grin, M. Armbrüster, Zeitschrift Für Anorg. Und Allg. Chemie 636 (2010) 1735–1739.
<https://doi.org/10.1002/zaac.201000097>.
- [55] A. V. Naumkin, A. Kraut-Vass, S.W. Gaarenstroom, C.J. Powell, NIST Standard Reference Database 20, Version 4.1 (Web Version)., 2012.
- [56] M.C. Militello, S.J. Simko, Surf. Sci. Spectra 3 (1994) 395–401.
<https://doi.org/10.1116/1.1247784>.
- [57] M. Brun, A. Berthet, J.. Bertolini, J. Electron Spectros. Relat. Phenomena 104 (1999) 55–60. [https://doi.org/10.1016/S0368-2048\(98\)00312-0](https://doi.org/10.1016/S0368-2048(98)00312-0).
- [58] C. Huang, Z. Wu, H. Luo, S. Zhang, Z. Shao, H. Wang, Y. Sun, ACS Appl. Energy Mater. 4 (2021) 9258–9266.

<https://doi.org/10.1021/acsaem.1c01502>.

- [59] F. Bleken, M. Bjørgen, L. Palumbo, S. Bordiga, S. Svelle, K.P. Lillerud, U. Olsbye, *Top. Catal.* 52 (2009) 218–228.
<https://doi.org/10.1007/s11244-008-9158-0>.
- [60] V. Bolis, B. Fubini, E. Garrone, E. Giamello, C. Morterra, *Stud. Surf. Sci. Catal.* 48 (1989) 159–166. [https://doi.org/10.1016/S0167-2991\(08\)60679-5](https://doi.org/10.1016/S0167-2991(08)60679-5).
- [61] S. Bordiga, E. Escalona Platero, C. Otero Areán, C. Lamberti, A. Zecchina, *J. Catal.* 137 (1992) 179–185. [https://doi.org/10.1016/0021-9517\(92\)90147-A](https://doi.org/10.1016/0021-9517(92)90147-A).
- [62] S. Bordiga, D. Scarano, G. Spoto, A. Zecchina, C. Lamberti, C. Otero Areán, *Vib. Spectrosc.* 5 (1993) 69–74. [https://doi.org/10.1016/0924-2031\(93\)87056-Y](https://doi.org/10.1016/0924-2031(93)87056-Y).
- [63] K. Khivantsev, N.R. Jaegers, L. Kovarik, J.C. Hanson, F. (Feng) Tao, Y. Tang, X. Zhang, I.Z. Koleva, H.A. Aleksandrov, G.N. Vayssilov, Y. Wang, F. Gao, J. Szanyi, *Angew. Chemie - Int. Ed.* 57 (2018) 16672–16677. <https://doi.org/10.1002/anie.201809343>.
- [64] L. Castoldi, R. Matarrese, S. Morandi, P. Ticali, L. Lietti, *Catal. Today* 360 (2021) 317–325. <https://doi.org/10.1016/j.cattod.2020.02.019>.

- [65] A. Ramirez, X. Gong, M. Caglayan, S.-A.F. Nastase, E. Abou-Hamad, L. Gevers, L. Cavallo, A. Dutta Chowdhury, J. Gascon, *Nat. Commun.* 12 (2021) 5914. <https://doi.org/10.1038/s41467-021-26090-5>.
- [66] M. Çağlayan, A. Lucini Paioni, E. Abou-Hamad, G. Shterk, A. Pustovarenko, M. Baldus, A.D. Chowdhury, J. Gascon, *Angew. Chemie Int. Ed.* 59 (2020) 16741–16746. <https://doi.org/10.1002/anie.202007283>.
- [67] D. Fu, A. Lucini Paioni, C. Lian, O. Heijden, M. Baldus, B.M. Weckhuysen, *Angew. Chemie Int. Ed.* 59 (2020) 20024–20030. <https://doi.org/10.1002/anie.202009139>.
- [68] C. Wang, Y. Chu, J. Xu, Q. Wang, G. Qi, P. Gao, X. Zhou, F. Deng, *Angew. Chemie* 130 (2018) 10354–10358. <https://doi.org/10.1002/ange.201805609>.
- [69] A.D. Chowdhury, A.L. Paioni, K. Houben, G.T. Whiting, M. Baldus, B.M. Weckhuysen, *Angew. Chemie Int. Ed.* 57 (2018) 8095–8099. <https://doi.org/10.1002/anie.201803279>.
- [70] A.D. Chowdhury, K. Houben, G.T. Whiting, S.-H. Chung, M. Baldus, B.M. Weckhuysen, *Nat. Catal.* 1 (2018) 23–31. <https://doi.org/10.1038/s41929-017-0002-4>.
- [71] A.D. Chowdhury, K. Houben, G.T. Whiting, M. Mokhtar, A.M. Asiri,

S.A. Al-Thabaiti, S.N. Basahel, M. Baldus, B.M. Weckhuysen, *Angew.*

Chemie 128 (2016) 16072–16077.

<https://doi.org/10.1002/ange.201608643>.

- [72] I. Yarulina, A.D. Chowdhury, F. Meirer, B.M. Weckhuysen, J. Gascon, *Nat. Catal.* 1 (2018) 398–411. <https://doi.org/10.1038/s41929-018-0078-5>.

A.4 (not published – submitted)

ACS Applied Materials & Interfaces

This document is confidential and is proprietary to the American Chemical Society and its authors. Do not copy or disclose without written permission. If you have received this item in error, notify the sender and delete all copies.

**From lab to technical CO₂ hydrogenation catalysts:
understanding PdZn decomposition**

Journal:	<i>ACS Applied Materials & Interfaces</i>
Manuscript ID:	am-2022-19357p
Manuscript Type:	Article
Date Submitted by the Author:	27-Oct-2022
Complete List of Authors:	Ticali, Pierfrancesco; University of Turin, Department of Chemistry, NIS Center and INSTM Reference Center Salusso, Davide; University of Turin, Department of Chemistry, NIS Center and INSTM Reference Center airi, alessia; Università degli Studi di Torino, Chemistry Morandi, Sara; Università degli Studi di Torino, Borfecchia, Elisa; Turin University, Chemistry Ramirez, Adrian; King Abdullah University of Science and Technology, Chemical Engineering, KAUST Catalysis Center Cordero-Lanzac, Tomás; University of Oslo Faculty of Mathematics and Natural Sciences, Centre for Materials Science and Nanotechnology (SMN) Gascon, Jorge; King Abdullah University of Science and Technology, Kaust Catalysis Center Olsbye, Unni; Universitetet i Oslo, Chemistry; Joensen, Finn; Haldor Topsoe AS, Bordiga, Silvia; Università degli Studi di Torino, Department of Chemistry;

SCHOLARONE™
Manuscripts

ACS Paragon Plus Environment

1
2
3
4
5
6
7
8
9
10
11
12
13
14
15
16
17
18
19
20
21
22
23
24
25
26
27
28
29
30
31
32
33
34
35
36
37
38
39
40
41
42
43
44
45
46
47
48
49
50
51
52
53
54
55
56
57
58
59
60

From lab to technical CO₂ hydrogenation catalysts: understanding PdZn decomposition

Pierfrancesco Ticali^a, Davide Salusso^a, Alessia Air^a, Sara Morandi^a, Elisa Borfecchia^a, Adrian

Ramirez^b, Tomás Cordero-Lanza^c, Jorge Gascon^b, Unni Olsbye^c, Finn Joensen^{d}, Silvia*

Bordiga^{a}*

^aUniversity of Turin, Via Giuria 7, Turin, Italy

^bKing Abdullah University of Science and Technology, Thuwal 23955, Saudi Arabia

^cSMN Centre for Materials Science and Nanotechnology, Department of Chemistry, University
of Oslo, Sem Sælands vei 26, 0371 Oslo, Norway

^dHaldor Topsøe, Kongens Lyngby, Denmark.

KEYWORDS: CO₂ conversion; PdZn alloy; hydrogenation; heterogenous catalysis; zeolites;
scale up

ABSTRACT

The valorization of CO₂ to produce high-value chemicals, such as methanol and hydrocarbons represents key technology in the future, net-zero society.

Herein, we report a further investigation of a PdZn/ZrO₂ + SAPO-34 catalyst for conversion of CO₂ and H₂ into propane, already presented in a previous work. The focus of this contribution is on the scale up of this catalyst. In particular, we explored the effect of mixing (1:1 mass ratio) and shaping the two catalyst functions into tablets and extrudates, using an alumina binder. Their catalytic performance was correlated with structural and spectroscopic characteristics, using methods, such as FT-IR and X-ray Absorption Spectroscopy.

The two scaled-up bifunctional catalysts demonstrated worse performance than a 1:1 mass physical mixture of the two individual components. Indeed, we demonstrated that the preparation negatively affects the element distribution. The physical mixture is featured by the presence of a PdZn alloy, as demonstrated by our previous work on this sample, and high hydrocarbon selectivity among products. For both tablets and extrudates, the characterization showed Zn migration to produce Zn aluminates from the alumina binder phase upon reduction. Moreover, the extrudates showed a remarkable higher amount of Zn aluminates before the activation rather than the tablets. Comparing tablets and extrudates with the physical mixture, no PdZn alloy was observed after activation and only the extrudates showed the presence of metallic Pd. Due to the Zn migration, SAPO-34 poisoning and subsequent deactivation of the catalyst could not be excluded.

These findings corroborated the catalytic results: Zn aluminates formation and Pd⁰ separation could be responsible for the decrease of the catalytic activity of the extrudates, featured by high

1
2
3
4 methane selectivity and unconverted methanol, while tablets displayed a reduced methanol
5
6 conversion to hydrocarbons mainly attributed to the partial deactivation of the SAPO-34.
7
8
9

10 11 **1. INTRODUCTION**

12
13
14 The Sixth Assessment Report released by IPCC^{1,2} demonstrates that human activity is
15 responsible for the increasing concentration of greenhouse gases in the atmosphere. As a matter
16 of fact, the electricity production is still dependent on oil, natural gas and coal which are the
17 main energy sources and continue to endanger the environment. Even though these energy
18 sources strongly contribute to CO₂ emissions in the atmosphere, they still represent an important
19 source in several parts of the world. According to the IEA,^{3,4} contribution from fossil fuels to the
20 world energy supply is still increasing. In 2018 they accounted for nearly 40% of global
21 emissions and coal was responsible for about 29% of energy-related emissions. Hence, it is clear
22 how significant reducing their consumption is, as well as mitigating the environmental
23 consequences of their utilization. Among all the activities humanity could implement, carbon
24 capture and utilization (CCU) is one of the best options.
25
26
27
28
29
30
31
32
33
34
35
36
37
38

39 To date, several research groups, start-ups and companies head towards processes aiming at
40 achieving efficient CO₂ reactivity with hydrogen, to produce organic molecules such as methanol
41 (MeOH) and possibly to transform them into hydrocarbons by the means of a bifunctional
42 catalyst. In particular, propane is a key feedstock molecule and strictly linked to the propylene
43 market.
44
45
46
47
48
49

50 To produce propane from carbon dioxide, several works⁵⁻⁸ described metal oxide systems as
51 supporting materials for other phases, physical mixtures and solid solutions, that could be
52 involved in CO₂ hydrogenation. Among the most studied metal oxides,^{9,10} some research groups
53
54
55
56
57
58
59
60

1
2
3
4 focused on Zn in combination with ZrO_2 ^{11,12} or Pd in combination with Zn, supported on oxidic
5 support like CeO_2 or similar.^{7,8} Zn is well-known to play a key role in heterolytic H_2 splitting,
6 due to its capability in producing oxygen vacancies,¹²⁻¹⁶ Moreover, the presence of Pd seems to
7 improve the activity of these catalysts in adsorbing CO_2 and enhancing CO_2 to methanol
8 conversion, by alloying with Zn.^{7,8}

9
10
11
12
13
14 Furthermore, ZrO_2 is reported as an excellent support for this kind of catalysts.¹¹ ZrO_2 has
15 been studied in many systems as a supporting material¹⁷. In fact, ZrO_2 has weak hydrophilic
16 properties, enhances reaction products and selectivity, it can bind reaction intermediates and
17 stabilizes active species,^{12,18} it reduces water adsorption^{9,19} and enhances H_2 dissociation.^{20,21}

18
19
20
21
22
23 To convert methanol into hydrocarbons, some authors proposed bifunctional catalysts made up
24 of an oxidic phase and a zeolite.^{22,23} According to the acidity and the type of the zeolite involved
25 in the reaction, methanol can be converted to different hydrocarbons with a different number of
26 carbon atoms.^{24,25}

27
28
29
30
31
32 Taking all these suggestions into account, we previously proposed a $PdZn@ZrO_2+SAPO-34$
33 bifunctional catalyst²⁶, which demonstrated to be highly selective towards propane (>50%
34 selectivity) with a conversion close to 40% at 350 °C, 50 bar and 1500 mL $g^{-1} h^{-1}$. According to
35 our previous results, the intimate contact between the metal oxide phase and the zeolite triggers
36 methanol to quickly reacts and pushes the equilibrium towards propane production. This type of
37 catalyst featured the formation of a $PdZn$ alloy surrounded by a polycrystalline and defective
38 ZnO shell during the activation in hydrogen, which was linked to the methanol production.
39 Instantly, the $MeOH$ formed on the $PdZn@ZrO_2$ reacted over the SAPO-34 to produce propene
40 following the methanol-to-olefins (MTO) process, while avoiding the fast deactivation due to the
41
42
43
44
45
46
47
48
49
50
51
52
53
54
55
56
57
58
59
60

1
2
3 high partial pressure of H₂ in the reaction medium.²⁷ The presence of Pd, and this hydrogen,
4 induced the hydrogenation of propene to propane, which resulted to be the main product.
5
6

7
8 Despite the outstanding performance of physical mixtures at laboratory scale, process scale-up
9 will require the development of technical catalysts, able to work in multiple reaction cycles and
10 with sufficient thermal and mechanical resistance. For this purpose, active phases are commonly
11 mixed with binders and inert fillers in certain optimal composition, which may unfortunately
12 cause modifications on catalytic performance.²⁸ In this work, we explored the catalytic
13 performance of different technical catalysts, prepared by scaled up synthesis routes.
14
15 Characterization of the stand-alone PdZn@ZrO₂ and combined PdZn@ZrO₂+SAPO-34 catalyst
16 in two different shapes were used to understand the different behavior of each prepared technical
17 catalyst. Spectroscopic characterization of these systems was performed by infrared spectroscopy
18 (FT-IR) and X-ray absorption spectroscopy (XAS). In case of pellets, PdZn alloy formation was
19 observed, as already found for the lab-scaled catalyst in our former works.²⁶ However, no
20 activity towards C₃ products was detected. On the other hand, extrudates did not show any PdZn
21 alloy and half of the propane selectivity was observed, when compared with the lab-scaled
22 catalyst. Further investigation demonstrated the presence of zinc aluminates due to the use of
23 Al₂O₃ in the preparation of the extrudates, hindering the catalytic activity.
24
25
26
27
28
29
30
31
32
33
34
35
36
37
38
39
40
41
42
43
44
45
46

47 2. MATERIALS AND METHODS

48 2.1. Catalyst preparation

49
50 Catalysts were prepared and shaped to form both tablets and extrudates. The PdZn@ZrO₂
51 precursor, PZZ-ox, was prepared by aqueous incipient wetness impregnation of Zn- and Pd-
52
53
54
55
56
57
58
59
60

1
2
3 nitrate on ZrO₂ (Aldrich), followed by drying and calcination at 500°C for 5 hours. The calcined
4 catalyst precursor was mixed with SAPO-34 (China Catalyst Holding CO.) and alumina binder
5 and pelletized to form a robust catalyst body (PZZ-ox-tab). The SAPO-34 was previously
6 calcined at 475 °C for 2 hours to remove template and carbonaceous residues in the as-received
7 material. Final composition of the tablets was approx. 45:45:10 wt% of PdZn@ZrO₂, SAPO-34
8 and Al₂O₃ respectively. Extrudates were prepared by mixing the calcined catalyst precursor with
9 the SAPO-34 and alumina binder with water to form a paste. The paste was extruded on a piston
10 extruder, dried and calcined 5 hours at 500 °C to obtain a catalyst, PZZ-ox-ext, with approx.
11 30:30:40 wt% of PdZn@ZrO₂, SAPO-34 and Al₂O₃, respectively. For both tablets and extrudates
12 a dual strategy was pursued, using calcined (PZZ-ox) and reduced (PZZ-red) precursors,
13 respectively. Reduction of the (calcined) PdZn@ZrO₂ precursor was performed in a flow of
14 hydrogen (2 vol%) in Ar at 400°C for 20 hours. The final catalysts with reduced precursors were
15 subjected to final calcination as described above to produce PZZ-red-ext (extrudates) and PZZ-
16 red-tab (tablets), except for a small sample, PZZ-red-tab-unc, which was pelletized using the
17 reduced precursor, PZZ-red, but not calcined, for use in spectroscopic studies.
18
19
20
21
22
23
24
25
26
27
28
29
30
31
32
33
34
35
36
37
38
39
40
41
42
43
44
45
46
47
48
49
50
51
52
53
54
55
56
57
58
59
60

Table 1. Summary of the prepared samples with their main physico-chemical properties

Sample Name	Sample description	Composition (wt%)*(rest to 100% is oxygen)	NH ₃ capacity (mmol/g)	Surface Areas (H ₂) m ² /g	Pore volume < 6Å Ar BET cm ³ /kg
SAPO-34	-	-	0.70	-	224
PZZ-ox	Precursors calcination	Pd(1.8) Zn(8.7) Zr(62.8)	-	16	-
PZZ-red	PZZ-ox reduction	Pd(1.8) Zn(8.8) Zr(62.4)	-	15	-
PZZ-ox-tab	PZZ-ox mixed with SAPO-34+Al(O)OH, tableted and calcined	Pd(0.7) Zn(3.9) Zr(27.4) Al(13.1) Si(0.9) P(9.1)	0.36	34	104
PZZ-red-tab	PZZ-red mixed with SAPO-34+Al(O)OH, tableted and calcined	Pd(0.8) Zn(3.9) Zr(27.4) Al(12.6) Si(0.9) P(9.2)	0.35	31	106
PZZ-ox-ext	PZZ-ox mixed with SAPO-34+Al(O)OH, extruded and calcined	Pd(0.5) Zn(2.7) Zr(19.2) Al(26.0) Si(0.6) P(5.4)	0.12	123	58
PZZ-red-ext	PZZ-red mixed with SAPO-34+Al(O)OH, extruded and calcined	Pd(0.5) Zn(2.7) Zr(19.5) Al(26.5) Si(0.6) P(5.5)	0.12	125	57

1
2
3
4
5
6
7
8
9
10
11
12
13
14
15
16
17
18
19
20
21
22
23
24
25
26
27
28
29
30
31
32
33
34
35
36
37
38
39
40
41
42
43
44
45
46
47
48
49
50
51
52
53
54
55
56
57
58
59
60

2.2. Activity measurement

Catalytic tests were carried out in a 4 channel Flowrence® from Avantium. The gas feed composition was: 24vol% of CO₂, 72 vol% of H₂ and 4 vol% of He as internal standard. We aimed to 6000ml/g/h per channel. Prior to feeding the reaction mixture all samples were reduced *in situ* with a pure H₂ atmosphere for 4 hours at 400°C. The reaction temperature was set at 350°C and the pressure at 30 bar. The reaction products were analyzed online in a gas chromatograph Agilent 7890B with two sample loops. One sample loop goes to TCD channel with 2 Haysep pre-column and MS5A, where He, H₂, CH₄ and CO are separated. Another sample loop goes to an FID with an Innowax pre-column, a Gaspro column and another Innowax column. Gaspro column separates C1-C8, paraffins and olefins, while Innowax column separates oxygenated and aromatics.

Conversion (X) and selectivity (S) are reported on C1 basis and are defined as follow:

$$X_{CO_2}(\%) = \frac{CO_{2,blk}/He_{blk} - CO_{2,R}/He_R}{CO_{2,blk}/He_{blk}} \times 100$$

$$S_{Cn}(\%) = \frac{n \cdot \frac{C_{Cn,R}}{C_{He,R}}}{\left(\frac{C_{CO_2,blk}}{C_{He,blk}} - \frac{C_{CO_2,R}}{C_{He,R}} \right)} \cdot 100$$

where C_{i,blk} and C_{i,R}, are the concentrations determined by GC analysis in the blank and in the reactor outlet, respectively, and n is the number of carbon atoms of each C_n product. Carbon balance closure was better than 2.5% in all cases.

1
2
3
4
5
6
7
8
9
10
11
12
13
14
15
16
17
18
19
20
21
22
23
24
25
26
27
28
29
30
31
32
33
34
35
36
37
38
39
40
41
42
43
44
45
46
47
48
49
50
51
52
53
54
55
56
57
58
59
60

2.3. Structural and spectroscopic characterization

The acidity of the samples was measured via NH_3 -TPD, using a TGA/DSC1 instrument (Mettler Toledo). In a typical analysis, 70 mg of the sample was degassed at 500 °C under a 31%He-69%Ar flow rate of 75 mL/min for 110 min at a heating rate of 20 °C/min. Next, the sample was cooled to 150 °C and then saturated with a mixture of 29%He-69%Ar and 2% ammonia (2% NH_3 /29%He/69%Ar) for 30 min. The sample was then purged with a 31%He-69%Ar flow for 233 min, to remove weakly and physically adsorbed NH_3 on the surface of the catalyst. After this operation, the sample was cooled to 140 °C, kept at that temperature for 10 min, heated back to 150 °C and then to 600 °C at a rate of 10 °C/min, under a flow of 31%He-69%Ar carrier gas (75 mL/min). The amount of ammonia was measured as mass loss recorded as a function of temperature and time.

The textural properties of the materials were determined from the Ar adsorption isotherm in liquid argon (-186 °C) measured on a Quantachrome Autosorb iQ apparatus with lowest pressure at $P/P_0 = 10^{-6}$. The sample (100 mg) was degassed in vacuum for 16 hours at 27 °C prior the analysis. The data were fitted using an NLDFT model based on a cylindrical pore model using ASiQwin software.

Model: NLDFT – Ar – zeolite/silica adsorption branch kernel at -186 °C based on a cylindrical pore model. This model is fit for zeolites with cylindrical pore channels such as Mordenite, ZSM-5 etc. The applicable pore range is 0.35 nm to 100 nm.

Catalyst samples were investigated by PXRD (Panalytical X'Pert Pro) in Bragg-Brentano Geometry in reflectance mode using Cu K α radiation source ($\lambda = 1.541 \text{ \AA}$) at ambient conditions. The scan range was 5–70° with a step size of 0.017°. Rietveld refinement was performed using Topas software provided by Bruker.

1
2
3 Wavelength-dispersive X-ray spectrometry was performed on a FEG-EPMA JEOL JXA-
4 8530F electron microprobe (d=1 μ m) operated at 20 kV, from 20 nA to 55 nA on cross sections
5 of shaped samples, embedded in epoxy and ground with silicon carbide.
6
7

8
9
10 Zn K-edge XAS spectra were collected on self-supporting wafers (diameter 1.3 cm²) obtained
11 by grinding and pressing the different catalysts in transmission mode using a Si(111) double-
12 crystal monochromator at the BM31 beamline of the European Synchrotron Radiation Facility
13 (ESRF). Spectra were measured in the 9.5-10.2 keV energy range with 0.5 eV energy step and
14 integration time of 0.1 s/point resulting in ca. 2.5 min/scan. 6 consecutive scans/sample were
15 averaged after energy alignment to Zn metal foil, background subtraction and jump
16 normalization conducted with the Athena software from the Demeter Package.²⁹ Spectra of
17 reference ZnO (Honeywell, >99%) was also measured in the form of self-supporting pellet while
18 spectra of Zn(10%)-Al₂O₃ model system were previously measured as described elsewhere.³⁰
19 These two spectra were used as references ($\mu^{ref}(E)$) for a linear combination fitting (LCF)
20 analysis of the samples spectra. LCF was performed with the ATHENA software trying to
21 minimize the R-factor defined as:
22
23
24
25
26
27
28
29
30
31
32
33
34
35
36
37
38
39
40
41
42
43
44
45
46
47
48
49
50
51
52
53
54
55
56
57
58
59
60

$$\sum_j [\mu_j^{exp}(E) - \mu_j^{LCF}(E)]^2 / \sum_j [\mu_j^{exp}(E)]^2$$

where j represents each experimental point in the fit-range (9645-9695 eV). $\mu^{LCF}(E)$ was
obtained by fitting $\mu^{exp}(E)$ as linear combination of two reference spectra $\mu_i^{ref}(E)$: $\mu^{LCF}(E) =$
 $w_1 \mu_1^{ref}(E) + w_2 \mu_2^{ref}(E)$. LCF was performed imposing $0 \leq w_i \leq 1$ but without constraining
 $\sum_i w_i = 1$. R-factor tendency to 0 i.e., $\mu^{exp}(E) = \mu^{LCF}(E)$ and the best fit values of $\sum_i w_i$ were
used as fit-quality indicators.

1
2
3
4 IR spectra were collected on pre-activated self-supporting s wafers inserted in a home-made
5 quartz cell with KBr windows suitable for *ex situ* and *in situ* experiments. Pellet activation
6 procedure consisted in the following steps: i) heating (5°C/min) under vacuum (5×10^{-4} mbar) up
7 to 400 °C, ii) 1h reduction at 400 °C under H₂ (50 mbar) and iii) outgassing and cooling down to
8 room temperature. The IR spectra were acquired in transmission mode with a Bruker Vertex 70
9 spectrophotometer equipped with a MCT cryodetector working at 20 KHz, collecting 32 scans
10 for each spectrum with 2 cm⁻¹ of resolution. Under acquisition, the samples were kept under
11 vacuum (5×10^{-4} mbar) through connection with a vacuum glass-line. The same line was used to
12 dose Carbon Monoxide (CO) for *in-situ* experiment at RT. Spectra were acquired at increasing
13 equilibrium pressure (e.p.) of CO up to 30 mbar.
14
15
16
17
18
19
20
21
22
23
24
25
26
27
28

29 3. RESULTS AND DISCUSSION

30 3.1. Catalytic performance of the technical catalysts

31
32 A summary of the scaled-up catalysts, synthesized in tablets and extrudates, is shown in Table
33 1, where a brief description of the preparation protocol and basic properties are detailed. For the
34 sake of comparison, the commercial SAPO-34 used as the acid function in the technical catalyst
35 is also included in the table. All these samples were tested in the tandem hydrogenation of CO₂
36 to hydrocarbons under typical conditions for this catalyst according to our previous results.²⁶
37 Figure 1a shows the CO₂ conversion and the product distribution obtained with the technical
38 catalysts. Please note that PZZ-ox and PZZ-red consist in a scaled up and optimized synthesis
39 protocol to which was previously reported elsewhere.²⁶ These two scaled up standalone
40 PdZn@ZrO₂ mixed oxides do produce methanol and CO as main products, in line with the
41 laboratory-scale PdZn@ZrO₂ catalyst. Nevertheless, the PZZ-red catalyst, which was reduced *ex*
42
43
44
45
46
47
48
49
50
51
52
53
54
55
56
57
58
59
60

1
2
3
4 *situ* after the synthesis, performed ostensibly better, with similar conversion and more than
5 double methanol selectivity due to the decrease in CO production (see left panel in Figure 1a and
6 detailed product distribution in Table S1).
7
8

9
10 To compare the catalytic performance of the technical catalysts, we have included the catalytic
11 results obtained with a physical mixture of PZZ-ox catalyst and the commercial SAPO-34 in
12 Figure 1a. Please note that the composition of each technical catalyst is slightly different so a
13 small decrease in CO₂ conversion could be expected from physical mixture to tablets and
14 extrudates (see Experimental section). As observed before, this physical mixture boosts CO₂
15 conversion (from ca. 12 to 25%) by converting *in situ* the produced methanol to hydrocarbons.
16 CO selectivity is significantly reduced (from ca. 86 to 65%) due to a shift in the reaction network
17 equilibria and methane selectivity is also minimized. Nonetheless, this behavior was not
18 observed for the technical catalysts. Looking at the tablet technical catalysts, both PZZ-ox-tab
19 and PZZ-red-tab catalysts are able to yield propane as the main hydrocarbon product. Besides,
20 PZZ-red-tab outperformed its non-reduced counterpart PZZ-ox-tab with double propane
21 selectivity (see Table S1), as one should expect after the comparison of the mixed oxides PZZ-ox
22 and PZZ-red. The catalytic performance of PZZ-red-tab is also very stable during the 72 hours
23 studied (see Figure 1b). Nevertheless, the catalytic performance of this technical catalyst is
24 significantly worse than the physical mixture, with a CO₂ conversion of only ca. 14% and a high
25 methane selectivity (10%, Table S1). This loss of activity becomes even worst when the
26 technical catalyst is shaped into an extrudate form (PZZ-ox-ext and PZZ-red-ext). The catalytic
27 activity is lost, without observing any propane in the product effluent. Surprisingly, the catalyst
28 converts CO₂ into methanol (with some DME) and methane as the main byproduct. This result
29
30
31
32
33
34
35
36
37
38
39
40
41
42
43
44
45
46
47
48
49
50
51
52
53
54
55
56
57
58
59
60

suggests a very likely poisoning of the SAPO-34 sites during catalyst shaping and potential modifications of the hydrogenation function, which is still able to hydrogenate CO₂.

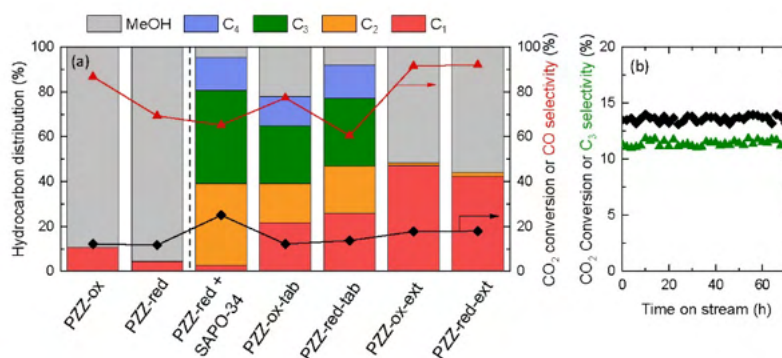


Figure 1. (a) CO₂ conversion and hydrocarbon distribution for the different technical catalysts and (b) evolution with time on stream of CO₂ conversion and C₃ selectivity for the PZZ-red-tab catalyst. Reaction conditions: 350 C, 30 bar, 6000 cm³/g/h, 1:3 CO₂:H₂.

3.2. Physico-chemical characterization of technical catalysts

To understand the reason and changes of the active phases during catalyst shaping, catalysts were characterized using several techniques. Table 1 summarizes the main physico-chemical properties of the studied catalysts, including their composition, surface area and ammonia capacities. Accounting the different composition targeted, the stand-alone PdZn@ZrO₂ (PZZ-ox and PZZ-red) mixed oxides have Pd and Zn amounts close to the nominal values of 2 and 10 wt%, respectively. Likewise, tablet and extrudate catalysts show the corresponding values

1
2
3 according to the concentration of active phase in the final catalyst (45 and 30 wt% of each
4 function in the tablets and extrudates, respectively). Regarding catalyst porous texture, the tablet
5 catalysts (PZZ-ox-tab and PZZ-red-tab) preserve the micropore volume ($<7 \text{ \AA}$): the micropore
6 volume of the SAPO-34 raw material is about $220 \text{ cm}^3/\text{kg}$ and with about 45 wt% of SAPO-34 in
7 the pelletized catalyst, a micropore volume just above $100 \text{ cm}^3/\text{kg}$ is reasonable. Same
8 conclusions can be extracted from ammonia capacity: 0.35 mmol/g with 0.70 mmol/g for the
9 SAPO-34 raw material. However, lower micropore volumes (58 and $57 \text{ cm}^3/\text{kg}$) and ammonia
10 capacities (both 0.12 mmol/g) than expected from their content of 30 wt% SAPO-34 are
11 observed for the extrudates. By simple interpolation, expected micropore volume and ammonia
12 capacity should be $66 \text{ cm}^3/\text{kg}$ and 0.20 mmol/g , respectively. Thus, a minor loss of micropore
13 volume, possibly within the uncertainty of measurement, and a significant reduction in ammonia
14 capacity has occurred during mixing and extrusion.

15
16
17
18
19
20
21
22
23
24
25
26
27
28
29
30
31
32
33
34
35
36
37
38
39
40
41
42
43
44
45
46
47
48
49
50
51
52
53
54
55
56
57
58
59
60
PXRD patterns in Figure 2 showed as the stand-alone $\text{PdZn}@ZrO_2$ (PZZ-ox) catalysts presented PdO, ZnO and monoclinic ZrO_2 reflections. After catalyst reduction ZnO and PdO reflections intensity decreased suggesting a consumption of their phase to form $\beta_1\text{-PdZn}$ alloy which (101) reflection is visible in PZZ-red pattern (Figure 2b).³¹ After tablets and extrudates preparation, SAPO-34 reflections were observed whilst PdZn signal disappear suggesting that decomposition of this phase might occur. Moreover, there is a loss of ZnO content in tablets and extrudates, which is more pronounced in the second case compared to the first one. These results points to some degree of ion-exchange of the SAPO-34 acid sites already taking place during the mixing and extrusion operations.

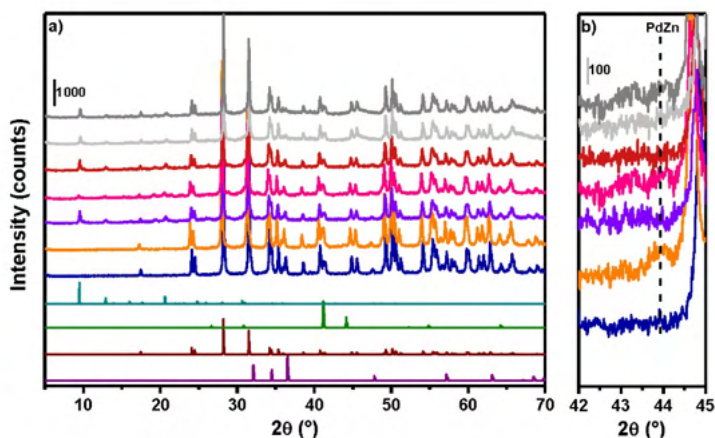


Figure 2. PXRD patterns (bottom to top) of: simulated h-ZnO (purple), m-ZrO₂ (wine), t-PdZn (green), SAPO-34 (light blue) and experimental PZZ-ox (dark blue), PZZ-red (orange), PZZ-ox-tab (violet), Tablets-red-unc (pink), PZZ-red-tab (dark red), PZZ-ox-ext (light grey) and Extrudates- red-calc (dark grey).

3.3. Morphology and element distribution of the technical catalysts

Selected WDS intensity mapping images of Zn, Zr and Pd on the shaped catalysts are shown in Figure 3. The images reveal that tableted and extruded catalysts exhibit the same pattern: Zn is distributed unevenly, forming ZnO islands observed by PXRD (Figure 2), while Pd is distributed more uniformly onto the ZrO₂ surface. The formation of ZnO islands renders a significant part of the ZrO₂ surface covered with Pd only. We further recorded element concentration profiles along lines across the shaped catalysts, as shown in Figure 4 (tablets) and Figure 5 (extrudates). These profiles strongly support that migration of Zn is an issue *irrespective* of the PdZn@ZrO₂ part of

1
2
3 the catalyst being *calcined* or *calcined & subsequently reduced* in hydrogen prior to shaping, and
4 whether in the form of extrudates or tablets. The profiles indicate that Zn tends to migrate onto
5 both the alumina binder (mainly in extrudates) and the SAPO-34 phases whereas Pd appears to
6 be strongly adsorbed on the ZrO₂ support, in line with ZnO loss observed by PXRD. For the sake
7 of completeness, it should be mentioned that no differences between PZZ-ox-tab and PZZ-red-
8 tab could be observed (SEM micrographs shown Figure S1, including the un-calcined PZZ-red-
9 tab version).
10
11
12
13
14
15
16
17
18
19
20
21
22
23
24
25
26
27
28
29
30
31
32
33
34
35
36
37
38
39
40
41
42
43
44
45
46
47
48
49
50
51
52
53
54
55
56
57
58
59
60

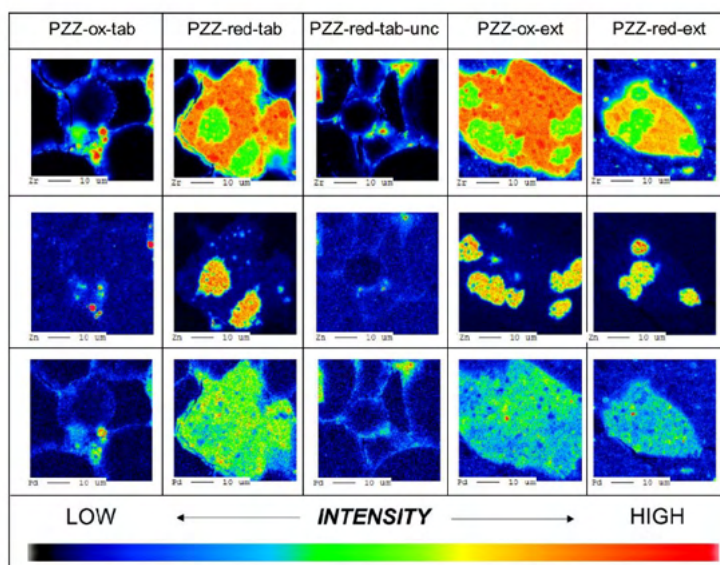


Figure 3. WDS intensity mapping of Zr, Zn and Pd in dual function catalysts shaped as tablets and extrudates, applying calcined and calcined & reduced PdZn@ZrO₂ precursors, respectively (all catalysts subjected to calcination at 500°C subsequent to shaping, except PZZ-red-tab-unc).

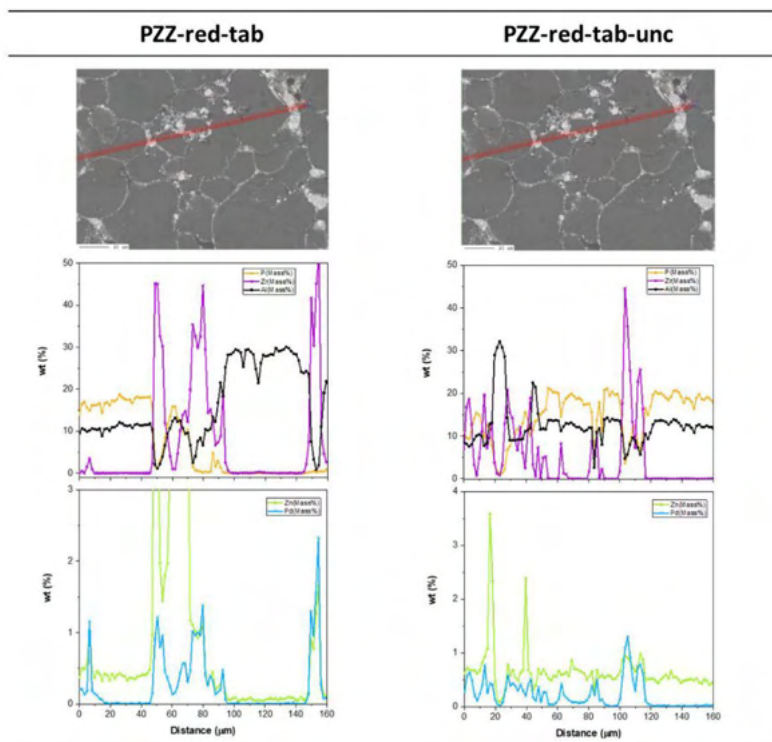
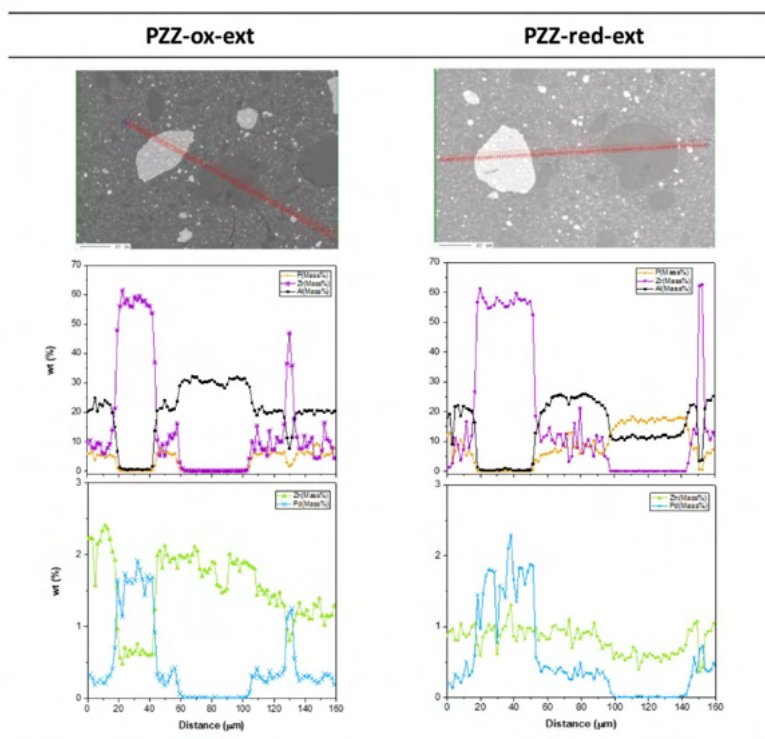


Figure 4. Tablet (TAB) element concentration (wt%) scans (μm). Pelletized using pre-reduced PdZn@ZrO₂ precursor: calcined subsequent to pelletization (PZZ-red-tab, left) and un-calcined (PZZ-red-tab-unc, right).



41
42
43
44
45
46
47
48
49
50

Figure 5. Extrudate (XTR) element concentration (wt%) scans (μm). PdZn@ZrO₂ precursor calcined (PZZ-ox-ext, left) and calcined & reduced (PZZ-red-ext, right) prior to mixing, extrusion and final calcination.

51
52
53
54
55
56
57
58
59
60

The uneven distribution of Zn leaves Pd partly and directly supported on ZrO₂, as further confirmed by FT-IR spectroscopy results (*vide infra*). Pd is known as an excellent catalyst for the

1
2
3 methanation reaction,^{32,33} both from CO and CO₂. Therefore, the deposition of only Pd on the
4 ZrO₂ surface (in the absence of Zn/ZnO) may be the primary cause for the high selectivity to
5 methane (Figure 1a) due to the impossibility to form the PdZn alloy (see results below). And for
6 the sake of the process, the methanation reaction is hydrogen-intensive and should be avoided or
7 at least minimized. In addition, the mobility of Zn/ZnO makes Zn species migrate to both the
8 alumina and SAPO-34 phases. Apart from losing Zn from the ZrO₂ support, migration to the
9 SAPO-34 is likely to cause ion-exchange of acid sites, already taking place during shaping,
10 thereby reducing acidity. It should also be noted that, apart from significant migration of Zn in
11 the preparative steps, Zn migration is likely to become exacerbated during operating conditions
12 due to the presence of steam at high temperatures. SAPO-34 itself is quite steam-tolerant, but
13 with steam facilitating and increasing the mobility of Zn we may expect extensive ion-exchange
14 to take place under operating conditions and regeneration, rendering the acid function catalyst
15 gradually less and less efficient in the conversion of methanol to hydrocarbons.
16
17
18
19
20
21
22
23
24
25
26
27
28
29
30
31
32

3.4. Spectroscopic characterization

33
34
35
36
37
38 Considering PdZn alloys, several previous studies exploited XAS to investigate Zn and Pd
39 speciation in the employed catalysts. However, since most of relevant information concerning
40 Pd chemical environment was hereafter extracted by FT-IR spectroscopy of CO adsorption, we
41 focused the XAS analysis on the Zn K-edge, which on the contrary is a silent-element from CO
42 viewpoint.^{26,34-37} As indicated by PXRD data and often reported in literature, during PdZn
43 preparation an excess of ZnO was observed. Indeed, PZZ-ox catalyst, prepared by precursors'
44 calcination, presented Zn with ZnO local geometry (Figure 6a). Even though a major fraction of
45 Zn was present as ZnO, the catalyst obtained after PdZn@ZrO₂-ox H₂ thermal treatment (namely
46
47
48
49
50
51
52
53
54
55
56
57
58
59
60

1
2
3
4
5
6
7
8
9
10
11
12
13
14
15
16
17
18
19
20
21
22
23
24
25
26
27
28
29
30
31
32
33
34
35
36
37
38
39
40
41
42
43
44
45
46
47
48
49
50
51
52
53
54
55
56
57
58
59
60

PZZ-red) presented a small energy shift of the Zn K absorption edge, clearly observable in the spectrum first derivative (Figure 6b), previously associated to PdZn alloy formation.^{26,37} Since PdZn fingerprint was also observed by PXRD (Figure 2) and CO adsorption (Figure 7), we can use this shift to track PdZn presence/absence along the catalyst treatments. To guarantee catalyst activity for the methanol-to-olefins reaction, PdZn@ZrO₂-ox/red were further mixed, pelletized/extruded and calcined with SAPO-34 and Al(O)OH binder. PZZ-ox-tab, the catalyst originated from PdZn@ZrO₂-ox despite of little variations rationalized below, presented a very similar spectrum to its precursor. On the contrary, PZZ-red-tab catalysts showed some differences in the white-line region: I) absence of PdZn-related energy shift and II) rise of shoulder in the lower-energy region of the spectrum. Since the Zn(PdZn) signal was still present in Tablets-red—unc (see Figure S1), Zn reoxidation can be considered as a direct consequence of the catalyst calcination. A different scenario was instead observed when tablets were replaced by extrusion. PZZ-ox-ext and -red-calc, obtained by extrusion and calcination of PdZn@ZrO₂-ox and PdZn@ZrO₂-red with SAPO-34 and Al(O)OH, respectively, presented similar Zn K-edge spectra to those of Zn-aluminates observed by Pinilla-Herrero et al.³⁰ Moreover, since Zn migration was not observed when mixing PdZn@ZrO₂ with SAPO-34,²⁶ Extrudates-ox/red-calc spectra suggested as Zn aluminates are most likely formed when contacting the catalyst with an Al₂O₃-based binder, which confirmed the results observed before by SEM analysis (Figure 3). These fingerprints, even though very weak, can be observed also in Tablets-ox/red-calc spectra as shoulders around 9663 eV, suggesting a minor Zn migration might take place also in Tablets.

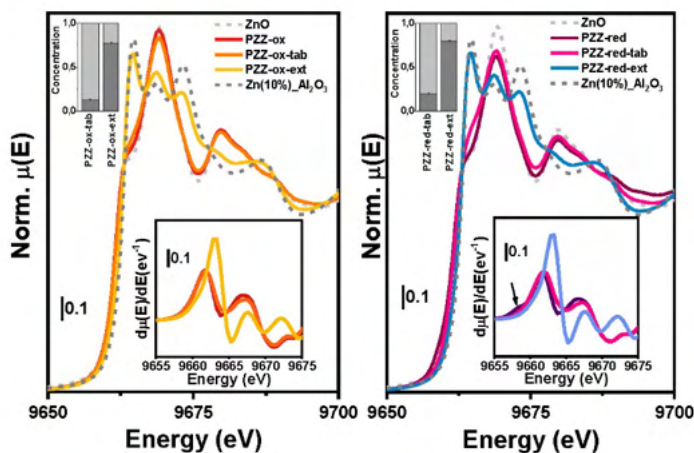


Figure 6. Zn K-edge EXAFS spectra for the analyzed samples, ZnO and Zn(10%)Al₂O₃. Spectra first derivative and LCF results are reported in the bottom and top insets, respectively. Zn(PdZn) contribution is indicated with the arrow.

Linear combination fit (LCF) analysis of the samples using ZnO and Zn(10%)-Al₂O₃ references was then applied to quantify the Zn-aluminate formation, related to Zn oxide-to-binder migration phenomena. As expected, we observed that Zn migration is limited to a $\approx 15\%$ total Zn by tablets process whilst it is enhanced to $\approx 80\%$ total Zn by the extrusion one. This result is in line with the observed loss of activity. Indeed, some activity for the formation of hydrocarbons via methanol was observed for the pelletized/tableted technical catalysts, whereas negligible amounts of propane was shown by extrudates (Figure 1).

1
2
3 To investigate the nature of the surface-active sites, FT-IR spectra of CO adsorbed at RT were
4 collected for the most relevant catalysts i.e., PZZ-red/PZZ-red-tab/PZZ-red-ext. The spectra of
5 PdZn@ZrO₂-red in presence of increasing equilibrium pressure (e.p.) of CO adsorbed at RT are
6 reported in the right panel of Figure 7a. The diagnostic stretching region of adsorbed CO is
7 reported subtracting the spectrum of pristine PdZn@ZrO₂-red from the ones obtained in presence
8 of the probe molecule. The first interaction of CO with the surface generates a signal centered at
9 2070 cm⁻¹ (lighter violet spectrum). This frequency is in line with CO adsorption on Pd⁰ sites in a
10 PdZn alloy studied in other previous works.^{26,34,38-40} Indeed, the observed frequency is slightly
11 lower than the one observed on metallic Pd (ref) and it can be explained by Zn-to-Pd charge
12 transfer that leads to a strengthening of the Pd(4d)-CO(2π) backdonation, described by a
13 downwards shift of ν(CO-Pd). Moreover, no bands related to bridged carbonyls, characteristic of
14 Pd⁰,⁴¹ are present below 2000 cm⁻¹. These results confirm PdZn alloy formation as revealed by
15 PXRD and XAS measurements. The blue shift observed upon CO adsorption up to 2082 cm⁻¹
16 (darker violet spectrum) can be explained considering the so called “chemical effect”, i.e. when
17 the surface coverage increases, CO σ-donation and π-backdonation contributions decrease,
18 weakening the bond of CO with the site and shifting the CO vibration frequency at lower and
19 higher frequencies, respectively, according to the dominating contribution.^{41,42}

20
21
22
23
24
25
26
27
28
29
30
31
32
33
34
35
36
37
38
39
40
41
42
43
44
45
46
47
48
49
50
51
52
53
54
55
56
57
58
59
60

Once the sample is subjected to CO dynamic outgassing, a persistent band of interacting CO is still present and moves back in frequency in the former position due to the abruption of the “chemical effect” (Figure 7a yellow line). The band is structured by a broad component at 2070 cm⁻¹, compatible with the formation of stable Pd⁰ linear carbonyls. Figure 7b reports the IR spectra collected for the bicomponent sample PZZ-red-tab. The OH stretching region of the IR spectrum of the activated powder, reported in the left panel of Figure 7b, is characterized by

1
2
3 several signals between 3800 and 3500 cm^{-1} . This contrasts with the case of sample
4
5 PdZn@ZrO₂-red, where no hydroxyls signals are visible (Figure 7a, left panel). These bands are
6
7
8
9
10
11
12
13
14
15
16
17
18
19
20
21
22
23
24
25
26
27
28
29
30
31
32
33
34
35
36
37
38
39
40
41
42
43
44
45
46
47
48
49
50
51
52
53
54
55
56
57
58
59
60

relatable to $\nu(\text{OH})$ bands of the typical isolated hydroxyl groups of SAPO-34 surface, namely Si-(OH) at 3745 cm^{-1} , P-(OH) at 3670 cm^{-1} . Moreover, two very intense vibrational bands are visible at 3620 and 3596 cm^{-1} corresponding to the $\nu(\text{OH})$ of bridged P-(OH)-Si (Bronsted acidic sites) located in two different crystallographic positions.⁴³ In the right panel of the same figure, the stretching region of CO adsorbed on the activated sample at RT is reported. Due to the weak interaction with CO, no adsorption at RT on the SAPO-34 of the catalyst is expected and the probe is considered to be selective for only interacting with metal sites (Pd). The spectra, collected at increased CO c.p. (from lighter to darker pink curves), are characterized by the typical roto-vibrational profile of the free vibrating CO centered at 2143 cm^{-1} . Differently from the parent PdZn@ZrO₂-red sample, any band associated with the formation of diagnostic Pd carbonyls could not be distinguished. The missing interaction between Pd and the CO probe can be explained with the decomposition of the PdZn alloy during the catalyst preparation to reasonably produce Pd/PdO (unknown) and ZnO. ZnO likely covers all Pd sites hampering the CO adsorption.⁴⁴ Again, this observation well aligns with the XAS results that demonstrated a relevant presence of oxidized Zn in PZZ-red-tab. In order to give an explanation on the observed catalytic activity of tablets, despite the absence of PdZn alloy, we supposed that the higher C1 (i.e., methane) amount produced from tablets rather than PZZ-red could be related to metallic Pd. Unfortunately, we had no evidence from FT-IR measurements, but we cannot exclude i) the presence of metallic Pd on the surface of ZrO₂ covered by a ZnO extra-phase or below the detection limit of the technique and ii) a possible influence of ZrO₂ support. As already mentioned, Pd is well known acting as a methanation catalyst^{32,33} and it could be the main

1
2
3 responsible of the methane production. Moreover, for extrudates, the role played by Zn-
4 aluminates cannot be ruled out. According to the literature,^{45,46} Zn aluminates can take part to
5 some CO₂ hydrogenation reaction that could lead to methane production. However, ZrO₂ has
6 already been demonstrated to influence the activity of some systems,⁴⁷ thus its role could not be
7 completely ruled out.
8
9

10
11
12
13
14 Figure 7c reports the IR spectra of the bifunctional catalyst PZZ-red-ext. Similarly, to PZZ-
15 red-tab, the intense $\nu(\text{OH})$ signals of SAPO-34 hydroxyls groups are visible in the left panel of
16 Figure 7c. In contrast to the former sample, the signals generated by defective sites (Si-OH and
17 P-OH) are more intense than ones associated with the Bronsted sites. An additional signal is also
18 visible at 3767 cm⁻¹ generated by Al-(OH). The presence of this species may be due to point
19 defects in the SAPO-34 framework or, reasonably, to alumina surface Al-(OH) (the binder in the
20 catalyst formulation). The massive presence of Al₂O₃ also affects the Zn K-edge XAS spectrum,
21 as previously described. The interaction of CO with the surface of PZZ-red-ext at increasing CO
22 e.p. induces the formation of a very broad and weak carbonyl band at 2090 cm⁻¹ (right panel of
23 Figure 7c). The upward shift of $\nu(\text{C}=\text{O})$ with respect to that observed for PdZn@ZrO₂-red
24 sample suggests the formation of linear carbonyls on metallic Pd⁰ centers not interacting with
25 Zn, evidencing the decomposition of the alloy. This should be result in the formation of bridged
26 carbonyls as well: reasonably, taking into account the very low intensity of the band at 2090 cm⁻¹
27 and, so, the very low amount of accessible Pd⁰ sites, the amount of bridged CO could be under
28 the detection limit. Following XAS results showing Zn migration to form aluminates, we can
29 conclude that ZnO (that covers Pd in PZZ-red-ext) is, in this case, migrated to the binder. This
30 result further confirms the hindered formation of the PdZn alloy, which was identified as the
31 main responsible for this catalyst outstanding activity to methanol. Moreover, the lack of
32
33
34
35
36
37
38
39
40
41
42
43
44
45
46
47
48
49
50
51
52
53
54
55
56
57
58
59
60

1
2
3 detected ZnO on the ZrO₂ surface in close proximity to Pd sites leads to the presence of metallic
4
5 Pd sites that boosts the undesired methanation reaction, clearly identified in our catalytic test
6
7
8 result.
9

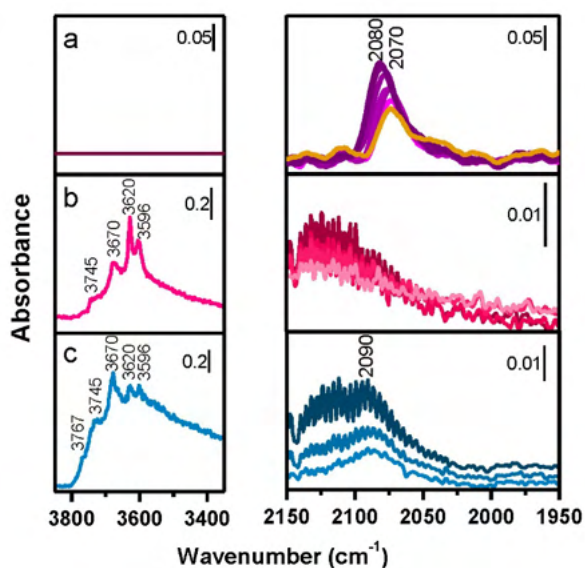


Figure 7. *In situ* IR spectra of: a) PdZn@ZrO₂-red, b) PZZ-red-tab, c) PZZ-red-ext. Left panels: OH stretching region of activated samples. Right panels: Adsorbed CO stretching region of activated samples in presence of increasing CO ep (from 0.005 to 30 mbar) at RT. Darker colors indicate higher CO pressure. The yellow line in a) refers to the PdZn@ZrO₂-red/CO interaction after outgassing at RT.

CONCLUSIONS

In this work a scaled up PdZn@ZrO₂+SAPO-34 catalyst was investigated. On the basis of catalytic and characterization results, it was demonstrated the catalyst is featured by a PdZn alloy as already studied for lab-scale catalysts.

The catalytic performances are remarkably influenced by the preparation method affecting and modifying the element distribution in the different phases (i.e. Zn migration in the alumina phase).

Comparing the results obtained by PZZ-red+SAPO-34 with tablets (PZZ-red-tab) and extrudates (PZZ-red-ext), a variation in the hydrocarbon distribution was observed. PZZ-red-tab did not show the presence of the alloy and its worse catalytic performances could be linked to the presence of ZnO extra-phase on ZrO₂ support. As reported by XAS LCF, a higher amount of Zn aluminates is observed after reduction, which could contribute to the observed C1 and MeOH production.

As for PZZ-red-ext, PdZn alloy is not present, the lack of conversion could be mainly explained by SAPO-34 poisoning, but also the Zn migration into the alumina phase cannot be ruled out. XAS LCF showed the highest amount of Zn aluminates and subsequent poisoning of SAPO-34. Moreover, FT-IR measurements following CO adsorption demonstrated the presence of metallic Pd. Hence, the high amount of methane in the hydrocarbon distribution could be explained by the capability of Pd to produce methane from CO₂ or CO, in addition to the production methanol molecules.

The results of the study may be interesting to highlight the critical point that could emerge during the development of scaled up bifunctional catalysts for CO₂ hydrogenation reactions.

1
2
3
4
5
6
7
8
9
10
11
12
13
14
15
16
17
18
19
20
21
22
23
24
25
26
27
28
29
30
31
32
33
34
35
36
37
38
39
40
41
42
43
44
45
46
47
48
49
50
51
52
53
54
55
56
57
58
59
60

AUTHOR INFORMATION

Corresponding Author

*Silvia Bordiga: e-mail silvia.bordiga@unito.it

*Finn Joensen: e-mail FJ@topsoe.com

Author Contributions

The manuscript was written through contributions of all authors. All authors have given approval to the final version of the manuscript.

ACKNOWLEDGMENTS

This project has received funding from the European Union's Horizon 2020 Research and Innovation Programme under grant agreement No. 837733.

REFERENCES

- (1) Masson-Delmotte, V.; Zhai, P.; Pirani, A.; Connors, S. L.; Péan, C.; Berger, S.; Caud, N.; Chen, Y.; Goldfarb, L.; Gomis, M. I.; Huang, M.; Leitzell, K.; Lonnoy, E.; Matthews, J. B. R.; Maycock, T. K.; Waterfield, T.; Yelekçi, O.; Yu, R.; Zhou, B. *Climate Change 2021: The Physical Science Basis. Contribution of Working Group I to the Sixth Assessment Report of the Intergovernmental Panel on Climate Change. Cambridge Univ. Press* **2021**, 3949.
- (2) Masson-Delmotte, V.; Zhai, P.; Pirani, A.; Connors, S. L.; Péan, C.; Berger, S.; Caud, N.; Chen, Y.; Goldfarb, L.; Gomis, M. I.; Huang, M.; Leitzell, K.; Lonnoy, E.; Matthews, J. B. R.; Maycock, T. K.; Waterfield, T.; Yelekçi, O.; Yu, R.; Zhou, B. Summary for Policymakers. In: *Climate Change 2021: The Physical Science Basis. Contribution of Working Group I to the Sixth Assessment Report of the Intergovernmental Panel on Climate Change. Cambridge Univ. Press. Press.* **2021**, 42.
- (3) *The Role of CCUS in Low-Carbon Power Systems*; Paris.
- (4) *Key World Energy Statistics 2021*; Paris, 2021.
- (5) Kattel, S.; Liu, P.; Chen, J. G. Tuning Selectivity of CO₂ Hydrogenation Reactions at the Metal/Oxide Interface. *J. Am. Chem. Soc.* **2017**, *139* (29), 9739–9754. <https://doi.org/10.1021/jacs.7b05362>.
- (6) Rodriguez, J. A.; Liu, P.; Stacchiola, D. J.; Senanayake, S. D.; White, M. G.; Chen, J. G. Hydrogenation of CO₂ to Methanol: Importance of Metal-Oxide and Metal-Carbide Interfaces in the Activation of CO₂. *ACS Catal.* **2015**, *5* (11), 6696–6706.

1
2
3
4
5
6
7
8
9
10
11
12
13
14
15
16
17
18
19
20
21
22
23
24
25
26
27
28
29
30
31
32
33
34
35
36
37
38
39
40
41
42
43
44
45
46
47
48
49
50
51
52
53
54
55
56
57
58
59
60

<https://doi.org/10.1021/acscatal.5b01755>.

- (7) Ojelade, O. A.; Zaman, S. F. A Review on Pd Based Catalysts for CO₂ Hydrogenation to Methanol: In-Depth Activity and DRIFTS Mechanistic Study. *Catal. Surv. from Asia* **2020**, *24* (1), 11–37. <https://doi.org/10.1007/s10563-019-09287-z>.
- (8) Ojelade, O. A.; Zaman, S. F.; Daous, M. A.; Al-Zahrani, A. A.; Malik, A. S.; Driss, H.; Shterk, G.; Gascon, J. Optimizing Pd:Zn Molar Ratio in PdZn/CeO₂ for CO₂ Hydrogenation to Methanol. *Appl. Catal. A Gen.* **2019**, *584* (May). <https://doi.org/10.1016/j.apcata.2019.117185>.
- (9) Wambach, J.; Baiker, A.; Wokaun, A. CO₂ Hydrogenation over Metal / Zirconia Catalysts CO CO Hydrogenation over Metal / Zirconia Catalysts. *Phys. Chem. Chem. Phys.* **1999**, *1*, 5071–5080. <https://doi.org/10.1039/A904923A>.
- (10) Wang, W.; Wang, S.; Ma, X.; Gong, J. Recent Advances in Catalytic Hydrogenation of Carbon Dioxide. *Chem. Soc. Rev.* **2011**, *40* (7), 3703–3727. <https://doi.org/10.1039/c1cs15008a>.
- (11) Li, Z.; Wang, J.; Qu, Y.; Liu, H.; Tang, C.; Miao, S.; Feng, Z.; An, H.; Li, C. Highly Selective Conversion of Carbon Dioxide to Lower Olefins. *ACS Catal.* **2017**, *7* (12), 8544–8548. <https://doi.org/10.1021/acscatal.7b03251>.
- (12) Ticali, P.; Salusso, D.; Ahmad, R.; Ahoba-Sam, C.; Ramirez, A.; Shterk, G.; Lomachenko, K. A.; Borfecchia, E.; Morandi, S.; Cavallo, L.; Gascon, J.; Bordiga, S.; Olsbye, U. CO₂ Hydrogenation to Methanol and Hydrocarbons over Bifunctional Zn-Doped ZrO₂/Zeolite Catalysts. *Catal. Sci. Technol.* **2021**, *11* (4), 1249–1268.

- 1
2
3
4
5
6
7
8
9
10
11
12
13
14
15
16
17
18
19
20
21
22
23
24
25
26
27
28
29
30
31
32
33
34
35
36
37
38
39
40
41
42
43
44
45
46
47
48
49
50
51
52
53
54
55
56
57
58
59
60
- <https://doi.org/10.1039/D0CY01550D>.
- (13) Kattel, S.; Ramirez, P. J.; Chen, J. G.; Rodriguez, J. A.; Liu, P. Comment on “Active Sites for CO₂ Hydrogenation to Methanol on Cu/ZnO Catalysts.” *Science* (80-.). **2017**, *357* (6354), 1296–1299. <https://doi.org/10.1126/science.aal3573>.
- (14) Rozanov, V. V.; Krylov, O. V. Hydrogen Spillover in Heterogeneous Catalysis. *Usp. Khim.* **1997**, *66* (2), 127–130. <https://doi.org/10.1070/rc1997v066n02abeh000308>.
- (15) Conner, W. C.; Falconer, J. L. Spillover in Heterogeneous Catalysis. *Chem. Rev.* **1995**, *95* (3).
- (16) Ye, J.; Liu, C.; Mei, D.; Ge, Q. Active Oxygen Vacancy Site for Methanol Synthesis from CO₂ Hydrogenation on In₂O₃(110): A DFT Study. *ACS Catal.* **2013**, *3* (6), 1296–1306. <https://doi.org/10.1021/cs400132a>.
- (17) Gu, H.; Ding, J.; Zhong, Q.; Zeng, Y.; Song, F. Promotion of Surface Oxygen Vacancies on the Light Olefins Synthesis from Catalytic CO₂ Hydrogenation over Fe[Sbnd]K/ZrO₂ Catalysts. *Int. J. Hydrogen Energy* **2019**, *44* (23), 11808–11816. <https://doi.org/10.1016/j.ijhydene.2019.03.046>.
- (18) Zander, S.; Kunkes, E. L.; Schuster, M. E.; Schumann, J.; Weinberg, G.; Teschner, D.; Jacobsen, N.; Schlögl, R.; Behrens, M. The Role of the Oxide Component in the Development of Copper Composite Catalysts for Methanol Synthesis. *Angew. Chemie Int. Ed.* **2013**, *52* (25), 6536–6540. <https://doi.org/10.1002/anie.201301419>.
- (19) ARENA, F.; BARBERA, K.; ITALIANO, G.; BONURA, G.; SPADARO, L.; FRUSTERI, F. Synthesis, Characterization and Activity Pattern of Cu–ZnO/ZrO₂

- 1
2
3 Catalysts in the Hydrogenation of Carbon Dioxide to Methanol. *J. Catal.* **2007**, *249* (2),
4
5 185–194. <https://doi.org/10.1016/j.jcat.2007.04.003>.
6
7
8
9 (20) Zhan, H.; Li, F.; Gao, P.; Zhao, N.; Xiao, F.; Wei, W.; Zhong, L.; Sun, Y. Methanol
10
11 Synthesis from CO₂ Hydrogenation over La–M–Cu–Zn–O (M = Y, Ce, Mg, Zr) Catalysts
12
13 Derived from Perovskite-Type Precursors. *J. Power Sources* **2014**, *251*, 113–121.
14
15 <https://doi.org/10.1016/j.jpowsour.2013.11.037>.
16
17
18 (21) Fisher, I. A.; Bell, A. T. In Situ Infrared Study of Methanol Synthesis from H₂/CO over
19
20 Cu/SiO₂ and Cu/ZrO₂/SiO₂. *J. Catal.* **1998**, *178* (1), 153–173.
21
22 <https://doi.org/10.1006/jcat.1998.2134>.
23
24
25 (22) Cheng, K.; Gu, B.; Liu, X.; Kang, J.; Zhang, Q.; Wang, Y. Direct and Highly Selective
26
27 Conversion of Synthesis Gas into Lower Olefins: Design of a Bifunctional Catalyst
28
29 Combining Methanol Synthesis and Carbon-Carbon Coupling. *Angew. Chemie - Int. Ed.*
30
31 **2016**, *55* (15), 4725–4728. <https://doi.org/10.1002/anie.201601208>.
32
33
34
35 (23) Jiao, F.; Li, J.; Pan, X.; Xiao, J.; Li, H.; Ma, H.; Wei, M.; Pan, Y.; Zhou, Z.; Li, M.; Miao,
36
37 S.; Li, J.; Zhu, Y.; Xiao, D.; He, T.; Yang, J.; Qi, F.; Fu, Q.; Bao, X. Selective Conversion
38
39 of Syngas to Light Olefins. *Science (80-.)*. **2016**, *351* (6277), 1065–1068.
40
41 <https://doi.org/10.1126/science.aaf1835>.
42
43
44
45 (24) Wang, S.; Wang, P.; Qin, Z.; Chen, Y.; Dong, M.; Li, J.; Zhang, K.; Liu, P.; Wang, J.;
46
47 Fan, W. Relation of Catalytic Performance to the Aluminum Siting of Acidic Zeolites in
48
49 the Conversion of Methanol to Olefins, Viewed via a Comparison between ZSM-5 and
50
51 ZSM-11. *ACS Catal.* **2018**, *8* (6), 5485–5505. <https://doi.org/10.1021/acscatal.8b01054>.
52
53
54
55
56
57
58
59
60

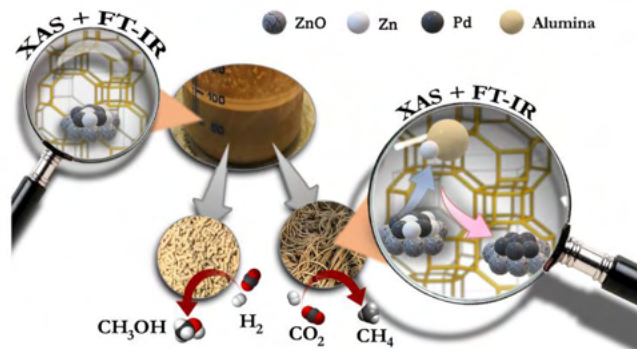
- 1
2
3
4
5
6
7
8
9
10
11
12
13
14
15
16
17
18
19
20
21
22
23
24
25
26
27
28
29
30
31
32
33
34
35
36
37
38
39
40
41
42
43
44
45
46
47
48
49
50
51
52
53
54
55
56
57
58
59
60
- (25) Olsbye, U.; Svelle, S.; Bjorgen, M.; Beato, P.; Janssens, T. V. W.; Joensen, F.; Bordiga, S.; Lillerud, K. P. Conversion of Methanol to Hydrocarbons: How Zeolite Cavity and Pore Size Controls Product Selectivity. *Angew. Chemie-International Ed.* **2012**, *51* (24), 5810–5831. <https://doi.org/10.1002/anie.201103657>.
- (26) Ramirez, A.; Ticali, P.; Salusso, D.; Cordero-Lanzac, T.; Ould-Chikh, S.; Ahoba-Sam, C.; Bugaev, A. L.; Borfecchia, E.; Morandi, S.; Signorile, M.; Bordiga, S.; Gascon, J.; Olsbye, U. Multifunctional Catalyst Combination for the Direct Conversion of CO₂ to Propane. *JACS Au* **2021**, *1* (10), 1719–1732. <https://doi.org/10.1021/jacsau.1c00302>.
- (27) Arora, S. S.; Nieskens, D. L. S.; Malek, A.; Bhan, A. Lifetime Improvement in Methanol-to-Olefins Catalysis over Chabazite Materials by High-Pressure H₂ Co-Feeds. *Nat. Catal.* **2018**, *1* (9), 666–672. <https://doi.org/10.1038/s41929-018-0125-2>.
- (28) Mitchell, S.; Michels, N. L.; Pérez-Ramírez, J. From Powder to Technical Body: The Undervalued Science of Catalyst Scale Up. *Chem. Soc. Rev.* **2013**, *42* (14), 6094–6112. <https://doi.org/10.1039/C3CS60076A>.
- (29) Ravel, B.; Newville, M. ATHENA, ARTEMIS, HEPHAESTUS: Data Analysis for X-Ray Absorption Spectroscopy Using IFEFFIT. *J. Synchrotron Radiat.* **2005**, *12* (4), 537–541. <https://doi.org/10.1107/S0909049505012719>.
- (30) Pinilla-herrero, I.; Borfecchia, E.; Cordero-lanzac, T.; Mentzel, U. V.; Joensen, F.; Lomachenko, K. A.; Bordiga, S.; Olsbye, U.; Beato, P.; Svelle, S. Finding the Active Species: The Conversion of Methanol to Aromatics over Zn-ZSM-5 / Alumina Shaped Catalysts. *J. Catal.* **2021**, *394*, 416–428. <https://doi.org/10.1016/j.jcat.2020.10.024>.

- 1
2
3
4
5
6
7
8
9
10
11
12
13
14
15
16
17
18
19
20
21
22
23
24
25
26
27
28
29
30
31
32
33
34
35
36
37
38
39
40
41
42
43
44
45
46
47
48
49
50
51
52
53
54
55
56
57
58
59
60
- (31) Peterson, E. J.; Halevi, B.; Kiefer, B.; Spilde, M. N.; Datye, A. K.; Peterson, J.; Daemen, L.; Llobet, A.; Nakotte, H. Aerosol Synthesis and Rietveld Analysis of Tetragonal (B1) PdZn. *J. Alloys Compd.* **2011**, *509* (5), 1463–1470. <https://doi.org/10.1016/J.JALLCOM.2010.09.149>.
- (32) Stangeland, K.; Kalai, D.; Li, H.; Yu, Z. CO₂ Methanation: The Effect of Catalysts and Reaction Conditions. *Energy Procedia* **2017**, *105*, 2022–2027. <https://doi.org/10.1016/j.egypro.2017.03.577>.
- (33) Wambach, J.; Baiker, A.; Wokaun, A. CO₂ Hydrogenation over Metal/Zirconia Catalysts. *Phys. Chem. Chem. Phys.* **1999**, *1* (22), 5071–5080. <https://doi.org/10.1039/a904923a>.
- (34) Tew, M. W.; Emerich, H.; Van Bokhoven, J. A. Formation and Characterization of PdZn Alloy: A Very Selective Catalyst for Alkyne Semihydrogenation. *J. Phys. Chem. C* **2011**, *115* (17), 8457–8465. <https://doi.org/10.1021/jp1103164>.
- (35) Gentzen, M.; Doronkin, D. E.; Sheppard, T. L.; Zimina, A.; Li, H.; Jelic, J.; Studt, F.; Grunwaldt, J. D.; Sauer, J.; Behrens, S. Supported Intermetallic PdZn Nanoparticles as Bifunctional Catalysts for the Direct Synthesis of Dimethyl Ether from CO-Rich Synthesis Gas. *Angew. Chemie - Int. Ed.* **2019**, *58* (44), 15655–15659. <https://doi.org/10.1002/anie.201906256>.
- (36) Ahoba-Sam, C.; Borfecchia, E.; Lazzarini, A.; Bugaev, A.; Isah, A. A.; Taoufik, M.; Bordiga, S.; Olsbye, U. On the Conversion of CO₂ to Value Added Products over Composite PdZn and H-ZSM-5 Catalysts: Excess Zn over Pd, a Compromise or a Penalty? *Catal. Sci. Technol.* **2020**, No. 1, 4373–4385. <https://doi.org/10.1039/D0CY00440E>.

- 1
2
3
4
5
6
7
8
9
10
11
12
13
14
15
16
17
18
19
20
21
22
23
24
25
26
27
28
29
30
31
32
33
34
35
36
37
38
39
40
41
42
43
44
45
46
47
48
49
50
51
52
53
54
55
56
57
58
59
60
- (37) Ruzzi, P.; Salusso, D.; Baravaglio, M.; Szeto, K. C.; De Mallmann, A.; Jiménez, L. G.; Godard, C.; Benayad, A.; Morandi, S.; Bordiga, S.; Taoufik, M. Supported PdZn Nanoparticles for Selective CO₂ Conversion, through the Grafting of a Heterobimetallic Complex on CeZrO_x. *Appl. Catal. A Gen.* **2022**, *635*, 118568. <https://doi.org/10.1016/J.APCATA.2022.118568>.
- (38) Gallagher, J. R.; Childers, D. J.; Zhao, H.; Winans, R. E.; Meyer, R. J.; Miller, J. T. Structural Evolution of an Intermetallic Pd-Zn Catalyst Selective for Propane Dehydrogenation. *Phys. Chem. Chem. Phys.* **2015**, *17* (42), 28144–28153. <https://doi.org/10.1039/c5cp00222b>.
- (39) Jerero, E.; Lebarbier, V.; Datye, A.; Wang, Y.; Vohs, J. M. Interaction of CO with Surface PdZn Alloys. *Surf. Sci.* **2007**, *601* (23), 5546–5554. <https://doi.org/10.1016/j.susc.2007.09.031>.
- (40) Föttinger, K. The Effect of CO on Intermetallic PdZn/ZnO and Pd₂Ga/Ga₂O₃ Methanol Steam Reforming Catalysts: A Comparative Study. *Catal. Today* **2013**, *208*, 106–112. <https://doi.org/10.1016/j.cattod.2012.12.004>.
- (41) Groppo, E.; Bertarione, S.; Rotunno, F.; Agostini, G.; Scarano, D.; Pellegrini, R.; Leofanti, G.; Zecchina, A.; Lamberti, C. Role of the Support in Determining the Vibrational Properties of Carbonyls Formed on Pd Supported on SiO₂-Al₂O₃, Al₂O₃, and MgO. *J. Phys. Chem. C* **2007**, *111* (19), 7021–7028. <https://doi.org/10.1021/jp0666434>.
- (42) Zecchina, A.; Scarano, D.; Bordiga, S.; Ricchiardi, G.; Spoto, G.; Geobaldo, F. IR Studies of CO and NO Adsorbed on Well Characterized Oxide Single Microcrystals. *Catal. Today*

- 1
2
3
4
5
6
7
8
9
10
11
12
13
14
15
16
17
18
19
20
21
22
23
24
25
26
27
28
29
30
31
32
33
34
35
36
37
38
39
40
41
42
43
44
45
46
47
48
49
50
51
52
53
54
55
56
57
58
59
60
- 1996**, *27* (3–4), 403–435. [https://doi.org/10.1016/0920-5861\(95\)00202-2](https://doi.org/10.1016/0920-5861(95)00202-2).
- (43) Schnabel, K. H.; Fricke, R.; Girmus, I.; Jahn, E.; Löffler, E.; Parlitz, B.; Peuker, C. Catalytic and Infrared Spectroscopic Investigations of the Molecular Sieve Types SAPO-34 and SAPO-11. *J. Chem. Soc. Faraday Trans.* **1991**, *87* (21), 3569–3574. <https://doi.org/10.1039/FT9918703569>.
- (44) Rodriguez, J. A. Physical and Chemical Properties of Bimetallic Surfaces. *Surf. Sci. Rep.* **1996**, *24* (7–8), 223–287. [https://doi.org/10.1016/0167-5729\(96\)00004-0](https://doi.org/10.1016/0167-5729(96)00004-0).
- (45) Kipnis, M. A.; Samokhin, P. V.; Volnina, E. A.; Magomedova, M. V.; Turkova, T. V. Features of Carbon Dioxide and Monoxide Hydrogenation in the Presence of ZnO/Al₂O₃ and ZnO. *Kinet. Catal.* **2022**, *63* (3), 292–303. <https://doi.org/10.1134/S0023158422030041/FIGURES/7>.
- (46) Liu, X.; Wang, M.; Yin, H.; Hu, J.; Cheng, K.; Kang, J.; Zhang, Q.; Wang, Y. Tandem Catalysis for Hydrogenation of CO and CO₂ to Lower Olefins with Bifunctional Catalysts Composed of Spinel Oxide and SAPO-34. *ACS Catal.* **2020**, *10* (15), 8303–8314. https://doi.org/10.1021/ACSCATAL.0C01579/SUPPL_FILE/CS0C01579_SI_001.PDF.
- (47) Dang, S.; Gao, P.; Liu, Z.; Chen, X.; Yang, C.; Wang, H.; Zhong, L.; Li, S.; Sun, Y. Role of Zirconium in Direct CO₂ Hydrogenation to Lower Olefins on Oxide/Zeolite Bifunctional Catalysts. *J. Catal.* **2018**, *364*, 382–393. <https://doi.org/10.1016/J.JCAT.2018.06.010>.

1
2
3
4
5
6
7
8
9
10
11
12
13
14
15
16
17
18
19
20
21
22
23
24
25
26
27
28
29
30
31
32
33
34
35
36
37
38
39
40
41
42
43
44
45
46
47
48
49
50
51
52
53
54
55
56
57
58
59
60



338x190mm (96 x 96 DPI)